Disorder in Laves Phases

DISSERTATION

Zur Erlangung des akademischen Grades

Doctor rerum naturalium
(Dr. rer. nat.)

vorgelegt

der Fakultät Mathematik und Naturwissenschaften
der technischen Universität Dresden

von

Dipl.-Ing. Alexander Kerkau
geboren am 9. Juni 1980 in Dresden

Eingereicht am:

Die Dissertation wurde in der Zeit von Dezember 2007 bis August 2012 am
Max-Planck-Institut für Chemische Physik fester Stoffe in Dresden angefertigt.

To Sina, Linus and Sophia

Acknowledgement

First of all, I would like to express my gratitude to Prof. Juri Grin for providing me this interesting topic and the opportunity to compose my doctoral thesis at the Max Planck Institute for Chemical Physics of Solids. I also want to thank Prof. Juri Grin and Prof. Dr. Bernd Kieback (Institut für Werkstoffwissenschaft, TU-Dresden) for being the referees of my thesis.

I want to express my deep and sincere gratitude to my supervisor Priv.-Doz. Dr. Guido Kreiner for his support and guidance throughout the research. His understanding, encouragement and help on a personal and professional level provided the basis for the successful completion of this work. And also his cakes were always highly appreciated.

I want to thank Dr. Alim Ormeci for his patience in explaining DFT and FPLO. Whenever I had a question, he has always taken the time for a detailed answer. I am grateful to Dr. Marek Mihalkovic (Institute of Physics, Slovak Academy of Sciences, Bratislava, Slovakia) for his explanations on DFT and VASP and for providing a number of computer scripts which have saved me a lot of time during the calculations. My warm thanks are due to Dr. Manuel Brando, who measured and taught me about the magnetic properties of materials. I want to thank Dr. Ulrich Burkhard, Ms. Sylvia Kostmann, Ms. Petra Scheppan and Ms. Monika Eckert for the preparation of metallographic specimens and their microscopy, Dr. Horst Borrmann and Mr. Steffen Hückmann for single crystal and powder X-ray diffraction, Dr. Stefan Hoffmann and Ms. Susann Scharsach for thermal analysis and Dr. Gudrun Aufferman, Ms. Ulrike Schmidt and Ms. Anja Völzke for countless chemical analyses.

This work was performed within the inter-institutional research initiative *The Nature of Laves Phases – From Atomic to Mesoscopic Phenomena* funded by the Max Planck Society. Some of the results presented in this study originate from a collaboration with research groups from other Max-Planck-Institutes. I want to thank Dr. Frank Stein (Max-Planck-Institut für Eisenforschung GmbH, Düsseldorf) and Dr. Andreas Leineweber (Max Planck Institute for Intelligent Systems, formerly Max Planck Institute for Metals Research, Stuttgart) for their encouragement and the interest in my topic during our regular workshops.

I would also like to thank all colleagues and friends at the institute for their constant helpfulness and friendship and for providing such a good working atmosphere. Finally I want to thank my parents as well as my own little family. I'll be home in half an hour.

Contents

Part I

General Part

1 Introduction

Intermetallic compounds are solid phases containing two or more metallic elements, whose crystal structure differs from that of its constituents [1]. The largest group among these compounds with more than 1400 binary and ternary representatives are the so-called *Laves phases*. The classification of an intermetallic compound as a Laves phase is solely based on the atomic configuration and the component ratio in the crystal structure. With the ideal composition AB_2, the Laves phases crystallize in three closely related structure types which are named after their representatives, $MgCu_2$ (C15, cubic), $MgZn_2$ (C14, hexagonal) and $MgNi_2$ (C36, hexagonal). Laves phases are built by almost all metals of the periodic system of the elements. A significant feature of many of these is the formation of broad homogeneity ranges by mutual substitution of atoms in combination with composition or temperature dependent phase transformations between the different Laves phase polytypes.

Laves phases have received considerable attention in recent years as potential structural and functional materials. They combine high melting points with considerable creep resistance, high strength and fracture toughness and good corrosion and oxidation resistance. Some Laves phases like $NbFe_2$ [2] or $TaFe_2$ [3] show intriguing magnetic and electronic properties which provide a deeper inside into phenomenons like quantum criticality. Especially transition-metal based Laves phases like $NbCr_2$ [4] and $ZrCr_2$ [5] are promising candidates for the development of new high-temperature structural materials. The major drawback of the Laves phases, however, is their low-temperature brittleness. Many experimental and theoretical investigations have shown, that the low-temperature ductility can be improved by controlling the crystal structure with the help of phase transformations, by mechanical twinning or the addition of third elements. The addition of ternary alloying elements can alter the physical and electronic properties of the Laves phases and plays an important role in the composition dependent stability of the different polytypes. Some ternary Laves phases show an interesting phenomenon called site occupation reversal. It describes a composition dependent behavior of the alloying elements which prefer to occupy different crystallographic sites at different concentrations. The understanding of the point defect structure/mechanism and the site occupation of the alloying elements is thus of critical importance for the proper description of phase stability.

The basis for the broad application of any metallic material is the knowledge of the corresponding phase diagram. The experimental determination of phase diagrams however, is tedious, time consuming and expensive work and the huge abundance of Laves phase makes this an impractical task. Thus, the time it takes to discover new advanced materials and to move them from the laboratory to the commercial market place is fairly long today. A cheap and fast enhancement for the development of new materials is the calculation of phase diagrams and physical properties using techniques like CALPHAD (CALculation of PHAse Diagrams) and DFT (Density Functional Theory).

Very recently the *Office of Science and Technology Policy* of the *United States White House* announced to provide a budget of $100 million to launch the *Materials Genome Initiative* [6, 7]. The aim of this initiative is to provide the infrastructure and training needed to discover, develop, manufacture, and deploy advanced materials in a more expeditious and economical way [8]. One of the project's three supporting legs is the calculation and prediction of crystal structures and physical properties using advanced *Computational tools*. "An early benchmark will be the ability to incorporate improved predictive modeling algorithms of materials behavior into existing product design tools. For example, the crystal structure and physical properties of the materials [...]." [8]. Their computational tools of choice are the same as used in this work to predict crystal structures and site occupation factors.

Contents of this work is the investigation of the substitutional disorder in binary and ternary Laves phases. This includes the experimental determination of the composition dependent stability of the Laves phase polytypes and the distribution of the substitution atoms in the crystal lattice of the respective phases, i.e., the site occupation factors (*s.o.f.*). For this purpose, detailed experimental studies on the two systems Cr–Co–Nb and Fe–Ta–V were performed and the Laves phase polytypes, their homogeneity ranges, the lattice parameters and the site occupation factors were determined. The experimental results are compared with the results obtained from quantum mechanical calculations. DFT is used to determine the composition dependent enthalpies of formation which serve as a measure for the stability of the different Laves phase polytypes. Additionally, the applicability of various approximations and their influence on the results has been checked. This study is thus also supposed to develop and improve the tools necessary for the calculation of phase stability and homogeneity ranges in ternary phases.

Chapter two in the first part of this work describes the crystal structures of the Laves phases in detail with focus on the polytype stability, the site occupation and the c/a-ratio of hexagonal C14 Laves phases. Subsequently, the phase diagrams of the investigated systems and the occurring Laves phases are discussed. Chapter three briefly describes the experimental and theoretical methods used in this work. The last section of part one gives a detailed explanation of how the phase stability, the lattice parameters and the site occupation factors are calculated. The second part "Results and discussion" contains the discussion of the experimental and theoretical results for the intensively investigated systems Co–Cr–Nb (chapter five) and Fe–Ta–V (chapter six). Several other ternary C14 Laves phases and their site occupation behavior are studied in chapter seven. The thesis is concluded with a summary in chapter eight. Several additional information is contained in the appendix.

2 Laves phases

2.1 General principles

Laves phases are intermetallic compounds with the ideal composition AB_2 and crystallize in one of the three crystal structure types $MgCu_2$ (C15, cubic), $MgZn_2$ (C14, hexagonal) and $MgNi_2$ (C36, hexagonal). They are structural polytypes, i.e., they are build up from common structural building units which are arranged in different stacking orders. In the first half of the last century the crystal structures of the three polytypes were described by FRIAUF [9, 10] and by LAVES and WITTE [11]. SCHULZE [12] emphasized the close relationship of the three crystal structures and established the term *Laves phases*. Since FRIAUF was the first one investigating the structures of $MgCu_2$ and $MgZn_2$ these phases were also referred to as Friauf-Laves phases. SAMSON [13] who investigated the building principles of Laves phases called them only Friauf phases.

Laves phases exhibit a distinct crystallographic arrangement of the atoms. The crystal structures can be described as a close packing of two different sized spheres A and B with an ideal ratio of 1:2. The A atoms are the larger and the B atoms the smaller of the two elements comprising the binary AB_2 structure. The ideal radius ratio r_A/r_B obtained from the hard sphere model is $\sqrt{3/2} \approx 1.225$. This corresponds to a space filling of 71%[1]. An analysis of all known Laves phase structures shows however, that Laves phases are forming with radius ratios in the range of 1.05 - 1.7 [4, 15]. The B atoms form a network of tetrahedra which are connected face-to-face or vertex-to-vertex. The larger A atoms fit into the interstices enclosed by the network of B atom tetrahedra. Since only tetrahedral voids are formed, FRANK and KASPER [16, 17] classified the Laves

---

[1] For comparison, the space filling for simple cubic, face-centered cubic, body-centered cubic and hexagonal close-packed structures are 52%, 74%, 68% and 74%, respectively [14].

phases as *tetrahedrally closed packed (tcp)* structures, a large group of intermetallic compounds also referred to as Frank-Kasper phases. Four different coordination type polyhedra with the coordination numbers (CN) 12, 14, 15 and 16 appear in *tcp* structures. These so called Frank-Kasper-polyhedra are the only four polyhedra that are convex with only triangular faces, and 5 or 6 triangles meeting at every vertex [18]. Laves phases represent the most simple *tcp* structures with only two coordination type polyhedra, CN12 and CN16. The Frank-Kasper-polyhedron with the coordination number 12 is a distorted icosahedron (20 faces), the one with the coordination number 16 an icosioctahedron (28 faces). The latter can be described as a fourfold capped truncated tetrahedron. The large A atom in the center of the CN16 polyhedron is surrounded by four A and twelve B atoms, and the smaller B atom in the center of the CN12 polyhedron by six A and six B atoms.

The building principles of Laves phases can also be described by the stacking of fundamental building blocks (slabs), build from B_4 tetrahedra and B_{12} truncated tetrahedra [13]. These slabs in turn are build by the stacking of different planar layers of atoms. Only two types of atomic layers, namely triangular and Kagomé nets are necessary for this description. They are shown in figure **2.1**.

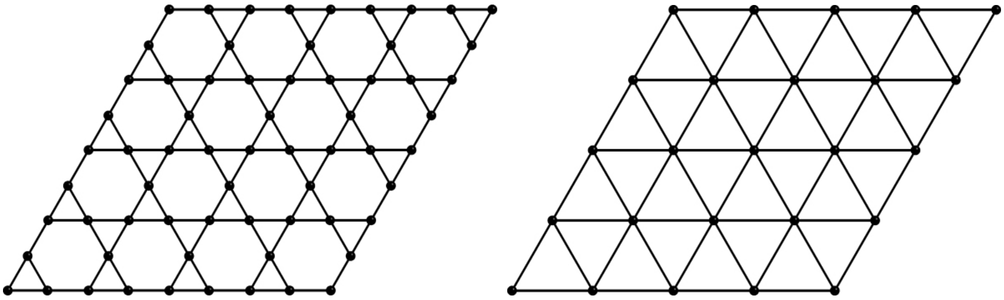

Figure 2.1: The fundamental atomic layers in the crystal structure of the Laves phases. B atoms form Kagomè (left) and triangular nets (right), A atoms form only triangular nets.

The smaller B atoms form triangular nets and Kagomé nets, while the larger A atoms form only triangular nets. Five of these planes are stacked parallel to the hexagonal ab-plane in the following order to form a `Samson` slab [15]:

(1)	Kagomé net of B atoms	$z = 0$
(2)	Triangular net of A atoms	$z = 3/8 \cdot h$
(3)	Triangular net of B atoms	$z = 1/2 \cdot h$
(4)	Triangular net of A atoms	$z = 5/8 \cdot h$
(5)	Kagomé net of B atoms	$z = h$

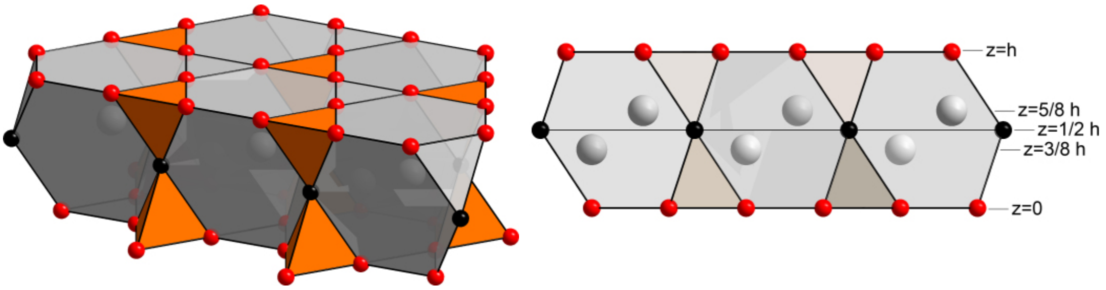

Figure 2.2: A SAMSON slab (left) is build from B_4 tetrahedra (orange) and B_{12} truncated tetrahedra (gray). The A atoms are located in the center of the B_{12} polyhedra. A slab (right) has the thickness h and is build from five planar atomic layers.

A schematic drawing of such a fundamental SAMSON slab is shown in figure **2.2** with special emphasis on the B_4 tetrahedra and B_{12} truncated tetrahedra and the comprising planar atomic layers. The thickness of a SAMSON slab is h which is equal to the distance between two Kagomé nets. The crystal structures of the Laves phases can now be described by a periodic stacking of these slabs. If the starting layer is denoted as A, the two possible shifted layers are denoted as B and C. An infinite number of stacking sequences would be possible, however due to energetic reasons only short stacking sequences are observed. The structures of C14, C15 and C36 correspond to the three shortest possible sequences AB', ABC and $AB'A'C$[2], respectively (see fig. **2.3**). The crystal structures of ternary compounds with more complicated stacking sequences and up to 21 slabs per unit cell have been investigated by KOMURA *et al.* [19–25] and are commonly referred to as Komura phases (see fig. **2.3**). The Komura phases may be considered as a subgroup of the Laves phases, however, no binary compounds with such complicated stacking sequences do exist. In the following sections the crystal structures of the three polytypes C15, C14 and C36 will be described in more detail with particular emphasis on the atomic environment of the different atoms.

---

[2] The prime denotes a rotation of the slab of about 180°.

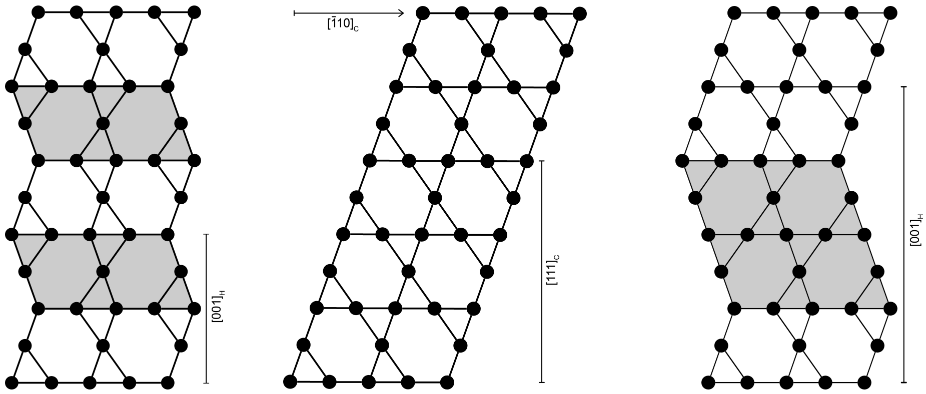

(a) C14 (b) C15 (c) C36

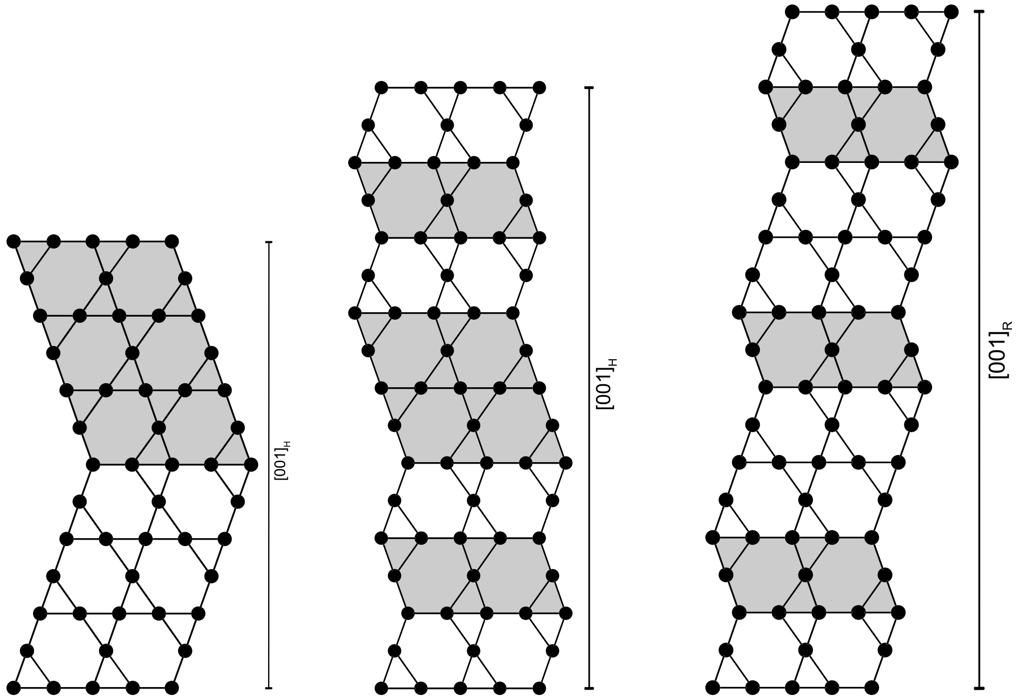

(d) Mg($Ni_{0.45}Cu_{0.55}$)$_2$ (e) Mg($Zn_{0.97}Ag_{0.03}$)$_2$ (f) MgCuAl

Figure 2.3: Stacking order and orientation of the fundamental building blocks in the Laves phase polytypes and three Komura phases. The polytypes C14, C15 and C36 contain two, three and four Samson slabs per unit cell, respectively. The Komura phases Mg($Ni_{0.45}Cu_{0.55}$)$_2$ [21] (d), Mg($Zn_{0.97}Ag_{0.03}$)$_2$ [24] (e) and MgCuAl [19] (f) contain six, eight and nine Samson slabs per unit cell, respectively. Other stacking variants with 10 and 21 layer phases have also been reported by Komura *et al.* [20, 22–25].

2.2 The Laves phase polytypes C15, C14 and C36

2.2.1 The $MgCu_2$ type (C15)

The prototype of the C15 structure type, $MgCu_2$ crystallizes in the face-centered cubic (fcc) lattice with space group $Fd\bar{3}m$ (No. 227) and eight formula units, i.e., 24 atoms per unit cell. The asymmetric unit of the crystal structure contains only two atoms, and thus all A and B atoms are symmetry equivalent. The two different coordination type polyhedra around the A and B atoms are shown in figure **2.4**.

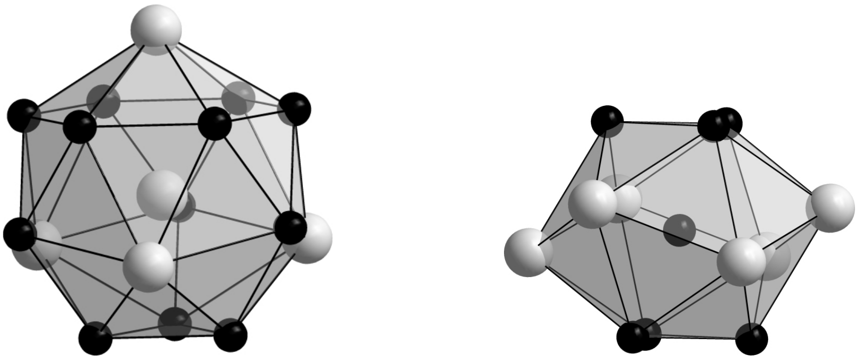

(a) $A(8b)$ (b) $B(16c)$

Figure 2.4: The coordination polyhedra in C15 type Laves phases: an icosioctahedron (CN16) around A and a distorted icosahedron (CN12) around B. A: large gray spheres, B: small black spheres. The Wyckoff positions are given in parentheses.

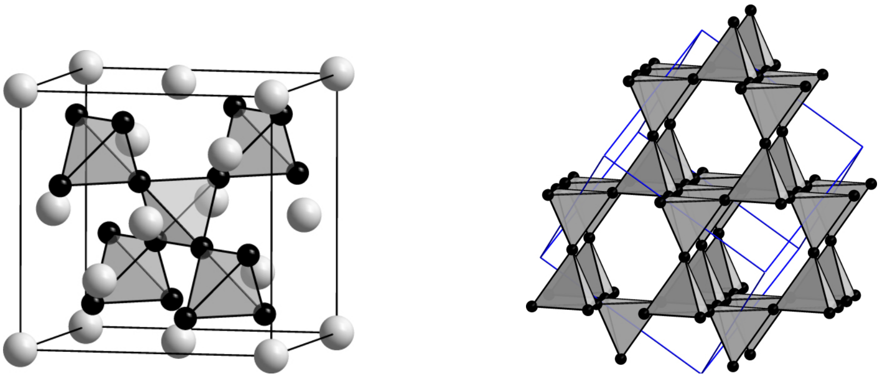

Figure 2.5: The unit cell ($Fd\bar{3}m$, origin choice 1) (left) and the tetrahedral network of the B atoms (right) in C15 type Laves phases. A: large gray spheres, B: small black spheres.

The large A atom is surrounded by four A and twelve B atoms, the smaller B atom by six A atoms in a chair like configuration and six B atoms. The B atoms are linked to an infinite three-dimensional network of vertex-sharing tetrahedra (fig. **2.5**), so that every B atom is connected with six other B atoms. The large voids are arranged like the carbon atoms in cubic diamond. The large A atoms occupy these voids and thus have the same arrangement. The stacking of the fundamental slabs in C15 occurs not along the crystallographic c direction but along the body diagonals of the cube, the $\langle 111\rangle$ directions. To allow for a better comparison with the other polytypes C15 can be viewed in the rhombohedral setting with hexagonal axes as reference. In this setting the stacking again occurs along the hexagonal c direction with the stacking order $ABC\ldots$. The consecutive slabs are shifted by $\pm 1/3$ along $[\bar{1}10]$ as shown in figure **2.3**. The fractional atomic coordinates of the C15 structure type are listed for different settings in table **2.1**.

Table 2.1: Fractional atomic coordinates of the C15 structure type in the cubic setting with origin choice 1 and 2 and in the rhombohedral setting with hexagonal axes.

Cubic: $Fd\bar{3}m$ (No. 227, origin choice 1), $Z = 8$

Atom	Wyckoff position	x	y	z	Figure symbol
B	16d	5/8	5/8	5/8	●
A	8a	0	0	0	○

Cubic: $Fd\bar{3}m$ (No. 227, origin choice 2), $Z = 8$

Atom	Wyckoff position	x	y	z
B	16c	0	0	0
A	8b	3/8	3/8	3/8

Rhombohedral: $R\bar{3}m$ (No. 166, hexagonal axes), $Z = 6$

Atom	Wyckoff position	x	y	z
$B1$	9d	1/2	0	1/2
A	6c	0	0	5/8
$B2$	3a	0	0	0

2.2.2 The $MgZn_2$ type (C14)

The prototype of the C14 structure type – $MgZn_2$ – crystallizes with the hexagonal space group $P6_3/mmc$ (No. 194) and four formula units, i.e., 12 atoms per unit cell. The asymmetric unit contains three atoms. All A atoms are symmetry equivalent, while the B atoms occupy two different crystallographic Wyckoff positions, $2a$ and $6h$. With the atomic coordinates x of the $B1(6h)$ atoms and z of the A atoms, and the c/a ratio of the hexagonal unit cell, the C14 structure exhibits more structural degrees of freedom than C15. These become manifest in structural distortions of the Kagomé nets often observed in C14 Laves phases. Due to the two different B sites, the C14 structure exhibits two different CN12 coordination type polyhedra around $B1(6h)$ and $B2(2a)$ which differ with respect to the arrangement of the A and the type and arrangement of the B atoms at their vertices. They are shown in figure **2.6**. $B1(6h)$ is surrounded by a non-planar hexagon of six A atoms in a boat-like conformation and by six B atoms, four $B1$ and two $B2$. The A atoms around $B2(2a)$ have a chair-like conformation and the six surrounding B atoms are all of the same type $B1$. The A atoms have only one type of CN16 coordination polyhedron. They are surrounded by four A and twelve B atoms (three $B2$ and nine $B1$).

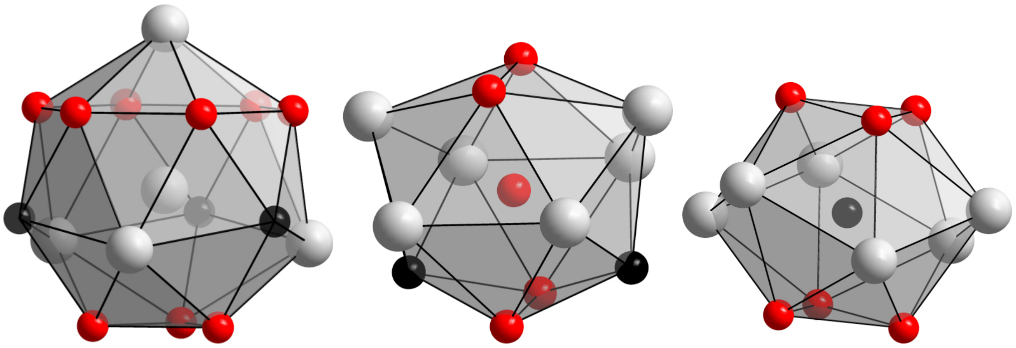
(a) $A(4f)$ (b) $B1(6h)$ (c) $B2(2a)$

Figure 2.6: The coordination polyhedra in C14 type Laves phases: an icosioctahedron (CN16) around A and the distorted icosahedra (CN12) around $B1$ and $B2$. A: large gray spheres, $B1$: small red spheres, $B2$: small black spheres. The Wyckoff positions are given in parentheses.

The B network in C14, shown in figure **2.7** (b), consists of alternately vertex- and base-connected tetrahedra, thereby forming infinite chains of apically-fused trigonal

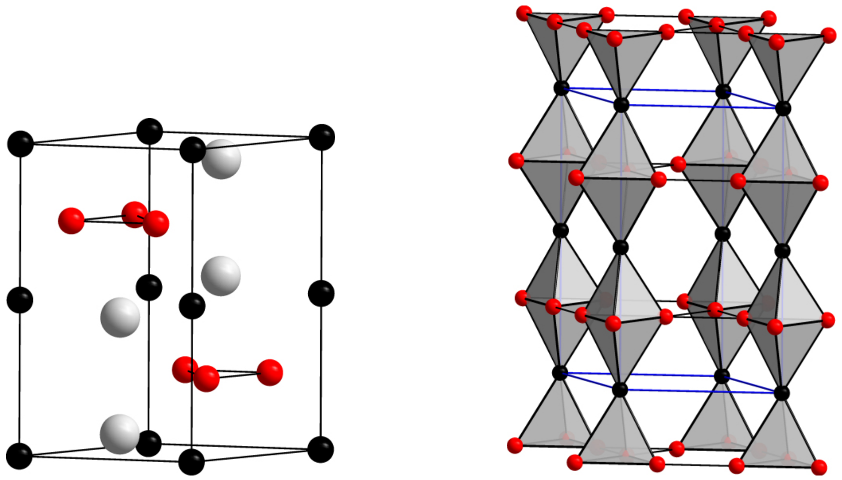

Figure 2.7: The unit cell (left) and the tetrahedral network (right) of the B atoms in C14 type Laves phases. A: large gray spheres, $B1$: small red spheres, $B2$: small black spheres.

bipyramids running along the crystallographic c direction [001]. These chains are linked by vertex connections in the ab-plane, thus forming large polyhedra in the geometrical shape of truncated tetrahedra. The tetrahedral voids are arranged like the carbon atoms in hexagonal diamond. The larger A atoms occupy the centers of these voids and form a three-dimensional four-connected network of wurtzite type. The C14 structure is build by the stacking of two of the fundamental slabs in the order $AB' \ldots$ along the crystallographic c direction (fig. **2.3**). The second slab B is rotated by 180° and shifted by 1/3 along $[\bar{1}10]$ with respect to A. The fractional atomic coordinates of the C14 structure type are shown in table **2.2**.

Table 2.2: Fractional atomic coordinates of the C14 structure type. Space group $P6_3/mmc$ (No. 194), $Z = 4$.

Atom	Wyckoff position	x	y	z	Ideal	Figure symbol
$B1$	$6h$	x	$2x$	1/4	$x = 1/6$	🔴
A	$4f$	1/3	2/3	z	$z = 9/16$	⚪
$B2$	$2a$	0	0	0		⚫

2.2.3 The $\mathrm{MgNi_2}$ type (C36)

The C36 structure is often viewed as the link between C15 and C14. Its structure is build by an alternating hexagonal (180° rotation + 1/3 shift along $[\bar{1}10]$) and cubic (1/3 shift along $[\bar{1}10]$) stacking of four of the fundamental slabs. The stacking sequence is given by $AB'A'C\ldots$ (fig. **2.3**). The C36 prototype $\mathrm{MgNi_2}$ crystallizes in the hexagonal space group $P6_3/mmc$ with eight formula units, i.e., 24 atoms per unit cell. The fractional atomic coordinates of the C36 structure type are shown in table **2.3**. The asymmetric unit contains five atoms, three sites for the smaller B atoms and two site for the larger A atoms. Accordingly, there are two different coordination polyhedra for the A and three for the B atoms which differ in the type and the arrangement of the atoms at their vertices. The icosahedron around $B1$ (fig. **2.8** (c)) has the A atoms arranged in a boat-like configuration, while around $B2$ and $B3$ (fig. **2.8** (d) and (e)) they are arranged in a chair-like configuration. Furthermore, the type of B atoms in the three icosahedra differ. $B1$ is surrounded by $B1$ and $B3$, $B2$ by $B2$ and $B3$, and $B3$ by $B1$ and $B2$.

Table 2.3: Fractional atomic coordinates of the C36 structure type. Space group $P6_3/mmc$ (No. 194), $Z = 8$.

Atom	Wyckoff position	x	y	z	Ideal	Figure symbol
$B1$	$6h$	x	$2x$	1/4	$x = 1/6$	●
$B2$	$6g$	1/2	0	0		🔴
$B3$	$4f$	1/3	2/3	z	$z = 1/8$	🟢
$A1$	$4f$	1/3	2/3	z	$z = 21/32$	⚪
$A2$	$4e$	0	0	z	$z = 3/32$	●

Figure **2.10** shows the network of the B atom tetrahedra of all three Laves phase polytypes viewed along the [110] direction. It emphasizes again their close structural relationship. From this figure it is obvious how the C14 and the C15 phase differ and that the C36 phase contains structural elements of both of them.

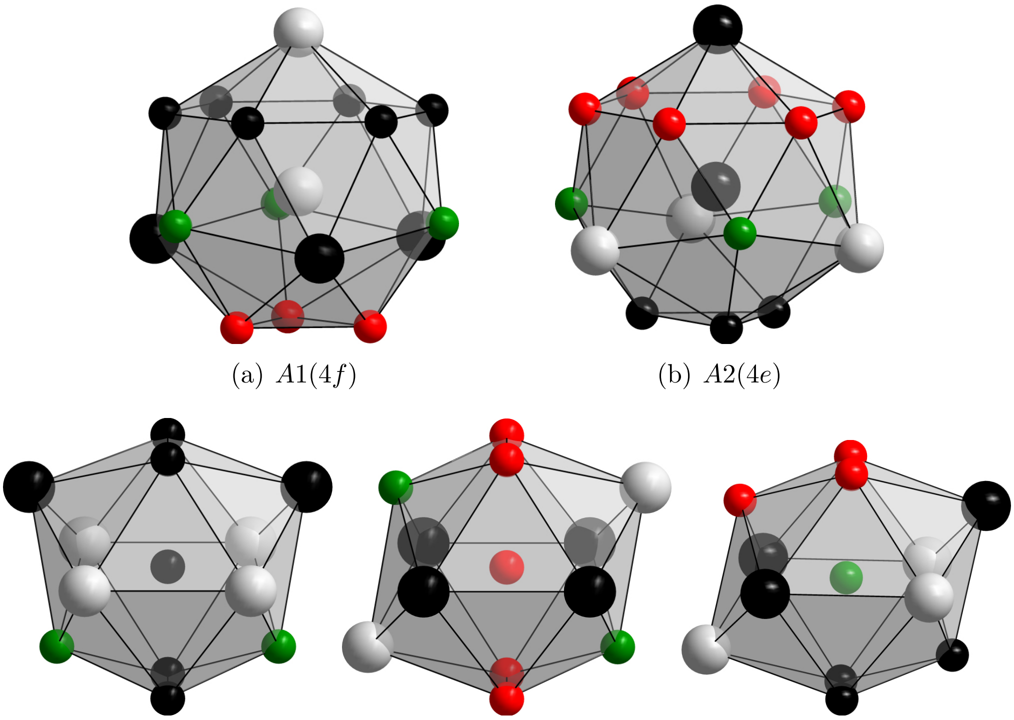

(a) $A1(4f)$ (b) $A2(4e)$

(c) $B1(6h)$ (d) $B2(6g)$ (e) $B3(4f)$

Figure 2.8: The coordination polyhedra in C36 type Laves phases: the icosioctahedra (CN16) around $A1$ and $A2$ and the distorted icosahedra (CN12) around $B1$, $B2$ and $B3$. $A1$: large gray spheres, $A2$: large black spheres, $B1$: small black spheres, $B2$: small red spheres, $B3$: small green spheres. The Wyckoff positions are given in parentheses.

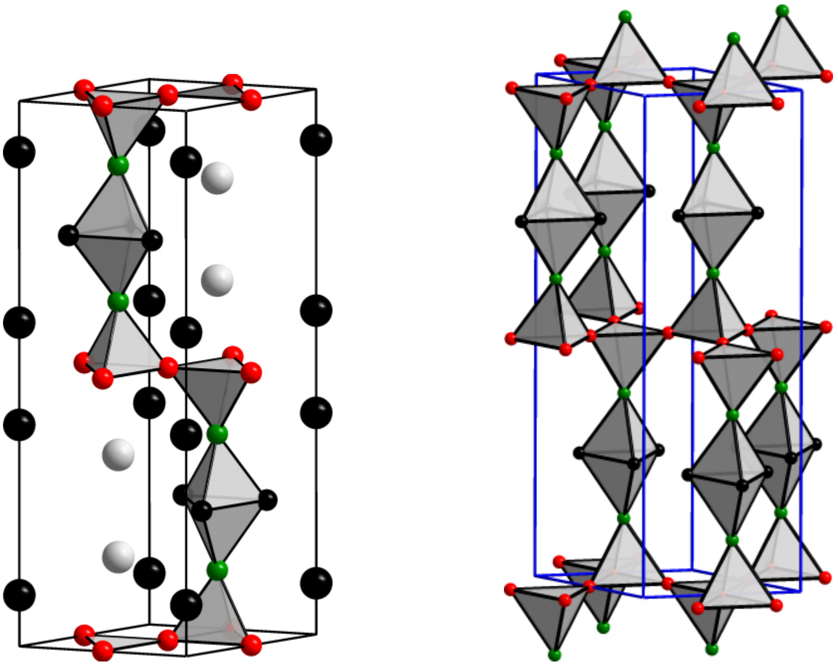

Figure 2.9: The unit cell (left) and the tetrahedral network of the B atoms (right) in C36 type Laves phases. $A1$: large gray spheres, $A2$: large black spheres, $B1$: small black spheres, $B2$: small red spheres, $B3$: small green spheres.

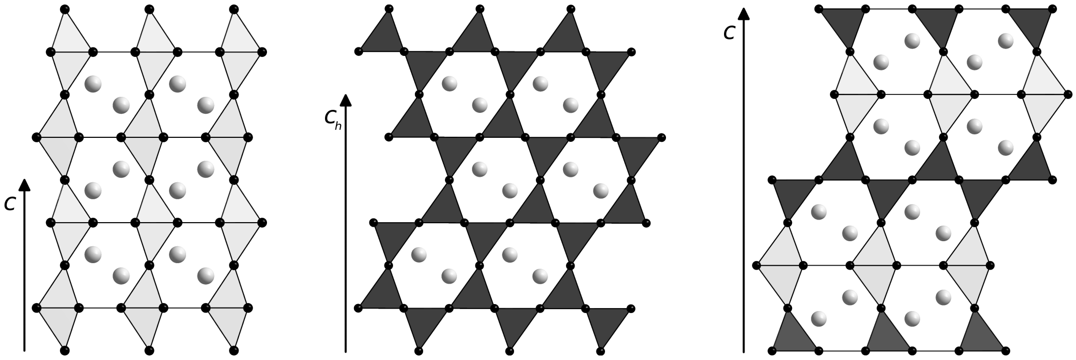

(a) C14 (b) C15 (rhombohedral) (c) C36

Figure 2.10: Comparison of the tetrahedral networks of B atoms of the different Laves phase structure types viewed along the [110] direction [26]. For better comparison, the C15 structure is viewed in the rhombohedral setting with hexagonal axes as reference.

2.3 Stability of polytypes

Due to the close relation between the structure types of the Laves phases, the differences in the structural energies are usually small. As a consequence two or more Laves phase polytypes are often observed as equilibrium phases in many binary and ternary systems and the stability of the particular polytype depends strongly on temperature and composition. In this section an overview is given on binary and ternary systems containing more than one Laves phase. The reasons for polytype stability given in the literature is discussed and it is shown, that there is not yet a sufficient description of the stability of the Laves phase polytypes.

2.3.1 Binary Laves phases

If two Laves phases exist in a binary system, the phase transformation can take place either composition- or temperature-dependent. Examples for the first case are the Co–Ti and the Fe–Zr systems. At the ideal stoichiometric composition AB_2, both $TiCo_2$ and $ZrFe_2$ crystallize in the cubic C15 phase. At higher Co and Fe contents, respectively a structural transformation takes place and C36 becomes the stable polytype. It is a general observation that if both cubic and hexagonal Laves phases exist in a binary system at the same temperature but different compositions, the cubic C15 polytype occurs around the stoichiometric and the C14 and C36 polytypes at off-stoichiometric compositions [27].

For several other binary systems a temperature-dependent change of the crystal structure is observed. The Cr–Nb system has been reported to contain a congruently melting intermediate phase $NbCr_2$ which has the hexagonal C14 structure at high temperatures and transforms into the cubic C15 structure at low temperature [28]. This particular phase transformation has however, just recently been called into question by Aufrecht and co-workers [29–32], see section 2.6.1. Other examples for phases diagrams of that type are Cr–Ti, Cr–Ta, Cr–Hf, Cr–Zr, Hf–Mo and Ta–V [27]. Interesting to note, if both cubic and hexagonal Laves phases exist at a particular composition in a binary system, then the cubic C15 polytype is the low-temperature phase and the C14 or C36 polytypes occur at higher temperatures [27].

Eventually, there are binary systems which contain all three different Laves phase polytypes, the most thoroughly investigated of which is the Co–Nb system [33].

The C15 Laves phase is stable around the stoichiometric composition with a broad homogeneity range from low temperatures up to the melting point. The C14 and C36 polytypes are found strongly off-stoichiometric, C14 near 64 at.% Co and C36 at 75 at.% Co. Both are stable only at elevated temperatures within small homogeneity ranges of less than 1 at.%.

An unusual behavior of polytype stability can be observed in binary rare earth metal Laves phases $RE\mathrm{Mg}_2$ [34] by consecutive substitution of the rare earth element. From LaMg_2 to SmMg_2 the cubic C15 Laves phase is formed, EuMg_2 is of the hexagonal C14 type, GdMg_2 is cubic again, and TbMg_2 to LuMg_2 are again of the hexagonal C14 type.

2.3.2 Ternary Laves phases

Basically, one can distinguish two different types of ternary $A(B'_{1-x}B''_x)_2$ type Laves phases. These are binary Laves phases with a certain solubility for the third element on the one hand and "true" ternary Laves phases on the other. The true ternary Laves phases can again be divided in different types, depending on the existence and the polytype of the Laves phases in the binary subsystems.

The first type can be regarded as a AB'_2-type binary phase with a certain solubility for the third element B''. The ternary phase field starts at one of the binary boundaries and ends somewhere within the ternary system. Many binary Laves phases can dissolve considerable amounts of a third element without undergoing structural changes. Up to three quarter of the Fe atoms in C14 TiFe_2 can be substituted by Al at 1000 °C maintaining the C14 structure type [35]. And more than 30 at.% V can be solved in C15 NbCr_2 [36]. Thereby, depending on the third element, both constituents A and B of AB_2 Laves phases can be substituted. In NbCr_2 for example, V will substitute for Cr while Ti will substitute for Nb [37–39]. If both of the binary systems contain a Laves phase of the same polytype, the ternary phase field may also extend through the whole ternary system from one binary boundary to the other.

The second type, the true ternary Laves phases are new ternary intermetallic compounds which are not present in any of the binary subsystems. The binary systems may contain either no Laves phase at all or Laves phases of a different polytype. In the systems Al–Ni–Ta [40], Cu–Ti–Zr [41], Al–Ni–Ti [42] or Ni–Ti–Zr [43], ternary Laves phases are forming although no Laves phases are present in any of the binary boundary systems. Remarkably, all ternary Laves phases in systems where none of the binary boundary system contains a Laves phase crystallize in the hexagonal C14 structure type. No example is known where such a Laves phase crystallizes with the C15 or C36 structure type. Moreover, in no case a temperature-dependent transformation to another polytype was reported [27].

A true ternary Laves phase is also formed if one, two or all three of the binary systems contain Laves phases which undergo a structural transformation into a different polytype upon addition of a third element. The earliest known example where only one of the binaries contains a Laves phase is the Al–Cu–Mg system. No stable[3] Laves phases exist in the Al–Mg and Al–Cu subsystem. However, upon addition of about 20 at.% Al to the cubic C15 Laves phase $MgCu_2$, it transforms into a new ternary Laves phase with C14 structure type. Adding Co to the C14 Laves phase $MgZn_2$ results in a transformation to the C15 polytype. By adding Ag instead of Co the sequence C14 → C36 → C15 is observed [27]. Other examples are HfV_2 + Nb (C15 → C14) [45], $ZrCr_2$ + Ni (C15 → C14 → C15) [46] or $ZrCo_2$ + Mn (C15 → C36) [47].

If two or three of the binary subsystems contain Laves phases mixing will result in one or more composition dependent changes of the stable polytype. An example is $CaAl_{2-x}Mg_x$. With increasing Mg content the sequence of Laves phase structures C15 → C36 → C14 is observed [26]. Mixing of $NbCr_2$ and $NbCo_2$ which have the C15 structure type results in the formation of a new true ternary Laves phase C14 $Nb(Cr_{1-x}Co_x)_2$ in the sequence C15 → C14 → C15. Other systems with a transformation sequence of that kind are ZrV_2–$ZrCo_2$ [48], ZrV_2–$ZrFe_2$ [27] or $RE\mathrm{Fe}_2$–$RE\mathrm{Al}_2$ with $RE =$ Gd, Ty, Dy, Ho, Er, Tm and Lu [49]. More complex sequences can be found already in mixtures of the prototype Laves phases. A Laves phases sequence of the type C14 → C15 → C36 was observed along the section $MgZn_2$–$MgNi_2$, and the sequence C14 → C36 → C15 is known for $MgZn_2$–$MgCu_2$ [50]. Even the sequence C15 → C14 → C15 → C14 with a threefold change of the stable polytype has been observed in $ZrFe_2$–$ZrAl_2$ [51] and $ScAl_2$–$ScFe_2$ [49].

---

[3] AKHTAR *et al.* [44] report on the possible formation of a metastable C14-type Laves phase in rapidly solidified Mg_2Al_3.

2.3.3 Factors controlling polytype stability

As has been shown so far, polytypic transformations in Laves phases are no anomaly but occur frequently both in binary and in ternary compounds. Several criteria based on geometric and electronic factors have been discussed in the literature in order to explain the stability of Laves phase polytypes. Since a detailed overview is given by STEIN *et al.* [15] and by GRÜNER [52] these criteria will only be discussed briefly here. The most prominent are the *atomic radius ratio* and the *valence electron concentration (VEC)*. Geometrically can be shown, that the closest packing of hard spheres is obtained for a radius ratio $r_A/r_B = \sqrt{3/2} \approx 1.225$. In nature however, Laves phases are forming with radius ratios ranging from 1.05 to 1.7 [4, 15] without a correlation between the size ratio and the structure type that is formed. This can clearly be seen in figure **2.11**. Additionally it is known, that the radii of atoms in Laves phases differ from those in the pure elements and that the atoms have the ability to contract or expand in order to get closer to the ideal radius ratio.

The enthalpies of formation of a large number of Laves phases of all polytypes were plotted versus the radius ratio by ZHU *et al.* [53] in figure **2.12**. Remarkably, the data points can be enveloped by a triangle with the maximum formation enthalpy at the ideal radius ratio of 1.225. That is, the most stable Laves phase may be found at the ideal radius ratio. The decreasing enthalpies of formation at lower and higher radius ratios may be explained by the elastic strain energies resulting from the expansion and compression of the atoms.

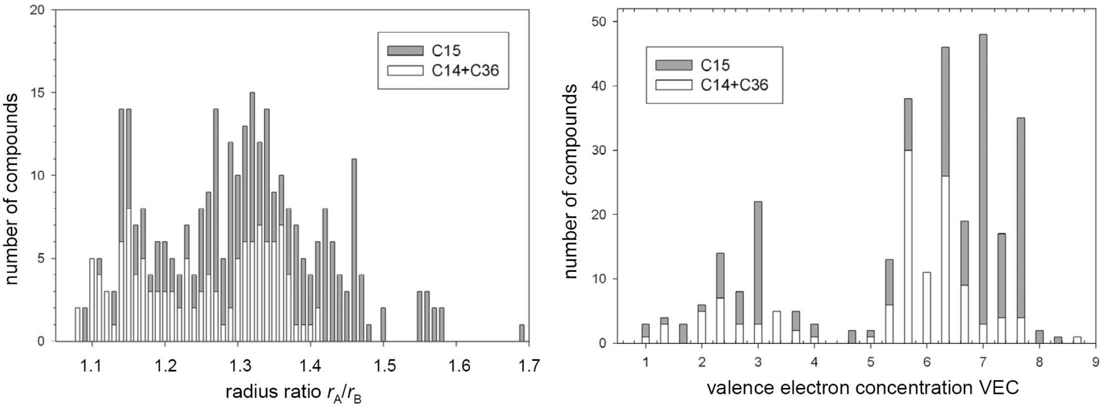

Figure 2.11: Frequency of Laves phase structure type versus atomic radius ratio (left) and valence electron concentration VEC (right) [15].

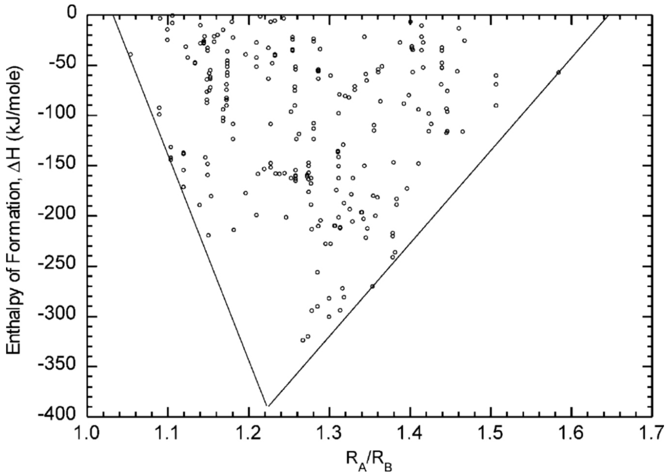

Figure 2.12: Enthalpy of formation versus atomic radius ratio [53].

In figure **2.11** the valence electron concentration is plotted against the number of compounds. Although for some particular series of compounds a relation between the VEC and the stable polytype was observed [15], a general prediction of the stable polytype solely on the VEC is not possible.

Another approach are so called structure maps were the stable polytypes are plotted as a function of two structure controlling factors such as for example radius ratio and VEC. Now areas or ranges of radius ratios and VECs can be identified were one polytype is dominantly present.

Recently, Ormeci *et al.* [54] investigated the stability of AB_2-type Laves phases by chemical bonding analysis using the *quantum theory of atoms in molecules* (QTAIM) and the *electron localizability indicator* (ELI-D). They found that the diversity of phases may be understood in terms of the charge transfer from A to B atoms caused by the electronegativity difference between A and B. If this difference is small, the charge transfer between A and B is also small and the corresponding Laves phases are characterized by multicenter bonding. When B is much more electronegative than A, the charge transfer from A to B is larger and the formation of $(B_2)^{\delta-}$ polyanions is indicated by the ELI.

However, "*. . . there is not yet a complete and consistent description which is valid for all the compounds of the large class of Laves phases*" [15]. The quantum-chemical calculations carried out in this work are intended to help to predict the stability of Laves phase polytypes, although calculations alone will not be able to explain the reasons for the stability of a particular polytype.

2.4 Site occupation

In crystallography the term *site occupation* describes the behavior of a specific atomic species with respect to a certain atomic position within the unit cell of the crystal structure. The *site occupation factor (s.o.f.)* is the corresponding quantitative measure of the fraction of a given element occupying a given atomic site. It is defined between 0 (empty) and 1 (full occupation). For example, the atoms of the chemical species A and B in an ideal cubic C15 type Laves phase AB_2 exclusively occupy the $8b$ and $16c$ sites, respectively. Thus, the site occupation factor of A on $8b$ and of B on $16c$ is 1. If 2 at.% of B on the $16c$ site are substituted with C, then the site occupation factors of B and C on the $16c$ site are 0.92 and 0.02, respectively. However, it is also possible that C will substitute for A and not B or even that C substitutes for both A and B. For a given composition one can distinguish three different types of distribution: (i) random distribution, (ii) ordered structures and (iii) *preferential site occupation*. The first case is characterized by the absence of short range order and a random distribution of the atoms. In the second case there is complete short range order which is determined by the long range order of the crystal structure. In the third case the short range order is not determined by the long range order of the crystal structure but depends on local interaction with a limited correlation length. An understanding of distribution of the atoms within the crystal structure and especially the phenomenon of preferential site occupation is very important for a proper description of phase stability.

2.4.1 Preferential site occupation

If a new element introduced into a compound does only (or mainly) substitute for a specific atom type (on one specific Wyckoff position) this is called *preferential site occupation*. ERSCHBAUMER *et al.* [55] studied the alloying behavior of Nb, V, Cr and Mn in γ-TiAl. They found that Cr and Mn substitute Al whereas Nb and V prefer the Ti site. Their results are in good agreement with a number of other theoretical and experimental studies. This is also of technological importance since Nb and V are found to improve the oxidation resistance while Cr and Mn enhance the ductility of γ-TiAl.

Another form of appearance of preferential site occupation can be observed if an atomic species occupies different Wyckoff position in the crystal structure. This is for example the case in hexagonal C14 AB_2 Laves phases. Here the atomic species A only and exclusively occupies the $4f$ site, while B occupies the two different atomic sites $2a$ and $6h$. If a ternary component C is added to substitute B, C can be distributed with even probability among the $2a$ and $6h$ sites or there can be a preferential site occupation of C on one of the two sites.

Furthermore, the site preference of a given atomic species depends on the temperature and on the composition of the compound. The strength of the site preference can vary and ultimately even change with temperature and/or composition.

In 1995 SLUITER *et al.* [56] published an article stating that "*A new phenomenon is predicted where a particular crystallographic site initially becomes enriched in one elemental species but then at some given temperature or composition reverses itself and becomes enriched in another species*". They investigated the Cr–Fe σ phase, a tetrahedrally closed packed (*tcp*) phase alike the laves phases. Its unit cell contains 30 atoms on five crystallographic inequivalent sites denoted A, B, C, D and E. In this theoretical study it was predicted that following the stable configurations going from pure Fe to pure Cr, first the E site takes up Cr, followed sequentially by the C, B and A site. So initially the various sites change their occupation from Fe to Cr one by one. However, towards increasing Cr content the A site reverses its occupation with the D site and this curious composition dependent behavior persists in a weakened form at finite temperatures. They called this phenomenon in the title of the article: "*Site occupation reversal in the Cr–Fe σ phase*". However, in this case site occupation reversal could not be observed experimentally since the composition for which the reversal is predicted lies outside the homogeneity range of the Cr–Fe σ phase.

HAO *et al.* [57] investigated the Al–Ti system addressing the problem that the reported occupations of ternary additions of Zr, Nb and Ga are consistent whereas those of V, Cr and Mn show marked differences among literature data. In an extensive experimental study they found that the site occupation behavior of elements depends on the Al–Ti alloy composition. The occupations of Nb and Fe do not change much with composition, but the occupations of V, Cr and Mn change considerably. At low Al contents Cr for example prefers to occupy the Al sites, but it prefers the Ti sites at higher Al content. The site occupation shows a composition dependence. This is the same behavior as described by Sluiter *et al.* [56], a site occupation reversal.

Jiang *et al.* studied the Al–Ni system, in particular γ'-Ni_3Al [58, 59]. By first-principles calculations they predicted that Pt has a predominant preference for the Ni site, while Hf and Cr have a preference for the Al site. The site preference of Ir however strongly depends on both the alloy composition and the temperature.

2.4.2 Site occupation in Laves phases

The main focus regarding site occupation in Laves phases was on ternary additions in C15 type phases. This is caused by the particular interest in C15 Laves phases as potential high temperature structural materials. The disadvantage of these materials, their low ductility and fracture toughness can be improved by adding a third element. The preferential site occupation of these elements is obviously very important for the understanding of the mechanisms leading to improved mechanical properties.

Legoas *et al.* [60] used LMTO-ASA calculations to investigate the magnetic behavior of 3*d* impurities in C15 $ZrFe_2$. It is clear that the magnetic behavior of the system depends on whether the impurity occupies a Zr or an Fe site and the calculation of site preference energies becomes very important in this case. They conclude that Sc, Ti and V impurities should occupy the Zr site, while Co and Ni prefer the Fe site. In case of Cr, Mn and Cu the site preference energy is very small and a definite conclusion is not possible. However, the magnetic moment of Cr depends drastically on the site preference: when placed on an Fe site, Cr develops a small negative moment of around 0.5 μ_B, but when placed at the Zr site its moment is large and positive with a value of around 2.5 μ_B. The experimentally observed moment for Cr impurities are large and positive, indicating that Cr occupies the Zr site. The site preference energy of Cu is also very small. This is consistent with experimental evidence for Cu impurities in $ZrFe_2$ which suggest they should occupy both sites.

Yao *et al.* [37–39] calculated the site occupation preference of ternary additions of Ti, V and W in C15 $ZrCr_2$ and $NbCr_2$. They found, that V and W preferentially substitute Cr while Ti substitutes Zr and Nb, respectively. The calculated heats of formation suggest that additions of W and Ti stabilize $ZrCr_2$ while V and Ti stabilize $NbCr_2$. Their results are in agreement with the work by

Kotula *et al.* [61], Chu *et al.* [36] and Okaniwa *et al.* [62] who experimentally found V(Ti) preferentially substituting Cr(Nb) in $NbCr_2$. However, their results disagreed regarding the site occupation of W in $ZrCr_2$ and $NbCr_2$. As a reason for this they already assumed, that this disagreement might originate from a composition dependence of the site preference of W. Encouraged by this findings Jiang *et al.* [63] further investigated ternary additions of transition elements in C15 $NbCr_2$ and indeed found that the site preference of Ti, V, Mo and W depends on the alloy composition. In Nb-rich $NbCr_2$ W prefers the Cr site while in the Cr-rich case it prefers the Nb site. Zr, Hf and Ta do always have a preference for the Nb sublattice.

Site occupation is not only of interest with respect to ternary additions, but also in pure binaries. The C36 Laves phase $Nb_{1-x}Co_{2+x}$ [64] crystallizes off-stoichiometric with Nb deficiency and a homogeneity range extending from 24.6(2) to 25.3(5) at.% Nb. The excess Co atoms do not occupy the two Nb positions evenly but with a preference for the Nb2 ($4e$) site. Approximately twice as much Co occupies the Nb2 site compared to the Nb1 ($4f$) site. The C14 Laves phase $Nb_{1+x}Co_{2-x}$ in the same system is only stable within a small homogeneity range around $x = 0.07$. Here the excess Nb atoms are substituting Co only on the $2a$ site, while no Nb atoms are found on the $6h$ site which stays fully occupied by Co [52,65].

2.4.3 Site occupation in ternary C14 Laves phases

The investigations of ternary hexagonal Laves phases are focused on the simple case of C14 $A(B'_{1-x}B''_x)_2$, especially on the composition-dependent distribution of B' and B'' among the crystallographic sites $2a$ and $6h$. No study is known dealing with the site occupation in ternary C36 type Laves phases. If small amounts of B' in AB'_2 are substituted with B'', B'' will occupy one of the two sites of the B sublattice, either $2a$ or $6h$[4]. In C14 $Zr(Cr_{1-x}Ni_x)_2$ the Ni atoms prefer the $2a$ site within the whole stability range of $0 \leq x \leq 0.4$ [66]. A preference of Al for the $2a$ site is observed by Rietveld refinements by Prymak *et al.* and Dovbenko *et al.* in $Nb(Cr_{1-x}Al_x)_2$ [67] and $Nb(Co_{1-x}Al_x)_2$ [68], respectively.

Often the site preference changes with an increasing amount of B''. As early as

---

[4] This is only valid if the A sublattice is fully and exclusively occupied with A atoms.

in 1963 Faller and Skolnick [48] conducted an elaborate experimental study on the atomic arrangements in the C14 Laves phase $Zr(V_{1-x}Co_x)_2$. Using the phenomenon of anomalous scattering they were able to distinguish Co and V by their scattering factors which are otherwise very close together. They have found that Co and V exhibit a composition dependent distribution over the nonequivalent positions $2a$ and $6h$. At high concentrations a species (Co or V) prefers to locate on $2a$-type sites, at low concentrations on $6h$-type sites. In other words, the minority component prefers the $6h$ site. This is as far as already known the first mention of the phenomenon of site occupation reversal. Site occupation reversal was also reported in C14 $Ti(Mn_{1-x}Al_x)_2$ which was thoroughly investigated by Yan *et al.* [69]. The solubility limit of Al in $TiMn_2$ at 900 °C is 43 ± 2 at.% Al ($x = 0.64$). For $x < 0.3$ Al atoms prefer the $6h$ site, for $x > 0.3$ the reverse is observed, so again the minority component prefers the $6h$ site. If Mn is replaced by Fe the solubility limit for Al decreases to 41 at.% Al. More interesting, the Laves phase $Ti(Fe_{1-x}Al_x)_2$ now shows no site occupation reversal but a slight preference of Al for the $2a$ site along the whole homogeneity range [70]. In the Al–Nb–Ni system the C14 Laves phase $Nb(Ni_{1-x}Al_x)_2$ is stable for $0.23 \leq x \leq 0.77$ [71]. Although not particularly mentioned by the authors the data indicate a site occupation reversal with two crossing points at approximately $x = 0.38$ and 0.65. Al atoms prefer to substitute for Ni on the $6h$ site at low and high Al contents, whereas it prefers the $2a$ site in between.

An unusual case is the C14 phase in the Zr–Ti–Cu system [41]. Unusual in the sense that the $4f$ site of the crystal structure in most reported compounds is only and exclusively occupied by one atomic species. Here however, the $4f$ site is shared between Zr and Ti atoms. Ti and Cu are found on the $6h$ site while the $4a$ site is exclusively occupied by Cu. Similarly unusual and complicated are the site preferences in the Al–Ni–Ti system in the boomerang-like shaped homogeneity range of the C14 Laves phase $Ti(Ti_yNi_xAl_{1-x-y})_2$ [42]. At high Al contents the Ti atoms are located only on the $4f$ site, the $2a$ site is almost fully occupied with Al, whereas a statistical distribution of Al and Ni atoms is observed on the $6h$ site. With decreasing Al content the occupations on the $6h$ site behave almost linearly. On the $2a$ site however, the Ni content increases drastically. At even higher Al contents and increasing Ti content the occupation of Ni on $2a$ stays almost constant while Ti starts to enter the $2a$ and $6h$ sites.

The influence of preferential site occupation on the crystal structure and and hence on the stability of Laves phase polytypes is self-evident, however, not well investigated to date. It becomes apparent for example in the Co–Si–V system. $V(Co_{1-x}Si_x)_2$ crystallizes in different $MgZn_2$-type based superstructures. A symmetry analysis revealed that the driving force for the superstructure formation is the preferential site occupation of Co and Si on different crystallographic sites [72].

Further data on site occupation in Laves phases can be found in [73] (Ti–M–Al) (M = Pd, Pt), [74] (Al–Yb–Zn), [75] (A_2M_3Si (A = Sc, Ti; M = Cr, Mn, Fe, Co, Ni)), [26] ($CaAl_{2-x}Mg_x$) and in the comprehensive review article by Stein *et al.* [27].

2.4.4 The origin of preferential site occupation

The most simple approach to explain preferential site occupation are *size effects*. Experimental work on $NbFe_2$ by Ishikawa *et al.* [76] for example revealed that Cr and Mn which have a larger atomic size than Fe prefer to occupy the Fe1 ($2a$) site for small and the Fe2 ($6h$) site for larger concentrations. In contrast, Co and Ni, whose atomic size is smaller than that of Fe preferentially occupy the Fe2 ($6h$) site, regardless of their concentration. In AB_2 type Laves phases A are always the larger and B the smaller atoms. If a third element is introduced with a atomic radius close to that of A it will most likely substitute for A. Third elements with a radius close to that of B will rather substitute for B. However, if the atomic radii of A and B are too similar (which is the case for most metals, especially the transition elements) or if the radius of the third element lies in between that of A and B, this approach looses its predictive power. Furthermore, it allows only for the discrimination of A or B and not for that of the different atomic B sites in hexagonal Laves phases. A deeper inside into the size effect can be gained by analyzing the volumes of the coordination polyhedra or the Voronoi cells around A and B in the three polytypes using the program *DISPOW* from the *NRCVAX* suite [77]. In Laves phase structures with ideal c/a ratio and ideal atomic coordinates the Voronoi cells of A are 23% larger than that of B in all three polytypes. However, in the hexagonal Laves phases C14 and C36 the Voronoi volumes of the different crystallographic B sites are equal. And even in real compounds like for example $Nb(Cr_{1-x}Co_x)_2$ with $x = 0.8$ with non-ideal atomic positions and c/a ratio, the volume differences are only about 0.8%. Therefore, no conclusion can be drawn on the site occupation among those different sites and the size effect as a reason for preferential site occupation is unlikely. Additionally, the atoms in Laves phases have the ability to contract or expand in order to obtain the ideal radius ratio and therefore their radii differ from those in the pure A and B metals [15].

Another explanation are *nearest neighbor* or *pair interactions* with the focus on the first coordination sphere around the atomic B sites in C14 type phases. This concept was introduced by Faller and Skolnick [48] and later used by Sluiter *et al.* [56]. However, already in 1939 Schulze [12] noticed that the spacing of the B atoms was always smaller in the compound than in the elements, indicating an attractive B–B interaction. On the other hand, the spacing between A and B atoms was unusually large so that no heteropolar bond between A and B could be effective [18]. The assumption of Faller and Skolnick is that two atomic species B' and B'' which are distributed among the $2a$ and $6h$ sites are either attracted to their own species or to the other species. That is, either homonuclear B'–B' and B''–B'' or heteronuclear B'–B'' contacts are energetically favored. The atoms will then arrange among $2a$ and $6h$ taking account of that.

While Faller and Skolnick discuss the bonding situation only qualitatively, Ormeci *et al.* [54] show the possibility of a quantitative analysis based on QTAIM and ELI calculations[5]. Depending on the electronegativity difference of the elements involved, either multicenter bonding or the formation of polyanions is preferred. When the electronegativity difference is small, the charge transfer is small and multicenter bonds are forming, i.e., homonuclear contacts are favored. If the difference is large, the charge transfer is also large and the formation of polyanions are indicated which causes heteronuclear bonds to be favored.

The coordination type polyhedra of the $2a$ and $6h$ sites are shown in figure **2.6**. Both sites are surrounded by 12 nearest neighbors, six A atoms and six B atoms. Besides the arrangement of the A atoms, chair like around $2a$ and boat like around $6h$, the main difference of the two sites is the type of the surrounding B atoms. While the $2a$ site is surrounded by six atoms on $6h$, the $6h$ site is surrounded by four atoms on $6h$ and two atoms on $2a$. In other words, the $2a$ site is surrounded only by equivalent sites while the $6h$ site is surrounded by four equivalent and two

---

[5] The study of Ormeci *et al.* [54] deals only with binary MN_2 type Laves phases. The transferability of their ideas on ternary Laves phases has to be further investigated

non-equivalent sites. Thus, if in a compound heteronuclear contacts B'–B'' are preferred then small amounts of B'' added to AB'_2 will preferentially occupy the $2a$ site since here six B'–B'' contacts are formed. If in contrast homonuclear bonds are favored then the minority component will prefer the $6h$ site since here four homo- and only two heteronuclear contacts are formed. This concept can even explain site occupation reversal. If for example like contacts are preferred, then B'' will substitute for B' on $6h$ to maximize the number of B''–B'' contacts. With increasing B'' content on $6h$ however, the environment of B' on $2a$ will become more and more enriched in B'', forming more and more energetically unfavorable unlike contacts and thus, at a certain point the site preference reverses. The composition at which a site occupation reversal is expected therefore depends on the ratio of the "bond strength" of the homonuclear contacts B'–B' and B''–B''. Additionally, non ideal values for the axial ratio and atomic positions affect the environment of $2a$ and $6h$ sites and alter the bond length and bond strength of homo- and heteronuclear contacts. SLUITER *et al.* [56] successfully applied this approach to the binary Cr–Fe σ phase which has as many as five crystallographically inequivalent sites with mixed occupation of Fe and Cr. Assuming that heteronuclear Cr–Fe contacts are favorable they were able to explain the complicated site preferences behavior in σ-FeCr.

Yet another reason also suggested by FALLER and SKOLNICK [48] is based on the consideration of the configurational entropy. The stability of crystalline phases depends upon certain geometric building principles which were expressed by Laves [78] as:

- *Space principle*: aiming for the best space filling
- *Symmetry principle*: aiming for the highest possible symmetry
- *Connection principle*: aiming for the highest possible coordination

Considering the geometric situation in C14 Laves phases these principles are better satisfied by the $2a$ site than by the $6h$ site. The coordination number (12) and the space filling (voronoi cells are of the same size) are equal for both site. However, the site symmetry of the $2a$ site ($\bar{3}m.$) is higher than for the $6h$ site ($mm2$). Thus, if the adherence to these geometric principles is associated with the stability of a certain site, then $2a$ sites are more stable than $6h$ sites. Obviously, this concept can only explain a preferential occupation of the minority component on the $6h$ site like in C14 $Zr(V_{1-x}Co_x)_2$ and breaks down if the minority component prefers the 2*a* site.

In summary it has to be stated that the only promising concept is that of pair interactions. An even this concept is not able to explain all observed phenomena like for example a site occupation reversal with two crossing point as in $\mathrm{Nb(Ni_{1-x}Al_x)_2}$.

2.5 *c/a* ratio of hexagonal Laves phases

When discussing the crystal structure of intermetallic compounds one is usually considering the packing of hard spheres. The ideal c/a ratio obtained from this simplified model is given by $\sqrt{8/3} = 1.633$. However, it is well known that the axial ratio in hexagonal phases often shows deviations from this ideal value. A popular example of the problem is the Cu–Zn system [79]. Pure Zn, a metal with hexagonal closed packed structure has a c/a ratio of 1.856, much larger than the ideal value of 1.633. Upon addition of less than 5 at.% Cu the axial ratio of the solid solution drops to a value even lower than the ideal value. At 10 at.% Cu the c/a ratio reaches a value as low as 1.56. For three Zn rich hexagonal phases in the Cu-Zn system Sofo *et al.* [79] have shown that ab-initio calculations can reproduce the very different c/a ratios in remarkable agreement with the experiment.

The c/a ratio is not only a crystallographic pettiness but of technological importance. Laves phases are used in NiMH batteries. During the repeated hydrogenation-dehydrogenation cycles these batteries show a hysteresis and the electrode tends to pulverize due to the stress induced by lattice expansion and contraction. Young *et al.* investigated $\mathrm{ZrCr_2}$ with ternary addition of Mo, Mn, Ni, Al, Co, V, Cu, Si, Zn, Sn and Fe and they found that a higher c/a ratio leads to a smaller hysteresis and a lesser degree of pulverization [80]. In tetragonal γ-TiAl the c/a ratio is seen to influence the ductility [55].

Deviations from the ideal c/a ratio have also been observed in other Laves phase studies, especially in ternary C14 phases with large homogeneity ranges. Already Faller and Skolnick [48] noticed a change in the axial ratio across the pseudobinary section $\mathrm{ZrV_2}$–$\mathrm{ZrCo_2}$. They assumed this to be associated with the non-random distribution of Co and V. However, the large deviations in c/a, hindered a detailed analysis. In C14 $\mathrm{Ti(Mn_{1-x}Al_x)_2}$ [69] the a and c lattice parameters increase with increasing Al content. However, both a and c show deviations from linearity. The c lattice parameter and therefore also the c/a ratio show an S-shape going through a minimum at $x = 0.3$ and a maximum at $x = 0.55$. In C14 $\mathrm{Nb(Ni_{1-x}Al_x)_2}$ stable at $0.23 \leq x \leq 0.77$ no S-shape is observed but a parabolic behavior with a minimum at 38 at.% Nb [71]. Similar parabolic shapes with pronounced minima are observed in the C14 Laves phases $\mathrm{Zr(Fe_{1-x}Al_x)_2}$, $\mathrm{Ti(Fe_{1-x}Al_x)_2}$ [70], $\mathrm{Ta(Ni_{1-x}Al_x)_2}$ and $\mathrm{Nb(Co_{1-x}Al_x)_2}$ [68]. The c/a ratio in C14 $\mathrm{Zr(Cr_{1-x}Ni_x)_2}$, stable for $0.0 \leq x \leq 0.4$ has a downward opening parabolic shape with a maximum at $x = 0.3$ [66].

2.5.1 c/a ratio versus preferential site occupation

Several authors have tried to establish a connection between the c/a ratio and the preferential site occupation in hexagonal Laves phases. If an atom B'' with an atomic diameter different from that of B' is introduced in a hexagonal AB'_2 Laves, the changes in the lattice parameters a and c will depend on whether the $2a$ or the $6h$ site is preferred by B''.

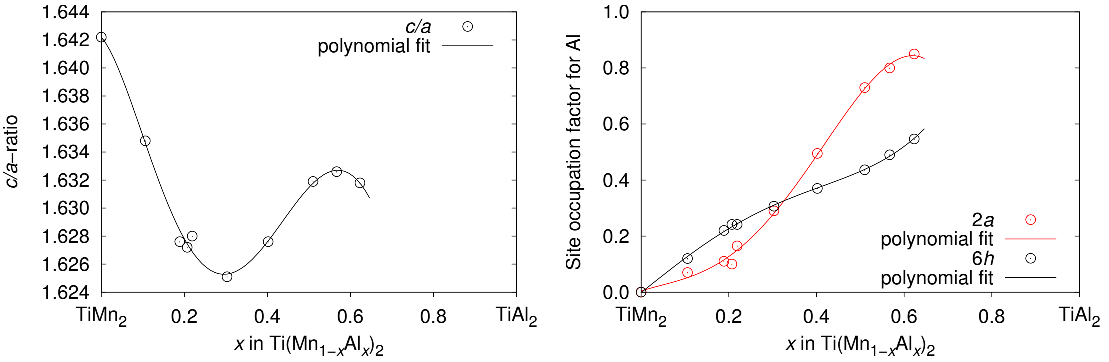

Figure 2.13: Experimental c/a ratio (left) and site occupation for Al (right) in C14 $\mathrm{Ti(Mn_{1-x}Al_x)_2}$. Data taken from Yan *et al.* [69].

For C14 $\mathrm{Ti(Mn_{1-x}Al_x)_2}$ with the c/a ratio showing an S-shape and the minority component preferentially occupying the $6h$ site (fig. **2.13** (a) and (b)) Yan *et al.* [69] argued in the following way. Al has a larger atomic diameter than Mn. The substitution of Mn by Al on the $6h$ site leads to an expansion of the unit cell preferably in the ab-plane because it mainly effects the shortest interatomic distance M1-M1, the triangles in the Kagomé layer. This expansion causes the a lattice parameter to increase stronger than the c lattice parameter inducing a downwards slope in the c/a ratio. At an Al content of $x = 0.3$ site occupation reversal occurs and c/a reaches a minimum. At Al contents higher that $x = 0.3$, Al preferentially occupies the $2a$ site. This now causes the interatomic distances M1-M2 pointing outwards of the ab-plane to increase more significantly and thus triggers a stronger increase of the c lattice parameter and an upwards slope of c/a. From $x = 0.5$ on the strength of the preference of Al for $2a$ decreases again causing the final downwards slope of the c/a ratio.

If Mn is replaced by Fe as in C14 $\mathrm{Ti(Fe_{1-x}Al_x)_2}$ [70] no site occupation reversal occurs but Al preferentially occupies the $2a$ site along the whole homogeneity range. In accordance with the above explanation, the c/a ratio shows no S-shape but an parabolic behavior with the minimum at $x = 0.5$. But this model fails in other cases. In C14 $\mathrm{Nb(Ni_{1-x}Al_x)_2}$ stable at $0.23 \leq x \leq 0.77$ [71] site occupation reversal with two crossing points is observed while the c/a ratio takes only a simple parabolic form with a minimum at $x = 0.6$.

Therefore, size effects alone can not explain the different shapes of the c/a ratio. Besides the freedom in the lattice parameters hexagonal Laves phases have additional degrees of freedom in the atomic positions of the A and B atoms. And thus the c/a ratio is the result of a complicated interplay of all of these degrees of freedom.

2.6 Laves phases in systems investigated in this work

2.6.1 The Cr–Nb system

The Cr–Nb system has just recently been the subject of a fierce debate [29–32]. The open question is whether or not the low-temperature cubic C15 Laves phase $\mathrm{NbCr_2}$, on the existence of which all previous authors agree, transforms into a high-temperature hexagonal C14 Laves phase. Already 1986 VENKATRAMAN *et al.* [81] mentioned that the existence of the high-temperature C14 phase requires clarification. Using high-temperature DTA and in-situ high-temperature neutron powder diffraction under carefully controlled high-purity conditions, AUFRECHT *et al.* [30] have proven that the phase transformation C15 → C14 does not take place. Instead they found, that small amounts of atmospheric contaminations induce the formation of an $\mathrm{Ti_2Ni}$-type phase, which partially melts in a temperature range around 1600 °C. This led to the earlier erroneous conclusion of the occurrence of a thermodynamically stable high-temperature modification of $\mathrm{NbCr_2}$. The formation of a metastable, non-equilibrium C14 phase during rapid solidification is however not challenged by their findings [82].

The most recent experimental phase diagram of the Cr–Nb system where the high-temperature C14 phase is still included is shown in figure **2.14** [83, 84]. It contains an intermediate phase, the Laves phase $NbCr_2$, which melts congruently at 1730 °C (1760 °C [30]). The Laves phase forms an eutectic with each of the terminal solid solutions Cr(Nb) and Nb(Cr). The Cr-rich eutectic $L \rightarrow Cr(Nb) + NbCr_2$ is observed at a Nb concentration of 18.5 at.% and a temperature of 1668 °C. The Nb-rich eutectic $L \rightarrow Nb(Cr) + NbCr_2$ appears at 1703 °C and 49.5 at.% Nb [84]. The homogeneity range of the Laves phase is strongly temperature dependent. It decreases with temperature from a maximum value of about 7.4 at.% (30.8 – 38.2 at.% Nb) down to 1.5 at.% (32.5 – 34 at.% Nb) at 900 °C [84]. According to this phase diagram the doubtful transformation from C14 to C15 occurs at 1600 °C for the stoichiometric composition $NbCr_2$. The terminal solid solutions Cr(Nb) and Nb(Cr) can solve up to 5.6 at.% Nb and 24.4 at.% Cr at the eutectic temperatures, respectively [84].

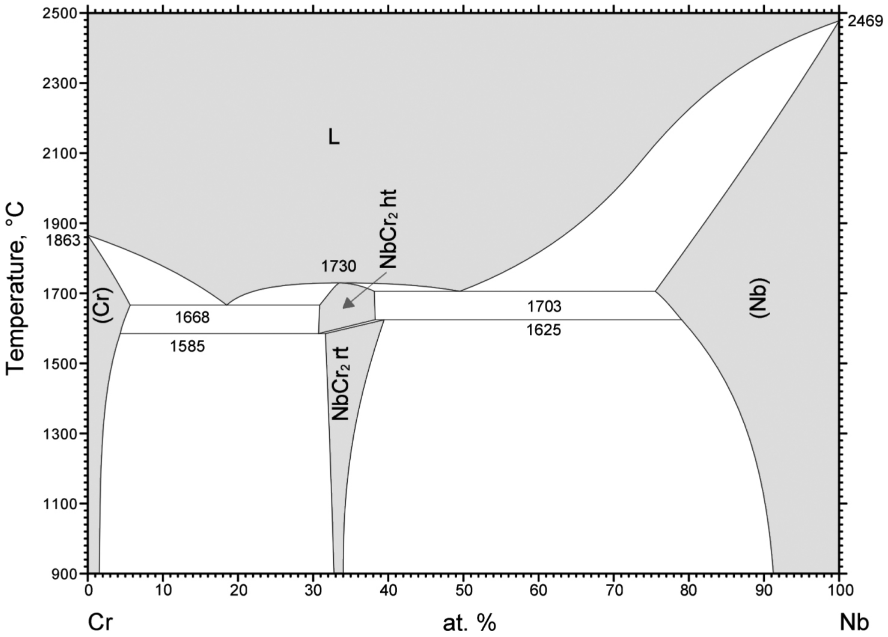

Figure 2.14: The Cr–Nb phase diagram [83, 84].

2.6.2 The Co–Nb system

The Co–Nb system has gained much attention in recent years and the phase diagram as well as some of the contained phases have been thoroughly investigated. The exceptional feature of this system is the occurrence of all three polytypes C14, C15 and C36 in one phase diagram. This makes it an excellent candidate for fundamental studies of the stability of Laves phases and intermetallic compounds in general. Moreover, Co and Nb are two important alloying elements for high temperature Nb- and Co-based superalloys, which make this a system of considerable interest. Recently, STEIN *et al.* [33] have experimentally redetermined the phase diagram in the whole range of compositions. In addition, the Co–Nb system has been assessed using CALPHAD methods by HE *et al.* and OKAMOTO [85,86]. Figure **2.15** shows the latest version of the Co–Nb phase diagram.

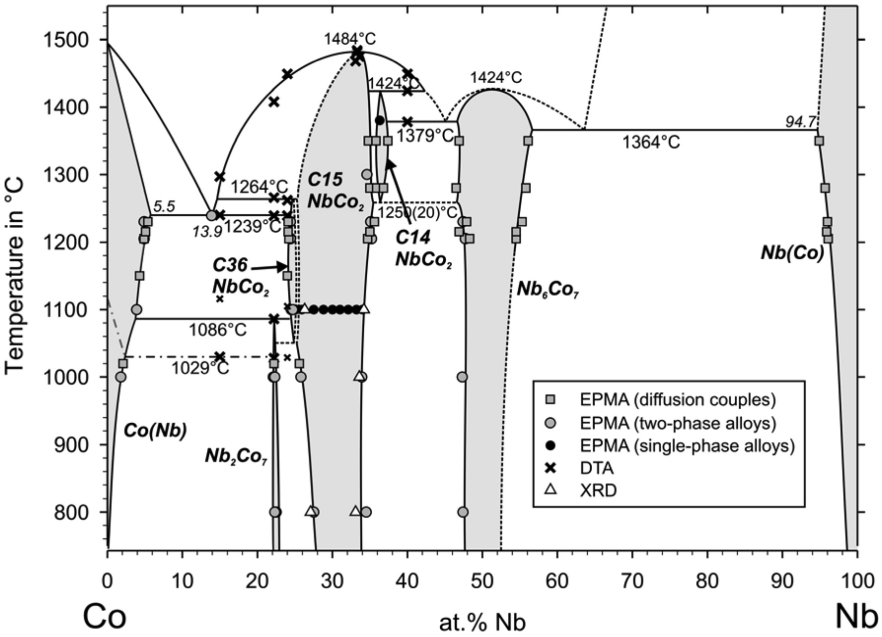

Figure 2.15: The Co–Nb phase diagram [33].

Besides the terminal solid solutions Co(Nb) and Nb(Co) the Co–Nb system contains five intermetallic phases listed in table **2.4**, the three Laves phases C36, C15 and C14, the μ-phase Nb_6Co_7 and Nb_2Co_7. The maximum solubility of Nb in Co and Co in Nb of the terminal solid solution at the eutectic temperature is 5.5 ± 0.2 and 5.3 ± 0.5 at.%, respectively. Nb_2Co_7 forms in a peritectoid reaction at 22.2 at.% Nb from the Co(Nb) solid solution and the C36 Laves phase at

Table 2.4: Observed phases in the Co–Nb system [33]. For more detailed data and lattice parameters see references [33, 64] and [87].

Phase	at.% Nb[1]	Pearson symbol	Space group	Structure type
Co(Nb)[2]	0 to 5.3	$hP2$ $cF4$	$P6_3/mmc$ $Fm\bar{3}m$	Mg Cu
Nb_2Co_7[3]	22.1 to 22.3	$mS18$	$C2/m$	Zr_2Ni_7
C36-$NbCo_2$	24.6 to 25.3[4]	$hP24$	$P6_3/mmc$	$MgNi_2$
C15-$NbCo_2$	26.0 to 35.3	$cF24$	$Fd\bar{3}m$	$MgCu_2$
C14-$NbCo_2$	35.8 to 37.4	$hP12$	$P6_3/mmc$	$MgZn_2$
μ-Nb_6Co_7	46.5 to 56.1	$hR13$	$R\bar{3}m$	W_6Fe_7
Nb(Co)	94.5 to 100	$cI2$	$Im\bar{3}m$	W

[1] Maximum width of the homogeneity range
[2] The hcp/fcc transformation temperature was not investigated in [33]
[3] [87]
[4] [64]

1086 ± 2 °C with a very small homogeneity range of 0.2 at.%. As the peritectoid reaction is very slow, this phase does not occur in as-cast samples but only after sufficiently long annealing times. Nb_2Co_7 shows an unusual mechanical behavior including plastic deformability which was investigated by SIGGELKOW *et al.* [88,89]. The crystal structure of Nb_2Co_7 is monoclinic and closely related to that of Zr_2Ni_7 with complex intrinsic stacking faults [87].

The C36 Laves phase is only stable at high temperatures and was investigated by GRÜNER *et al.* [64]. It forms at 1264 ± 2 °C in a peritectic reaction from the C15 Laves phase and the liquid close to the composition $NbCo_3$ and is thus the most Co-rich Laves phase in this system. The stability range ends in an eutectoid reaction between 1000 and 1100 °C forming Nb_2Co_7 and C15. The homogeneity range extends from 24.6(2) to 25.3(5) at.% Nb. Due to the strong deviation from the ideal composition $NbCo_2$, the excess Co atoms substitute the Nb atoms with a preferential occupation of the crystallographic $4e$ site (approximately twice as much as the $4f$ site). At the Nb-rich side a very small two-phase field (≤ 0.5 at.%) separates the C36 from the C15 phase. The cubic C15 phase is stable in a large composition range from approximately 26.0 to 35.3 at.%. Its homogeneity range includes the stoichiometric composition $NbCo_2$ and is strongly extended to the Co-rich side. The width of the homogeneity range decreases with decreasing temperature but the C15 phase is stable down to room temperature. At 1484 °C the C15 phase melts congruently. At even higher Nb contents another Laves phase with the C14 structure type is formed, separated from the C15 phase only by a small two-phase field. Alike the C36 phase, C14 exists only in a small, off-stoichiometric homogeneity range at high temperatures. However, whereas C36 occurs at the Co-rich side, the C14 phase is observed at the Nb-rich side of the stoichiometric composition. C14 forms in a peritectic reaction between the C15 phase and the liquid at 1424 ± 4 °C. At 1250 ± 20 °C it transforms into C15 and the μ-phase in an eutectoid reaction. The homogeneity range of the C14 phase is reported to be 35.8 to 37.4 at.% Nb. The most Nb-rich intermetallic phase in the Co–Nb system is the μ-phase Nb_6Co_7 which is stable from 46.5 to 56.1 at.% Nb. It melts congruently at approximately 1424 °C.

2.6.3 The Co–Cr–Nb system

Only few data are available on the ternary system Co–Cr–Nb. An overview on the available literature with emphasis on the binary phases in the Co–Cr–Nb system is given by Gupta [90]. Drapier *et al.* [91] investigated the Co-rich region (55–90 at.% Co) of the phase diagram at 1200 °C with special emphasis on the mechanical hardness and aging. They report the observation of multi-phase samples containing a C36 type Laves phase. A more detailed investigation on a sample with 5 wt.% Cr and 5 wt.% Nb aged at 600 °C revealed a superstructure formation of a cubic Laves phase and an additional C14 type phase. Ganglberger *et al.* [92] reported the formation of a single phase C14 Laves phase in a Co–Cr–Nb 1:1:1 compound (no temperature given). A more detailed investigation among the whole compositional range was carried out by Kaloev *et al.* [93]. An isothermal section at 1000 °C is shown in figure **2.16**. Besides the solid solutions Nb(Cr,Co), Cr(Nb,Co) and Co(Nb,Cr), four intermetallic phases are found in this system: the σ-phase, the μ-phase and two Laves phases with C15 and C14 type structure. The σ-phase Nb_6Co_7 can dissolve up to 5 at.% Cr. The μ-phase (Co,Cr) shows a large expansion into the ternary region with a maximum Nb solubility of about 20 at.%. The Laves phases C15 and C14 are forming along the quasi-binary section $NbCr_2$–$NbCo_2$. Its formula can be given as $Nb(Cr_{1-x}Co_x)_2$. However, a small homogeneity range of about 5 at.% for Nb is also expected from the phase diagram. The Laves phase polytype that is formed depends on the composition x. Zhu [4] investigated the quasi-binary section and found the following homogeneity ranges at 1100 °C:

$0.00 \leq x < 0.05$: C15
$0.05 \leq x < 0.12$: C15 + C14
$0.12 \leq x < 0.92$: C14
$0.92 \leq x < 0.96$: C14 + C15
$0.96 \leq x \leq 1.00$: C15

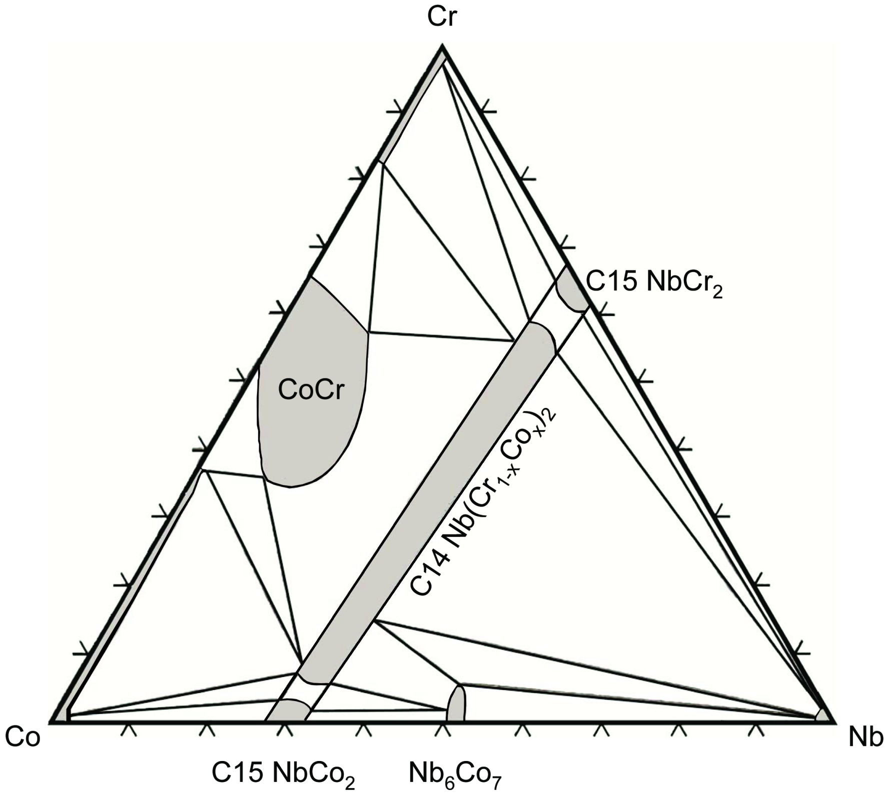

Figure 2.16: Isothermal section of the Co–Cr–Nb phase diagram at 1000 °C. Redrawn from reference [93].

2.6.4 The Ta–V system

Tantalum and vanadium have both body-centered cubic (bcc) crystal structures with similar lattice parameters (difference ≈ 10%). Thus, Ta and V are favorable to the formation of a continuous series of solid solutions. Indeed, there is a general agreement that Ta and V form a continuous bcc solid solution at elevated temperatures and that an intermediate phase forms from this solid solution only at lower temperatures [94]. The existence of this phase was first reported by Rostoker *et al.* [95]. The most recent phase diagram by Smith *et al.* [96] based on all available experimental data is shown in figure **2.17** (a). At high temperatures Ta and V show complete miscibility in the liquid and the solid phase. Below the liquidus line a bcc solid solution (Ta,V) starts to crystallize until below approx. 1900 °C all melt is transformed into the solid solution. At 1310 ± 10 °C and a composition of 33 at.% Nb the intermediate phase TaV_2 with the cubic C15 structure type forms in a solid-solid reaction with a homogeneity range of approximately 3 at.%. This phase is stable down to room temperature. Large two-phase fields exist on both sides of the Laves phase.

A different version of the phase diagram is reported by Savicky *et al.* [97] and by Nefedov *et al.* [98]. It is shown in figure **2.17** (b). The authors agree that TaV_2 has the cubic C15 structure type, but they report that the structure changes to the hexagonal C14 structure type at higher temperatures. The transformation temperature from the solid solution to the Laves phase was found already at 1430 °C. However, no other appearance of a C14 phase in the Ta–V system is reported and other authors [94] mistrust the results obtained by Savicky *et al.*

The most recent investigations were carried out by Danon *et al.* [99] and by Pavlů *et al.* [100] who calculated the Ta–V phase diagram based on the CALPHAD method considering both scenarios, the existence of only the C15 phase and the existence of a C15 low-temperature and a C14 high-temperature phase. Both found a good agreement between the calculated and the experimental phase diagrams, however, "*More experimental evidence would be needed to establish definitely the behavior of the Laves phase* TaV_2 " [99]. Additionally, a short review on recent literature is given by Okamoto [101].

2.6.5 The Fe–Ta system

The phase diagram of the Fe-Ta system contains the six phases listed in table **2.5**, two of which are intermediate phases [103]. Figure **2.18** shows the most recent version of the phase diagram. Three solid solutions of Fe exist on the Fe-rich side of the first eutectic at 1442 °C. δ-Fe shows the largest solubility for Ta of 2.5 at.% at the eutectic temperature. The other two solid solution α-Fe and γ-Fe are stable at lower temperatures with solubilities less than 1 at.% Ta. At compositions around 33.3 at.% Ta a Laves phase $TaFe_2$ (also called ϵ phase) of C14 structure type is formed with a homogeneity range from 28 to 38 at.% Nb. It melts congruently with a melting temperature of 1750 °C [104]. The C14 phase was reported by several authors [95, 104–109] but has never been thoroughly studied. The reported lattice parameters vary only slightly ($a = 4.805 - 4.852$ Å, $c = 7.835 - 7.914$ Å). At a composition of approximately 42 at.% Ta an eutectic formed by the Laves phase and the μ phase is observed at 1570 °C. The μ phase forms directly from the melt close to a composition of Ta_6Fe_7 at 1870 °C with a maximal homogeneity range of 10 at.% Ta. Another eutectic appears between the μ phase and the Ta(Fe) solid solution at 1670 °C. The maximal solubility of Fe in Ta is 6 at.% at the eutectic temperature.

Table 2.5: Observed phases in the Fe–Ta system [103].

Phase	at.% Ta[1]	Pearson symbol	Space group	Structure type
α-Fe	0 to 0.7	$cI2$	$Im\bar{3}m$	W
γ-Fe	0 to 0.9	$cF4$	$Fm\bar{3}m$	Cu
δ-Fe	0 to 2.5	$cI2$	$Im\bar{3}m$	W
ϵ-$TaFe_2$	28 to 38[2]	$hP12$	$P6_3/mmc$	$MgZn_2$
μ-Ta_7Fe_6	49 to 59[2]	$hR13$	$R\bar{3}m$	W_6Fe_7
Ta(Fe)	94 to 100[2]	$cI2$	$Im\bar{3}m$	W

[1] Maximum width of the homogeneity range
[2] More current data from [104]

2.6.6 The Fe–Ta–V system

No data on the ternary Fe–Ta–V system is available in the literature. Neither a phase diagram nor any ternary compounds are reported. It is only known, that the binaries TaV_2 and $TaFe_2$ crystallize with the C15 and C14 structure type, respectively. Considering other ternary systems like the Co–Cr–Nb system one can expect TaV_2 and $TaFe_2$ to solve certain amounts of the ternary element. However, the behavior along the section TaV_2–$TaFe_2$ is unknown and will be a subject of this work.

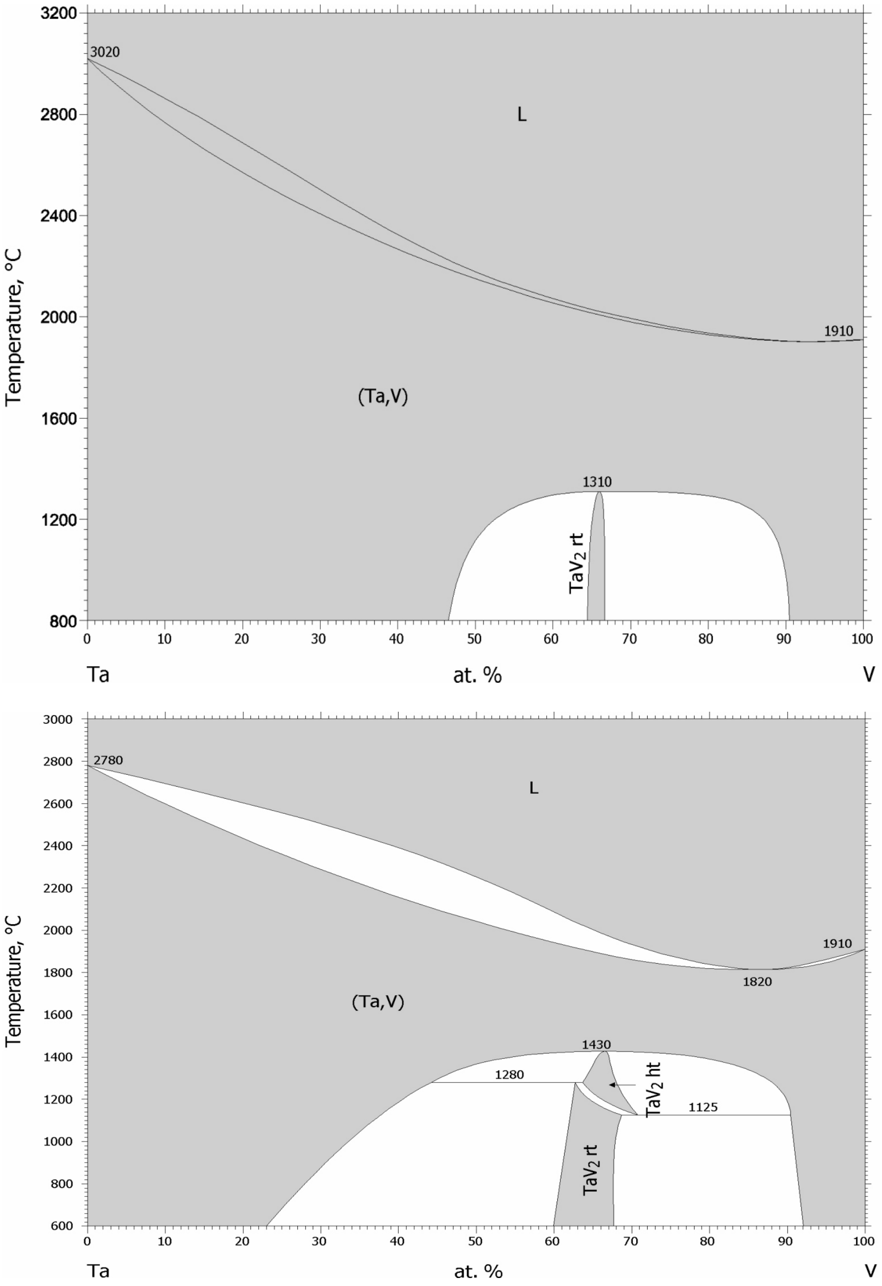

Figure 2.17: The Ta–V phase diagram with (bottom) and without (top) high temperature phase transformation C14 ⇒ C15 [94, 96, 97, 102].

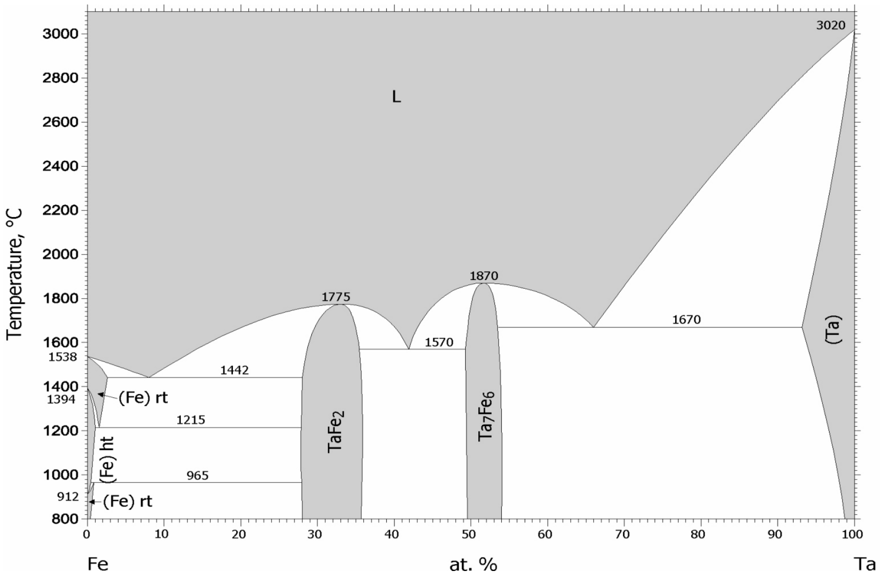

Figure 2.18: The Fe–Ta phase diagram [102, 103, 110].

3 Experimental and theoretical methods

3.1 Sample preparation

The specimens were prepared by argon arc-melting mixtures of high purity elements on the water-cooled copper hearth of an electric arc furnace (Series 5BJ, Centorr Vacuum Industries). The high purity elements used as starting materials are listed in table **3.1**. The total mass of each specimen was about 2 g. The corresponding amounts of the elements were placed in the cups of the copper hearth. The furnace chamber was repeatedly evacuated and flushed with argon. A slightly reduced argon pressure of about 700 mbar was then used for the preparation. Prior to the melting procedure the argon atmosphere was purified from oxygen by melting an ingot of titanium several times. To ensure compositional homogeneity the specimens were remelted and turned over several times (3-6 times, depending

Table 3.1: Starting materials.

Element	Form	Vendor	Purity (metals basis)
Al	granules	ChemPur	99.99%
Co	pieces	MPIE	99.92%
Cr	pieces	Chempur	99.99%
Fe	foil	Alfa Aesar	99.995%
Nb	pieces	MPIE	99.9%
Ta	foil	Alfa Aesar	99.95%
Ta	foil	ChemPur	99.9+%
V	foil	Alfa Aesar	99.8%
V	pieces	Chempur	99.9%
Zr	foil	Chempur	99.8%

(a) starting elements (b) bell jar electric arc furnace (c) electric arc furnace inside argon filled glove box

(d) melted button and an open Ta ampule (e) Ta ampules inside argon filled fused silica tube (f) XRPD, synchrotron XRPD and single crystal X-ray diffraction specimen holder

Figure 3.1: Sample preparation.

on the composition). The typical mass loss was 0.1% – 0.5% in the Co–Cr–Nb and < 0.1% in the Fe–Ta–V system, respectively.

For the following heat treatment each specimen was encapsulated in a clean weld-sealed niobium or tantalum ampule under argon atmosphere. These ampules in turn were jacketed in fused silica tubes under a pressure of about 200 mbar argon and annealed isothermally at temperatures between 1000 and 1300 °C for 30 days in muffle furnaces (Nabertherm). Finally the samples were quenched in water. The silica tubes were simultaneously crushed to ensure a maximum quenching rate.

For higher annealing temperatures and a more precise temperature control some heat treatments were carried out in a vertical tube furnace with a maximal temperature of 1700 °C (LORA/i, Reetz). Figure **3.1** shows some images to illustrate the preparation methods. The high-temperature tube furnace is shown in figure **3.2**. Due to their high hardness and to prepare the necessary sample shapes for physical properties measurements and metallographic analyses, some samples were cut on a low-speed saw (IsoMet, Buehler) using diamond coated cutting blades.

Figure 3.2: The high-temperature vertical tube furnace (LORA/i, Reetz) can continuously operate at up to 1700 °C (maximum temperature 1750 °C).

3.2 X-ray diffraction

3.2.1 Powder diffraction

X-ray powder diffraction was employed for phase identification and lattice parameter determination. The samples were crushed in a tungsten-carbide mortar and subsequently ground to fine powders in an agate mortar. The powders were sieved to a grain size of $\leq 40\,\mu m$ and spread on a Vaseline coated Mylar foil of a flatbed sample mount (fig. **3.1** f).

An image-plate Guinier-camera (Huber G670) was used to record the X-ray powder diffraction patterns at room temperature in an angular range of $3° \leq 2\theta \leq 100°$. Depending on the sample composition the patterns were recorded with Cu or Co $K\alpha_1$-radiation (Cu $K\alpha_1 = 1.540562\,\text{Å}$, germanium monochromator; Co $K\alpha_1 = 1.788965\,\text{Å}$, quartz monochromator) to avoid fluorescence effects.

The unit cell parameters were determined by a least-squares refinement of the diffraction angles in the range of $20° \leq 2\theta \leq 100°$ using silicon (Si, NIST SRM 640c, $a = 5.43119(9)\,\text{Å}$) or lanthanum hexaboride (LaB_6, NIST SRM 660a, $a = 4.1569(1)\,\text{Å}$) as an internal standard. Peak positions and lattice parameters were determined using the program `Stoe WinXPOW` [111]. For crystal structure refinements by means of the Rietveld method [112,113] the program `Jana2006` [114] was used.

Selected samples were investigated using synchrotron radiation at the European Synchrotron Radiation Facility (ESRF) in Grenoble, France. The high resolution powder diffraction beamline ID31 has Debye-Scherrer geometry with a rotating glass capillary as sample container (fig. **3.1** f). The patterns where recorded in an angular range of $0° \leq 2\theta \leq 60°$. The X-ray wavelength was determined by using LaB_6 as external standard. The wavelength was about 0.4 Å and slightly different in two different experimental setups.

3.2.2 Single crystal structure analysis

For single crystal structure analyses a fraction with a grain size between 20 µm and 40 µm was extracted from the sample powders and spread on a petri dish. Selected single crystals of irregular shape and metallic luster were mounted onto sharpened Lindemann glass fibers using two-component epoxy resin adhesive. The quality of the crystals was checked with a Stoe IPDS1 diffractometer. The data collection was carried out on Rigaku R-axis Rapid, Rigaku AFC7 or Rigaku R-axis Spider diffractometers equipped with Mo and Ag $K\alpha_1$-radiation (Mo $K\alpha_1 = 0.71073\,\text{Å}$, Ag $K\alpha_1 = 0.56084\ \text{Å}$), respectively. Lorentz-polarization and multi-scan absorption correction were made using the program `CrystalClear` [115]. For averaging of symmetrically equivalent reflections and full-matrix least squares refinement on F^2, the program `Jana2006` [114] has been used.

3.3 Metallography

Metallographic analyses were performed on thermally annealed specimens. Fragments of selected samples of about 3 mm in diameter were hot-embedded in a combination of conductive and non-conductive bakelit resin (Struers Polyfast and Multifast). After leveling the sample surfaces with wet abrasive paper (silicon carbide, P500), the samples were preparated using automated grinding and polishing machines following the preparation route in table **3.2**. After each step the sample surfaces were rinsed with deionized water and ethanol.

Table 3.2: Steps of the metallographic preparation.

	Mount	Grinding-/Polishing agent	Pressure (N)/Time (s)
1	wet abrasive paper	SiC, P1000	20/60
2	wet abrasive paper	SiC, P2000	20/120
1	MD Largo	Diamond[1], 9 µm	25/180
2	MD Dac	Diamond[2], 3 µm	25/60
3	MD Chem	SiO_2[3], 0.05 µm	20/30
		Rinse with deionized H_2O	-/30

[1] Struers DiaDuo, diamond-water suspension with lubricant

[2] Struers DP-S, diamond-water suspension + Struers lubricant blue

[3] Struers OP-S, colloidal SiO_2-ethanol suspension

The examination of the microstructure was carried out using light optical microscopy (Axioplan 2, Zeiss) in brightfield, polarized light and differential interference contrast (DIC). Selected samples were examined using scanning electron microscopy (Philips XL 30, Philips, Netherlands), field emission scanning electron microscopy (FE-SEM, JEOL JSM-7000F equipped with Oxford EDXS and WDXS instruments) and electron backscatter diffraction (EBSD) (Zeiss LEO 438 VP equipped with TSL, EDAX EBSD system). The composition of single phase samples was determined using at least three independent measurements on an electron probe microanalyzer (Cameca SX 100) with standardless ZAF correction. For WDXS measurements the pure elements were used as standard materials.

3.4 Chemical analysis

The starting materials as well as the samples have been analyzed concerning their chemical composition. The concentration of nonmetallic impurities of hydrogen, carbon, nitrogen and oxygen were checked with the combustion technique and the carrier gas hot extraction method, respectively. In the combustion technique (Leco C-200 CHLH, Leco) the sample was burned in presence of an oxygen flow. The carbon content was then determined by infrared detectors in form of CO and CO_2.

The oxygen content was determined with the carrier gas hot extraction method (Leco TCH-600, Leco). Approximately 100 mg of the sample material were heated in a graphite crucible to a temperature of 2400 K together with tin and nickel as melt-forming additives. The oxygen forms CO and CO_2 which is then detected in the helium carrier gas by infrared detectors. The amounts of hydrogen and nitrogen are determined by heat conductivity detectors.

Inductively coupled plasma-optical emission spectrometry (ICP-OES, Varian, Vista RL) was used to check the composition of the heat treated samples. For each analysis 20 mg of the sample material were dissolved in a mixture of hydrofluoric and nitric acid in a microwave oven at a temperature of 150 °C. The filtered solution was then sprayed into an argon plasma torch.

The results of the chemical analysis given in wt.% are converted to at.% under the assumption that only the metallic constituents are contained in the sample. The standard deviation was calculated under the assumption that all uncertainties add up to the largest possible error.

3.5 Thermal analysis

For the determination of melting and transition temperatures, high-temperature DSC/DTA measurements (Netzsch DSC 404, Netzsch STA 449) were carried out. Approximately 70 mg of the samples were heated in Y_2O_3, Pt-Rh (with Al_2O_3 inlay) or Ta crucibles from room temperature up to 1550 °C.

The determination of the reaction temperatures was based on onset and peak temperatures in the heating curve.

3.6 Electrical resistivity and magnetization measurements

Electrical resistivity $\rho(T)$ of polycrystalline specimens was measured by a conventional 4-contact dc method between 4 K and 320 K. For the measurements, prismatic blocks with approximate dimensions 1 x 1 x 5 mm were cut from selected polycrystalline samples. A cryostat integrated in a glove box system was utilized where sample preparation and handling could be carried out under argon gas.

The temperature (T) and field (B) dependencies of the magnetization (M) were measured with a standard SQUID magnetometer (Quantum Design, MPMS). Polycrystalline fragments of the samples of approximately 70 mg were measured in a maximum field of 1000 Oe between 2 and 300 K.

3.7 Electronic structure calculations

This section gives an overview how first principles density functional theory (DFT) calculations can be used as a tool to estimate the stability of compounds. A very brief introduction of DFT is be followed by a description of how large amounts of data can be handled and evaluated using the computer and scripting languages.

3.7.1 Density functional theory as a tool

The challenge in computational solid state chemistry is the calculation of macroscopic, physical properties of solids solely based on the microscopic arrangement of its constitutive atoms – its crystal structure. A solid is an accumulation of heavy, positively charged nuclei and lighter, negatively charged electrons. All this particles are bound together by electromagnetic interactions. This *many-body problem* can be described by a many-body wavefunction which could be obtained by solving the Schrödinger equation for this problem. However, this differential equation is far to complex to be solved analytically or numerically, even for small systems, due to the huge number of degrees of freedom. A first approximation to simplify this problem is the BORN-OPPENHEIMER-approximation [116]. Since the nuclei are about three orders of magnitude heavier than the electrons, their motion is much slower and they can be regarded as frozen at a fixed position at each time. The lighter electrons are assumed to always be in an instantaneous equilibrium with the nuclei. This approximation thus allows to separate the motion of the nuclei from the motion of the electrons and the nuclei are reduced to be an external potential acting in the electron cloud. Although this greatly reduces the complexity of the problem, the equations are still far to difficult to be solved.

Density functional theory is one way out of this (simplified) many-body problem. It is based on theorems put forth by Hohenberg, Kohn and Sham [117, 118] in the mid 1960s. At the heart of DFT is the statement, that for a given external potential there exists only one ground state electron density. If the ground state density is known, all other observables of the system like the total energy for example can be determined as functionals of this density. And even the ground-state wavefunction which is known to contain all possible information of the system, is a functional of the ground-state density. This is called the first Hohenberg-Kohn theorem. The second theorem, the Hohenberg-Kohn variational principle, defines a functional for the energy and proves, that the ground state energy of a given external potential can be found my minimizing this functional under the constraint of a fixed particle number. This yields the ground-state energy, however, the formulation for the ground state density is still not known. It is described by the sum of single-particle wave functions which finally lead to the Kohn-Sham equations. With their help it becomes possible to transform the problem of calculating the ground state electron density from a many-body Schrödinger equation into many single-particle problems. The great achievement is that the Kohn-Sham equation poses a self-consistency problem which can be solved iteratively. So far DFT looks like a single-particle theory, many-body effects are included via the so-called exchange-correlation functional.

3.7.2 Exchange-correlation energy functionals

The ability of calculating the ground state energy and the physical properties of a solid compound only from its crystal structure is associated with the problem of constructing a reliable approximation for the exchange-correlation energy functional. Different approaches have been developed and are frequently used by theoreticians. The *local-density approximation (LDA)*, which is derived from the theory of the homogeneous electron gas, is one of the commonly used functionals in weakly correlated systems where the electron density varies only slowly. In LDA the functional depends only on the density at the coordinate where the functional is evaluated. The solid is divided into small cells and for each cell a homogeneous electron density is assumed. The exchange-correlation energy for each cell can now be determined from the exchange-correlation energy in the model system, the homogeneous electron gas. Quantum Monte Carlo simulations for the energy of the homogeneous electron gas for several intermediate values of the density provide accurate values of the correlation energy density. Different mathematical treatments of the problem have resulted in different LDA functionals, for example Barth and Hedin or Perdew and Wang. The LDA is known to overestimate binding energies resulting in too short atom-atom distances while the calculated ground state energy of atoms comes out a little too low. The introduction of the spin of the electrons results in the local spin density approximation (LSDA).

The accuracy of the functional can be improved by considering not only the electron density itself, but also its gradient at the same coordinate. This is the so called *generalized gradient approximation (GGA)*. It comes in different mathematical flavors and is associated with more realistic molecular geometries but also with greater computational effort.

In strongly correlated systems the description of a slowly varying electron density is not valid anymore and the behavior of the electrons cannot be described as non-interacting particles. For those systems the Coulomb repulsion between electrons has to be introduced and more complicated functionals like LSDA+U are used.

3.7.3 DFT codes – the muffin-tin, the pseudopotential and the full potential approach

Different DFT schemes have been developed in order to calculate the properties of natural materials, with the aim to find a compromise between accuracy and computational efficiency. The main difference of these schemes is the treatment of the electrons and the description of the potential. Within the *muffin-tin approximation (MT)*, non-overlapping spheres are centered on the atomic positions. The potential experienced by an electron within these regions is approximated to be spherically symmetric around the nucleus. In the remaining interstitial region, the potential is approximated as a constant. The integration over these sphere will however not result in the correct charge density since the spheres do not cover the whole volume of the solid. Therefore, within the *atomic-sphere approximation*

(ASA) the spheres are allowed to overlap and the size of the spheres is chosen so that they cover the entire solid.

In a natural solid the inner electrons are strongly bonded to the nuclei. They do not participate in the chemical bond since their wave functions overlap only very little with the core electron wave functions from neighboring atoms. The materials physical and chemical properties are mainly ruled by the quasi free valence electrons. The *pseudopotential approach (PP)* takes advantage of this by combining the strongly bonded core electrons and the nuclei into an effective potential. Only the remaining valence electrons are treated explicitly within this effective potential. This results in a considerably reduced computational effort. Pseudopotential codes make it possible to treat large system (>1000 atoms) or to relax many atoms at once within reasonable computation times. The pseudopotential code VASP [119–122] which is used in this work offers different potentials for each element where more or less electrons are treated as core electrons.

Full potential, all electron codes treat all electrons explicitly. This is regarded as the most precise calculational method. Full potential calculations are however only applicable to smaller system (up to 100 atoms) and are more time demanding. The available codes differ in the treatment of their basis, e.g., muffin-tin orbitals or a local orbital basis.

3.7.4 Describing disorder - VCA, CPA and supercells

The main problem of describing disorder like vacancies, interstitial atoms and substitutional atoms in compounds and phases with ab-initio methods is the lack of periodicity. With the choice of a finite unit cell as input for the calculations one always introduces artificial periodicity and therefore looses information. However, several ways have been proposed to attenuate this problems.

The most simple approach is the *rigid-band approximation.* Here, the Fermi level is simply shifted according to the number of electrons introduced to or taken out of the system. Since neither the wave function, nor the Hamiltonian is modified this is a rather crude approximation.

An alternative is the *virtual crystal approximation (VCA)* where the disordered atomic site under consideration is occupied with a "virtual" atom. The number of valence electrons of this virtual atom is adjusted to the average number of valence electrons on this site and the nuclear charge is modified correspondingly to achieve neutrality. This method is however only applicable to the first horizontal neighbors in the periodic table, i.e., elements with consecutive atomic numbers.

A more accurate approach is the *coherent potential approximation (CPA)* where the solid is described by the averaged ensemble of all possible occupation configurations. The wave functions are replaced by Green's functions which are scattered at the homogeneity of the lattice.

Another possibility to describe vacancies or substitution is the construction of large supercells. In a way this is the most accurate approach of describing disorder since no approximation is made in calculating the properties of the completely ordered supercells. The drawback of that approach is that the almost infinite number of possible configurations is represented by a small number of artificial supercell configurations which again causes the loss of information. Furthermore, the use of supercells always introduces a certain amount of short range order which is not necessarily present in the actual compound. Additionally the calculation of supercell configurations is more time demanding and the size of the supercells have to increase with decreasing impurity concentration. Even if the computer power is large enough to handle larger and larger supercells and hence more and more configurations, the physical properties of an intermetallic compound are always the result of an average over different atomic configurations.

In this work the supercell approach is preferred over VCA and CPA for several reasons. The VCA is not applicable since the elements involved in the phases under investigation do not have consecutive atomic numbers. The reasons for not applying CPA are manifold. The experience with CPA have shown that it is highly unstable for ternary compounds and for more than one disordered atomic site. The determination of the total energy in CPA is not done using the linear tetrahedron method. Therefore, the total energies of different structures (C14/C15) are not comparable. And the CPA method as implemented in FPLO5 is not capable of relaxing lattice parameters and atomic coordinates which is necessary for investigating the c/a ratio in hexagonal Laves phases.

3.7.5 Calculational methods used in this work

In this work the calculations were performed with two different DFT codes, VASP and FPLO. The Vienna Ab-Initio Simulation Package VASP (version 4.6.35, April

3rd 08) [119–122] is a pseudopotential code employing the projector-augmented wave (PAW) method [123, 124]. The exchange-correlation functional is taken as the Perdew-Wang generalized gradient approximation (GGA). The k-point grids are constructed using the scheme proposed by Monkhorst and Pack [125] for the cubic and gamma-centered grids for the hexagonal structures. The structures are fully relaxed in both atomic coordinates and lattice parameters using a quasi-Newton algorithm. Due to the dependence of the basis set on the volume, consecutive calculations (i.e., stop and restart) were performed to fully relax the structures. The reported total energies are obtained from a final static calculation.

The full potential local-orbital minimum-basis code fplo (version 9.01-35) [126, 127] uses the local (spin) density approximation (L(S)DA) to solve the Kohn-Sham equations. fplo is used to verify some of the vasp results and to study the differences obtained with these two codes.

All calculations were performed on a cluster of three workstations running the operating system openSUSE linux with 56 CPUs and 192 GB RAM in total.

3.7.6 Computer aided data processing

To calculate stability ranges and site occupations along a quasi-binary section of a ternary system it is necessary to determine the number and the atomic arrangement of all possible ordered configurations for each composition. An example: In a ternary hexagonal C14 Laves $A(B'_{1-x}B''_x)_2$ there are four atomic sites for the A and eight atomic sites for the B atoms. Given an equal B' and B'' content (i.e. $x = 0.5$) four B' and four B'' atoms have to be distributed over the eight atomic sites. In this case there are 70 possible combinations. However, many of these configurations are symmetrically equivalent. They will have the same total energy and do not need to be calculated. In the present case the number of unique, symmetrically and energetically distinguishable configurations reduces to nine. Given a 2 x 1 x 1 supercell of a hexagonal C14 Laves phase these numbers rapidly increase to 12870 possible combinations and 776 unique configurations at the composition $x = 0.5$.

The determination of the unique configurations for a whole quasi-binary section is therefore a laborious task and the analysis of the calculated data is quite complex. For the calculation of the thermal equilibria of the site occupation, numerical values from several thousands of files have to be extracted and processed. All this tasks and more, like the control over starting the calculations one after the other can be greatly simplified by using computer programs. For the thesis at hand a significant number of computer scripts have been developed using the programming language `python`, the Linux shell `bash` and various Linux command line tools like `awk` and `sed`. They serve as tools for determining the configurations, for setting up the directory environment and the actual input files for the calculations, for starting and controlling them and for the examination and the extraction of the data from the calculated output. A more detailed explanation of how these scripts work is given in the next chapter.

4 Computation of phase stability, lattice parameters and site occupation

This chapter describes how the unique configurations are determined, how the input files for the calculations are created and how the calculations itself are started and controlled. It is explained how the output of the calculations is parsed for the values of interest and how these values can be analyzed. Finally, with the help of examples the calculation of the thermal equilibria of the site occupation factors and the lattice parameters is explained.

4.1 Generating the unique configurations

For a given composition x in $A(B'_{1-x}B''_x)_2$ there is a large number of configurations, i.e., possible distributions of B' and B'' among the atomic B sites of the unit cell. Since many of these have the same symmetry and thus the same total energy, it is only necessary to calculate the total energy of the unique configurations. The way of determining the unique configurations which is explained in the following is applicable to any structure but will be illustrated below for the hexagonal C14 structure of $\mathrm{Ta(V_{1-x}Fe_x)_2}$. The process is implemented as a python script called `super` and divided in two steps:
(i) Creating all possible combinations for all compositions for the given structure.
(ii) Determination of the symmetrically independent configurations.

The unit cell of C14 $\mathrm{Ta(V_{1-x}Fe_x)_2}$ contains four formula units. Therefore, it can be written as $\mathrm{Ta_4V_{8-N}Fe_N}$ with $N = 8 \cdot x$. In this model, the four $4f$ sites are always fully and exclusively occupied by Ta atoms. Thus, only changes in the occupation of the $2a$ and $6h$ positions by V and Fe atoms are taken into account. Since DFT can only handle integer numbers of atoms[1] there is only a finite number $N+1$ of discrete compositions that can be realized. For the present case there are nine compositions (seven ternary and two binary) listed in table **4.1**.

Table 4.1: Possible compositions, the number of combinations $A(N)$ and the unique configurations $C(N)$ for a C14 unit cell with a composition $Ta_4V_{8-N}Fe_N$.

N	x	$Ta_4V_{8-N}Fe_N$	$Ta(V_{1-x}Fe_x)_2$	$A(N)$	$C(N)$
0	0.000	Ta_4V_8	TaV_2	1	1
1	0.125	$Ta_4V_7Fe_1$	$Ta(V_{0.875}Fe_{0.125})_2$	8	2
2	0.250	$Ta_4V_6Fe_2$	$Ta(V_{0.75}Fe_{0.25})_2$	28	5
3	0.375	$Ta_4V_5Fe_3$	$Ta(V_{0.625}Fe_{0.375})_2$	56	7
4	0.500	$Ta_4V_4Fe_4$	$Ta(V_{0.5}Fe_{0.5})_2$	70	9
5	0.625	$Ta_4V_3Fe_5$	$Ta(V_{0.375}Fe_{0.625})_2$	56	7
6	0.750	$Ta_4V_2Fe_6$	$Ta(V_{0.25}Fe_{0.75})_2$	28	5
7	0.875	$Ta_4V_1Fe_7$	$Ta(V_{0.125}Fe_{0.875})_2$	8	2
8	1.000	Ta_4Fe_8	$TaFe_2$	1	1

The first step (i) – creating all possible combinations for each N – is done by permutation. The script simply generates all combinations by swapping atom types on the available atomic positions. For each single combination $A(N)$ a `xyz.*` file[2] is written which fully describes the cell. It contains the unit cell parameters, the fractional atomic coordinates and the atom type on each atomic position. The created files are stored in different directories in sets of equal composition N. Details on the file format can be found in the appendix A.1. The number of solutions $A(N)$ to distribute N atoms among eight atomic positions is a good measure of whether the script is giving the correct results. It can be derived from statistics [128] and is given by:

$$A(N) = \frac{8!}{(8-N)! * N!} \tag{4.1}$$

For 2 x 1 x 1 supercell with 16 B position the above formula is altered by replacing

---

[1] The virtual crystal approximation (VCA) and the coherent potential approximation (CPA) are able to treat non-integer numbers of atoms. See section 3.7.4

[2] the * stands for a string of lower case letters denoting the particular configuration.

8 with 16.

In the second step (ii) the unique configurations are determined for each set of equal N. To achieve this, the different configurations have to be compared with each other to figure out which of the created combinations are symmetrically equivalent. The equivalent combinations will be discarded from the set to keep only one representative of each unique symmetry in the set. A simple comparison of the `xyz.*` files is not possible since even combinations which are symmetrically equal can have different `xyz.*` files. A method which can be easily implemented is the comparison of interatomic distances. For that purpose the `super`-script calls `xyzi`[3] on each `xyz.*` file and pipes the output to a file called `xyz.*.dist`. The program `xyzi` generates a list of interatomic pair distances for a given unit cell configuration. The `xyz.*.dist` files can now easily be compared. Equivalent files denote equivalent configurations. The first file of the set is compared to all other files of the set one by one. If the compared files are different both will remain in the set. If they are equal the latter of the two is being deleted. The script then continues with the second file and compares it with all others, and so on. In this manner all combinations of set are compared with all others until the final set contains only unique and distinguishable configurations. During this step it is crucial to keep track of the number of equivalent configurations, i.e., the number of deleted files. This number is denoted as the multiplicity g. If for example during the comparison of the first `xyz.*.dist` six other files are discarded from the set, than the multiplicity g of this configuration is seven (six plus the configuration itself). The multiplicity is written into a third file called `xyz.*.dist.equal`. It becomes important for the calculation of the site occupation factors, see section 4.5. Finally, there are $N + 1$ folders according to the different compositions which contain the `xyz.*`, `xyz.*.dist` and `xyz.*.dist.equal` files of the unique configurations.

Since this script deals only with interatomic distances and not with the symmetry of the structures itself, it can be easily modified to work for other structures like C15 or C36 or it can be applied to supercells. For that, only the lattice parameters, the number of atoms and the fractional atomic coordinates have to be changed in the script. To get an impression of the quantity of files that are created and processed the data for all examples in this work are listed in table **4.2**. All that

---

[3] `xyzi` is a combination of `awk` and `csh` code written by Marek Mihalkovic

Table 4.2: Configurations and compositions for a C15, C14 and C36.

Structure type	C15	C14	C14 (2 x 1 x 1)	C36
No. of atoms per unit cell/supercell	24	12	24	24
No. of atomic positions	16	8	16	16
No. of compositions, N	17	9	17	17
No. of configurations, $\sum A(N)$	65536	256	65536	65536
No. of unique configurations, $\sum C(N)$	201	39	4282	6040

is described above is only implemented in form of scripts without great effort to optimize the code. Furthermore, external programs are called and a lot of hard disk activity (write, read, delete) is done. Therefore, depending on the structure it takes between 10 minutes and 20 hours to create the unique configurations for all compositions of a whole quasi-binary section.

4.2 Setting up, running and controlling the calculations

The last section explained how the unique configurations are created and that each configuration is represented by an `xyz.*` file. In order to perform a calculation, the VASP input files have to be generated based on the structural information stored in these files. The four basic input files for VASP are:

- `INCAR` - the central input file of VASP, it contains the instructions that control the calculation
- `POSCAR` - contains the lattice geometry and the atomic coordinates
- `POTCAR` - contains the pseudopotential for each atomic species
- `KPOINTS` - contains the instructions to generate the k-point grid

The `POTCAR` file is identical for all calculations within the same ternary system. It is generated once, placed in the root directory of the calculation and later copied into the folder of each configuration. The `POSCAR` file is the VASP counterpart of the `xyz.*` file. It contains the same structural information in a slightly different format. However, the information on the type of atoms, i.e., the elements, is contained only in the `POTCAR` file. A script called `xyz2pos`[4] takes care about the generation of `POSCAR` files from `xyz.*` files. An additional script `pos2xyz` does it

---

[4] `xyz2pos` and `pos2xyz` are a combination of `awk` and `csh` code written Marek Mihalkiovic

vice versa.

Due to the dependence of the basis set on the volume in DFT calculations it is advisable to perform consecutive calculations (i.e., stop and restart) to fully relax the structures. Here, three calculations in total are performed on each structure. During the first two runs the structures are relaxed, i.e., the atomic coordinates and lattice parameters are optimized. The first run results in an optimized structure which is taken as input for the second run. The resulting structure of the second run is then regarded as sufficiently optimized. A final static calculation without any optimization is performed to gain precise total energy values. The reported total energies in this work are always only obtained from this last run. Since these three calculations need different `INCAR` files and the resulting optimized structure of one run has to be prepared as input structure for the following run a `jobscript` is necessary to control the three calculations. Additionally, this script creates the `KPOINTS` file before starting the first run. This `jobscript` is the same for all structures and is placed in the same directory as the `POTCAR` file. Its task is to

- generate the `KPOINTS` file
- start the first run and wait for its successful termination
- redirect the terminal output of `vasp` into a file called `output`
- rename all files so that they do not disturb the following calculations
- convert the optimized output structure as the new input
- create a new `INCAR` file and
- start the next run.

Details on the `jobscript` can be found in the appendix A.1.

A script called `set_dirs` will now perform all the necessary steps. It creates a subdirectory with the same name as the `xyz.*` file for each structure, copies the `jobscript` and `POTCAR` files into that directory and calls `xyz2pos` on the `xyz.*` file to create the `POSCAR` file. Now the whole directory tree is set up and ready for being processed one by one.

Since thousands of the calculations cannot be easily started by hand, another script called `fake_pbs` takes care about starting the calculations. First it counts the number of running `vasp` processes. If there is free CPU time it cycles through the current directory and detects all finished and running calculations. Then it starts the next calculation in the queue and writes the current numbers of not-started, running and finished calculations into a logfile. `fake_pbs` can be run as a linux cronjob every 10 minutes to automatically start calculations every time of the day.

4.3 Parsing and analyzing the output

After the successful termination of the calculations the values of interest have to be determined for each calculation from the output files of VASP. These values are

- the chemical composition of the current set of calculations
- the number of configurations in that directory
- the name of each configuration
- the multiplicity of that configuration
- the total energy of that configuration
- the relaxed lattice parameters
- the number of Co (Cr, V, Fe, ...) atoms on $2a/6h$ sites

The data is contained in the VASP output files `CONTCAR`, `OUTCAR` and the redirected terminal output file `output`. The parsing of the output files is accomplished by the scripts `occu8` (for 12 atom cells) and `occu16` for (24 atom cells). The extracted values are written in table form into a `datafile`. Additionally, these scripts calculate the energy difference between the current and the most stable configurations, the unit cell volumes and the thermal equilibria of the site occupation factors and the lattice parameters as described in the sections 4.5 and 4.6.

Sometimes a running calculation terminates unsuccessful due to network problems, power loss or other reasons and not always is this easily recognized. The script `test_dir` can cycle through all calculations in a directory searching for any type of anomalies, warnings, errors or aborted calculations that ever appeared during the calculations carried out in this work. These calculations will then be restored with the help of `renew_vasp_calc`.

4.4 Calculation of the Gibbs energy

A thermodynamic system in contact with a pressure and a heat reservoir is said to be in equilibrium when its Gibbs energy is a minimum. The Gibbs-Helmholtz equation relates the Gibbs energy G to the enthalpy H and the entropy S of the system.

$$G = H - TS \tag{4.2}$$

T is the absolute temperature. Upon forming a solution the change in the Gibbs energy ΔG is given by[5]

$$\Delta G = \Delta H - T\Delta S \tag{4.3}$$

The change in enthalpy ΔH that accompanies the formation of a solid solution such as $A(B'_{1-x}B''_x)_2$ from its constituents, the chemical elements A, B' and B'' is represented by the enthalpy of formation $\Delta_f H$ (denoted as ΔH in the following). It is calculated from the total energy values E of the compound $A(B'_{1-x}B''_x)_2$ and the total energy values of the constituents A, B' and B'' according to their fractions:

$$\begin{aligned} E_{A(B'_{1-x}B''_x)_2} &= E_A + 2\cdot(1-x)\cdot E_{B'} + 2\cdot x\cdot E_{B''} + \Delta H \\ \Delta H &= E_{A(B'_{1-x}B''_x)_2} - E_A - (2-2x)\cdot E_{B'} - 2x\cdot E_{B''} \end{aligned} \tag{4.4}$$

The entropy S is modeled applying the concept of the ideal solution. The ideal solution model is derived from the ideal gas model which describes a theoretical gas composed of randomly moving, non-interacting point particles. However, opposed to the ideal gas, the intermolecular interactions in liquids are strong and cannot be neglected. Instead it is assumed, that the strength of the interactions between the constituents of the solution are equal. That is, in a mixture of A and B, the strength of the interactions A–A, B–B and A–B are equal. There is no enthalpy change and no change in volume associated with the rearrangement of the atoms A and B [129]. Thus, the change in entropy ΔS upon the formation of a disordered solution phase depends only on the fractions and not the type of the components of the mixture. It is given by:

$$\Delta S = -R(x_A \ln x_A + x_B \ln x_B) \tag{4.5}$$

---

[5] Under conditions of constant volume $\Delta V = 0$ the Helmholtz free energy F is used instead of the Gibbs energy G. The enthalpy H is then replaced by the internal energy U, since $\Delta H = U + p\Delta V$: $\Delta F = \Delta U + T\Delta S$.

with R being the universal gas constant and x_A and x_B the mole fractions of the components A and B. With $x_A = x$ and $x_B = 1 - x$ in $A(B'_{1-x}B''_x)_2$ equation 4.5 can be rewritten as:

$$\Delta S = -R(x \ln x + (1-x)\ln(1-x)) \tag{4.6}$$

Thus, the final equation for calculating the Gibbs energy ΔG for the formation of $A(B'_{1-x}B''_x)_2$ from its constituents A, B' and B'' is given by:

$$\begin{aligned}\Delta G =& \Delta H - T\Delta S \\ =& E_{A(B'_{1-x}B''_x)_2} - E_A - (2-2x)\cdot E_{B'} - 2x \cdot E_{B''} + \\ & RT(x \ln x + (1-x)\ln(1-x))\end{aligned} \tag{4.7}$$

Since the total energy values are calculated only for discrete compositions, the resulting Gibbs energy values will be no continuous function. Therefore, it is necessary to choose an appropriate function for a least squares fit of the discrete values of ΔG for each phase. In thermodynamics the Gibbs energy of mixing G^{ϕ}_m for an actual (non-ideal) disordered solution phase ϕ with N constituents is expressed as:

$$G^{\phi}_m = \sum_{i=1}^{N} x_i G^{0,\phi}_{m,i} + RT \sum_{i=1}^{N} x_i \ln x_i + G^{E,\phi} \tag{4.8}$$

For a binary solution ($N = 2$) this yields

$$G^{\phi}_m = (x_1 G^{0,\phi}_{m,1} + x_2 G^{0,\phi}_{m,2}) + RT(x_1 \ln x_1 + x_2 \ln x_2) + G^{E,\phi} \tag{4.9}$$

$G^{E,\phi}$ is the excess Gibbs energy. It represents the additional interactions between the constituents which distinguish a non-ideal from an ideal solution. $G^{E,\phi}$ is most commonly represented with an ansatz by REDLICH and KISTER [130, 131], the Redlich-Kister binary excess model or Redlich-Kister polynomial:

$$G^{E,\phi} = \sum_{i=1}^{n-1} \sum_{j=i+1}^{n} x_i x_j L_{i,j} \tag{4.10}$$

with

$$L_{i,j} = \sum_{k=0}^{m} {}^{k}L_{i,j}(x_i - x_j)^k \tag{4.11}$$

and

$${}^{k}L_{i,j} = {}^{k}A_{i,j} + {}^{k}B_{i,j}T \tag{4.12}$$

These formulas describe the binary interactions in a multicomponent system. $L_{i,j}$ are the binary interaction parameters. For an ideal solution phase all $L_{i,j}$ are zero, thus $G^{E,\phi}$ is zero. For a non-ideal binary solution phase $G^{E,\phi}$ is then given by:

$$G^{E,\phi} = x_1 x_2 {}^{0}L_{1,2} + {}^{1}L_{1,2}(x_1 - x_2) + {}^{2}L_{1,2}(x_1 - x_2)^2 + {}^{3}L_{1,2}(x_1 - x_2)^3 \dots \tag{4.13}$$

If the phase ϕ A(B'$_{1-x}$B"$_x$)$_2$ is considered a quasi-binary system with the two components AB'_2 and AB''_2 at $T = 0\,K$ equations 4.9 and 4.13 become

$$G^{\phi}_{m} = (x_1 G^{0,\phi}_{m,AB'_2} + x_2 G^{0,\phi}_{m,AB''_2}) + x_1 x_2 \sum_{k=0}^{m} {}^{k}A_{1,2}(x_1 - x_2)^k \tag{4.14}$$

Equation 4.14 is now adopted to fit the calculated Gibbs energy values of a the given phases C14 and C15 in the form of

$$\Delta G = (x_1 G_{AB'_2} + x_2 G_{AB''_2}) + x_1 x_2 \sum_{k=0}^{4} {}^{k}A(x_1 - x_2)^k \tag{4.15}$$

$G_{AB'_2}$ and $G_{AB''_2}$ are Gibbs energies of the constituents of the quasi-binary system. Since the mixing entropy for the pure binary compounds is zero, $G_{AB'_2}$ and $G_{AB''_2}$ are replaced by $\Delta H_{AB'_2}$ and $\Delta H_{AB''_2}$, respectively For the fractions x_1 and x_2 of constituents AB'_2 and AB''_2 in $A(B'_{1-x}B''_x)_2$ the relation $x_1 = 1 - x_2$ holds. ${}^{k}A$ are the refineable parameters of the function. The final form of the equation is then given by

$$\begin{aligned}\Delta G =& ((x-1)\Delta H_{AB'_2} + x\Delta H_{AB''_2}) + (x - x^2) \\ & [{}^{0}A + {}^{1}A(2x-1) + {}^{2}A(2x-1)^2 + {}^{3}A(2x-1)^3 + {}^{4}A(2x-1)^4]\end{aligned} \tag{4.16}$$

The calculation of the Gibbs energy values from the total energy values according to equation 4.7 and the least-squares fitting procedure against equation 4.16 is done with `gnuplot` [132].

To estimate the width of the stability ranges at elevated temperatures the tangent construction is used. The contact points of the common tangent of two curves ΔG^{C14} and ΔG^{C15} define the borders of the single phase fields of C14 and C15. However, the analytic calculation of the common tangent of two complex functions like equation 4.16 is very complicated. In this work an algorithm [133] originally intended to calculate the convex hull of a given 2-d scatter plot is modified and used for that. For that purpose the algorithm is feed with value tables calculated with variable accuracy from the functions ΔG^{C14} and ΔG^{C15}. The program then calculates the convex hull and prints the two lowest innermost points which belong to the convex hull. These two points are the contact points of the common tangent and define the tangent function. The graphical output of an example calculation is shown in figure **4.1**.

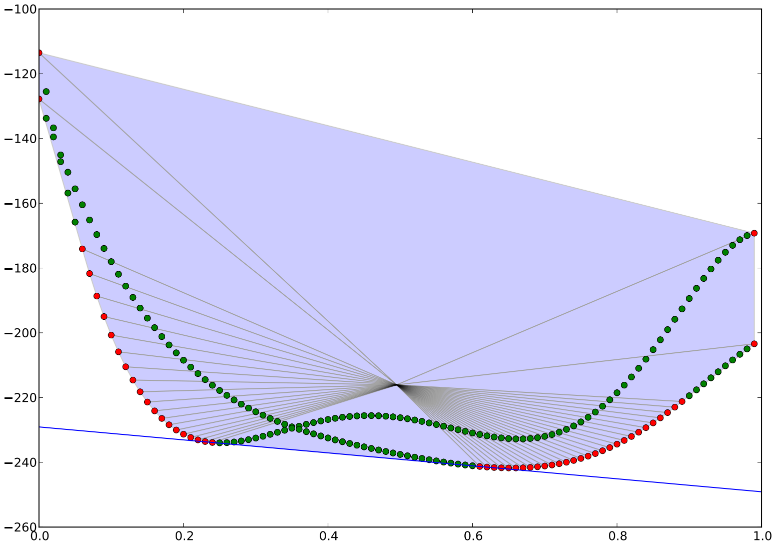

Figure 4.1: Graphical output of the convex hull algorithm. The blue area represents the convex hull of the given scatter plot. Red dots belong to the convex hull, green dots lie within it. The function of the common tangent shown in blue is determined from the two innermost points of the convex hull which represent the contact points of the tangent with the functions.

4.5 Calculation of site occupation factors

Site occupation factors are usually calculated using a simulation method based on Monte Carlo or molecular dynamics techniques with the effective interactions derived from first-principles total energy calculations. In such approaches the emphasis is on the accuracy of the configurational entropy contributions: a large number of atoms are included in the simulation to sample a larger portion of the configurational phase space. The trade-off is the loss of some accuracy in the internal energy term, since the quantum mechanical treatment of interatomic interactions are replaced by some fitted atomistic potentials. In this work a simple statistical mechanical approach is employed where total energies are used directly without any fitting schemes. Thus, the emphasis is more on the accuracy of the internal energy contributions, and the trade-off is a much smaller configurational phase space that the method can cover. This method is applicable to any C14 pseudobinary system. Here the procedure will be illustrated through the example of $\mathrm{Ta(V_{1-x}Fe_x)_2}$.

The unit cell of the C14 structure contains four formula units, thus it can be written as $\mathrm{Ta_4V_{8-N}Fe_N}$. As explained in detail in section 4.1 the N Fe atoms can be distributed over the $2a$ and $6h$ positions in various ways. Many of these configurations will have the same total energy due to being symmetrically equivalent. Consequently, for each value of N first-principles total-energy calculations were only performed for the symmetrically distinct, the unique configurations. The representative configurations will be denoted by $T_{N,p;\sigma}$, where p is the number of Fe atoms placed at $2a$ sites ($N-p$ Fe atoms occupy $6h$ sites), and σ is an index for labeling the symmetrically inequivalent configurations. For a given N corresponding to a Fe concentration of $x = N/8$ the actual, disordered crystal is assumed to be formed by an ensemble of crystals with composition $\mathrm{Ta_4V_{8-N}Fe_N}$ in their standard unit cells. If there are $C(N)$ symmetrically inequivalent configurations, then the ensemble will have $C(N)$ different energy levels. If the total energy of the configuration $T_{N,p;\sigma}$ is denoted by $E_{N,p;\sigma}$ and if $g_{N,p;\sigma}$ stands for the total number of configurations that are symmetrically equivalent to $T_{N,p;\sigma}$, then the partition function for this ensemble is given by

$$Z_N = \sum_{\sigma=1}^{C(N)} g_{N,p;\sigma} \exp(-E_{N,p;\sigma}/(k_B T)) \tag{4.17}$$

where k_B is the Boltzmann constant and T the absolute temperature. The configurational entropy $S_{N,p;\sigma}$ is related to the multiplicity $g_{N,p;\sigma}$ through $S_{N,p;\sigma} = k_B \ln g_{N,p;\sigma}$. Hence, the summand can be expressed as $\exp(-F_{N,p;\sigma}/(k_B T))$, where $F_{N,p;\sigma} = E_{N,p;\sigma} - S_{N,p;\sigma}T$. Then equation 4.17 becomes

$$Z_N = \sum_{\sigma=1}^{C(N)} \exp(-F_{N,p;\sigma}/(k_B T)) \tag{4.18}$$

The Helmholtz free energy for a given value of N can be obtained from the partition function via $F_N = -k_B T \ln Z_N$. The corresponding entropy S_N is calculated by using the expression $-(\partial F_N/\partial T)_V$.

The thermal averages of the $2a$ and $6h$ occupations by Fe atoms can be computed by

$$\begin{aligned} n^{(2a)}_{N,Fe} &= \frac{1}{Z_N} \sum_{\sigma=1}^{C(N)} p_{N;\sigma} \cdot g_{N,p;\sigma} \exp(-E_{N,p;\sigma}/(k_B T)) \\ n^{(6h)}_{N,Fe} &= \frac{1}{Z_N} \sum_{\sigma=1}^{C(N)} (N - p_{N;\sigma}) \cdot g_{N,p;\sigma} \exp(-E_{N,p;\sigma}/(k_B T)) \end{aligned} \tag{4.19}$$

Note that $p_{N;\sigma}$ can be 0, 1 or 2, since it is the number of Fe atoms located at $2a$ sites in the configuration $T_{N,p;\sigma}$. The site occupation factors of the $2a$ and $6h$ positions by Fe atoms are then given by

$$\begin{aligned} s.o.f.^{(2a)}_{N,Fe} &= n^{(2a)}_{N,Fe}/2 \\ s.o.f.^{(6h)}_{N,Fe} &= n^{(6h)}_{N,Fe}/6 \end{aligned} \tag{4.20}$$

The accuracy and the validity of this approach will get better as larger unit cells (supercells) are used to calculate the energies $E_{N,p;\sigma}$ and the multiplicities $g_{N,p;\sigma}$. Basically, the accuracy will be comparable to the accuracy of a Monte Carlo simulation if both calculations cover similar numbers of pairs of neighbors.

That is, if the configurations allowed by the supercell used contain all possible pairings of neighbors included within the interaction-cutoff distance of the Monte Carlo simulation, then the results are expected to have comparable accuracy. Therefore, the present calculation should be more accurate than a Monte Carlo calculation that includes interactions only up to the second nearest neighbors in the B network, and somewhat less accurate than a third-nearest-neighbor Monte Carlo simulation.

In this work the approach was applied to C14 unit cells as well as C14 2 x 1 x 1 supercells which induces some changes in the calculations. The number of unique configurations increases drastically from 39 to 4282 when using the supercells (see table **4.2** on page 70). The number of atoms on $2a$ and $6h$ sites increases from two and six in the unit cell (equ. 4.20) to four and twelve in the 2 x 1 x 1 supercell, respectively. Consequentially, $p_{N;\sigma}$, the number of atoms on $2a$ sites now takes the values 0, 1, 2, 3 and 4.

The calculation of the partition function according to equation 4.17 and the thermal averages of the site occupation factors according to equations 4.20 is implemented in the scripts `occu8` for the unit cell and `occu16` for the supercell. Although only a simple statistical mechanical method was employed, it will be shown that the computed values are seen to capture the observed trends in the investigated systems.

4.6 Calculation of lattice parameters

The result of the calculation of a single configuration $T_{N,p;\sigma}$ are the total energy $E_{N,p;\sigma}$ and the optimized cell geometry defined by the lattice parameters a, b, c and the angles α, β, γ. However, the optimization of the cell geometry strongly depends on the way how the program VASP deals with symmetry. In VASP the symmetry of a given structure is not specified by the user but it is determined by the program itself based on a symmetry analysis of the cell geometry and the atomic positions. The initial cell geometry of a hexagonal C14 unit cell – $a = b$, c and $\alpha = \beta = 90°$, $\gamma = 120°$ – will only be maintained if the calculation is carried out in the appropriate space group. Since all the unique configurations of a given compound $A(B'_{1-x}B''_x)_2$ differ in the distribution of B' and B'' among the atomic sites $2a$ and $6h$, they also differ in symmetry. Thus, VASP will use different space groups and therefore apply different symmetry restrictions to the lattice parameters and atomic positions. This will cause, that for some configurations for example $a = b$ will be maintained and for others not. This is an unsatisfactory situation for a consistent evaluation of the lattice parameters. VASP offers the possibility to switch off the symmetry evaluation and therefore allows to circumvent inconsistent results. If the relaxation is done without symmetry, i.e., in space group $P1$, all lattice parameters and atomic positions will be optimized independently and the initial cell geometry will be destroyed. However, the average observed differences of the a and b (hexagonal) and the a, b and c (cubic) lattice parameters after the optimization were usually very small, in the range of 0.04 Å and 0.03 Å, respectively. The maximum observed difference was 0.2 Å. The same is true for the angles. In case of the hexagonal C14 phases, the average deviation from the initial $\alpha = \beta = 90°$ and $\gamma = 120°$ were 0.15° and 0.6°, respectively. The maximum observed deviation was about 0.8° for α and β and 2.9° for γ. For the cubic C15 phases the average deviation from $\alpha = \beta = \gamma = 90°$ was 0.7° (maximum was 3.3°).

If calculated lattice parameters are evaluated in this work, the hexagonal a lattice parameter is always taken as the average value of a and b, the cubic lattice parameter as the average of a, b and c. The hexagonal c lattice parameter is taken as calculated. The a, b and c lattice parameters were evaluated independently only if appropriate. The unit cell volume is calculated as from a triclinic cell from the exact values according to equation 4.21.

$$V = a \cdot b \cdot c \cdot \sqrt{1 - \cos\alpha^2 - \cos\beta^2 - \cos\gamma^2 + 2\cos\alpha\cos\beta\cos\gamma} \tag{4.21}$$

The thermal averages of the lattice parameters and angles can be calculated in an analog way to the site occupation factors from the partition function (equation 4.17). Again this is implemented in the scripts `occu8` and `occu16`.

$$X = \frac{1}{Z_N} \sum_{\sigma=1}^{C(N)} X_{N,p;\sigma} \cdot g_{N,p;\sigma} \exp(-E_{N,p;\sigma}/(k_B T)) \tag{4.22}$$

with $X = a, b, c, \alpha, \beta, \gamma, V$

4.7 Accuracy and convergence of the calculations

To judge the reliability and the width of the error margins of the calculations a detailed study of the influence of the numerous calculational parameters is necessary. The hexagonal C14 phase $\mathrm{Nb(Cr_{1-x}Co_x)_2}$ serves as an example to study the influence of selected parameters on the total energies, the lattice parameters and the site occupation factors.

4.7.1 Potentials

The program VASP comes with a variety of different potentials, the choice of which influences the obtained total energies and the resulting lattice parameters and site occupation factors. The potentials offered by VASP are ultrasoft pseudopotentials of the LDA and GGA type [123] and potentials generated with the projector augmented wave method (PAW) of GGA and PBE type [124, 134, 135]. A series of calculations using these different potentials has been conducted on C14 $\mathrm{Nb(Cr_{1-x}Co_x)_2}$ in order to study the influence of the potentials on the results. The calculated lattice parameters and site occupation factors are shown in figure **4.2**.

The obtained lattice parameters differ mainly in their absolute values. The largest lattice parameters are obtained with the GGA potentials, the by far smallest with the LDA potentials. This is in good agreement with the theory which states that in general the lattice parameters are underestimated by LDA and slightly overestimated by GGA. The results with the two paw potentials are almost equal and slightly smaller than those with GGA. The general shape of the lattice parameter curves however is not effected by the choice of the potential. This is also valid for the c/a ratio and the site occupation factors. Again the LDA potential shows the largest deviation from all other potentials. Regarding the site occupation factors, the *s.o.f.* of the $6h$ site is mainly unaffected while the *s.o.f.* of the $2a$ site depends stronger on the potential choice. Overall it can be stated, that the absolute values of the lattice parameters and site occupation factors depend only slightly on the chosen potential and the general shape of the curves is not effected at all. Thus, the calculated results are very robust and reliable and almost independent of the chosen potential. The required computing time depends on the chosen potential. Figure **4.3** shows the average required computing time per configuration vs. the composition x. The PAW potentials require approximately

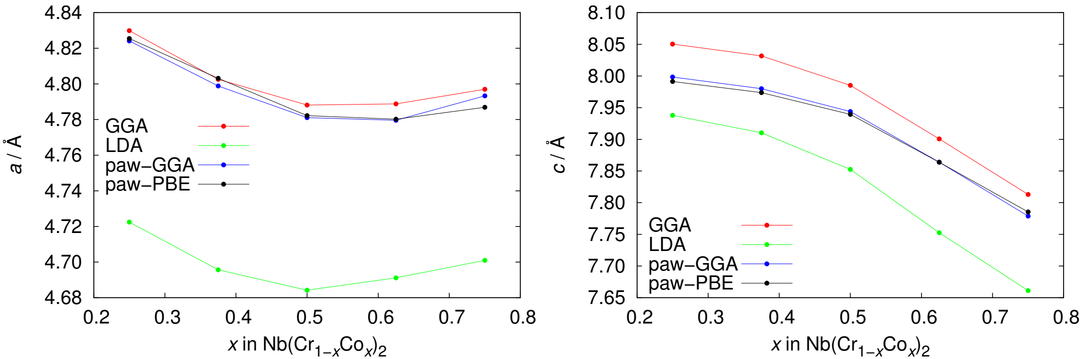

(a) *a* lattice parameter (b) *c* lattice parameter

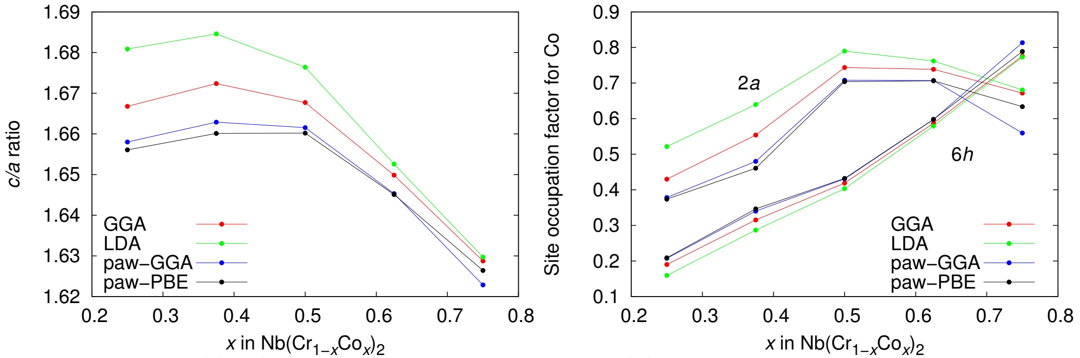

(c) *c*/*a* ratio (d) Site occupation factor fo Co

Figure 4.2: Comparison of the calculated lattice parameters *a* (a) and *c* (b), the *c*/*a* ratio (c) and the site occupation factors for Co (d) in C14 $Nb(Cr_{1-x}Co_x)_2$ using different pseudopotentials.

three times as much computing time as the more simple GGA and LDA potentials. Since PAW potentials are considered more precise, for all calculations carried out with VASP in this work the PAW-GGA potential were chosen. This is also the recommended choice of the VASP authors.

4.7.2 Convergence

For the determination of many properties in DFT calculations one needs to calculate integrals over the first Brillouin zone. This region of space can be mapped by a continuous set of k-points and the occupied states at each k-point contribute to the electronic potential. If the k-point set is continuous, there is an infinite number of k-points in the Brillouin zone at which the wavefunctions must be calculated. However, at k-points that are very close together the electronic wavefunctions will be almost equal. For this reason it is possible to represent

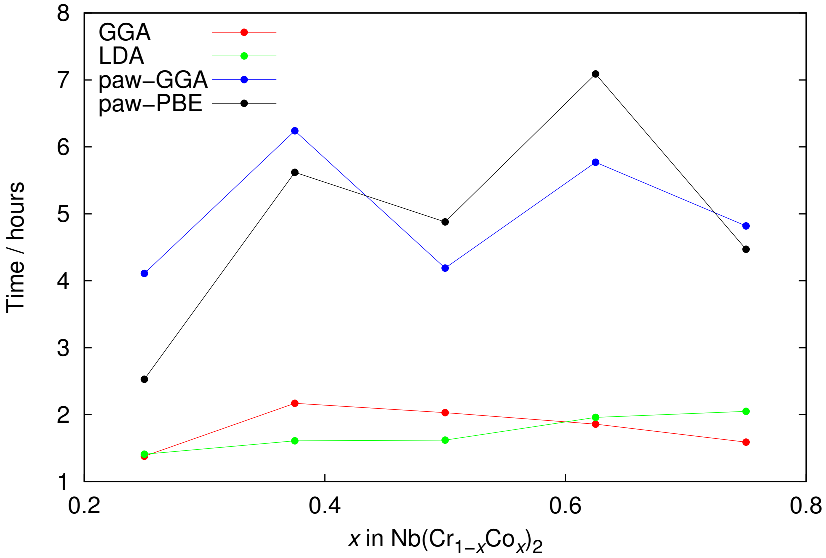

Figure 4.3: Average computing time per configuration for different pseudopotentials as a function of the composition x.

the electronic wavefunction over a region of reciprocal space at a single k-point. This approximation allows for the calculation of the electronic potential at a finite number of k-points and therefore the determination of the total energy. To minimize the error caused by this approximation a sufficiently dense k-point set has to be chosen for the calculations. This can be achieved by controlling the convergence of the total-energy in dependence of the number of k-points. However, the chosen k-point set is always a compromise between accuracy and calculation time. Such a convergence test is made for each of the calculated systems in this work. An example is shown in figure **4.4** for a C14 unit cell and a C14 2 x 1 x 1 supercell of $\mathrm{Nb(Cr_{1-x}Co_x)_2}$.

The time for a complete calculation increases rapidly with increasing number of k-points. The total energy however, converges quite fast. The k-point sets for all calculations in this work are carefully chosen to be converged within a few meV.

4.7.3 Relaxation strategy

Different degrees of structural relaxation are possible in VASP and the choice of the relaxation strategy strongly influences the lattice parameters, atomic positions and site occupation factors of the optimized structures. For a given structure VASP can relax the atomic positions, the cell shape and the cell volume independently or in combination. Thus, different optimization levels are possible chosen with a single parameter in the `INCAR` file.

Table 4.3: Optimization levels provided by VASP.

Parameter	relax ions	change cell shape	change cell volume
2	yes	no	no
3	yes	yes	yes
4	yes	yes	no
5	no	yes	no
6	no	yes	yes
7	no	no	yes

The symmetry and the space group in VASP are not chosen by the user, but are determined by program itself based on a symmetry analysis of the given structure. Restrictions for special atomic positions or restrictions on the lattice parameters and angles are automatically taken care of by VASP. However, since the distribution of the B' and B'' atoms among the unit cell are different for each calculated configuration, the symmetry analysis of VASP will yield a different space group for each configuration and thus apply different symmetry restrictions to atomic positions and the cell geometry. This will results in optimized lattice parameters of the different configurations which cannot easily be compared with each other. This problem can be solved by entirely switching of the symmetry detection and performing all calculations in space group $P1$, with two major drawbacks: increased calculation times and the complete loss off symmetry of the optimized structures. The optimization itself is a computationally intensive process and the more parameters are optimized the more time is needed for each calculational step. To investigate the influence on the total-energy and the site occupation factors different relaxation strategies were applied to a $\mathrm{Nb(Cr_{1-x}Co_x)_2}$ unit cell. The results are shown in figure **4.5**.

The absolute values of the total-energy change only slightly with the varying structural degrees of freedom. However, it is not the absolute values that matter. It is the energy differences between the configurations at a given composition that enter the subsequent calculations. A closer look on the energy differences for the configurations with the composition $x = 0.5$ is shown in the inset in figure **4.5** (a). For calculations with all parameters fixed or only volume relaxation, the range of energy values for the different configurations is small. With an increasing number of structural degrees of freedom the absolute values of the total-energy increase. But more important, the energy differences between the different configurations gets larger. These larger differences enter the partition function with a notable effect on the calculated site occupation factors (*s.o.f.*s). With increasing energy differences the influence of the most stable configuration on the partition function increases and the canonical ensemble is more and more governed by the most stable configuration. This effect can be observed by plotting the *s.o.f.*s calculated from the total-energy values of the different relaxation schemes. If the energy differences between the configurations were zero, all configurations would be equally weighted in the partition function and the *s.o.f.*s would show a completely random distribution. This is indicated by the dashed line in **4.5** (b). If the energy differences were infinitely large, the partition function would contain only the most stable configuration and the *s.o.f.* at each composition x would correspond to the site occupation of the most stable configuration.

For calculations with a small energy range the site occupation factors show the smallest deviation from randomness. For the calculations with a larger total-energy range one observes a larger deviation of the *s.o.f.* from randomness. The results are also in good agreement with *s.o.f.*s obtained from total-energy calculations with the full potential code FPLO also shown ind figure **4.5** (b). Again, the choice of varying relaxation strategies influences to absolute values but not the general behavior of the curves.

Although most time-consuming, all calculations in this work were carried out with full structural relaxation in $P1$, including the cell geometry, cell volume and the atomic positions. The reasons for structural relaxation are obvious. Preferential site occupation is a phenomenon closely related to the crystal structure and the analysis of the c/a ratio depends on the relaxation of a and c.

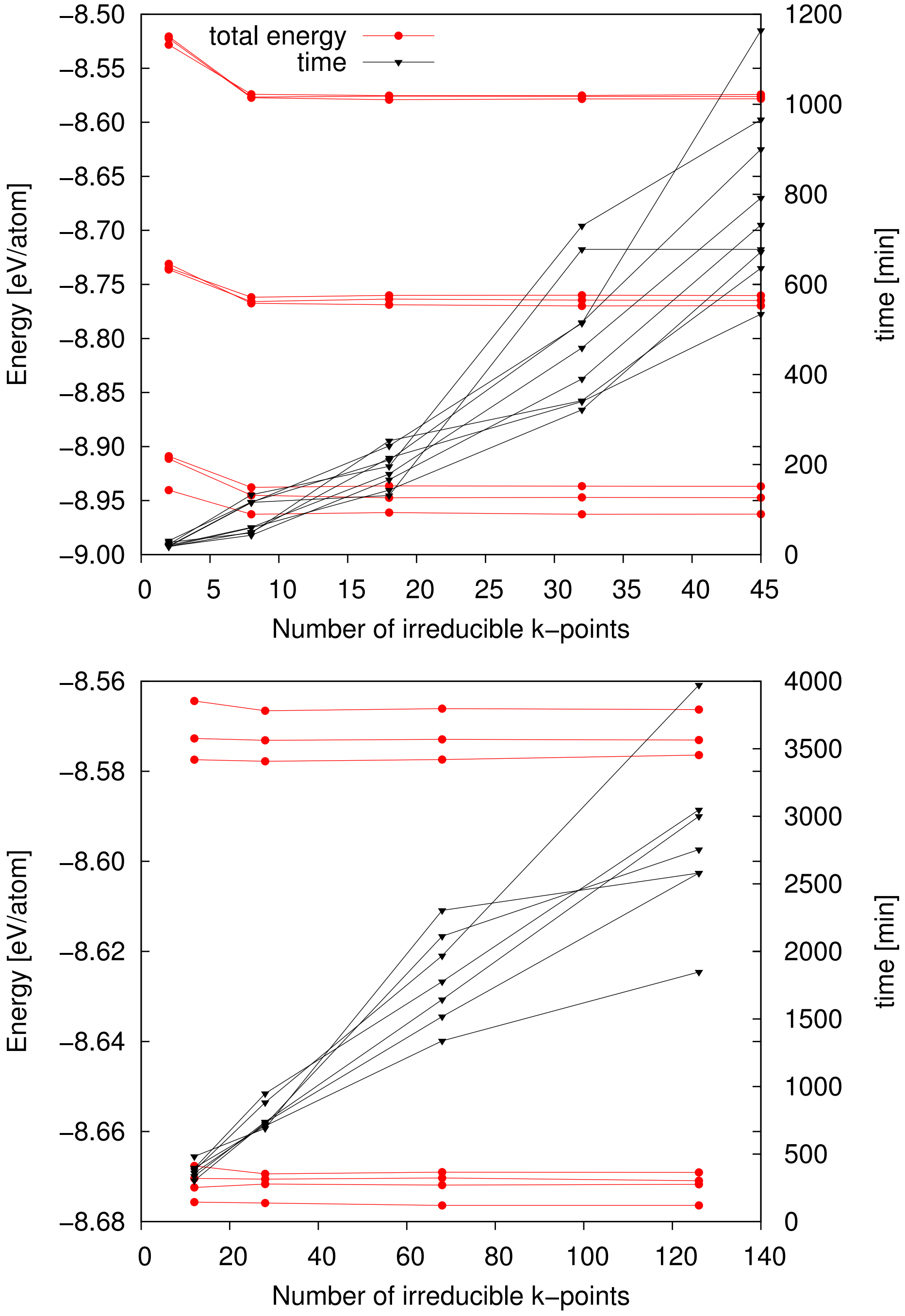

Figure 4.4: Total energy (red) as a function of the number of k-points for selected configurations of a C14 unit cell (top) and a C14 2 x 1 x 1 supercell (bottom) of Nb($Cr_{1-x}Co_x$)$_2$ with different compositions x. The required time in minutes for a complete calculation (three runs) is shown in black.

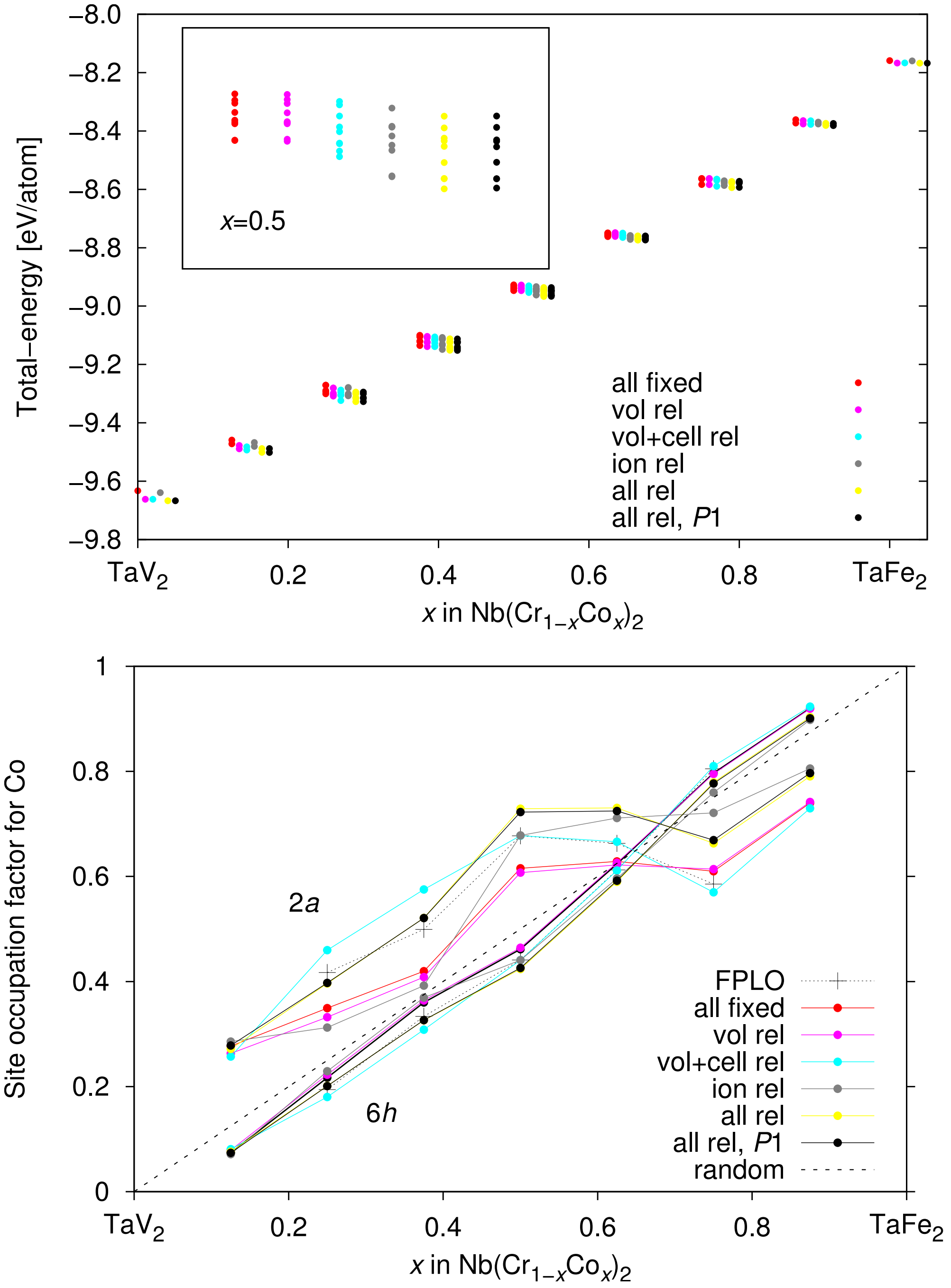

Figure 4.5: Different relaxation strategies lead to different results for the calculated total-energy (top) and the site occupation factors for Co (bottom) in C14 Nb(Cr$_{1-x}$Co$_x$)$_2$. Different strategies cause wider or narrower total-energy ranges as shown in the inset in (a). Narrow energy ranges cause smaller, wide energy ranges cause larger deviations of the *s.o.f.*s from randomness.

Part II

Results and discussion

5 The Laves phases $\mathrm{Nb(Cr}_{1-x}\mathrm{Co}_x)_2$

In this chapter the experimental and calculated results for the Laves phases in the Co–Cr–Nb system are discussed. The experimental work in this system was started in the doctoral thesis of Daniel Grüner [52], extended in the diploma thesis of the current author [136] and finalized in this work. Most of the experimental results are taken from references [136] and [52] and were published in reference [137].

5.1 Phase analysis

The results of the phase analysis as obtained from X-ray powder diffraction, metallographic examinations and quantitative chemical analysis are summarized in table **5.1**. The results of the chemical analysis for Nb, Cr and Co in at.% are shown with their standard deviations besides the nominal compositions. The substitution parameter x is given as nominal value and has been calculated from the chemical analysis based on a fixed Nb content of 33.33 at.%. The results of the analytical investigation by ICP-OES agree well with the nominal compositions. The results from X-ray powder diffraction are given in form of the lattice parameters and the identified phases.

Table 5.1: Results of the phase analysis of annealed Co–Cr–Nb alloys. Data from diploma thesis of the current author [136].

	x in $Nb(Cr_{1-x}Co_x)_2$			Composition Nb/Cr/Co in at.%		Lattice parameters
Sample	nominal	observed*	Phases	nominal	ICP-OES	a, (c) in pm
1	0		C15	33.3/66.7/0	33.4(5)/66.6(5)/0	699.46(4)
2	0.02	0.019	C15	33.33/65.33/1.34	33.9(2)/64.9(3)/1.3(1)	698.94(4)
3	0.03	0.029	C15	33.33/64.67/2.00	34.2(4)/63.9(4)/1.9(1)	698.69(4)
4	0.05	0.051	C15	33.33/64.67/3.34	34.4(7)/62.3(7)/3.3(1)	698.17(6)
5	0.08	0.080	C15 + C14	33.33/61.33/5.34	34.2(5)/60.5(5)/5.3(1)	
6	0.10	0.103	C15 + C14	33.33/60.00/6.67	33.2(4)/59.9(4)/6.9(1)	
7	0.15	0.159	C14	33.33/56.67/10.00	33.9(3)/55.6(4)/10.5(1)	491.38(3), 807.26(4)
8	0.20	0.203	C14	33.33/53.33/13.34	33.0(2)/53.4(2)/13.6(1)	490.64(2), 805.75(2)
9	0.25	0.253	C14	33.33/50.00/16.67	33.3(3)/49.9(3)/16.9(1)	489.93(2), 804.33(3)
10	0.33	0.332	C14	33.30/44.60/22.10	33.1(4)/44.6(5)/22.2(4)	488.67(8), 801,3(2)
11	0.40	0.403	C14	33.33/40.00/26.67	33.0(2)/40.0(2)/27.0(2)	487.94(2), 799.12(3)
12	0.42	0.429	C14	33.30/38.70/28.00	33.6(5)/37.9(6)/28.5(5)	487.65(2), 798.28(3)
13	0.50	0.500	C14	33.33/33.33/33.34	33.3(6)/33.3(6)/33.4(6)	486.90(6), 795.53(9)
14	0.57	0.574	C14	33.30/28.70/38.00	33.3(3)/28.5(3)/38.3(3)	485.83(2), 792.25(3)
15	0.60	0.603	C14	33.33/26.67/40.00	33.3(1)/26.5(1)/40.2(1)	485.68(2), 791.39(2)
16	0.67	0.681	C14	33.33/22.23/44.44	33.8(5)/21.1(3)/45.1(5)	484.86(5), 788.69(7)
17	0.75	0.740	C14	33.30/16.70/50.00	32.7(3)/17.5(3)/49.8(5)	483.66(3), 785.79(3)
18	0.80	0.801	C14	33.33/13.33/53.34	33.0(1)/13.3(1)/53.6(2)	483.18(4), 784.74(5)
19	0.90	0.876	C14	33.33/6.67/60.00	32.6(2)/8.3(1)/59.1(3)	481.54(3), 782.65(4)
20	0.92	0.9161	C14	33.33/13.33/53.34	33.0(1)/13.3(1)/53.6(2)	483.18(4), 784.74(5)
19	0.90	0.876	C14	33.33/6.67/60.00	32.6(2)/8.3(1)/59.1(3)	481.54(3), 782.65(4)
20	0.92	0.916	C14	33.30/5.60/61.10	32.9(3)/5.6(1)/61.5(3)	481.28(3), 782.44(4)
21	0.94	0.940	C14 + C15	33.33/4.00/62.67	33.0(1)/4.0(1)/63.0(1)	
22	0.98	0.950	C15	33.33/1.33/65.34	32.5(3)/3.4(1)/64.1(4)	678.19(3)
23	1.00		C15	33.33/0/66.67		678.35(4)

*Calculated from the results of the chemical analysis with the Nb content fixed at 33.33 at.%.

At 1100 °C $NbCr_2$ and $NbCo_2$ crystallize with the cubic C15 structure type and a new true ternary Laves phase C14 $Nb(Cr_{1-x}Co_x)_2$ is forming with a large homogeneity range. Three representative powder diffractograms of single phase C15 $Nb(Cr_{0.98}Co_{0.02})_2$ (no. 2), a two-phase sample $Nb_{33.3}Cr_{60.0}Co_{6.7}$ (no. 6), and single phase C14 $Nb(Cr_{0.50}Co_{0.50})_2$ (no. 13) are shown in figure **5.1** (a), (b), and (c), respectively. The reflections of the C15 phase in the two-phase sample (b) exhibit a different profile shape compared to single phase C15. A similar feature has been observed in the Co–V–Zr system [48]. Furthermore, in the inset in (b) two weak reflections at approximately 44.5° and 47.5° are marked with stars. They can be attributed to an impurity phase with Ti_2Ni structure type (space group $Fd\bar{3}m$, $a \approx 1140$ pm). These reflections are not observed in the powder diffractograms of all samples, but metallographic analyses reveal that tiny amounts ($\ll$1 vol.%) of this phase are present in most samples. Due to the small two-phase fields between the C15 and C14 phases, these two phases cannot be distinguished unambiguously using optical microscopy, neither in bright field, nor in polarized light, due to low contrast and interfering orientation contrast. However, two phases can clearly be distinguished in the optical microscope using differential interference contrast (DIC) after etching, an example of which is shown for sample no. 6 in figure **5.2**. A comparison with an EBSD phase map (shown as inset) obtained from a polished surface of the same sample shows that the rough surfaces of the etched sample correspond to the C14 phase. This observation agrees with the amounts of phases as expected from the lever rule and estimated from X-ray powder diffractograms. The discrimination of the two phases C15 and C14, quantitative analysis of the composition and the determination of the width of the two-phase fields were possible using a SEM equipped with a field-emission-gun (FEG). Figure **5.3** shows the SEM (BSE) images of the two-phase samples no. 6 (Cr-rich) and no. 21 (Co-rich) together with WDXS linescans for the respective minority component. The results from the WDXS measurements are shown in table **5.2**. As expected from the phase diagram the C14 phase is found to be Co-rich in sample no. 6 whereas it is Cr-rich in sample no. 21. No significant differences in the Nb content of the two phases could be detected. The width of the two-phase region is approximately 2 at.% and smaller than 1 at.% for the Cr-rich and the Co-rich side, respectively. The maximum solubility of Co in C15 $NbCr_2$ is approximately 6 at.% ($x = 0.095$), while C15 $NbCo_2$ can solve up to

Table 5.2: Composition (in at.%) of the C14 and C15 phases for sample no. 6 and 21, averaged from five WDXS measurements per phase.

Sample number	Phase	Nb	Cr	Co	$\sum$
6	C15	33.8(2)	59.8(3)	6.3(3)	99.9
	C14	33.6(4)	58.0(4)	8.4(1)	100
21	C15	34.1(3)	3.5(2)	62.3(2)	99.9
	C14	34.5(2)	4.1(2)	61.4(3)	100

approximately 3.5 at.% Cr ($x = 0.95$). The homogeneity range of the C14 phase $Nb(Cr_{1-x}Co_x)_2$ extends from $0.127(3) \leq x \leq 0.937(3)$ at 1100 °C. These values differ only slightly from the values reported by ZHU *et al.* [4] at 1000 °C. The mean atomic volume V_{atom} for $Nb(Cr_{1-x}Co_x)_2$ with $0 \leq x \leq 1$ is plotted versus the composition x in figure **5.4**. With increasing Co content, V_{atom} decreases. This is expected since Co atoms are slightly smaller than Cr atoms. The composition dependence of the volume reveals a linear behavior according to Vegard's volume rule. Equation 5.1, obtained by a least squares fit, gives 14.25 Å^3 and 12.96 Å^3 for hypothetical C14 phases $NbCr_2$ and $NbCo_2$, respectively. These values are close to the mean atomic volumes of the corresponding C15 phases, 14.26 Å^3 and 13.01 Å^3, respectively.

$$V_{atom}^{C14} = (-1.29(1)x + 14.248(5)) \cdot \text{Å}^3 \tag{5.1}$$

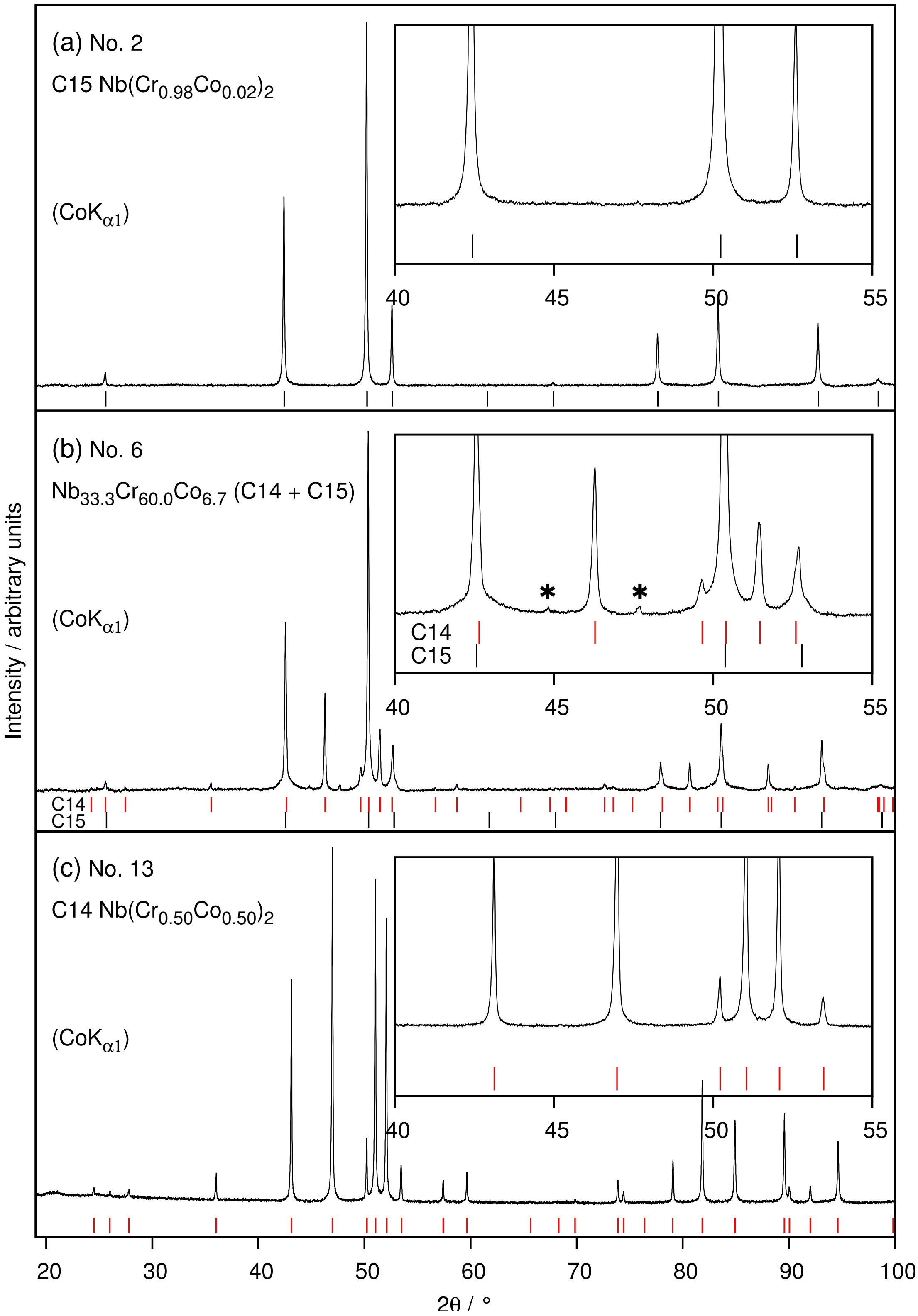

Figure 5.1: X-ray powder diffractograms of (a) C15 Nb($Cr_{0.98}Co_{0.02}$)$_2$ (no. 2), (b) two phase $Nb_{33.3}Cr_{60.0}Co_{6.7}$ (no. 6) and (c) C14 Nb($Cr_{0.50}Co_{0.50}$)$_2$ (no. 13). Tic marks indicate the reflection positions of the respective phases. Two reflections marked with stars in the inset in (b) were attributed to an impurity phase, see text.

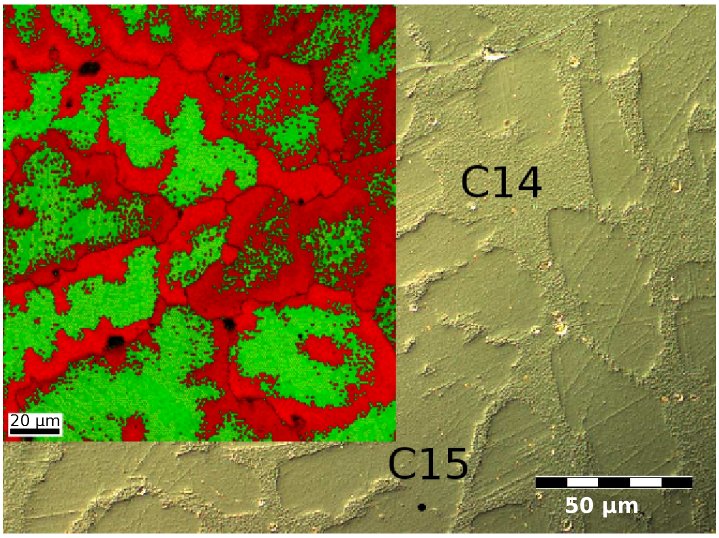

Figure 5.2: Optical micrograph (DIC) of sample no. 6 $Nb_{33.3}Cr_{60.0}Co_{6.7}$ (C15 + C14), after etching. Rough surfaces correspond to the C14 phase. The inset shows an EBSD phase map of another region of the same sample (red: C14, green: C15).

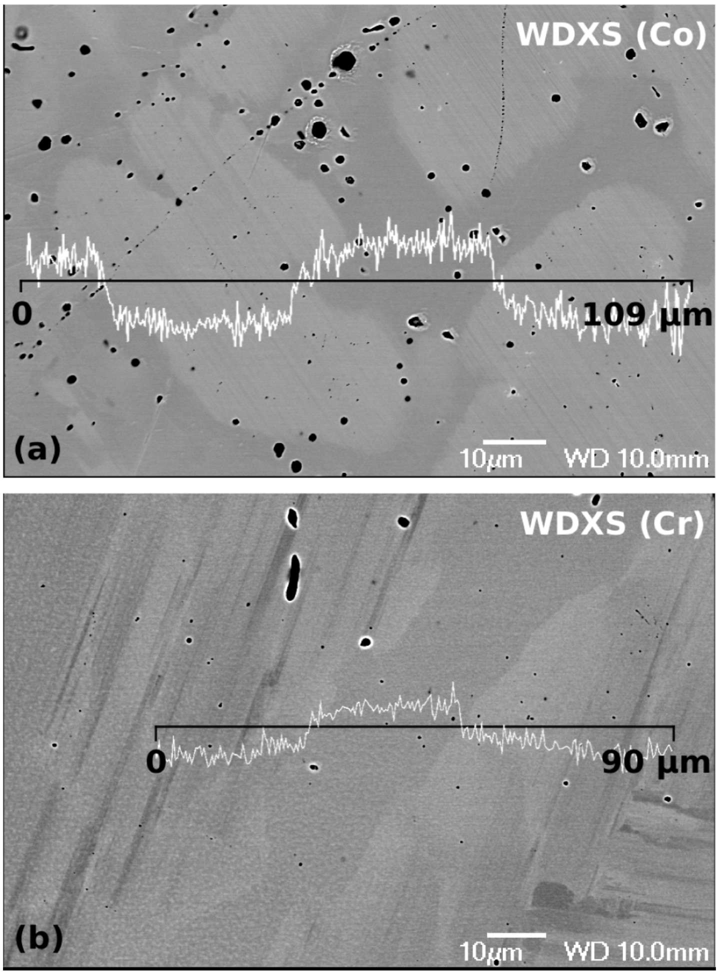

Figure 5.3: SEM (BSE) images of (a) sample no. 6 $Nb_{33.3}Cr_{60.0}Co_{6.7}$ and (b) sample no. 21 $Nb_{33.3}Cr_{4.0}Co_{62.7}$ (both C15 + C14) with the WDXS linescans of Co (a) and Cr (b).

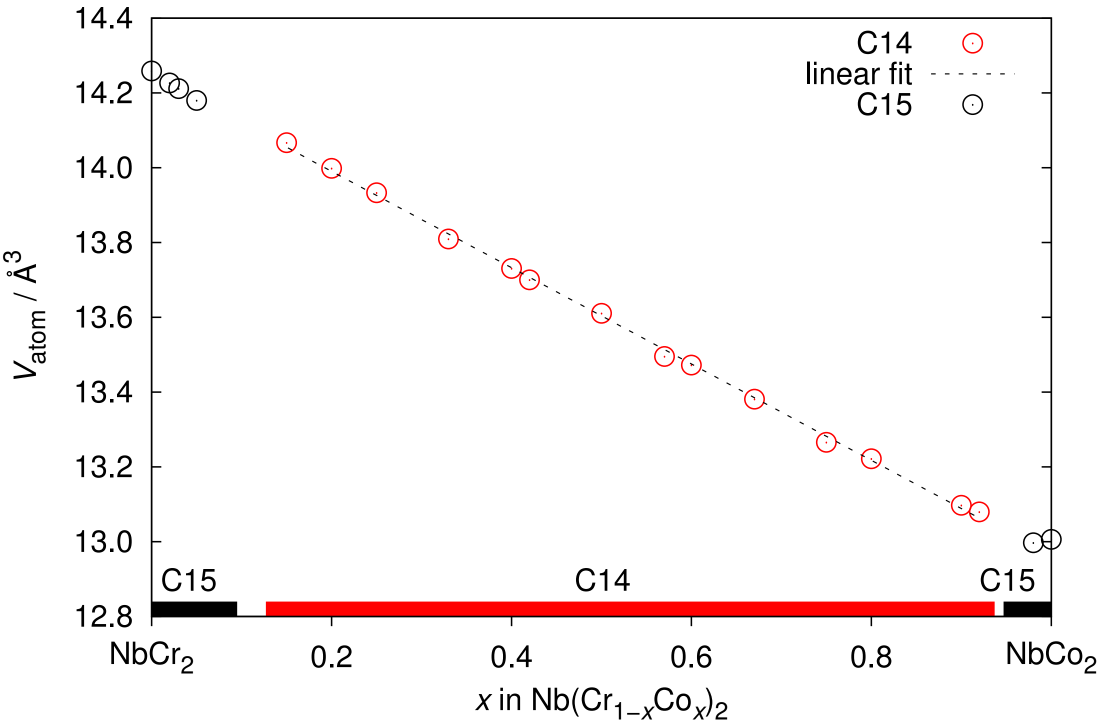

Figure 5.4: Experimental mean atomic volume of single phase C14 and C15 $Nb(Cr_{1-x}Co_x)_2$ as a function of x. The bars at the bottom indicate the experimental homogeneity ranges of the C15 and C14 phases. The borders of the single phase fields were determined by WDXS measurements on two phase samples.

5.2 Calculation of Gibbs free energy and stability ranges

From the experiment it was known that $NbCr_2$ and $NbCo_2$ crystallize with the cubic C15 structure type while a ternary C14 phase is forming with a large homogeneity range from $0.127(3) \leq x \leq 0.937(8)$ at 1100 °C. In order to check if first-principles calculations are able to model the homogeneity ranges of C15 and C14, the total energies for C15 and C14 $Nb(Cr_{1-x}Co_x)_2$ were calculated for $0 \leq x \leq 1$. From these values and the total energies of the elements Cr, Co and Nb the Gibbs energies were calculated. The calculations were carried out using VASP on a C15 unit cell and a C14 2 x 1 x 1 supercell of $Nb(Cr_{1-x}Co_x)_2$ with full structural relaxation in space group $P1$. The lattice parameters and site occupation factors were also calculated from these data. Additionally, the site occupation factors were computed for a $Nb(Cr_{1-x}Co_x)_2$ unit cell with VASP (full structural relaxation) and FPLO (fixed lattice parameters and atomic position). The total energies of the elements Co, Cr and Nb which are necessary to compute the Gibbs energies were calculated considering the magnetic properties of the elements, i.e., the ferromagnetism of Co and the antiferromagnetism of Cr. Nb is paramagnetic. The calculation of the C14 and C15 phases were carried out paramagnetic. The pseudobinary sections were calculated with VASP medium precision due to the high computational effort. For higher accuracy the pure binaries were calculated with high precision. Tables **5.3**, **5.4** and **5.5** give an overview on the calculations carried out in the Co–Cr–Nb system.

The optimized lattice parameters of the elements are close to the experimental values. For Co and Cr the computed values are slightly smaller than the literature data. The c/a ratio for Co is smaller than the ideal value which is correctly reproduced by the calculation. For Nb the calculated lattice parameter is slightly larger than the experimental value. These calculations were carried out with medium precision to provide consistency with the calculations of the pseudobinary sections. The lattice parameters of the binaries C15 $NbCo_2$ and $NbCr_2$ agree well with the experimental values.

Figure **5.5** shows the calculated total energy values of all configurations of C14 and C15 $Nb(Cr_{1-x}Co_x)_2$. With increasing Co content the total energy increases. The dispersion of the total energy values for the different configurations at a given composition x is small. The maximum difference of 80.8 meV/atom is observed

Table 5.3: Calculations carried out in the Co–Cr–Nb system — Elements.

Phase	Co	Cr	Nb
Composition	Co	Cr	Nb
Atoms per unit cell	2	2	2
Space group	$P6_3/mmc$	$Im\bar{3}m$	$Im\bar{3}m$
Lattice parameters			
optimized			
a [Å]	2.479	2.835	3.318
c [Å]	4.003	–	–
c/a	1.615	–	–
experimental[1]			
a [Å]	2.5071	2.8848	3.3004
c [Å]	4.0686	–	–
c/a	1.6228	–	–
Total energy [eV/atom]	-7.0092	-9.4672	-10.0448
Details	VASP, medium precision		
	ferromagnetic	antiferromagnetic	paramagnetic

[1] [138]

for C14 at $x = 0.4375$. This indicates that for all compositions no configuration is extraordinary stable compared to the other and no super structure formation is expected. The difference between the total energies of the different phases C14 and C15 is also very small.

Since at 0 K only the configuration with the lowest energy is stable, figure **5.6** shows the total energy only of the most stable configurations of C15 and C14 at each x. The values are fitted with Redlich-Kister polynomials of 4^{th} order. The numerical data for this graph and the coefficient of the Redlich-Kister polynomials are given in the appendix A.2 in table **1.6** and **1.7**.

The overall shape of the curve is the same as in the previous figure. Already noticeable, $NbCr_2$ and $NbCo_2$ have lower total energies in the C15 structure type as in the C14 structure type. Thus, one can estimate $NbCr_2$ and $NbCo_2$ to crystallize with the C15 structure type. For all ternary compositions C14 has a lower energy than C15. Thus one would expect C14 to be the stable structure type for all calculated ternary compounds. The described behavior becomes much more clear when the entropy is incorporated and the Gibbs energy is calculated. This is shown in figure **5.7**.

Table 5.4: Calculations carried out in the Co–Cr–Nb system — Binaries.

Phase	C14 $NbCo_2$	C14 $NbCr_2$	C15 $NbCo_2$	C15 $NbCr_2$
Composition of the unit cell	Nb_4Co_8	Nb_4Cr_8	Nb_8Co_{16}	Nb_8Cr_{16}
Space group	$P6_3/mmc$	$P6_3/mmc$	$Fd\bar{3}m$	$Fd\bar{3}m$
Lattice parameters				
optimized (VASP)				
a [Å]	4.771	4.886	6.739	6.931
c [Å]	7.769	8.070	–	–
c/a	1.629	1.652	–	–
experimental				
a [Å]	–	–	6.784	6.995
Total energy [eV/atom]	-8.1830	-9.6829	-8.1855	-9.6985
Details	VASP, high precision, paramagnetic			
Optimized lattice parameters (FPLO)				
a [Å]	4.78	4.91	6.75	6.96
c [Å]	7.77	8.09	–	–
c/a	1.63	1.65	–	–

The calculated values are again fitted with Redlich-Kister polynomials of 4^{th} order. The numerical data for this graph and the coefficients of the Redlich-Kister polynomials are given in the appendix A.2 in table **1.8** and **1.10**.

From this figure one can now estimate the homogeneity ranges of the C15 and C14 phases. The phase boundaries associated with the first-order transition between C15 and C14 structure type were located using the tangent construction. Due to the limited number of data points, the tangent construction fails on the Co-rich side. In agreement with the experiment the calculations predict that $NbCr_2$ and $NbCo_2$ crystallize with the cubic C15 structure type. A small solubility of 2 at.% Co in C15 $NbCr_2$ is expected followed by a two-phase field C15/C14 up to 12 at.% Co. The location of the two-phase field C14/C15 on the Co-rich side cannot be determined by the tangent construction. However, a small solubility for Cr in C15 $NbCo_2$ followed by a two-phase field C15/C14 is expected from the calculated data. A true ternary C14 phase $Nb(Cr_{1-x}Co_x)_2$ should form with a broad homogeneity range of $0.14 \leq x \lessapprox 0.96$. The predicted homogeneity ranges are in good agreement with the experimental data as shown by the top

Table 5.5: Parameters of the calculations carried out in the Co–Cr–Nb system — Pseudobinary sections. The calculations for the unit cell of C14 $Nb(Cr_{1-x}Co_x)_2$ where carried out with VASP and FPLO.

Phase	C14 $Nb(Cr_{1-x}Co_x)_2$	C14 $Nb(Cr_{1-x}Co_x)_2$	C15 $Nb(Cr_{1-x}Co_x)_2$
Composition of the unit cell	$Nb_4(Cr,Co)_8$	$Nb_8(Cr,Co)_{16}$	$Nb_8(Cr,Co)_{16}$
Space group	$P6_3/mmc$	$P6_3/mmc$	$Fd\bar{3}m$
Details	VASP, medium precision, paramagnetic		
	FPLO, paramagnetic		
	unit cell	2 x 1 x 1 supercell	unit cell
	39 configurations	4282 configurations	201 configurations

and bottom bars in figure **5.7**.

The differences in the total energy and the Gibbs energy of the two different structure types C15 and C14 of the binary compounds are however small. C15 $NbCr_2$ is stable by 15.6 meV/atom, C15 $NbCo_2$ is stable by only 1.6 meV/atom. For the ternary compounds the energy differences are much larger. Therefore, the calculations for the binaries have been repeated with much higher accuracy with VASP and in addition with the full-potential code FPLO. The results in form of the Gibbs energy are shown in table **5.6**. With VASP both compounds are stable as C15 type, $NbCr_2$ by 16 meV/atom and $NbCo_2$ by 3 meV/atom. For $NbCr_2$ FPLO supports this results, C15 is stable by 12.7 meV/atom. However, according to the FPLO calculations, C15 $NbCo_2$ is unstable compared to C14 by 1.5 meV/atom. The reasons for this discrepancy between VASP and FPLO have not yet been investigated. Since FPLO is regarded as the more precise method one might argue that for $NbCo_2$ a structural transformation from C15 to C14 is expected at lower temperatures. However, this would be in contradiction with the experiment and with the general observation of C14 being the high-temperature and C15 the low-temperature modification (cf. section 2.3). Another reason might be the insufficient relaxation of the lattice parameters and the atomic coordinates when using FPLO. However, here the lattice parameters in FPLO were optimized by hand by calculating the total energy for different lattice parameters searching for the lowest energy (see table **5.4**). A further optimization of the atomic coordinates of C14 $NbCo_2$ would probably even increase its stability compared to C15.

In conclusion one can state, that the computations are capable of predicting the

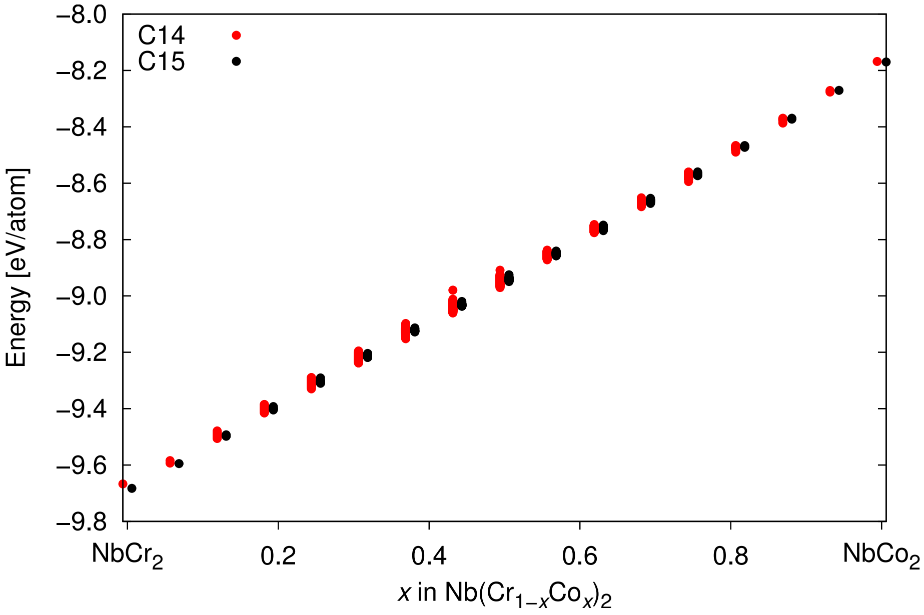

Figure 5.5: Total energy values of all configurations for C14 (4282) and C15 (201) $\mathrm{Nb(Cr_{1-x}Co_x)_2}$. For better clarity, the values for C15 and C14 are slightly shifted to the left and right from their nominal composition, respectively.

homogeneity ranges of the C15 and C14 phases in the pseudobinary section $\mathrm{NbCr_2}$–$\mathrm{NbCo_2}$. The calculated homogeneity range for the C14 phase $\mathrm{Nb(Cr_{1-x}Co_x)_2}$ $0.14 \leq x \lessapprox 0.96$ is in very good agreement with the experimental values of $0.127(3) \leq x \leq 0.937(8)$. Contradictory results are however obtained for the binary compounds.

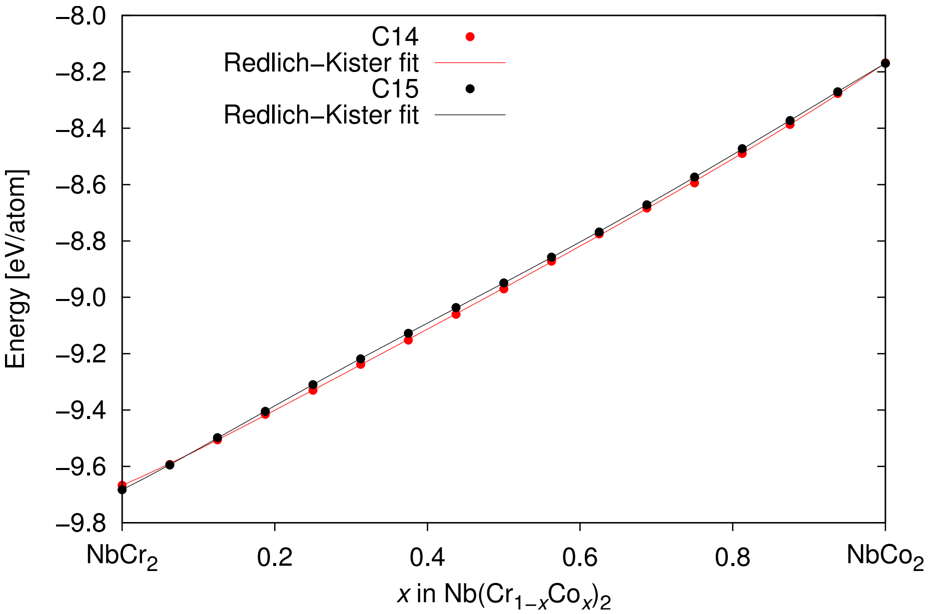

Figure 5.6: Total energy values of the stable configurations of C15 and C14 Nb(Cr$_{1-x}$Co$_x$)$_2$. The values are fitted with Redlich-Kister polynomials of 4^{th} order. The numerical data and the coefficients of the Redlich-Kister polynomials are given in the appendix A.2.

Table 5.6: Gibbs energy for C15 and C14 NbCr$_2$ and NbCo$_2$ calculated at 1150 °C. Comparison between values obtained with VASP and FPLO with high accuracy. The stable compounds are printed in bold face.

Phase	VASP [meV/atom]	FPLO [meV/atom]
C15 NbCr$_2$	**-37.84**	**-20.37**
C14 NbCr$_2$	-21.84	-7.63
C15 NbCo$_2$	**-156.98**	-127.11
C14 NbCo$_2$	-154.03	**-128.57**

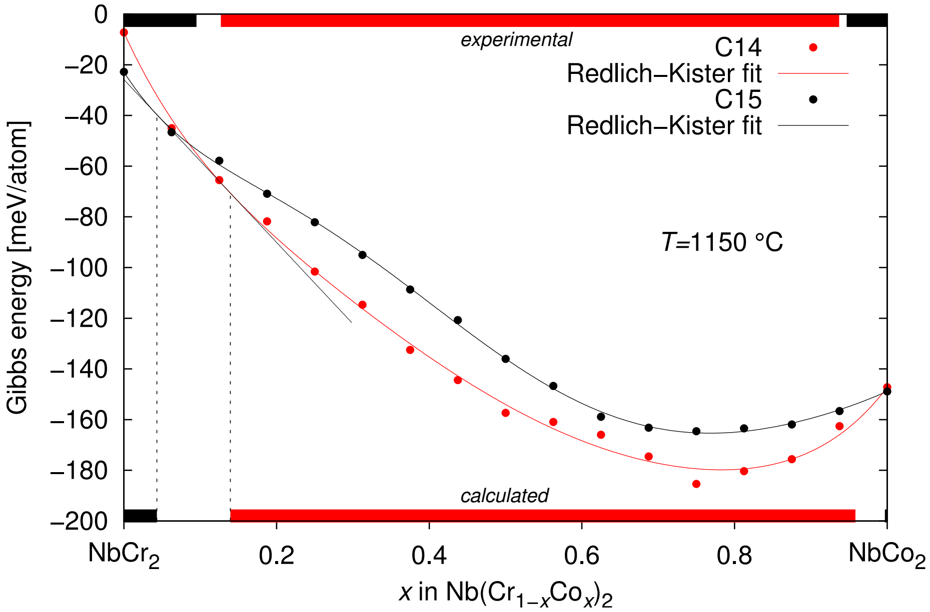

Figure 5.7: Gibbs energy G of the stable configurations of C15 and C14 $\mathrm{Nb(Cr_{1-x}Co_x)_2}$ calculated from equation 4.7 at a temperature of $T = 1150\,°\mathrm{C}$. The values are fitted with Redlich-Kister polynomials of 4^{th} order. The top and bottom bars indicate the experimentally obtained and the calculated width of the single phase fields of C15 and C14. The dashed lines mark the contact points of the common tangent with the G curves. The numerical data and the coefficients of the Redlich-Kister polynomials are given in the appendix A.2.

5.3 Crystal structure of C14 Nb(Cr$_{1-x}$Co$_x$)$_2$

In this section the crystal structure of the C14 phase will be investigated as a function of the composition x. The experimental results will be compared with the lattice parameters and site occupation factors obtained from the calculations.

The experimental homogeneity range of C14 Nb(Cr$_{1-x}$Co$_x$)$_2$ extends from $0.127(3) \leq x \leq 0.937(8)$ at 1100 °C. Figure **5.8** shows the experimentally determined unit cell parameters a and c as well as the c/a ratio and the mean atomic volume of the C14 phase. Only data obtained from single phase samples are included in these figures since overlapping Bragg reflections of the C15 and C14 structures in X-ray powder diffraction prevent a precise determination of lattice parameters inside the two-phase region. The error bars of the experimental values are smaller than the diameter of the circles in these plots. Both, the a and c lattice parameters, decrease approximately linearly with increasing Co content, however, the c parameter with a steeper slope ($\Delta a = 0.13$ Å, $\Delta c = 0.34$ Å for $\Delta x = 1$). With increasing Co content, c/a decreases not linearly, but shows an S-like shape. At low Co contents the axial ratio starts to decrease from $c/a = 1.643$. With increasing Co content c/a decreases stronger until the inflection point of the curve at $x = 0.5$. The geometrically ideal c/a ratio is reached at $x = 0.51$. The decreasing of c/a gets weaker again until the minimum of the curve at $x = 0.82$ and $c/a = 1.624$. After the minimum c/a increases again up to $c/a = 1.626$. This behavior of the c/a is very interesting, but not unusual as discussed in section 2.5.

In order to model this behavior, the lattice parameters were computed from the 2 x 1 x 1 supercell calculations on C14 Nb(Cr$_{1-x}$Co$_x$)$_2$ as explained in section 4.6. The results are shown in figure **5.9**. The calculated and the experimental lattice parameters, the axial ratio and the mean atomic volume versus the composition x are plotted side by side. The calculated unit cell parameters are slightly smaller than the experimental values, a about 0.05 Å (1%), c about 0.04 Å (0.5%). Both of the calculated curves for a and c show a slight S-shape with contrary orientation. This feature is especially pronounced on the Co-rich side. The c lattice parameter decreases almost linearly until $x = 0.5$ and then decreases more rapidly giving the curve a downwards shape. Contrarily, the a lattice parameter decreases less rapidly from $x = 0.6$ on producing an upward shape. The same deviations from linearity can be observed in the experimental data, however, much less pronounced as in

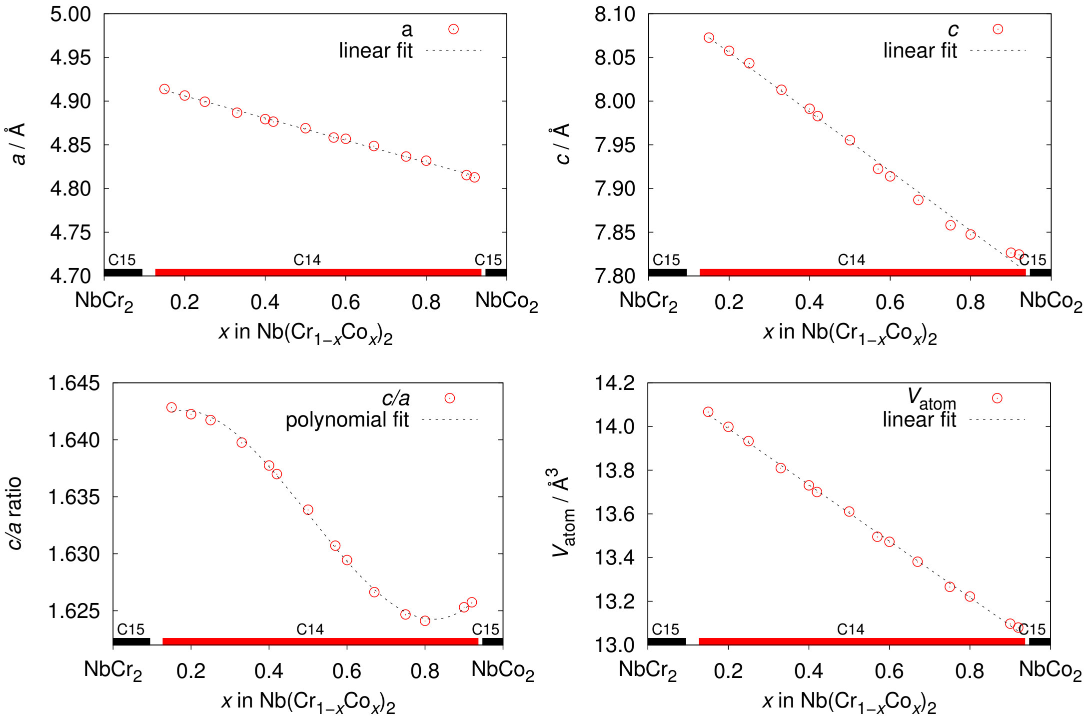

Figure 5.8: Experimental lattice parameters a and c, axial ratio c/a and mean atomic volume for C14 Nb(Cr$_{1-x}$Co$_x$)$_2$. To emphasize the different slopes of the curves for a and c, the graphs are scaled to the same range. The corresponding data are listed in table **5.1**.

the calculated data. The calculated and the experimental mean atomic volume show a linear composition-dependence and follow Vegard's volume rule. The deviations in a and c compensate each other resulting in a linear behavior. The calculated data is about $0.4\,\text{Å}^3$ (3%) smaller than the experimental values. The small deviations of calculated and experimental values of the lattice parameters and the mean atomic volume are well within the expectations for DFT results.

As for the experimental data, the curve shape of the calculated c/a ratio can be described by an S-type behavior with the minimum at $x = 0.8$ and the inflection point at $x = 0.6$. The absolute values of the calculated axial ratio differ markedly from the experimental values. These deviations are a consequence of the deviations and the exaggerated curve shapes of the a and c lattice parameters. However, the general shape of the curve, the location of the inflection point and the minimum and maximum are well captured by the calculations.

Depending on the chosen potentials, the over- or underestimation of the lattice

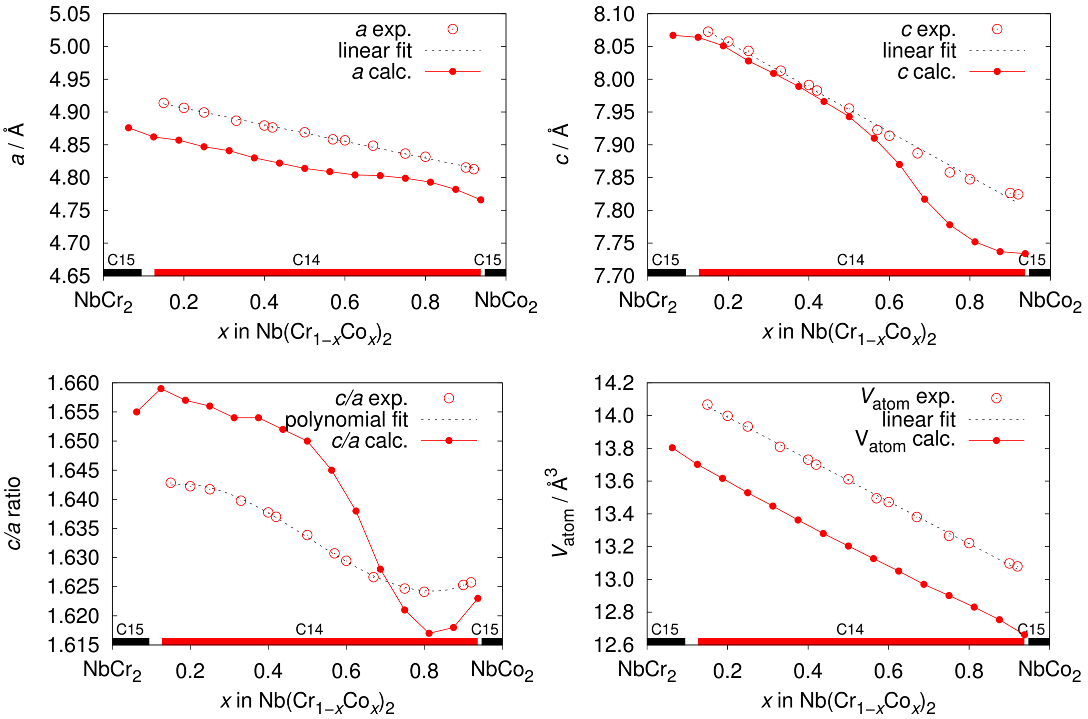

Figure 5.9: Experimental and calculated lattice parameters a and c, c/a ratio and mean atomic volume for C14 $\mathrm{Nb(Cr_{1-x}Co_x)_2}$.

parameters and the unit cell volume is an inherent property of DFT calculations. To compensate for this effect, the curves of the calculated a and c lattice parameters can be fitted to the experimental lattice parameters by simply adding a constant value. Both data sets can nearly be brought into coincidence and agree well after this correction as shown in figure **5.10** (a) and (b). The mean atomic volume calculated from the corrected lattice parameters shows a very good agreement with the experimental values. The axial ratio c/a is mainly unaffected from this corrections, only a slight shift to lower values is observed. The strongly exaggerated S-type behavior however, still remains. The c/a ratio curve can be better fitted to the experimental data by scaling the temperature T in the Boltzmann distribution using the minimum of the experimental c/a ratio as point of reference. For this the temperature factor in equation 4.22 is gradually changed (in the script `occu16`) and the values for c/a are calculated until a satisfactory agreement with the given reference point is achieved. The result of this correction is shown in figure **5.10** (c). The curve shape of the calculated and the experimental data agree well and the absolute deviations of the values is small.

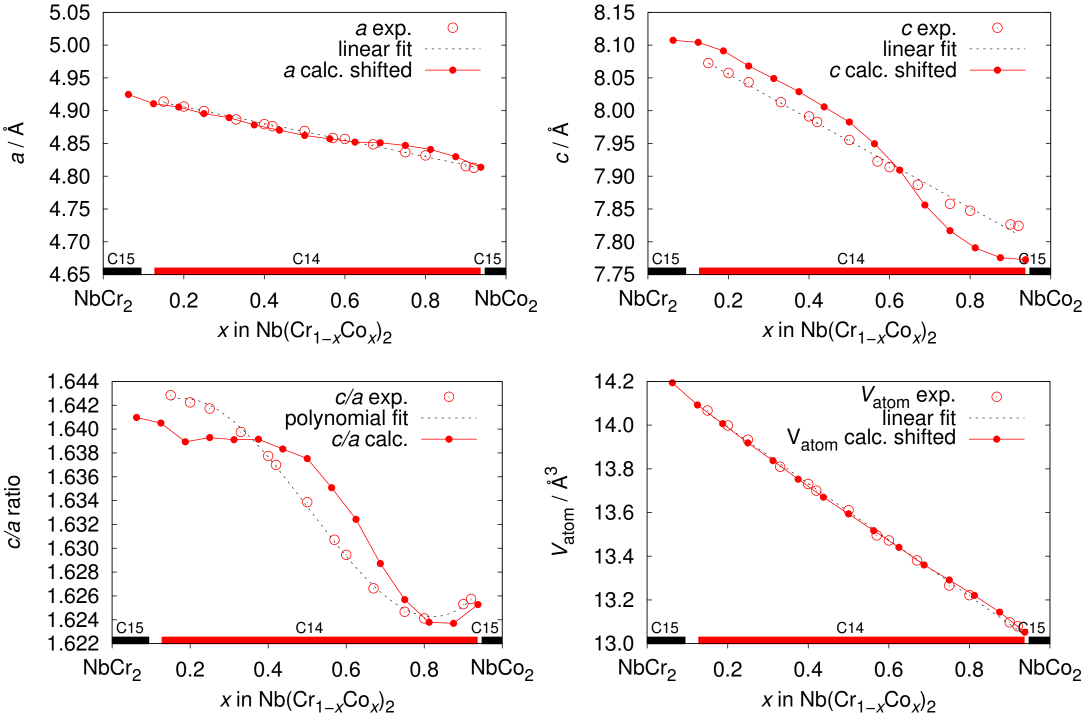

Figure 5.10: Calculated lattice parameters a and c, c/a ratio and mean atomic volume for C14 Nb($Cr_{1-x}Co_x$)$_2$ fitted onto the experimental data by adding a constant shift to a and c or by scaling the temperature factor T in equation 4.22.

The necessity of these different corrections to fit the calculated onto the experimental data my appear very complicated. However, if the calculations are considered reliable with respect to the overall shape of the curves, then they help to drastically minimize the number of required experiments. Since the computations predict the general curve shape, the calculated data can be corrected by only a very small number of experiments. Furthermore, the system can be probed for unexpected behavior prior to the experiment.

5.3.1 Single crystal structure analysis

The atomic scattering factors for X-ray diffraction for Cr and Co are very similar due to their proximity in the periodic table of elements which causes a low phase contrast in X-ray diffraction studies. A discrimination of Cr and Co by Rietveld analysis of X-ray powder diffraction data is thus hardly possible. To analyze the crystal structure of C14 Nb($Cr_{1-x}Co_x$)$_2$ and to obtain reliable data on the site occupation factors of Cr and Co, single crystal structure analysis were performed on selected samples with different composition. Single crystals of the C14 phase of irregular shape and metallic luster were obtained from crushed specimens of samples no. 10 (22.1 at.% Co), no. 13 (33.3 at.% Co), no. 16 (44.4 at.% Co) and no. 18 (53.3 at.% Co)[1]. As starting parameters for the structure refinement of the C14 phases the fractional coordinates (see tab. **2.2**) of an idealized crystal structure according to the hard sphere model in a standardized description [139] have been used. The Laue symmetry $6/mmm$ and extinction symbol $(P--c)$ of the investigated single crystals are in agreement with the reported space group symmetry $P6_3/mmc$ of the C14 phase. In the initial cycles of the refinement the A sites were occupied with Nb atoms and the B sites were occupied with Cr atoms. Subsequently randomly mixed occupation of the B sites was introduced. The total occupation for each site was constrained to full occupation and the anisotropic displacement parameters of Co and Cr atoms on these sites were constrained to be equal. The site occupation factors of the Nb sites were checked in the final cycles of the refinement. No indication of a mixed occupation or constitutional vacancies was detected. Table **5.7** contains the crystallographic data and details on data collection and refinement. Tables **5.8**, **5.9** and **5.10** contain the refined atomic parameters, the anisotropic displacement parameters and the interatomic distances, respectively.

The single crystal structure refinements for the various compositions reveal substantial deviations from the idealized crystal structure: (i) the networks of the smaller atoms, Cr or Co, and of the Nb atoms are distorted; (ii) there is Cr/Co substitutional disorder at $2a$ and $6h$ Wyckoff positions, however with preferential occupation of the respective minority component at the $2a$ site. The distortion of the crystal structure is noticeable by the deviation of the observed axial ratios from the ideal value of 1.633, and the shift of $x(M1)$ and $z(\mathrm{Nb1})$ from the ideal parameters 1/6 and 9/16, respectively. In the crystal structure of C14 type one half of the triangles in the Kagomé layers (Cr or Co at $6h$) are capped by Cr or Co at $2a$, while the other half are uncapped. The observed distortion can be

---

[1] Single crystals of sample no. 10, 13 and 16 were analyzed by D. GRÜNER [52] and published in reference [137]. In the following only the data for sample no. 18 is shown. The data for all four single crystal structure refinements is compiled in the appendix in tables **1.2**, **1.3**, **1.4** and **1.5**

Table 5.7: Crystallographic data and details on data collection and refinement of C14 Nb($Cr_{1-x}Co_x$)$_2$ at nominal $x = 0.80$.

Crystallographic data	
Refined composition	Nb($Cr_{0.22}Co_{0.78(2)}$)$_2$ / 52(1) at.% Co
Z	4
Formula weight / g·mol^{-1}	207.66
$F(000)$	374.6
Crystal system	hexagonal
Space group	$P6_3/mmc$
a^* / pm	483.19(2)
c^* / pm	784.79(2)
Volume* / nm^3	0.15868(1)
Density / g·cm^{-3}	8.693
Crystal size / μm^3	20 × 20 × 20
Data collection	
Diffractometer	Rigaku R-Axis Spider, Imaging Plate, Rotating anode
Radiation, wavelength	AgKα, $\lambda = 56.088$ pm
Monochromator	Osmic X-ray optics
Temperature / K	293(2)
Scan	ω
Bragg angle range 2θ	7.67–115.96°
Index ranges	$-14 \leq h \leq 8$, $-12 \leq k \leq 13$, $-23 \leq l \leq 21$
Absorption correction	multi-scan
μ / mm^{-1}	32.84
$T_{\mathrm{min.}}/T_{\mathrm{max.}}$	0.604
Measured reflections	7178
Unique reflections	912
R_{int}	0.033
Obs. reflections, $I > 2\sigma(I)$	725
Structure refinement	
Method	full-matrix least-squares on F^2
No. of parameters	13
$R(F)$ / $R(F^2)$ ($I > 2\sigma(I)$)	0.035 / 0.055
$R(F)$ / $R(F^2)$ (all data)	0.044 / 0.057
Goodness-of-fit on F^2	1.504
Extinction coefficient x	0.033(3)
$\Delta\rho_{\mathrm{min/max}}$ / 10^{-6} e·pm^{-3}	−3.74 / 3.72

* from calibrated powder data

Table 5.8: Atomic parameters and equivalent displacement parameters (in pm^2) for C14 $\mathrm{Nb(Cr_{1-x}Co_x)_2}$ at nominal $x = 0.80$.

Atom	Site	x	y	z	U_{eq}	Occ.
$M1$	$6h$	0.16956(3)	$2x$	1/4	57.7(4)	0.20(1) Cr + 0.80 Co
Nb1	$4f$	1/3	2/3	0.56412(3)	68.9(4)	1
$M2$	$2a$	0	0	0	61.1(7)	0.29(2) Cr + 0.71 Co

Table 5.9: Anisotropic displacement parameters (in pm^2) for C14 $\mathrm{Nb(Cr_{1-x}Co_x)_2}$ at nominal $x = 0.80$.

Atom	U_{11}	U_{22}	U_{33}	U_{23}	U_{13}	U_{12}
$M1$	57.2(6)	40.6(7)	69.7(8)	0	0	$U_{22}/2$
Nb1	68.0(5)	U_{11}	70.9(6)	0	0	$U_{22}/2$
$M2$	66.6(9)	U_{11}	50(1)	0	0	$U_{22}/2$

described as an elongation of the edges of the capped triangles (basal triangles of trigonal bipyramids) and a contraction of the edges of the uncapped triangles.

The distortion of the B partial structure of the four crystals is nearly independent of the composition within the range $0.33 \leq x \leq 0.80$. Furthermore, the anisotropic displacement parameters and the difference Fourier density plots do not indicate any local displacement near the mixed occupied sites. On the other hand, the z parameter of the Nb position changes with composition, as does the c/a ratio (see fig. **5.8** (a)). As the main focus of this study is on substitutional disorder, the distortions will not be discussed here. Details can be found in reference [52].

5.3.2 Site occupation factors and site occupation reversal

Whereas no clear trend for the distortion of the B network is observable, the single crystal data clearly reveal a composition dependence of the site preference, including evidence for a composition dependent site occupation reversal. Figure **5.11** shows a plot of the site occupation factors for Co on the $2a$ and $6h$ sites as obtained from single crystal structure refinements. In the case of the Cr-rich crystal ($x = 0.33$), Co atoms prefer the $M2$ ($2a$) site, whereas in the Co-rich crystals ($x = 0.67$ and 0.80), Cr prefers the $M2$ ($2a$) site. The crystal with $x = 0.50$ exhibits almost no preference of Cr/Co for either of the sites. In other words, the minority component prefers the $2a$ site, i.e., the apex of the trigonal

Table 5.10: Interatomic distances ($d < 320\,\mathrm{pm}$) in pm for C14 Nb(Cr$_{1-x}$Co$_x$)$_2$ at nominal $x = 0.80$.

			$x = 0.80$
Nb1 –	3	$M1$	282.06(2)
	6	$M1$	282.23(1)
	3	$M2$	283.47(1)
	1	Nb1	291.75(4)
	3	Nb1	296.57(2)
$M1$ –	2	$M1$	237.40(5)
	2	$M1$	245.79(5)
	2	$M2$	242.12(2)
	2	Nb1	282.06(2)
	4	Nb1	282.23(1)
$M2$ –	6	$M1$	242.14(2)
	6	Nb1	283.47(1)

bipyramids in the crystal structure of C14 Nb(Cr$_{1-x}$Co$_x$)$_2$. The site occupation reversal takes place at a composition of $x \approx 0.55$.

The difference between the $2a$ and $6h$ site occupations for one element, say Co, serves as a simple measure (order parameter) for the extent and the type of site preference (equ. 5.2):

$$\Delta\mathrm{occ} = \mathrm{occ}(\mathrm{Co}, 2a) - \mathrm{occ}(\mathrm{Co}, 6h) \tag{5.2}$$

Obviously, $\Delta\mathrm{occ} = 0$ for a random arrangement of Co and Cr atoms without site preference. The minimum and maximum values, $\Delta\mathrm{occ} = \pm 1$, correspond to two hypothetical, ordered compounds, Nb_2Cr_3Co and Nb_2CrCo_3. Thus, $\Delta\mathrm{occ}$ may be considered as a parameter describing short range order (which may lead to long range order in special cases). Values of $\Delta\mathrm{occ}$, calculated using equation 5.2 for C14 Nb(Cr$_{1-x}$Co$_x$)$_2$ with nominal $x = 0.33$, 0.50, 0.67 and 0.80 are compiled in table **5.11**.

Because Cr and Co atoms have a low phase contrast in X-ray diffraction studies, the quality of the refinement was checked – especially correlations between ADPs and site occupation – by collecting diffraction data for one sample up to $\sin(\theta)/\lambda = 1.51\,\text{Å}^{-1}$. The estimated standard deviations for all structural parameters are an order of magnitude smaller than those obtained for the remaining data sets with

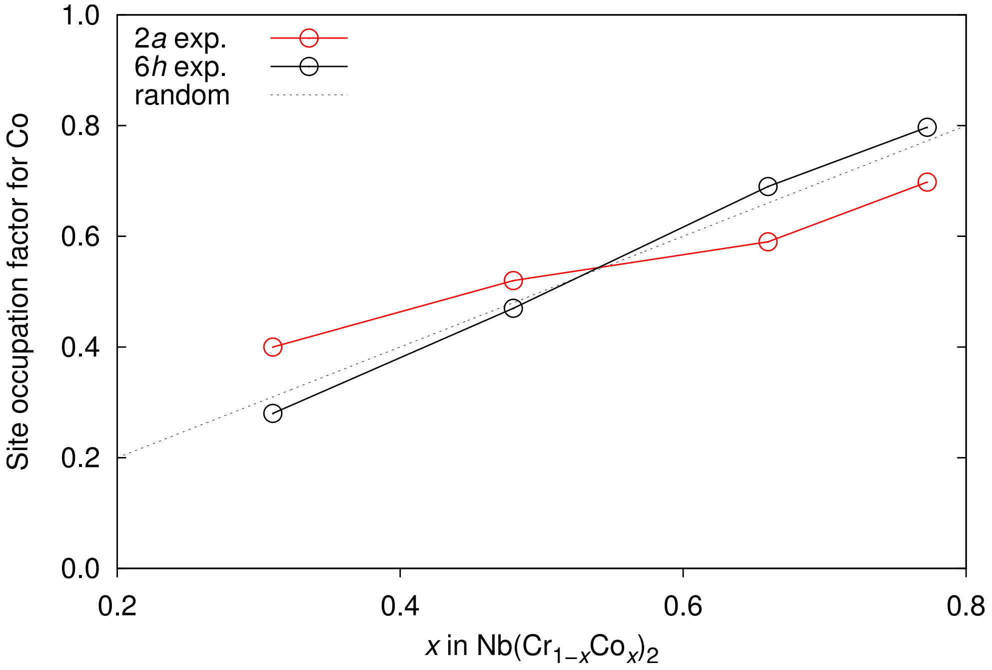

Figure 5.11: Experimental site occupation factors for Co on 2a and 6h sites in C14 Nb(Cr$_{1-x}$Co$_x$)$_2$ obtained from singly crystal structure refinements. The dashed line indicates a completely random distribution of Co and Cr atoms among the 2a and 6h sites.

$\sin(\theta)/\lambda = 0.81\,\text{Å}^{-1}$. By artificially lowering the resolution to $\sin(\theta)/\lambda = 0.81\,\text{Å}^{-1}$ similar values for the site occupation factors are obtained, however, with larger e.s.ds. To understand the origin of the observed site preference and site occupation reversal, size effects are considered first. To characterize the two different sites in the B network, the volumes of the corresponding Voronoi polyhedra were calculated. It turns out that the volumes of polyhedra around the 2a and 6h sites are almost equal. The Voronoi polyhedron at the 2a site is slightly larger than that at the 6h site (by approx. 1%) in all investigated crystal structures. The

Table 5.11: Differences of the site occupation of the 2a and 6h sites in the crystal structures of C14 Nb(Cr$_{1-x}$Co$_x$)$_2$ at nominal $x = 0.31$ 0.50, 0.67 and 0.80.

C14 Nb(Cr$_{1-x}$Co$_x$)$_2$	Δocc
$x = 0.33$	0.12
$x = 0.50$	0.05
$x = 0.67$	−0.10
$x = 0.80$	−0.09

significant change of the c/a ratio which passes through the ideal value roughly in the middle of the homogeneity range of C14 Nb(Cr$_{1-x}$Co$_x$)$_2$ does not alter the order of Voronoi polyhedron volumes. Therefore, the size effect as a cause for site preference is unlikely.

In order to model the site occupation behavior and the site occupation reversal in C14 Nb(Cr$_{1-x}$Co$_x$)$_2$, the site occupation factors for Cr and Co on the $2a$ and $6h$ site were computed with the help of equations 4.17, 4.19 and 4.20 (page 78) from the total energy and the atomic arrangement of the most stable configurations. In the following the results from four different calculational methods will be compared to the experimental values. The four different sets of calculated site occupation factors are obtained from

(i) FPLO calculations for a single unit cell with fixed lattice parameters, cell geometry and atomic coordinates,
(ii) FPLO calculations for a single unit cell with fixed cell geometry and atomic coordinates but with variable lattice parameters[2],
(iii) VASP calculations for a single unit cell with full structural relaxation and
(iiii) VASP calculations for a 2 x 1 x 1 supercell also with full structural relaxation.
Figure **5.12** shows the experimental and the calculated site occupation factors obtained from the FPLO calculations. Subfigure (a) contains the results from the calculations with fixed lattice parameters, subfigure (b) the results with variable lattice parameters.

The calculations are capturing the experimentally observed trend of a composition dependent site occupation reversal. The $6h$ Co occupation is linearly dependent on the Co concentration. The computed values coincide well with the four experimental points. Regarding the $2a$ occupation, the computed values suggest that above a critical value (possibly somewhat higher than 50%), the occupation of the $2a$ site remains constant or slightly decreases. Hence, according to these calculations, the further increase of the Co concentration above a critical value

---

[2] The lattice parameter optimization for many FPLO calculations by hand is very time-consuming. Since it is known, that the a and c lattice parameters have an approximately linear dependence on the composition x, only the lattice parameters of C14 NbCr$_2$ and NbCo$_2$ were carefully optimized by hand. The variable composition dependent lattice parameters of the ternary compounds were than obtained by linear interpolation between NbCr$_2$ and NbCo$_2$. For the calculations with fixed lattice parameters the values at $x = 0.5$ have been used for all compositions.

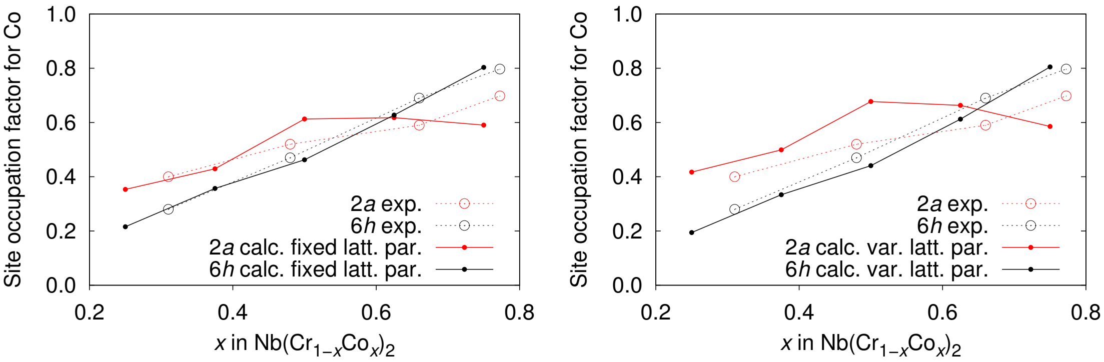

Figure 5.12: Calculated and experimental site occupation factors for Co on $2a$ and $6h$ sites in a C14 $Nb(Cr_{1-x}Co_x)_2$ unit cell. FPLO with fixed (left) and with variable lattice parameters (right).

($x \geq 0.5$) are achieved by replacing only the Cr atoms occupying the $6h$ position with Co atoms. However, the experimental data do not show such saturation. The point of site occupation reversal in the calculated data is shifted to a higher value ($x = 0.65$) as compared with the experimental values ($x = 0.55$). The effect of variable lattice parameters when using FPLO is small. The $6h$ site remains nearly unaffected while the $2a$ site become slightly larger.

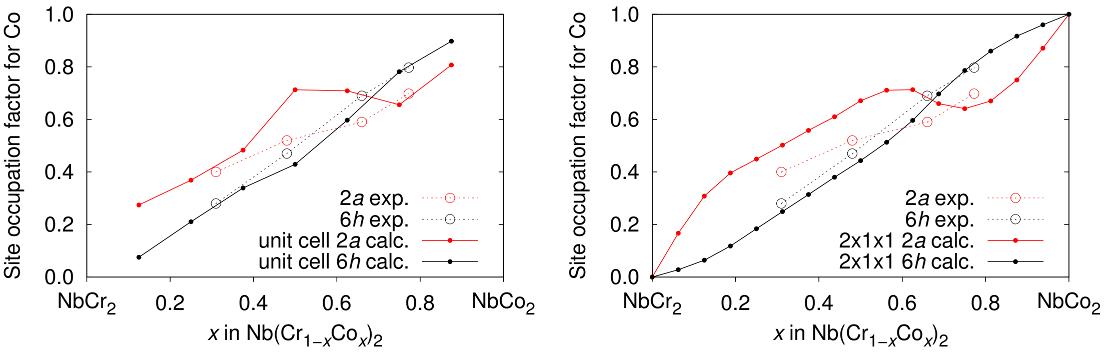

Figure 5.13: VASP calculated and experimental site occupation factors for Co on $2a$ and $6h$ sites in a C14 $Nb(Cr_{1-x}Co_x)_2$ unit cell (left) and a 2 x 1 x 1 supercell (right).

In figure **5.13** the results of the calculations with VASP with full structural relaxation are shown. The site occupation factors obtained within a unit cell of $Nb(Cr_{1-x}Co_x)_2$ are contained in subfigure (a), subfigure (b) shows the results from the 2 x 1 x 1 supercell. The site occupation factors for the unit cell are nearly equal to those obtained with FPLO and varying lattice parameters. The agreement of these two different calculational methods gives confidence in the reliability of the obtained results. The point of site occupation reversal is shifted to a slightly higher Co concentration ($x = 0.69$). The calculations for the 2 x 1 x 1 supercell (fig. **5.13** b) yield many more sampling points. Naturally, at $x = 0$ and $x = 1$ the occupation of Co on $6h$ and $2a$ is 0 and 1, respectively. The curve shape for the $6h$ occupation with Co is similar with all previous results. The $2a$ Co occupation increases up to $x = 0.6$, then it strongly decreases and from $x = 0.75$ on it increases again. The point of site occupation reversal remains unaffected by going from the unit cell to the supercell. The pronounced maximum at $x = 0.5$ in the unit cell calculation is not observed. Summarizing the calculations it can be stated, that the $6h$ site is always in good agreement, while the calculated preferred occupation for the $2a$ site is much stronger than expected from the experiments. The general trend is however in good agreement and the effect of site occupation reversal is well captured.

5.4 Summary

The experimental and theoretical results obtained for $Nb(Cr_{1-x}Co_x)_2$ show that the two binary phases $NbCr_2$ and $NbCo_2$ crystallize in the cubic C15 structure type with only narrow homogeneity ranges. In the range of $0.127(3) \leq x \leq 0.937(3)$ a new true ternary Laves phase with the hexagonal C14 structure type and a large homogeneity range is found experimentally. The calculations yield a homogeneity range slightly shifted to higher Co concentrations with values of $0.14 \leq x \lesssim 0.96$. Narrow C14/C15 two-phase regions separate the two phases in agreement with the calculations. The mean atomic volume, the lattice parameters and also the unusual S-shape of the c/a ratio within the stability range of the C14 structure type is qualitatively reproduced by the calculations. The range of values and especially the minimum of the c/a ratio is well captured. Cr and Co on the two crystallographic sites $2a$ and $6h$ show a site occupation reversal where the minority component preferentially occupies the $2a$ site. The calculated site occupation factors confirm the experimentally observed behavior and the existence and the type of site occupation reversal. Depending on the type of calculation, the point of site occupation reversal is shifted by $x = 0.08 - 0.14$ to higher Co concentrations.

6 The Laves phases $\mathbf{Ta(V_{1-x}Fe_x)_2}$

In the last chapter it was shown, that first principles total energy calculations in the Cr–Co–Nb system are able to model the experimental homogeneity ranges of the Laves phases C15 and C14 along the pseudobinary section $NbCr_2$–$NbCo_2$. In addition, the calculations yield lattice parameters and site occupation factors for the C14 phase in good agreement with the experimental findings. In the case of the Cr–Co–Nb system, the experiment was followed by the calculations. The idea for this chapter was to do the calculations first, followed by the experimental work. For this the Fe–Ta–V was chosen. No information for this system is available in the literature, except that $TaFe_2$ and TaV_2 crystallize with the C14 and the C15 structure, respectively. Thus, Fe–Ta–V is a very interesting system in order to use calculations as predictive tool whose predictions can be checked by experiments afterwards. Additionally, $TaFe_2$ shows some very interesting magnetic properties similar to those of $NbFe_2$ which has been thoroughly investigated. In this chapter the calculations will be discussed first followed by the experiments and the comparison of the calculated and the experimental results.

6.1 Calculation of Gibbs free energy and stability ranges

From the literature it is known that TaV_2 crystallizes with the cubic C15 structure type, while $TaFe_2$ crystallizes with the hexagonal C14 structure type at 1150 °C. Nothing is known about the pseudobinary section TaV_2–$TaFe_2$, no ternary compounds and no phase diagram are reported. In order to compute the homogeneity ranges of C15 and C14 the total energies for C15 and C14 $Ta(V_{1-x}Fe_x)_2$ were calculated for $0 \leq x \leq 1$. From these values and the total energies of the elements Fe, Ta and V the Gibbs energies were calculated. The total energy calculations were carried out using VASP on a C15 unit cell and a C14 2 x 1 x 1 supercell of $Ta(V_{1-x}Fe_x)_2$ with full structural relaxation in space group $P1$. The total energy of Fe was calculated considering its ferromagnetism, V and Ta are paramagnetic. The calculation of the C14 and C15 phases were carried out paramagnetic. The pseudobinary sections were calculated with VASP medium precision due to the high computational effort. The calculated Gibbs energies of the stable configurations were fitted with Redlich-Kister polynomials of 4^{th} order. The homogeneity ranges of the C14 and the C15 phases where then determined via the tangent construction. The pure binaries TaV_2 and $TaFe_2$ where calculated with high precision with VASP and FPLO. Tables **6.1**, **6.2** and **6.3** list all calculations carried out in the Fe–Ta–V system.

Table 6.1: Calculations carried out in the Fe–Ta–V system — Elements.

Phase	Fe	Ta	V
Composition	Fe	Ta	V
Atoms per unit cell	2	2	2
Space group	$Im\bar{3}m$	$Im\bar{3}m$	$Im\bar{3}m$
Lattice parameters			
optimized			
a [Å]	2.813	3.315	2.942
experimental[1]			
a [Å]	2.8665	3.303	3.024
Total energy [eV/atom]	-8.2049	-11.7297	-8.8795
Details	VASP, medium precision		
	ferromagnetic	paramagnetic	paramagnetic

[1] [138]

The calculated lattice parameters of the elements Fe, Ta and V in table **6.1** are close to the experimental values. For Fe and V they are slightly under-, in the case of Ta slightly overestimated. The calculated nuclear magnetic moment of Fe is $2.17\,\mu_B$, close to the experimental value of $2.22\,\mu_B$ [148]. The lattice parameters of the binary compounds C14 $TaFe_2$ and C15 TaV_2 calculated with either VASP or FPLO are equally well in agreement with the experiment. In all cases the calculated values are slightly smaller than the experimental. The c/a ratio in C14 $TaFe_2$ is close to the ideal value and well captured by the calculations.

Figure **6.1** shows the calculated total energy values of all configurations for the cubic C15 and the hexagonal C14 structures of Ta($V_{1-x}Fe_x$)$_2$. The total energy increases with increasing Fe content. The dispersion of the total energy

Table 6.2: Calculations carried out in the Fe–Ta–V system — Binaries.

Phase	C14 TaV_2	C14 $TaFe_2$	C15 TaV_2	C15 $TaFe_2$
Composition of the unit cell	Ta_4V_8	Ta_4Fe_8	Ta_8V_{16}	Ta_8Fe_{16}
Space group	$P6_3/mmc$	$P6_3/mmc$	$Fd\bar{3}m$	$Fd\bar{3}m$
Lattice parameters				
optimized (VASP)				
a [Å]	5.083	4.754	7.129	6.729
c [Å]	8.100	7.773	–	–
c/a	1.594	1.635	–	–
experimental				
a [Å]	–	4.806-4.852[1]	7.160[2]	–
c [Å]	–	7.846-7.896[1]	–	–
c/a	–	1.624-1.634[1]	–	–
Total energy [eV/atom]	-9.9812	-9.5923	-9.9683	9.5631
Details	VASP, high precision, paramagnetic			
Optimized lattice parameters (FPLO)				
a [Å]	5.09	4.76	7.14	6.74
c [Å]	8.10	7.78	–	–
c/a	1.59	1.63	–	–

[1] [105–108, 140–146], [2] [147]

values for the different configurations at a given composition is small and in the same order of magnitude as in the Cr–Co–Nb system. The dispersion for the C14 values is always larger than for the C15 values. The maximum difference is observed for C14 at $x = 0.375$ with 66.1 meV/atom. One configuration of the C15 structure type at a composition of $x = 0.75$ has an exceptional lower total energy ($\Delta E = 21.2$ meV/atom) compared to the other configurations. This might be an indication for an expected superstructure formation. The same is observed at other compositions, however, with smaller energy differences.

In order to determine the homogeneity ranges of the C14 and C15 phases along the pseudobinary section, only the most stable configurations with the lowest energy are important. These are fitted with Redlich-Kister polynomials in figure **6.2**. The numerical data for this graph and the coefficients of the Redlich-Kister polynomials are given in the appendix A.3 in table **1.12** and **1.13**.

The total energies of C14 TaV_2 and $TaFe_2$ are lower than those of the C15

Table 6.3: Parameters of the calculations carried out in the Fe–Ta–V system — Pseudobinary sections.

Phase	C14 $Ta(V_{1-x}Fe_x)_2$	C14 $Ta(V_{1-x}Fe_x)_2$	C15 $Ta(V_{1-x}Fe_x)_2$
Composition of the unit cell	$Ta_4(V,Fe)_8$	$Ta_8(V,Fe)_{16}$	$Ta_8(V,Fe)_{16}$
Space group	$P6_3/mmc$	$P6_3/mmc$	$Fd\bar{3}m$
Details	VASP, medium precision, paramagnetic		
	unit cell	2 x 1 x 1 supercell	unit cell
	39 configurations	4282 configurations	201 configurations

structure type. For $TaFe_2$ this is in agreement with C14 being the reported stable polytype. For TaV_2 this result is in contradiction with the literature data where C15 is the reported stable polytype. The energy difference of 14.3 meV/atom is however small. Furthermore, it is known, that pseudopotential calculations tend to make wrong predictions in the case of V containing Laves phases [149]. On the Fe-rich side the C14 structure type is always lower in energy, while on the V-rich side the C15 structure type is lower in energy. The crossing point of the two G curves is at $x \approx 0.34$.

The Gibbs energy calculated from the total energy of the stable configurations at 1150 °C and the total energy of the pure elements Fe, V and Ta is shown in figure **6.3**. The numerical data and Redlich-Kister coefficients are given in the tables **1.14** and **1.15** in appendix A.3. The contact points of the common tangent on the two G curves of C14 and C15 define the borders of the single phase fields. The calculations predict a solubility of Fe in TaV_2 up to 24 at.% ($x = 0.255$) and of V in $TaFe_2$ up to 39 at.% ($x = 0.525$). A two phase field C15/C14 is expected for compositions $0.255 \leq x \leq 0.525$. An additional phase change from C15 to C14 close to TaV_2 and the stability of C14 TaV_2 is expected from the calculated data. This is however, inconsistent with the available experimental data. The bars at the bottom of figure **6.3** illustrate the calculated width of the single phase fields.

Due to the discrepancy regarding the stability of TaV_2 as C14 or C15 structure type, the Gibbs energies of the binary compounds TaV_2 and $TaFe_2$ have been calculated with high accuracy using VASP as well as FPLO. The results are listed in table **6.4**. With VASP, even with the highest accuracy, the results remain contradictory to the experimental data. C14 TaV_2 is more stable than C15 TaV_2.

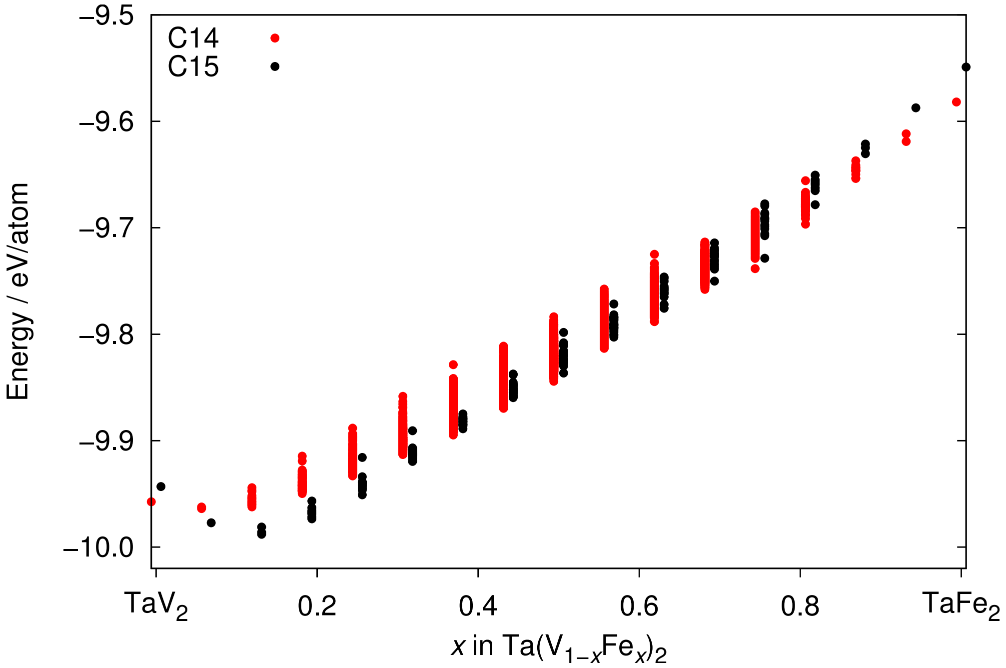

Figure 6.1: Total energy values of all configurations for C15 (201 data points) and C14 (4282 data points) $Ta(V_{1-x}Fe_x)_2$. For clarity the values for C15 and C14 are slightly shifted to the right and left from their nominal composition, respectively.

With 12.9 meV/atom the energy difference is slightly smaller. C14 $TaFe_2$ is stable with the C14 structure type in agreement with the experiment. If FPLO is used and the lattice parameters are optimized by hand, C15 TaV_2 becomes the stable polytype by 9.9 meV/atom.

Table 6.4: Calculated Gibbs free energy for C15 and C14 TaV_2 and $TaFe_2$. Comparison between values obtained with VASP and FPLO with high precision. The stable compounds are printed in bold face.

Phase	VASP [meV/atom]	FPLO [meV/atom]
C15 TaV_2	-105.76	**-120.18**
C14 TaV_2	**-118.70**	-110.31
C15 $TaFe_2$	-176.68	-168.09
C14 $TaFe_2$	**-205.95**	**-176.10**

As a conclusion of this section the calculated homogeneity ranges of the C14 and C15 phase and the two phase regions along the pseudo binary section TaV_2–$TaFe_2$ are listed in the following.

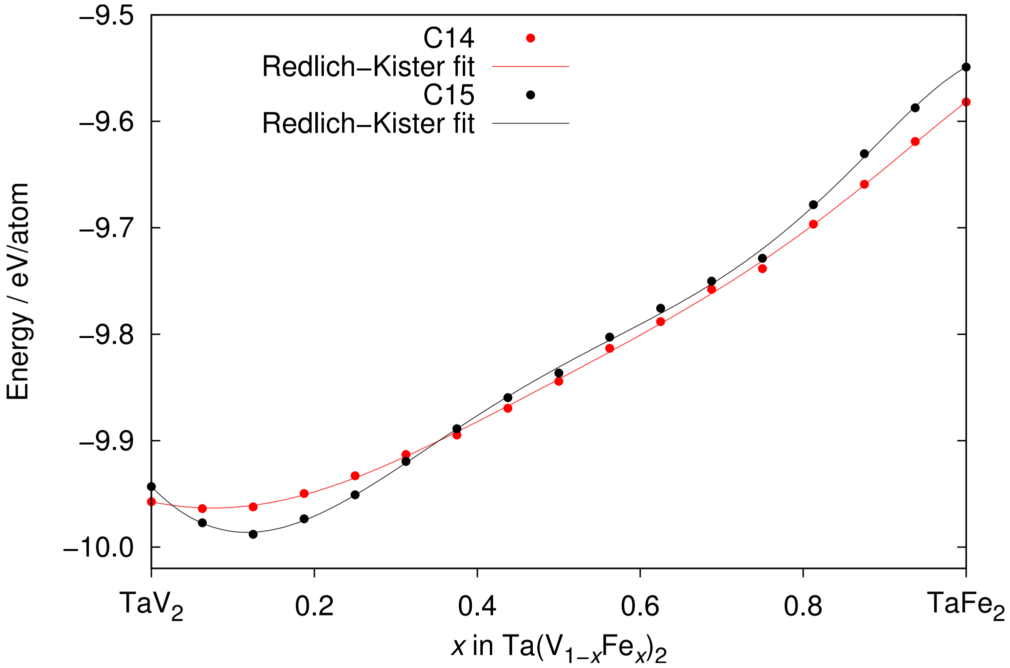

Figure 6.2: Total energy values of the stable configurations of C15 and C14 $Ta(V_{1-x}Fe_x)_2$. The numerical data and the coefficients of the Redlich-Kister polynomials are given in the appendix A.3.

$$
\begin{aligned}
0.000 \leq \quad & x \quad \leq 0.255: \quad \text{C15} \\
0.255 \leq \quad & x \quad \leq 0.525: \quad \text{C15} + \text{C14} \\
0.525 \leq \quad & x \quad \leq 1.000: \quad \text{C14}
\end{aligned}
$$

The structural change from C15 to C14 close to TaV_2 is disregarded since it is in contradiction with the experimental data. This data can now be compared with the results obtained from experimental work in the Fe–Ta–V system.

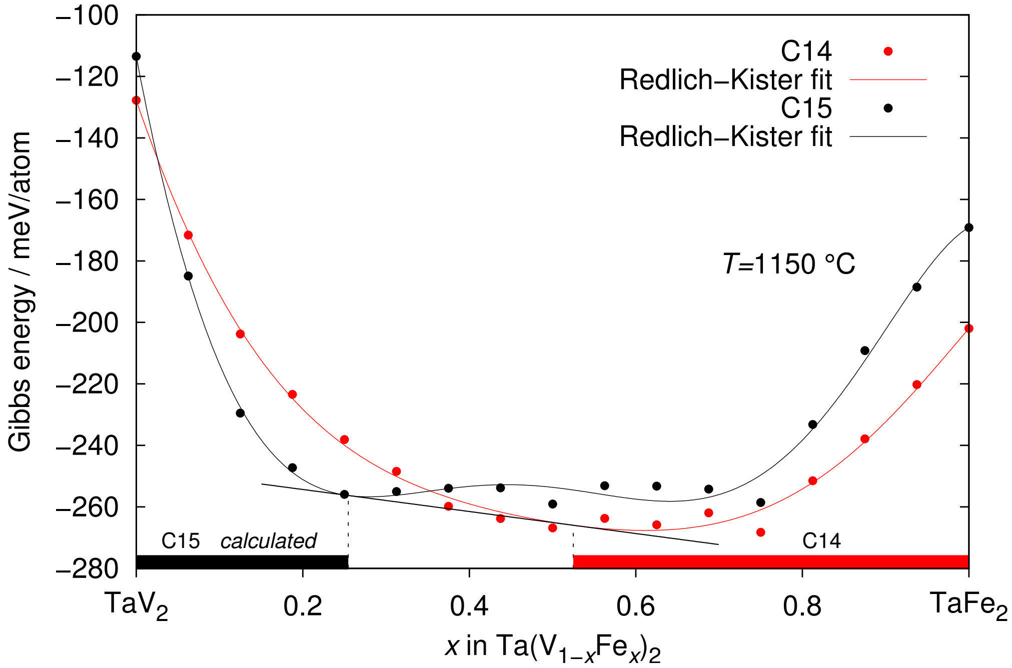

Figure 6.3: Gibbs energy G of the stable configurations of C15 and C14 Ta(V$_{1-x}$Fe$_x$)$_2$ calculated from 4.7 at a temperature of $T = 1150\,°\text{C}$. The values are fitted with Redlich-Kister polynomials of 4th order. The bottom bars indicate the calculated homogeneity ranges of the C14 and C15 phases. The dashed lines mark the contact points of the common tangent with the G curves. The numerical data and the coefficients of the Redlich-Kister polynomials are given in the appendix A.3.

6.2 Phase analysis

The calculations explained in the previous section were concluded by the prediction of homogeneity ranges for the C14 and C15 structure type along the pseudobinary section TaV$_2$–TaFe$_2$. In order to check the reliability of the calculations and to experimentally investigate the pseudobinary section, samples of Ta(V$_{1-x}$Fe$_x$)$_2$ with $0 \leq x \leq 1$ have been synthesized and characterized. The results of the phase analysis as obtained from X-ray powder diffraction, metallographic examinations and quantitative chemical analysis are summarized in table **6.5**. The nominal compositions of the samples are listed besides the results from the chemical analysis for Ta, V and Fe in at.% with their standard deviations. The substitution parameter x is given as nominal value and has been calculated from the chemical analysis based on a fixed Ta content of 33.33 at.%.

Table 6.5: Phase analysis of annealed Fe–Ta–V alloys.

	x in Ta(V$_{1-x}$Fe$_x$)$_2$			Composition Ta/V/Fe in at.%		Lattice parameters
Sample	nominal	observed*	Phases	nominal	ICP-OES	a, (c) in pm
1	0.00	0.000	bcc	33.33/66.67/0.00	33.3(4)/66.7(4)/0	
2	0.00	0.000	bcc+C15	33.33/66.67/0.00	33.5(6)/66.5(6)/0	716.54(2)
3	0.00	0.000	bcc+C15	33.33/66.67/0.00	33.0(15)/67.0(15)/0	716.67(2)
4	0.03	0.025	bcc+C15	33.33/64.67/2.00	33.9(9)/64.4(9)/1.7(1)	715.04(2)
5	0.1	0.098	bcc+C15	33.33/60.00/6.67	33.3(7)/60.1(9)/6.5(3)	711.39(2)
6	0.125	0.123	bcc+C15	33.33/58.33/8.33	33.6(5)/58.2(6)/8.2(2)	710.79(3)
7	0.25	0.246	C15	33.33/50.00/16.67	33.4(3)/50.2(5)/16.4(3)	706.40(3)
			C36			499.3(2), 1631.9(2)
8	0.29	0.292	C36	33.33/47.33/19.33	33.2(6)/47.3(7)/19.5(5)	498.30(4), 1628.3(1)
9	0.3	0.301	C36	33.33/46.67/20.00	33.4(4)/46.5(5)/20.0(3)	498.17(4), 1628.1(1)
10	0.3	0.298	C36	33.33/46.67/20.00	33.6(11)/46.7(14)/19.8(9)	498.27(4), 1628.3(2)
11	0.31	0.313	C36	33.33/46.00/20.67	32.9(3)/46.1(4)/21.0(3)	497.67(3), 1626.7(2)
12	0.31	0.312	C36	33.33/46.00/20.67	33.1(4)/46.0(5)/20.9(3)	498.09(3), 1627.9(1)
13	0.325	0.328	C36	33.33/45.00/21.67	33.6(3)/44.6(5)/21.8(4)	497.74(3), 1627.4(2)
14	0.33	0.331	C36	33.33/44.67/22.00	33.1(6)/44.7(6)/22.2(3)	497.62(3), 1628.6(2)
			C14			497.62(4), 814.28(9)
15	0.35	0.351	C14	33.33/43.33/23.33	33.4(2)/43.2(3)/23.4(2)	497.04(2), 813.53(3)
16	0.40	0.402	C14	33.33/40.00/26.67	33.3(2)/39.9(3)/26.8(3)	495.72(4), 811.21(6)
17	0.45	0.450	C14	33.33/36.67/30.00	33.3(2)/36.7(4)/30.0(3)	494.60(2), 809.09(3)
18	0.50	0.506	C14	33.33/33.33/33.33	33.2(6)/33.0(7)/33.8(7)	493.62(3), 807.06(6)
19	0.50	0.502	C14	33.33/33.33/33.33	33.5(4)/33.1(6)/33.4(6)	493.52(2), 807.07(4)
20	0.60	0.604	C14	33.33/26.67/40.00	32.9(5)/26.6(8)/40.5(7)	491.36(4), 802.83(8)
21	0.65	0.652	C14	33.33/23.33/43.33	33.7(6)/23.1(5)/43.2(8)	490.47(1), 800.89(2)
22	0.70	0.699	C14	33.33/20.00/46.67	33.4(1)/20.0(1)/46.6(1)	489.23(2), 798.41(4)
23	0.70	0.701	C14	33.33/20.00/46.67	33.4(8)/19.9(7)/46.7(11)	489.35(2), 798.63(3)

Table 6.5: Phase analysis of annealed Fe–Ta–V alloys.

	x in Ta($V_{1-x}Fe_x$)$_2$			Composition Ta/V/Fe in at.%		Lattice parameters
Sample	nominal	observed*	Phases	nominal	ICP-OES	a, (c) in pm
24	0.75	0.749	C14	33.33/16.67/50.00	33.4(5)/16.7(4)/49.9(7)	488.29(3), 796.57(4)
25	0.80	0.801	C14	33.33/13.33/53.33	33.3(6)/13.2(3)/53.4(7)	487.20(3), 794.40(4)
26	0.80	0.800	C14	33.33/13.33/53.33	33.4(3)/13.3(3)/53.3(4)	487.33(3), 794.52(6)
27	0.85	0.850	C14	33.33/10.00/56.67	33.9(7)/09.9(3)/56.2(8)	486.20(3), 792.52(5)
28	0.85	0.849	C14	33.33/10.00/56.67	34.0(2)/10.0(1)/56.1(2)	486.21(2), 792.53(4)
29	0.90	0.900	C14	33.33/06.67/60.00	33.8(6)/06.6(2)/59.6(7)	485.14(5), 790.88(7)
30	0.90	0.899	C14	33.33/06.67/60.00	33.9(7)/06.7(2)/59.4(8)	485.02(2), 790.69(4)
31	0.91	0.913	C14	33.33/06.00/60.67	33.4(6)/05.8(2)/60.8(7)	484.67(3), 790.04(4)
32	0.95	0.949	C14	33.33/03.33/63.33	33.9(7)/03.4(1)/62.7(8)	483.79(2), 789.05(4)
33	0.95	0.950	C14	33.33/03.33/63.33	34.1(9)/03.3(2)/62.6(10)	483.73(3), 788.83(4)
34	0.98	0.983	C14	33.33/01.33/65.33	33.6(7)/01.1(1)/65.2(8)	483.02(3), 788.13(5)
35	1.00	1.000	C14	33.33/00.00/66.67	33.9(6)/0/66.1(6)	482.57(3), 787.62(6)
36	1.00	1.000	C14	33.33/00.00/66.67	33.7(8)/0/66.3(8)	482.65(4), 787.69(6)
37	1.00	1.000	C14	33.33/00.00/66.67	33.0(4)/0/67.0(4)	482.54(3), 787.59(5)
38	1.00	1.000	C14	33.33/00.00/66.67	33.6(5)/0/66.4(5)	482.56(4), 787.63(6)
39	1.00	1.000	C14	33.33/00.00/66.67	32.9(2)/0/67.1(2)	482.45(3), 787.44(5)
40	1.00	1.000	C14	33.33/00.00/66.67	33.1(4)/0/66.9(4)	482.51(5), 787.51(7)

*calculated from the results of the chemical analysis with the Ta content fixed at 33.33 at.%.

The nominal compositions agree well with the results of the analytical investigation by ICP-OES. The maximal observed deviations from the nominal compositions are about 0.7 at.%. The results from X-ray powder diffraction are given in form of the lattice parameters and the identified phases.

Samples with the composition TaV_2 quenched after 30 days annealing at 1150 °C crystallize with the cubic C15 structure type while $TaFe_2$ crystallizes with the hexagonal C14 structure type. The maximum solubility of Fe in C15 TaV_2 estimated from X-ray powder diffraction of single and multi-phase samples is approximately 8 at.% ($x = 0.125$). C14 $TaFe_2$ can solve up to approximately 43 at.% V ($x = 0.35$). In addition, a new true ternary Laves phase with the hexagonal C36 structure type is observed with a small homogeneity range of approximately $0.29 \leq x \leq 0.32$. The precise determination of the width of the C36 phase field and the adjacent two-phase fields C15/C36 and C36/C14 is hindered by the strong overlap of the Bragg peaks in X-ray powder diffraction.

Representative powder diffractograms of three ternary phases with C15, C36 and C14 structure type are shown in figure **6.4**. The sample with C15 structure type was measured on a laboratory diffractometer with Co $K\alpha_1$ radiation ($\lambda = 1.788965\,\text{Å}$), while the other two samples with C36 and C14 structure were measured using synchrotron radiation ($\lambda = 0.4\,\text{Å}$) at the beamline ID31 of the European Synchrotron Radiation Facility (ESRF). V-rich samples need very long annealing times to transform the bcc solid solution (Ta,V) which is present in as-cast samples, into the thermodynamically stable C15 structure type. Small amounts of the bcc phase are therefore still present in all investigated C15 samples. The weak reflection at $2\theta = 48°$ marked with a star in the diffractogram of the C15 phase (fig. **6.4** b) can be attributed to that bcc phase. The broad reflection at $2\theta = 20.5°$ originates from the Vaseline coated mylar foil of the flatbed sample holder. Micrographs of sample no. 6 with the C15 structure type are shown in figure **6.5**. The bcc impurities are not visible in brightfield (a) but only as material contrast in the SEM (BSE) as the small dark areas in subfigure (b). EDXS analysis show the bcc phase to be V-rich with a composition of $Ta_{22}V_{74}Fe_4$ in this sample.

Another often observed Ta-rich impurity is of the Ti_2Ni structure type (space group $Fd\bar{3}m$). This phase was also found in many samples in the Co–Cr–Nb system. Although it is not observed in the diffraction patterns of all samples, metallographic analyses reveal tiny amounts of this phase to be present in many samples in the Fe–Ta–V system. Especially ternary Fe-rich C14 samples and binary $TaFe_2$ contained larger amounts of this phase. In the SEM (BSE) micrograph of sample no. 20 (fig. **6.6**) this phase is visible as bright streaks.

The identification of a single phase C36 sample is difficult due to the strong overlap of Bragg peaks. While C15 and C36 can still be identified in the X-ray diffraction pattern of a two-phase sample it is very difficult to distinguish C36 and C14. And also metallographic analyses of such samples fail to determine the amount of phases, if the width of the two phase region is very small and the two phases have almost identical composition. Thus, the phase contrast in backscattered electron images in the scanning electron microscope is too low and polarized light in light optical microscopy does also not help since both phases show orientation contrast.

Figure **6.4** (b) shows the diffraction pattern of a sample with the C36 structure type. With a composition of $x = 0.31$ it is located right in the middle of the determined homogeneity range of the C36 phase and is thus assumed to be single phase C36. The powder diffraction pattern shows no additional reflections and light optical as well as electron microscopy including EDXS analysis (not shown) shows no evidence for a second phase. What is striking in the diffraction patterns of all C36 samples is that some of the Bragg reflections are considerably broader than others. The most prominent of these are marked with arrows in figure **6.4** (b). The difference in the diffraction patterns of a C14 and a C36 phase in low angular ranges are small. The C36 phase can only be identified on the basis of a few additional reflections which do not appear in the C14 phase. A systematic analysis shows that all those additional reflections in the diffraction pattern of sample no. 11 (fig. **6.4** b) are broadened. If these broadened reflections are interpreted as stacking faults within the crystal structure, this is a strong indication that the C36 phase is forming from the C14 phase. This is proven by the fact that sample no. 12 with the same composition ($x = 0.31$) exhibits the C14 structure type in the as-cast state and transforms into the C36 structure type after long annealing at 1150 °C. The corresponding diffraction patterns are shown in figure **6.7**. It is clearly visible that a C36 phase is forming from the C14 phase at annealing temperatures of 1150 °C. Two reflections marked with a star can be attributed to the Ti_2Ni type impurity phase. The crystallinity of all samples with the C36 phase is however so bad, that a Rietveld refinement of the structures fails, even with data obtained from synchrotron X-ray powder diffraction. If the same sample is annealed at 1600 °C for 24 hours, a clean C14 pattern is observed again. It is thus concluded, that C14 is stable at high temperatures while a phase transformation C14 → C36 takes place at temperatures somewhere above 1150 °C.

A DSC investigation (Netzsch DSC 404) was carried out to find the C14 → C36 transition temperature. 75 mg of sample no. 12 where heated to 1350 °C with 10 K/min in a Pt-Rh crucible with Al_2O_3 inset. After annealing for 24 hours the sample was slowly cooled (1 K/min) to 1000 °C. However, no signal could be detected in the temperature range between 1350 °C and 1000 °C. This leads to the conclusion that the phase transformation takes place between 1350 °C and 1600 °C. Thus, a high-temperature DTA measurement (Netzsch STA 449) was carried out. 80 mg of sample no. 12 were heated up to 1550 °C with 10 K/min in a Ta crucible. The heating curve of this measurement is shown in figure **6.8**. A significant endothermic reaction is observed with an onset temperature of 1309 °C and a peak temperature of 1401 °C and two smaller endothermic peaks at slightly lower temperatures. The bulk sample material did not melt or react with the tantalum crucible. The powder diffraction pattern after the DTA measurement (cooling rate 1 K/min to 1000 °C, natural cooling to room temperature) shows a mixture of C14 and C36. It is thus concluded that the large endothermic reaction with the onset temperature of 1309 °C corresponds to the phase transformation of the low-temperature C36 to the high-temperature C14 phase of samples with the composition $Ta(V_{0.69}Fe_{0.31})_2$. The origin of the two smaller endothermic reactions is not clear so far.

The synchrotron powder diffraction pattern of a single phase C14 sample $Ta(V_{0.35}Fe_{0.65})_2$ (no. 21) is plotted in figure **6.4** (c). No additional impurity phases and no unusual peak shapes are observed. Metallographic analysis and EDXS measurements support the single phase character of the sample. The corresponding micrographs are shown in figure **6.9**. The contrast in both images is caused by differently oriented single crystalline grains of the hexagonal C14 phase. The mean atomic volume V_{atom} of the Laves phases $Ta(V_{1-x}Fe_x)_2$ with $0 \leq x \leq 1$ is plotted versus the composition x in figure **6.10**. The experimental homogeneity ranges of C15, C36 and C14, which were roughly determined from the composition of single phase samples are indicated by the solid bars in the lower part of the graph. As expected, the mean atomic volume decreases with increasing Fe content since Fe atoms are smaller than V atoms. The composition dependence of the mean atomic volume shows a linear behavior according to Vegard's volume rule. Most important in this graph is the comparison of the calculated (see also figure **6.3**) and the experimental homogeneity ranges. As indicated by the top and bottom bars, calculated and experimental homogeneity ranges are in reasonable agreement. The C15 phase on the V-rich side shows a smaller, the Fe-rich C14 phase a larger homogeneity range. The deviations might be attributed to the absence of the C36 phase in the calculations. If the C36 phase were stable around the composition $x = 0.31$, the tangent construction would result in a decrease of the width of both, C15 and C14 homogeneity ranges.

To verify the stability of the C36 phase, the total energy of C36 $\mathrm{Ta(V_{1-x}Fe_x)_2}$ was calculated for selected compositions x (see appendix A.3, figure **1.1**). For most compositions the total energy of C36 lies in between that of C14 and C15 and the energy differences are negligible. For $x = 0.3125$, experiments showed the C36 phase to be stable. And indeed, the calculations show C36 to be more stable than C14 by only 0.004 meV/atom. The C15 phase at the same composition is even more stable by 0.003 meV/atom. However, due to the close relation of the three structure types, the calculated energy differences regarding the C36 phase are too small to be meaningful. Nevertheless, given that the calculations were performed with a comparably low accuracy, the calculated and the experimental results are in satisfying agreement.

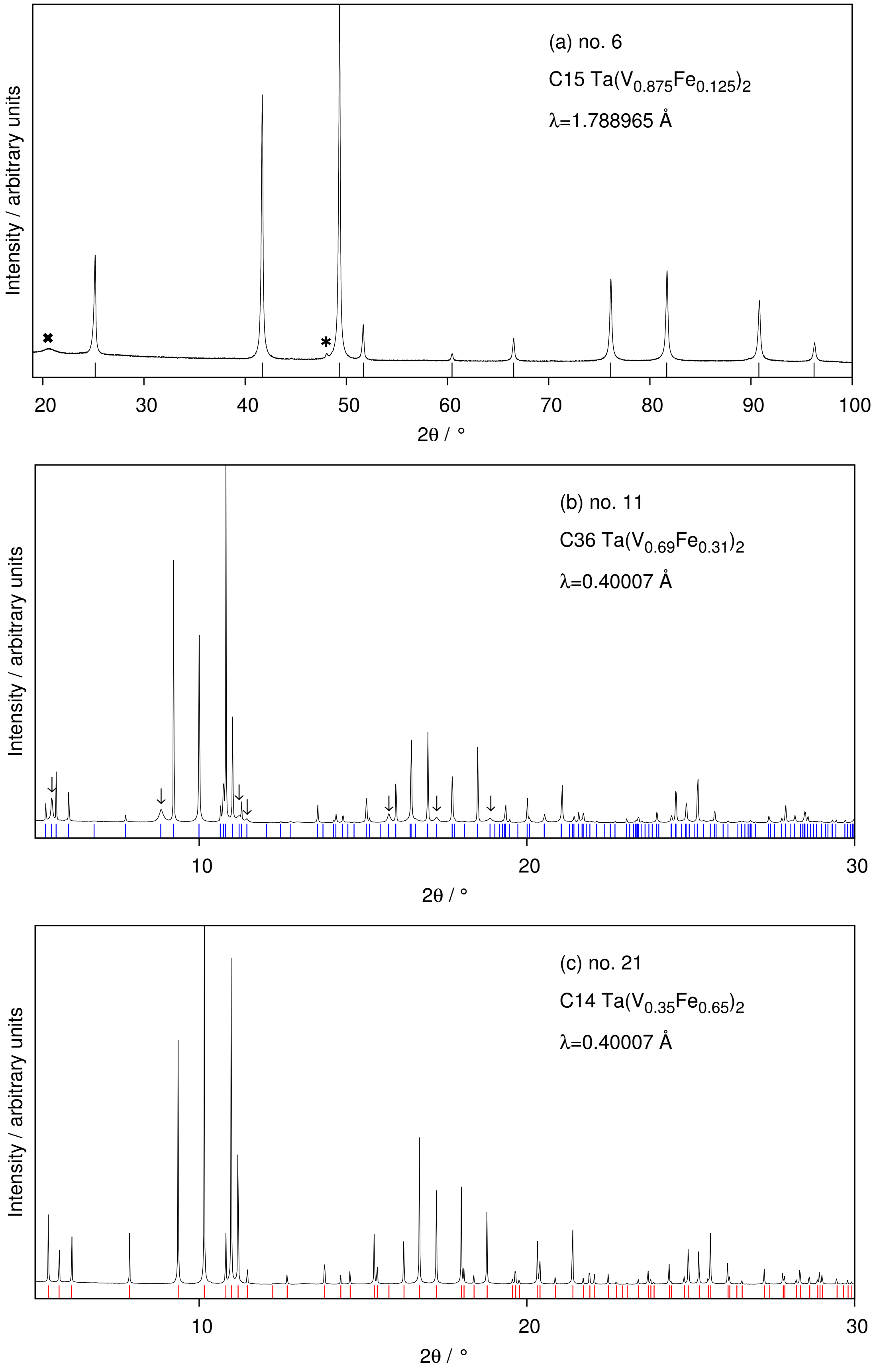

Figure 6.4: X-ray powder diffractograms of (a) C15 Ta($V_{0.875}Fe_{0.125}$)$_2$ (no. 6), (b) C36 Ta($V_{0.69}Fe_{0.31}$)$_2$ (no. 11) and (c) C14 Ta($V_{0.35}Fe_{0.65}$)$_2$ (no. 21). Tic marks indicate the theoretical reflection positions of the respective phases. For the description of the symbols and arrows in (a) and (b) see text.

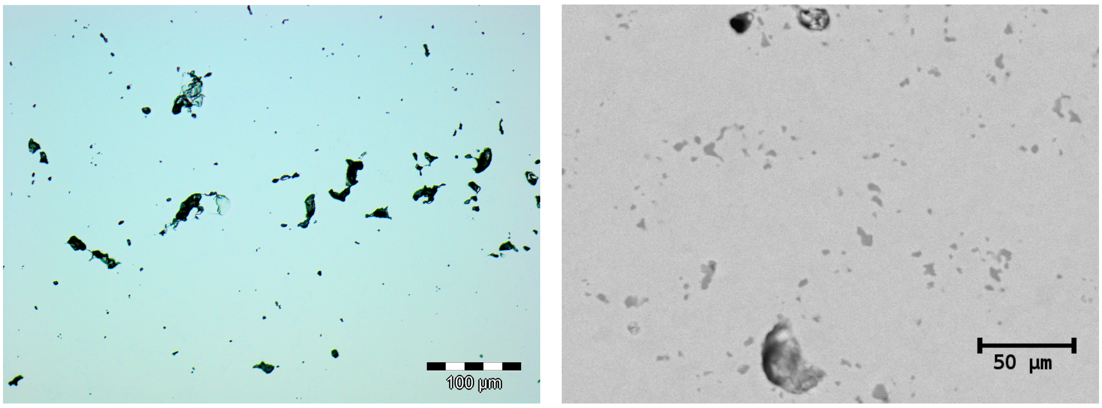

(a) LOM (brightfield) (b) SEM (BSE)

Figure 6.5: Micrographs of C15 Ta($V_{0.875}Fe_{0.125}$)$_2$ (no. 6). The light optical microscopy image shows a homogeneous sample with many large pores. The V-rich bcc phase is only visible as the small dark areas in the SEM (BSE) image.

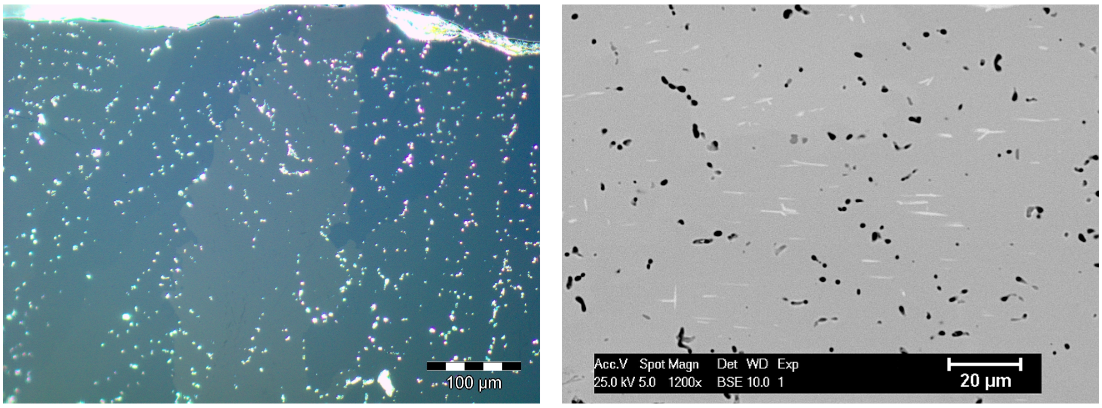

(a) LOM (polarized light) (b) SEM (BSE)

Figure 6.6: Micrographs of C14 Ta($V_{0.4}Fe_{0.6}$)$_2$ (no. 20). The Ta-rich Ti_2Ni-type impurity phase is observable in the SEM (BSE) as the bright streaks. The dark areas are pores. The light optical microscopy image (a) shows the contrast between differently oriented grains of the hexagonal C14 phase in polarized light. Pores appear as white spots.

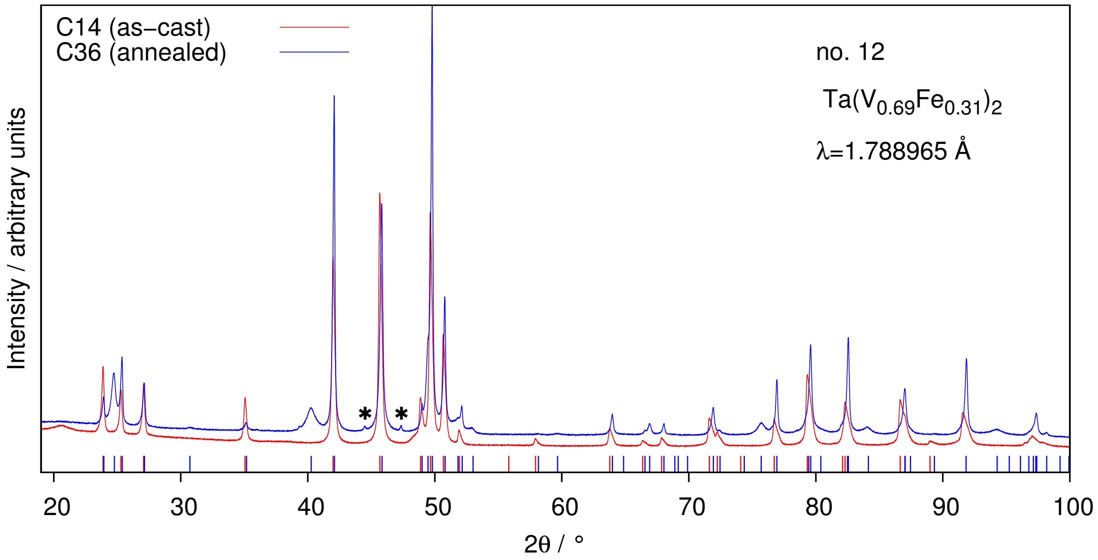

Figure 6.7: X-ray powder diffractograms of $Ta(V_{0.69}Fe_{0.31})_2$ (no. 12) in the as-cast state (red) and after annealing (blue) at 1150 °C. Tic marks indicate the theoretical reflection positions of the respective phases C14 and C36. Two reflections marked with a star can be attributed to the Ti_2Ni type impurity phase.

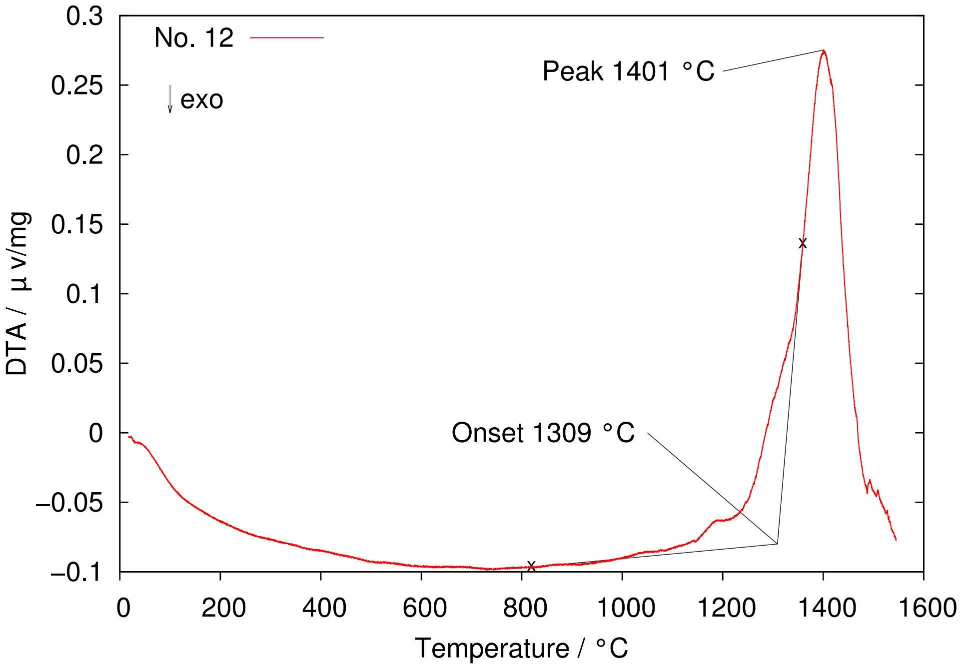

Figure 6.8: Heating curve (10 K/min) of high-temperature DTA measurement of $Ta(V_{0.69}Fe_{0.31})_2$ (no. 12).

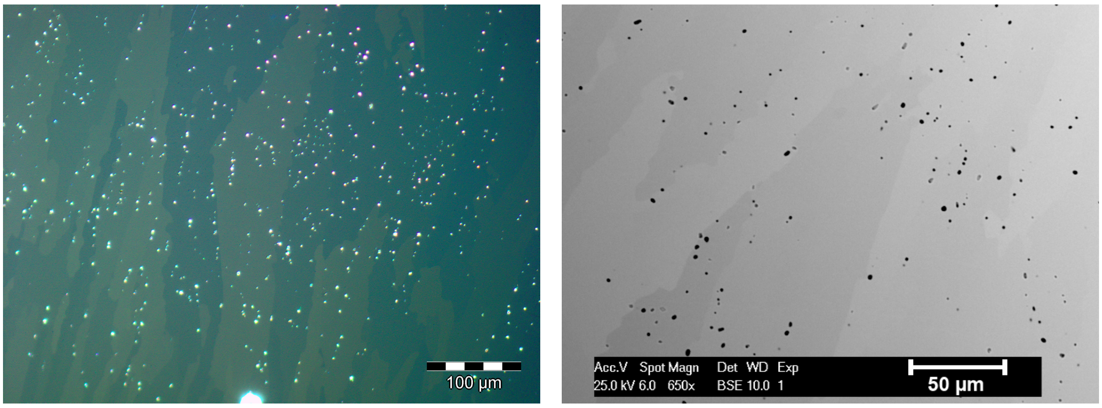

(a) LOM (polarized light) (b) SEM (BSE)

Figure 6.9: Micrographs of single phase C14 Ta($V_{0.35}Fe_{0.65}$)$_2$ (no. 21). The contrast in both light optical microscopy and scanning electron microscopy (BSE) originates from differently oriented single crystalline grains of the hexagonal C14 phase.

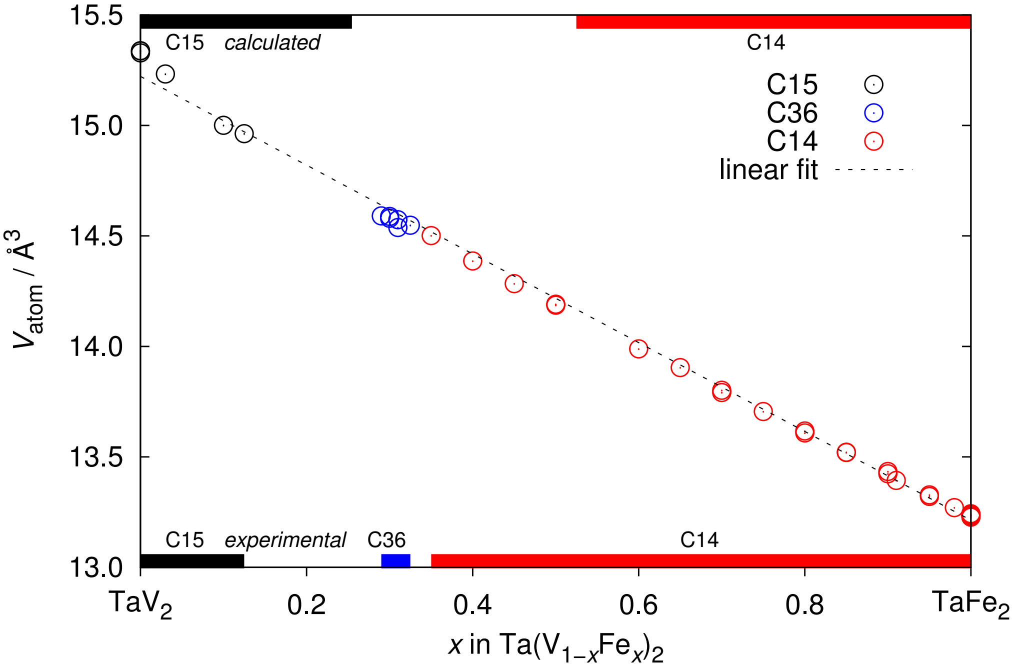

Figure 6.10: Experimental mean atomic volume V_{atom} of C15, C36 and C14 Ta($V_{1-x}Fe_x$)$_2$ as a function of x. Only single phase samples are shown in this plot. The top and bottom bars indicate the calculated and experimental homogeneity ranges.

6.3 Crystal structure of C14 $Ta(V_{1-x}Fe_x)_2$

In this section the crystal structure of C14 $Ta(V_{1-x}Fe_x)_2$ will be investigated as a function of the composition x and the calculated lattice parameters and site occupation factors will be analyzed and compared with the available experimental data. The phase analysis in the previous section revealed an experimental stability range of the C14 phase $Ta(V_{1-x}Fe_x)_2$ from $0.35 \leq x \leq 1$ at 1150 °C. The experimental mean atomic volume V_{atom} of single phase samples within this range is compared to the calculated values in figure **6.11**. As in the case of C14 $Nb(Cr_{1-x}Co_x)_2$, the calculated volumes are smaller than the experimental data, by approximately 0.58 Å (4%). If the calculated data would be shifted by a constant value of 0.58 Å, the slope of the curve is in agreement with the Vegard like behavior of the experimental data with the calculated data having a slightly steeper slope. Hence, the calculations predicted the proper behavior of the mean atomic volume after a correction which is possible by only few experimental data points.

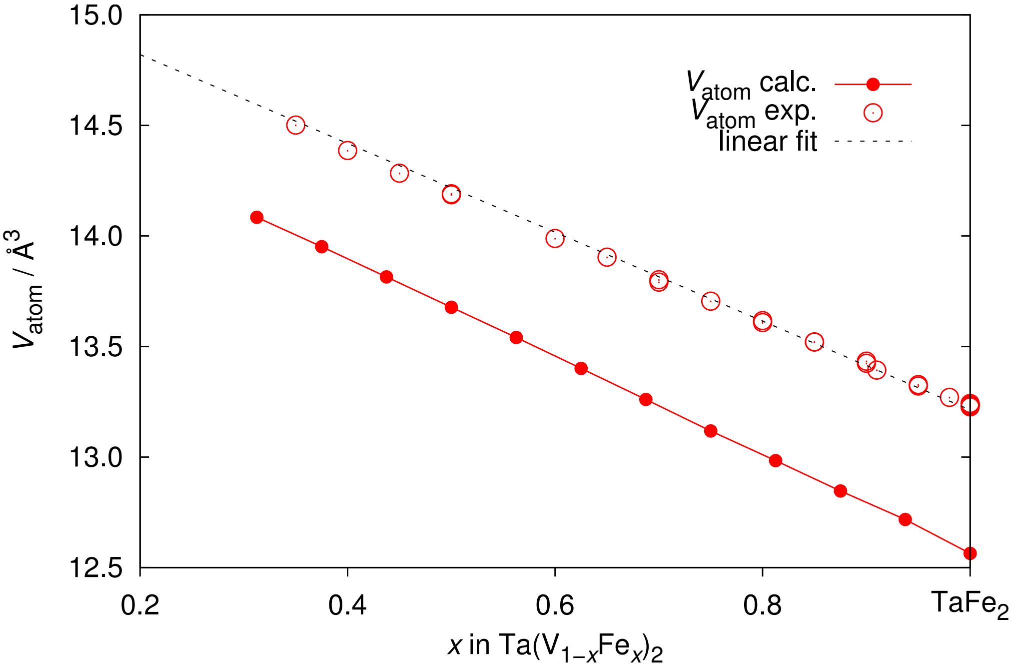

Figure 6.11: Experimental and calculated mean atomic volume of C14 $Ta(V_{1-x}Fe_x)_2$.

The a and c lattice parameters are plotted in figure **6.12**. Their evaluation is

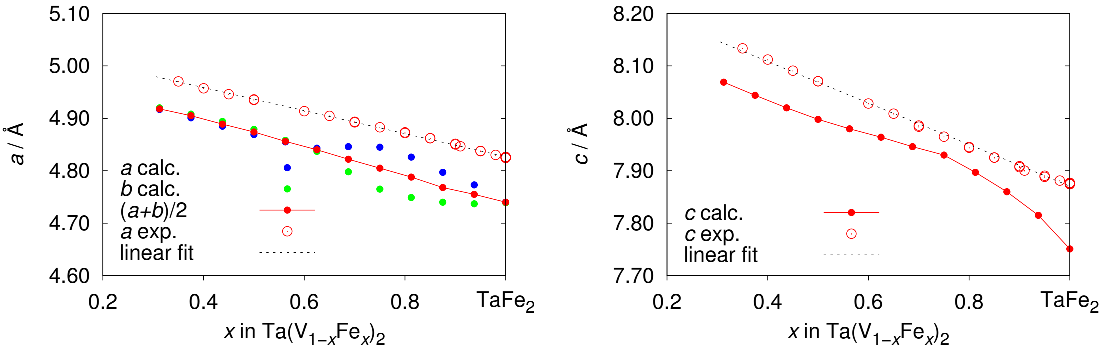

Figure 6.12: Experimental and calculated lattice parameters a (left) and c (right) of C14 Ta($V_{1-x}Fe_x$)$_2$. In order to compare the slopes of the curves, the plots are showing the same range of values.

more complicated than in the case of C14 Nb($Cr_{1-x}Co_x$)$_2$. The a and c lattice parameters are calculated via the Boltzmann distribution (equ. 4.22) from the total energy values of the stable configurations of a 2 x 1 x 1 supercell. Thus, in the initial state of the calculations the a lattice parameter is exactly twice as long as the b lattice parameter ($a/2 = b$)[1]. Since the structural optimization is carried out in space group $P1$, all lattice parameters are optimized independently. Thus, in the final state after the optimization a is not exactly twice as long as b anymore ($a \neq b$). In the case of C14 Nb($Cr_{1-x}Co_x$)$_2$, the differences between a and b were always very small in the range of $0.002 - 0.02$ Å. The shape of the two curves was very similar and a was always smaller than b. The actually evaluated lattice parameter was then simply the arithmetic mean of a and b.

In the present case of C14 Ta($V_{1-x}Fe_x$)$_2$ the differences of the values of a and b is four times as large, up to 0.08 Å. Thus, both are plotted independently in figure **6.12**, together with their arithmetic mean value and the experimental data. The calculated data are smaller than the experimental data which can be corrected by a constant shift of 0.073 Å. On the V rich side of the homogeneity range of the C14 phase no deviations of a and b are observable. However, large deviations occur on the Fe-rich side. Beginning at $x = 0.625$ a increases drastically up to $x = 0.8$ and then decreases again. At the same time b strongly decreases. At $x = 1$, TaFe$_2$, both a and b are equal again. Due to that contrasting behavior

---

[1] To improve the readability of the text, $a/2$ will only be denoted as a in the following discussion and the plots.

however, the mean value is close to the experimental values, so that experimental and calculated data agree well. The calculated curve has only a slightly steeper slope than the experimental. The distortions which are induced by the deviations of a and b might be attributed to the magnetic peculiarities of C14 Ta(V$_{1-x}$Fe$_x$)$_2$ which take place in the same compositional range and are discussed in section 6.4. And indeed does the consideration of magnetism in the calculations reduce these deviations and improve the agreement of calculated and experimental values.

The evaluation of the c lattice parameter in figure **6.12** is more simple. The calculated values are smaller by approximately 0.06 Å. In contradiction to C14 Nb(Cr$_{1-x}$Co$_x$)$_2$ where the c lattice parameter shows a much steeper slope than a, here both have approximately the same slope. This slope of c is well captured by the calculations, although the calculated values show some noticeable deviations from the experiment. For $x = 0.75$ the curve shows some kind of a maximum, while for TaFe$_2$ the c parameter is strongly underestimated. However, what applies to a and b also applies to c: the consideration of the magnetic properties of C14 Ta(V$_{1-x}$Fe$_x$)$_2$ reduces these deviations and perceptibly improves the agreement between experimental and calculated data as shown in section 6.4.

The c/a ratio is evaluated in figure **6.13**. The curve of the experimental values

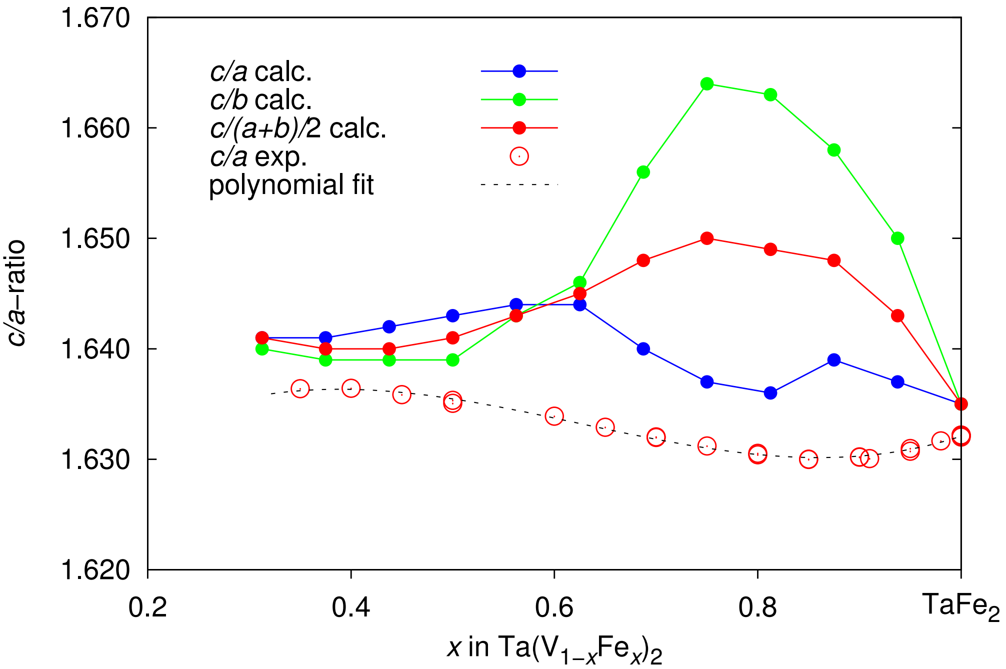

Figure 6.13: Experimental and calculated c/a ratio of C14 Ta(V$_{1-x}$Fe$_x$)$_2$.

shows an s-like shape equal to that of C14 Nb($Cr_{1-x}Co_x$)$_2$. However, with ≈ 0.006 the range of the values is much smaller than for for C14 Nb($Cr_{1-x}Co_x$)$_2$ (≈ 0.02). The highest value of c/a (1.6364) is observed on the V rich side for $x = 0.35$. The ideal c/a ratio of $\sqrt{8/3} = 1.633$ is reached almost exactly in the middle of the C14 homogeneity range at $x = 0.65$. The minimum value of 1.630 is observed at $x = 0.85$. Due to the deviations of the a and b lattice parameters from each other, one can calculate different values for the c/a ratio: c/a, c/b and $c/(a+b)/2$, respectively. All three curves are overestimated and have a completely different shape[2]. None of them shows an agreement with the experimental data. The reason for this are the distortions of the supercell caused by the deviating a and b lattice parameters and also the discrepancy of the calculated and the experimental c lattice parameter. Furthermore, due to the narrow range of values, the c/a is very sensitive to deviations of the lattice parameters. If magnetism is introduced in the calculations, the agreement of experimental and calculates values does improve (see section 6.4).

Finally, the calculated site occupation factors of Fe in C14 Ta($V_{1-x}Fe_x$)$_2$ are shown in figure **6.14**. Both data sets obtained from a unit cell and a 2 x 1 x 1 supercell of C14 Ta($V_{1-x}Fe_x$)$_2$ show a site occupation reversal with the minority component preferentially occupying the 6h site. This is the opposite behavior as observed for C14 Nb($Cr_{1-x}Co_x$)$_2$ where the 2a site is preferentially occupied by the minority component. However, the two data sets differ quite strongly from each other. The point of site occupation reversal for the unit cell calculations lies at $x = 0.57$, for the supercell calculations it is shifted to $x = 0.3$ and thus lies outside the homogeneity range of the C14 phase. Unfortunately, there is no experimental data available for comparison.

---

[2] For C14 Nb($Cr_{1-x}Co_x$)$_2$ all three curves haves the same shape and the absolute values differ only slightly from each other.

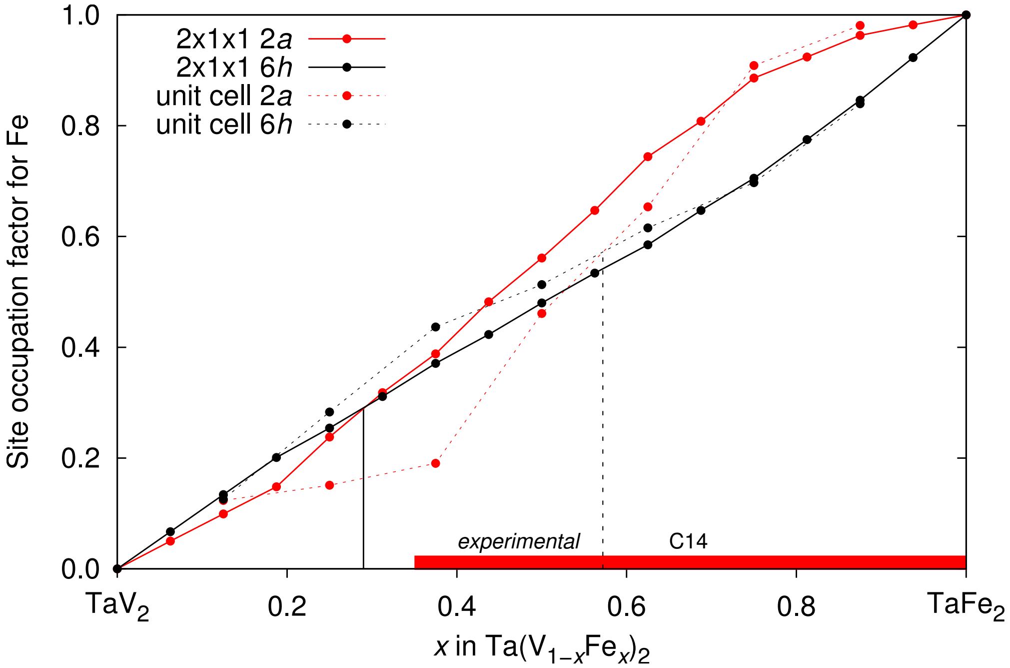

Figure 6.14: Calculated site occupation factors obtained from a unit cell (dashed lines) and a 2 x 1 x 1 supercell (solid lines) of C14 $Ta(V_{1-x}Fe_x)_2$. The bottom bar indicates the experimental homogeneity range of the C14 phase. The vertical lines mark the point of site occupation reversal.

6.4 Magnetic properties of C14 $Ta(V_{1-x}Fe_x)_2$

As mentioned previously, the C14 phase $Ta(V_{1-x}Fe_x)_2$ and $TaFe_2$ in particular show peculiar magnetic properties. In the compositional range of $0.75 \leq x \leq 0.95$ it was reported to be an itinerant antiferromagnet (AFM), whereas for $x \geq 0.95$ the magnetic susceptibility of the system, measured with a magnetic field of 1 T, did not show any phase transition but very high values for a band magnet, indicating the proximity of $TaFe_2$ to a ferromagnetic (FM) instability [3]. In other words, $TaFe_2$ is considered to be paramagnetic (PM) with strong FM and AFM spin fluctuations. This statement is supported by the chemical and electronic similarity of $TaFe_2$ to $NbFe_2$, which has been investigated in some detail by Brando and co-workers [2, 150, 151]. By adjusting the precise composition within a narrow homogeneity range or by applying hydrostatic pressure, $NbFe_2$ can be tuned from ferromagnetism via an intermediate spin-density-wave (SDW) modulated state to a quantum critical point (QCP). Since the atomic volume of $TaFe_2$ is 13.25 Å^3 and thus slightly smaller than that of $NbFe_2$ (13.35 Å^3) $TaFe_2$ is expected to be closer to the QCP than $NbFe_2$.

In order to get insight into the magnetic properties of Ta($V_{1-x}Fe_x$)$_2$, the temperature (T) and field (B) dependent magnetization (M) were measured on several polycrystals with $0.7 \leq x \leq 1$. The uniform susceptibility $\chi = M/B$ at $B = 1\,\mathrm{T}$ is plotted in figure **6.15** for selected samples and temperatures from 300 to 2 K: The arrows mark the peak in χ at the Néel temperature T_N, indicating a phase transition from a PM state into a low-T AFM state. For Ta($V_{1-x}Fe_x$)$_2$ at high

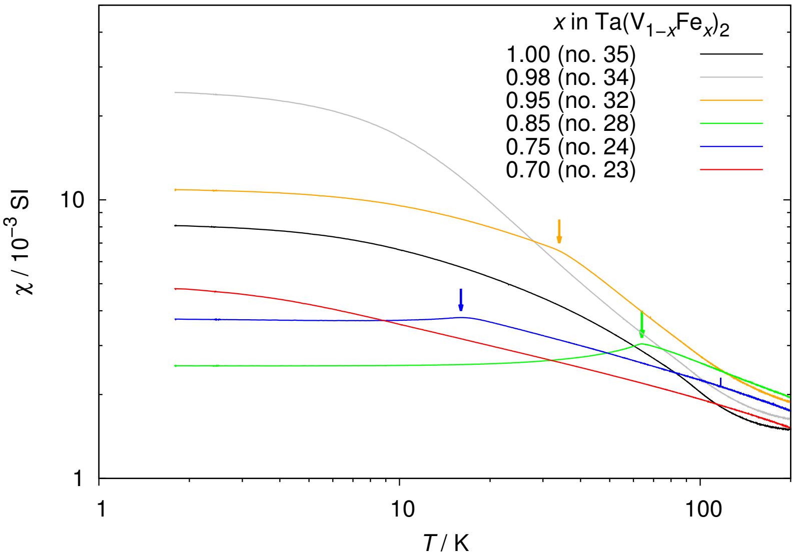

Figure 6.15: Temperature dependence of the dc susceptibility χ of selected samples with $0.7 \leq x \leq 1$ taken at $B = 1\,\mathrm{T}$. The antiferromagnetic transition temperatures T_N are indicated by the arrows.

($x = 0.7$, no. 23) and low ($x = 0.98$, no. 34) V contents and for $TaFe_2$ (no. 35) no phase transition is observed and the ground state is paramagnetic. However, there is a great difference between the values of the susceptibility for $x = 0.7$ (red line) and $x = 0.98$ (gray line) at 2 K. For sample no. 34 with $x = 0.98$ the susceptibility is enhanced by spin fluctuations by a factor of ≈ 240 (Stoner factor) compared to the bare susceptibility estimated from band structure calculations. In $NbFe_2$ this factor is ≈ 180 [2]. This value confirms that the system at $x \approx 1$ is close to a FM instability. To know how large the fluctuating moment is in this sample, χ^{-1} vs. T is plotted in figure **6.16** to analyze the Curie-Weiss behavior: The dashed line is a linear fit to the data yielding a fluctuating moment of $1.04\,\mu_B$ which is much larger than the induced magnetic moment of about $0.055\,\mu_B$ measured at

7 T (see fig. **6.17**). This is a common property observed in all itinerant magnets. More evidence for the presence of the AFM state is given by the field dependent magnetization shown in figure **6.17** for three PM and one AFM sample with $x = 0.75$. The AFM sample shows an inflection point at around 3 T emphasized in the inset where the derivative dM/dB is plotted vs. B. dM/dB shows a clear peak which shifts to lower fields with increasing temperature, as expected for an antiferromagnet. The magnetic phase diagram of $\mathrm{Ta(V_{1-x}Fe_x)_2}$ as determined from the susceptibility measurements at $B = 1\,\mathrm{T}$ is displayed in figure **6.18**. The red points indicate the Néel temperatures as observed in the present experiments, while the black ones have been extracted from reference [3], where the susceptibility has also been measured at 1 T. A clear AFM dome emerges in the PM phase of the diagram. There is a certain systematic discrepancy between these points, which is difficult to clarify. It could be explained by the fact that here the V content has been estimated by chemical analysis while the nominal one is given in reference [3]. However, if there is a systematic difference in x, one would expect T_N in the present experiments to be higher on one side and lower on the other side of the dome maximum. The overall behavior is consistent though.

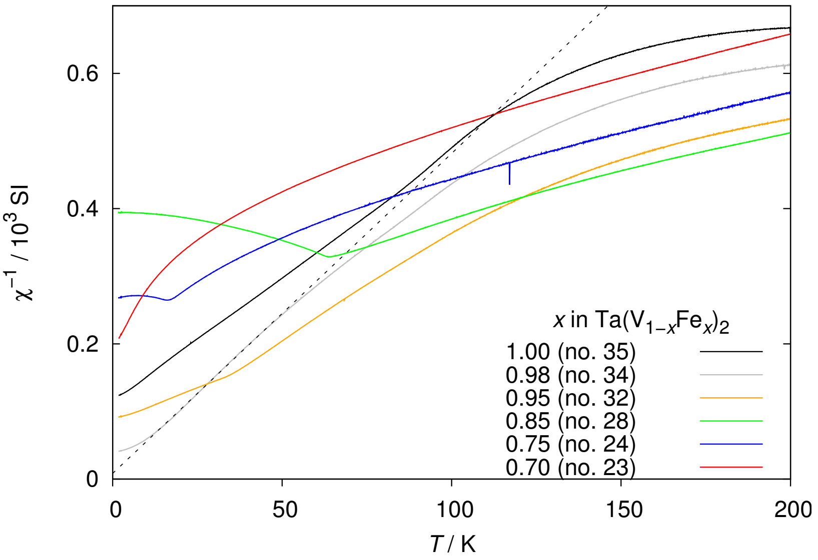

Figure 6.16: χ^{-1} plotted versus T for selected samples to emphasize the Curie-Weiss behavior at low T. The dashed line is a linear fit to the data for the $x = 0.983$ sample below 50 K.

Considering the above results, one can expect spin polarization to play an impor-

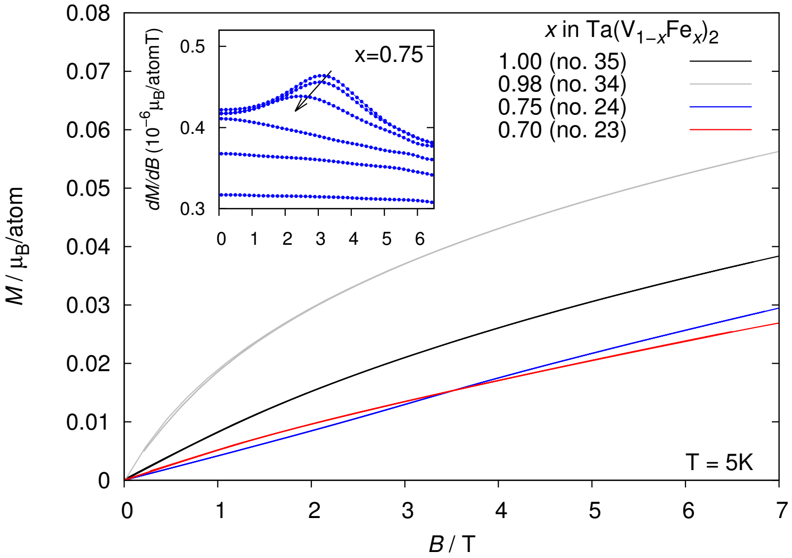

Figure 6.17: Magnetization taken at 5 K of two paramagnetic samples with $x = 1$ and 0.701, and an AFM sample with $x = 0.749$ and $T_N = 18$ K. Inset: Field derivative of the magnetization at different temperatures (2, 5, 10, 20, 30, 50 K) inside and outside the AFM phase for the sample with $x = 0.749$: The arrow indicates how the critical field which suppresses the AFM state shifts to lower values with increasing temperature.

tant role in the stability of these compounds. However, due to the large number of structural and magnetic configurations and the increased computation times, spin polarization was not included in the calculations up to now. One cheap approach could be to repeat the calculations only for the stable configuration of each composition and introduce magnetism only for these calculations. However, it is unlikely, that the stable nonmagnetic configurations remain the stable configurations if magnetism is introduced. Thus, all configurations for each composition have to be recalculated. The measurements revealed the Fe-rich samples of C14 Ta($V_{1-x}Fe_x$)$_2$ to be antiferromagnetic. Thus, the initial magnetic structures for the calculations should be also antiferromagnetic. If one considers antiferromagnetism in the 24-atom 2 x 1 x 1 supercell of TaFe$_2$, eight spin up (↑) and eight spin down (↓) have to be distributed among the 16 Fe sites. From section 4.1 one can calculated that this will result in 12870 possible magnetic configurations with 776 of those being unique. This means 776 calculations are necessary to find the magnetic ground state structure only for TaFe$_2$. If Ta($V_{1-x}Fe_x$)$_2$ with $x = 0.8125$ is considered, there are 48 unique structural configurations, each having 1716 possible magnetic configurations. It is thus evident, that the consideration of antiferromagnetism in

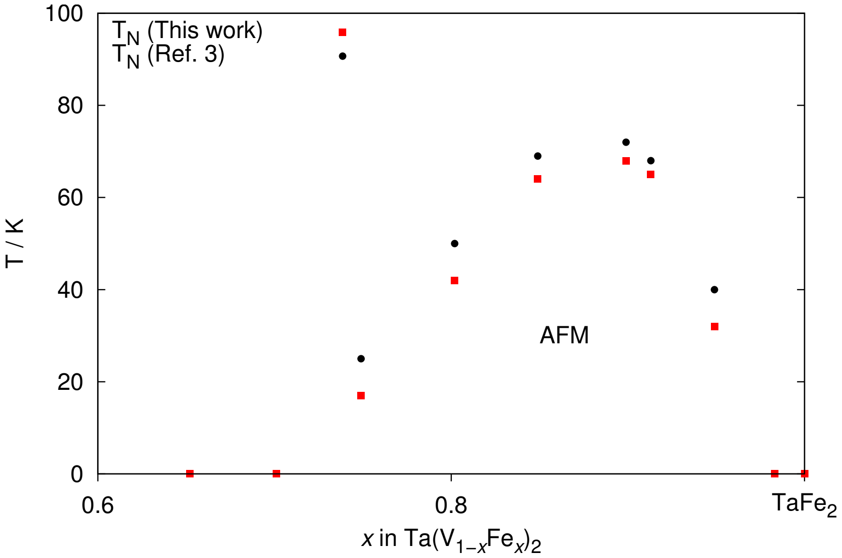

Figure 6.18: Magnetic phase diagram of C14 Ta(V_{1-x}Fe$_x$)$_2$. The red points have been obtained from dc susceptibility measurements with $B = 1\,\mathrm{T}$, whereas the black points are taken from reference [3].

the present calculational scheme is not feasible. Furthermore, a single calculation incorporating magnetic spin polarization will take approximately three times as long as without magnetism.

However, to investigate the influence of magnetism on the results of the calculations one can initially introduce ferromagnetism as an approximation. For each structural configuration there is only one magnetic configuration. Therefore, from TaFe$_2$ ($x = 1$), up to $x = 0.6875$ all configurations (502 in total) were repeatedly calculated taking ferromagnetism into account[3]. The calculations will thus cover the compositional range where magnetism is also found experimentally. The calculations were performed for the C14 as well as for the C15 structure type. The results are discussed in the following.

Figure **6.19** shows the total energy values of the stable configurations for the magnetic and the nonmagnetic calculations. The corresponding data can be found

---

[3] Magnetism in the present calculations regards only to spin magnetism. Spin-orbit coupling which couples the magnetic spin to the crystal structure is only implemented as beta feature in VASP 4.6.35. In the most recent version 5.2.2 it is regarded as final. Thus, the total energy does not depend on the direction of the magnetic moment but only on its absolute value, i.e. rotating all magnetic moments by the same angle results in the same energy. This approximation is adequate since $3d$ transition elements show only spin magnetism with nearly no contribution from orbital motion [152].

in the appendix A.3 in table **1.18**. The magnetic calculations are lower in energy

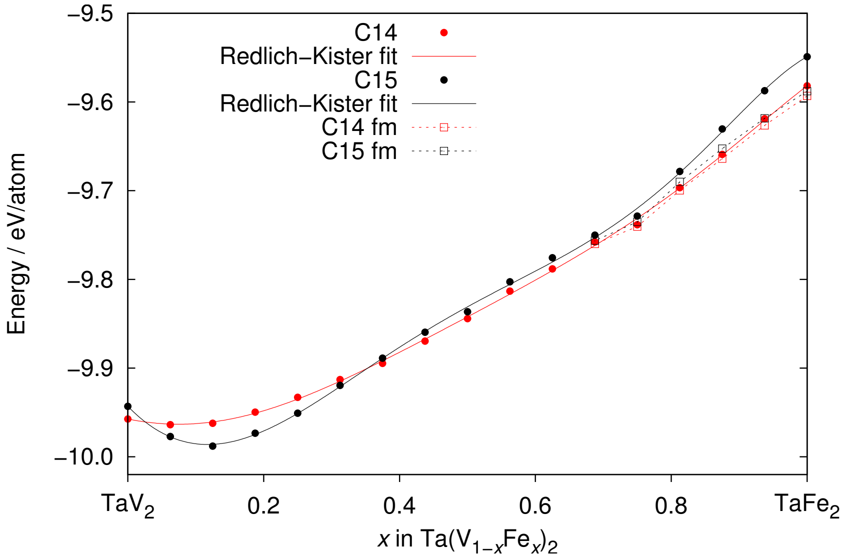

Figure 6.19: Total energy values of the stable configurations of C15 and C14 Ta($V_{1-x}$$Fe_x$)$_2$ for the magnetic and the nonmagnetic calculations.

compared to the nonmagnetic calculations for both C14 and C15 structures. The decrease is however much stronger for the C15 structure type. The differences between magnetic and nonmagnetic calculations are getting smaller with decreasing Fe content due to the reduction of magnetic Fe atoms. For $x = 0.6875$ there is almost no difference in energy. This is in good agreement with the experiment which shows no magnetic ordering for samples with $x \leq 0.7$. The Gibbs energy values calculated from the total energy are accordingly lower for the magnetic calculations. They are shown in figure **6.20**. The corresponding data can be found in the appendix A.3 in table **1.19**. Especially for C15 a drastic decrease of the energy is observed while C14 is still the stable structure type. Due to the small amount of data points they are not fitted but connected by (dashed) lines. However, from the trend of this few points one can draw conclusions on the development of the homogeneity ranges. Since the magnetic values are lower in energy, the fitted G curves on the Fe-rich side would be accordingly lower. Thus, the slope of the common tangent will increase which results in a shift of the contact points of the common tangent with the G curves to the left (in the direction of TaV_2). This causes the C15 phase field to shrink and the C14 phase field to grow and thus improves the agreement with the experimental data.

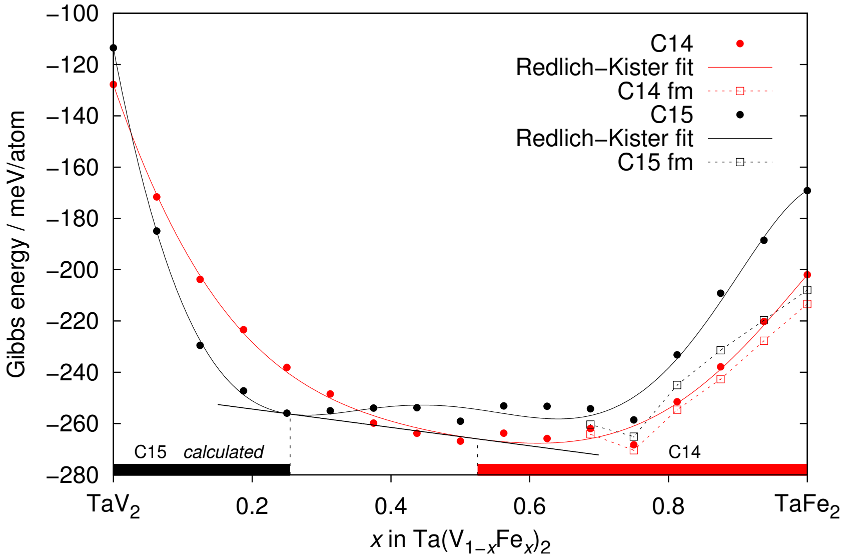

Figure 6.20: Gibbs energy G of the stable configurations of C15 and C14 $Ta(V_{1-x}Fe_x)_2$ for the magnetic and the nonmagnetic calculations. The bottom bars indicate the calculated homogeneity ranges of the C14 and C15 phases from the nonmagnetic calculations. The dashed lines mark the contact points of the common tangent with the G curves.

The results for the lattice parameters and c/a ratio of the C14 phase are plotted in figure **6.21**. The black curves represent the ferromagnetic calculations, while the red curves show the results of the nonmagnetic calculations. The values for the long a axis of the $2 \times 1 \times 1$ supercell do not change while the short b axis is expanding. Thus, the values for $(a + b)/2$ in the ferromagnetic calculations are slightly larger than in the nonmagnetic case. This is however compensated by the applied shift, since the linear behavior is maintained. For clarity, the individual lattice parameters a and b are not shown in subfigure (a), but only $(a + b)/2$. The agreement between calculated and experimental c lattice parameter does improve markedly if magnetism is considered as shown in subfigure (b). The local maximum at $x = 0.75$ disappears and the value for $TaFe_2$ is much higher and now fits the experimental data. The required shift to scale the calculated data is slightly reduced from 0.06 to 0.05 Å. Also the slope of the calculated curve does now agree with the experimental values. As a result, the c/a ratio shows the opposite behavior compared to the nonmagnetic calculations and is in better agreement with the experiment. From a high value for $TaFe_2$ c/a decreases with increasing V content. A minimum is observed around $x = 0.8$ in accordance with

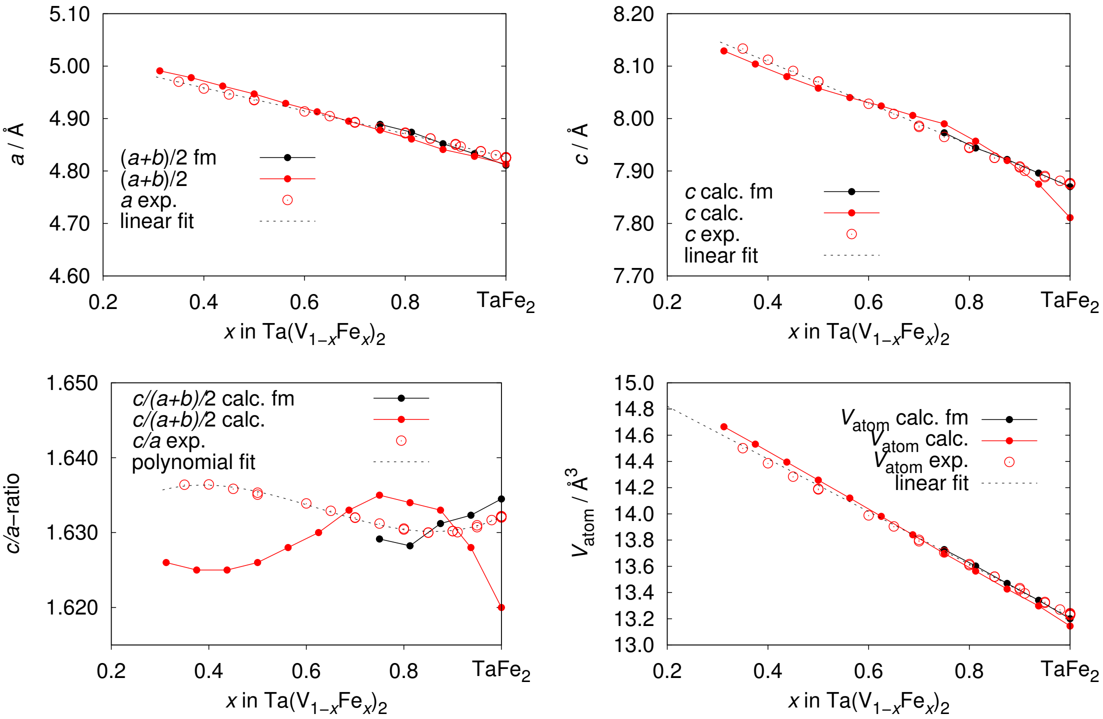

Figure 6.21: Calculated lattice parameters a and c, axial ratio c/a and mean atomic volume for C14 Ta$(V_{1-x}Fe_x)_2$ with (red) and without (black) considering ferromagnetic ordering of the Fe atoms.

the experimental curve. The absolute values do still differ slightly, but the overall curve shape is correctly reproduced. The mean atomic volume undergoes virtually no change, only the required shift is somewhat reduced.

The results presented above show clearly that the deviations observed between experimental and calculated values in section 6.3 are due to the disregardance of the magnetic interactions, at least on the Fe rich side of the binary section TaV_2–$TaFe_2$. Since the incorporation of ferromagnetism is only an approximation to the experimentally observed antiferromagnetism, it can be expected, that the results will further improve if the correct magnetic structures are used.

6.5 Summary

The calculations for C14 Ta$(V_{1-x}Fe_x)_2$ predict a preferential site occupation of Fe and V with a site occupation reversal. In contrast to Nb$(Cr_{1-x}Co_x)_2$ the minority component preferentially occupies the 6h site of the crystal structure. The calculated stability ranges are qualitatively in agreement with the experimental results. $TaFe_2$ crystallizes in the hexagonal C14 structure type with a large solubility of up to 43 at.% V ($x = 0.35$). TaV_2 crystallizes in the cubic C15 structure type with a smaller homogeneity range. It can dissolve up to 8 at.% Fe ($x = 0.125$). A new true ternary Laves phase with the hexagonal C36 structure type and a small homogeneity range of approximately $0.29 \leq x \leq 0.32$ is observed experimentally. The single phase fields along the quasi-binary section TaV_2 – $TaFe_2$ are separated by a larger and a smaller two-phase region between C15/C36 (11 at.% Fe) and C36/C14 (∼2 at.% Fe), respectively. The calculations predict an additional phase transition C15→C14 for $Ta(V_{1-x}Fe_x)_2$ at very low Fe contents close to TaV_2 which is not observed experimentally. A theoretical investigation of the stability of C36 can not be provided by the calculations due to the narrow homogeneity range of the C36 phase and the small number of theoretical data points. The agreement of the lattice parameters obtained from the nonmagnetic calculations is not satisfactory. The mean atomic volume as well as the lattice parameters differ in the slope and the c lattice parameter shows significant deviations from the experiment close to $TaFe_2$. The calculated curve shape of the c/a ratio is in contradiction to the experimental results.

When magnetism is taken into account the results improve markedly. The agreement of calculated and experimental lattice parameters is significantly better, particularly near $TaFe_2$. The shape of the c/a ratio now shows the experimentally observed behavior. The agreement of the C14 and C15 homogeneity ranges is improved with respect to the experimental results, while the general stability of the polytypes does not change.

7 Site occupation in other ternary C14 Laves phases

7.1 $Zr(V_{1-x}Co_x)_2$

The ternary phase diagram of the Co–V–Zr system shows some marked similarities with that of the Co–Cr–Nb system. The two terminal phases ZrV_2 and $ZrCo_2$ crystallize with the cubic C15 structure and a new true ternary Laves phase with the hexagonal C14 structure type and a large homogeneity range is formed along the binary section ZrV_2–$ZrCo_2$ [153]. A phase diagram of this section is shown in figure **7.1** [154]. The homogeneity ranges at 1000 °C according to this phase diagram are listed in table **7.1**. Homogeneity ranges for the complete binary section were also reported by Elliot and Rostoker [145] at 1100 °C and by shaltiel *et al.* [155] at 900 °C. With this broad homogeneity range of the C14 phase, $Zr(V_{1-x}Co_x)_2$ is another promising example to study the site occupation behavior in C14 phases and to verify the reliability of the types of calculations presented in this work. Experimental work in this system was carried out already in 1963 by Faller and Skolnick [48]. They investigated the distribution of Co and V over the non-equivalent crystallographic sites in C14 $Zr(V_{1-x}Co_x)_2$ by an anomalous X-ray scattering technique. Six alloys across the pseudobinary section ZrV_2–$ZrCo_2$ revealed a non-random composition dependent distribution of the V and Co atoms among the $2a$ and $6h$ sites. At high V content, Co preferentially occupies the $6h$ sites and V the $2a$ sites. At low V content the reverse is observed. In other words, the minority component preferentially occupies the $6h$ site. This is the opposite behavior as observed for C14 $Nb(Cr_{1-x}Co_x)_2$ where the minority component preferentially occupies the $2a$ site. The experimental site occupation factors at 1000 °C for Co in C14 $Zr(V_{1-x}Co_x)_2$ from reference [48] are listed in table **7.2** and plotted in figure **7.2**. These values however are flawed with large errors and have to be used with care. For example, the experimentally obtained occupation with Co on the 6*h* site of 0.384 for the first data point is higher than theoretically possible (0.267) for the respective composition. The same is true for the second data point. Data point number five shows a rather strong deviation from the trend. Therefore the first two data points are corrected to the maximum possible values while the fifth data point is not included in the following. Nevertheless, the effect of a site occupation reversal with the minority component preferentially occupying the 6*h* site is clearly observable from the data. Site occupation reversal occurs at around $x = 0.5$.

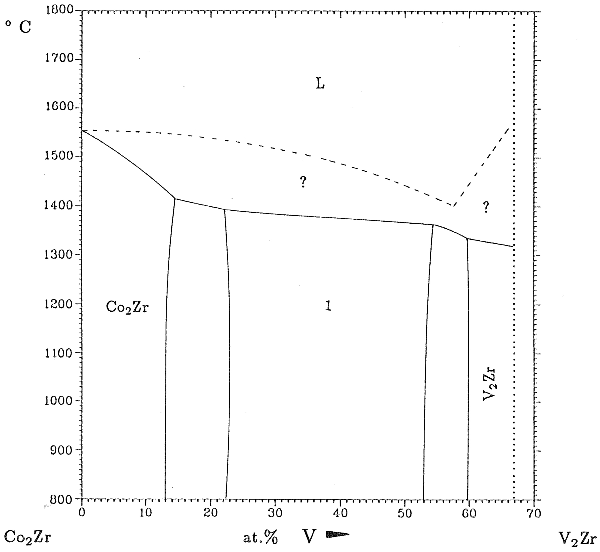

Figure 7.1: The binary section ZrV_2–$ZrCo_2$ [154]. The order of ZrV_2 and $ZrCo_2$ is inverted compared to the convention used in this work.

$0.0 \leq$	x	< 0.1:	C15
$0.1 \leq$	x	< 0.2:	C15 + C14
$0.2 \leq$	x	< 0.66:	C14
$0.66 \leq$	x	< 0.8:	C14 + C15
$0.8 \leq$	x	≤ 1.0:	C15

Table 7.1: Homogeneity ranges of C15 and C14 in $Zr(V_{1-x}Co_x)_2$ as a function of x at 1000 °C.

After successfully computing the site occupation in C14 $Nb(Cr_{1-x}Co_x)_2$ where the minority component preferentially occupies the 2*a* site, it is interesting whether or not the calculations can yield the correct results for a system with the opposite site occupation behavior. It was already shown in the diploma thesis of the current author [136] that full-potential FPLO calculations without any structural relaxation already yield qualitatively correct results. In this work the calculations where carried out with the pseudopotential code VASP with full structural relaxation. The results for both types of calculation are shown in figure **7.2**. The site occupation

Table 7.2: Experimental [48] and calculated Site occupation factors for Co in C14 $Zr(V_{1-x}Co_x)_2$.

x	*s.o.f.* Co (2a)	*s.o.f.* Co (6h)
Experimental		
0.2	0.0	0.384 ± 0.062
0.3	0.0	0.403 ± 0.023
0.4	0.28	0.440 ± 0.033
0.5	0.812	0.396 ± 0.040
0.6	0.714	0.562 ± 0.036
0.7	0.829	0.657 ± 0.030
FPLO		
0.250	0.083	0.306
0.375	0.304	0.399
0.500	0.509	0.497
0.625	0.651	0.616
0.750	0.837	0.721
VASP		
0.125	0.104	0.132
0.250	0.083	0.306
0.375	0.148	0.451
0.500	0.396	0.535
0.625	0.703	0.599
0.750	0.858	0.714
0.875	0.944	0.852

values have been calculated at 1000 °C to match the experimental conditions.

Both types of calculations yield results in very good agreement with the experimental data. The type of preferential occupation with the minority component on the 6h site is correctly reproduced. The FPLO data behave more like straight lines with a crossing point at $x = 0.5$ perfectly capturing the experimental point of site occupation reversal. The VASP data, which also include structural relaxation show an ever better agreement. It nicely reflects the shape of the two curves of the 2a and 6h occupation. The point of site occupation reversal is only slightly shifted to $x = 0.55$. In both cases, the values for the 2a occupation at $x = 0.2$ and 0.3 are not in agreement which can however most probably be attributed to the erroneous experimental data. In summary, it can be stated that the calculations

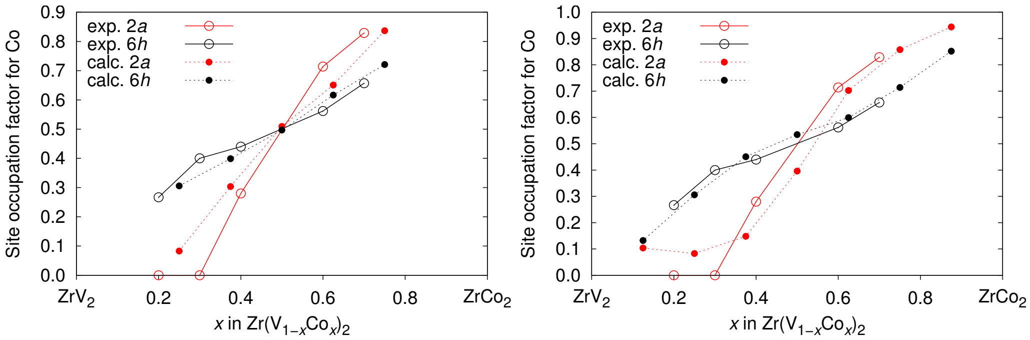

Figure 7.2: Site occupation of Co in C14 $Zr(V_{1-x}Co_x)_2$ at 1000 °C calculated with two different DFT codes, FPLO (left) and VASP (right). The corrected experimental values (see text) have been used for these figures.

are well suitable to predict the site occupation behavior in this compound.

7.2 Nb($Ni_{1-x}Al_x$)$_2$

The Al–Nb–Ni system was studied by YAN *et al.* [71]. They investigated ten alloys of Nb($Ni_{1-x}Al_x$)$_2$ in the range of $0.15 \leq x \leq 0.85$ by means of X-ray powder and single-crystal diffraction, optical microscopy and electron probe microanalysis. They found a new true ternary C14 Laves phase Nb($Ni_{1-x}Al_x$)$_2$ and investigated its crystal structure details. This C14 phase is unusual because neither $NbNi_2$ nor $NbAl_2$ exist as binary Laves phases. X-ray powder diffraction and electron probe microanalysis revealed almost single phase C14 type Laves phases for specimens annealed at 1000 °C with a large homogeneity range of $0.23 \leq x \leq 0.77$ with traces of a secondary phase. The site occupation factors for Ni and Al were determined from Rietveld refinements. As the heavy scatterers, the Nb atoms are undoubtedly located on the $4f$ sites, whilst Ni and Al atoms randomly share the $2a$ and $6h$ sites at different mixing levels. The experimental and calculated site occupation factors are compiled in table **7.3**. A graphical representation is given in figures **7.3** and **7.4**.

Table 7.3: Experimental [71] and calculated site occupation factors for Al in C14 Nb($Ni_{1-x}Al_x$)$_2$.

x	*s.o.f.* Al ($2a$)	*s.o.f.* Al ($6h$)	*s.o.f.* Al ($2a$)	*s.o.f.* Al ($6h$)
Experimental				
0.228	0.350(10)	0.165(7)		
0.306	0.435(10)	0.277(7)		
0.383	0.385(10)	0.375(5)		
0.461	0.425(5)	0.470(2)		
0.539	0.450(5)	0.563(3)		
0.617	0.580(5)	0.640(3)		
0.695	0.760(5)	0.668(5)		
0.772	1.000	0.720(5)		
VASP	nonmagnetic		ferromagnetic	
0.125	0.063	0.146	0.067	0.144
0.250	0.181	0.273	0.322	0.226
0.375	0.023	0.493	0.333	0.389
0.500	0.640	0.453	0.236	0.588
0.625	0.849	0.550	0.845	0.552
0.750	0.827	0.725	0.990	0.670
0.875	0.809	0.897	0.811	0.897

The site occupation of Al in C14 Nb(Ni$_{1-x}$Al$_x$)$_2$ is quite unusual. At low Al contents the Al atoms prefer the 2*a* site. At $x = 0.38$ a site occupation reversal occurs and now the 6*h* is preferred. However, another site occupation reversal occurs at $x = 0.65$ and again 2*a* becomes the preferred site for Al atoms. This is in other words a case of preferential site occupation with two points of site occupation reversal, the only reported case as far as known by the author.

It will thus be very interesting to calculate the site occupation factors for Al in C14 Nb(Ni$_{1-x}$Al$_x$)$_2$ and compare them with the experimentally obtained values. This calculations were carried out with VASP and the results are plotted in figure **7.3**.

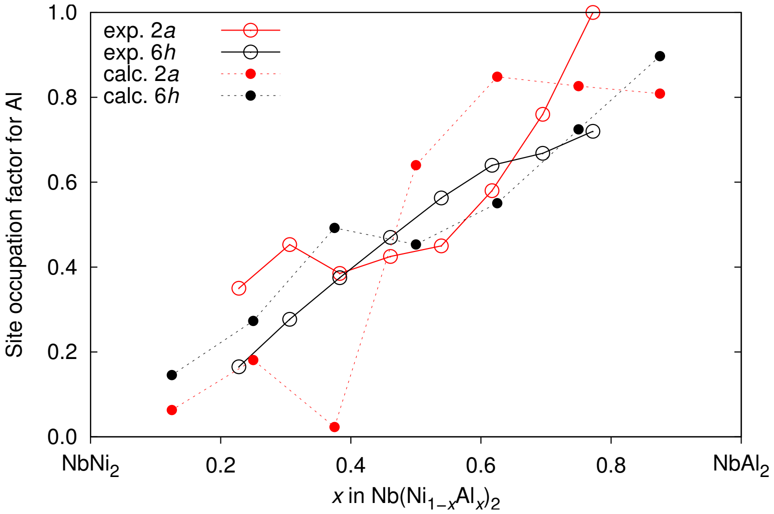

Figure 7.3: Calculated nonmagnetic versus experimental site occupation factors for Al in C14 Nb(Ni$_{1-x}$Al$_x$)$_2$.

At first glance the calculated results look promising since they predict two points of site occupation reversal just as observed experimentally. However the actual preferred site for Al does not agree with the experimental values. At low Al contents the 6*h* site is preferred while it is the 2*a* site experimentally. And also for all other compositions the calculated results show nearly the opposite behavior as observed experimentally. A reason for this discrepancy might again be the disregardance of magnetism in the calculations. Ni as an element is ferromagnetic, while nothing is known about the magnetic properties of C14 Nb(Ni$_{1-x}$Al$_x$)$_2$. Thus, the above calculations were repeated taking magnetism into account. An initial magnetic moment of $1\,\mu_B$ was applied to all Ni atoms in a ferromagnetic arrangement. The results of these calculations are plotted in figure **7.4**. The shape

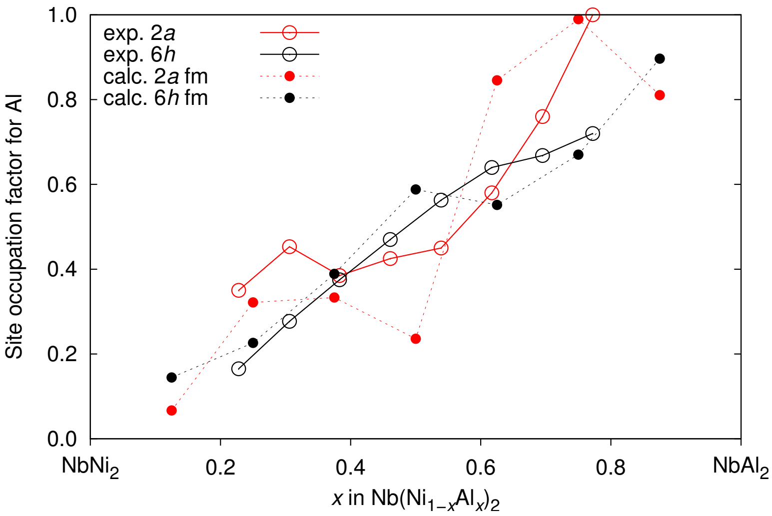

Figure 7.4: Calculated site occupation factors considering ferromagnetic ordering versus the experimental values for Al in C14 $Nb(Ni_{1-x}Al_x)_2$.

of the calculated curves is still far from matching the experimental values but they are now in much better agreement than without magnetism. The calculated curves shows four points of site occupation reversal, two of which lie outside the experimental homogeneity range of the C14 phase. The two inner reversal points agree with the experimental data. They are only shifted to slightly lower Al concentrations. The observed trends are now correct: at low Al concentration the $2a$ site is preferred, at concentrations of Ni and Al around 1:1 its the $6h$ site and for Al-rich samples its again the $2a$ site.

The incorporation of magnetic moments into the calculations was able to markedly improve the agreement with the experimental results. However, since no experimental data is available on the magnetism in C14 $Nb(Ni_{1-x}Al_x)_2$ the results of these calculations are only of theoretical nature.

7.3 $Nb(Al_{1-x}Cr_x)_2$

The Laves phases in the Al–Cr–Nb system were investigated by Prymak *et al.* [67,156]. Based on the new experimental data a thermodynamical assessment of the phase diagram using the CALPHAD technique was performed by He *et al.* [157]. Reference [158] gives an overview about the recent data on the Al–Cr–Nb system. An isothermal section at 1150 °C is shown in figure **7.5**. The cubic C15 Laves

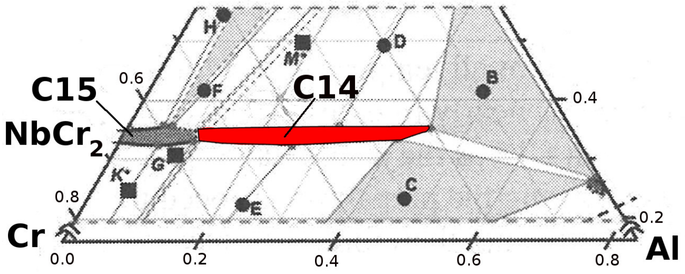

Figure 7.5: Part of an isothermal section of the Al–Cr–Nb system at 1150 °C [67]. The C14 phase field is shown in red.

phase $NbCo_2$ can dissolve up to 12 at.% Al at 1150 °C [67] followed by a small two-phase field C15/C14 of approximately 2 at.% Al. A true ternary C14 Laves phase $Nb(Al_{1-x}Cr_x)_2$ is forming with a large homogeneity range extending from 14 to 45 at.% Al. No Laves phase exists in the binary system Al–Nb.

The site occupation factors of Al and Cr in the C14 phase were determined by Rietveld refinements on samples quenched at 1150°C. According to the phase diagram, the C14 phase shows a homogeneity range for Nb with a maximum value of approximately 1.5 at.%. All refinements were carried out on two-phase samples, either on the Nb-rich (>33.3 at.% Nb) or on the Nb-poor side (<33.3 at.% Nb). Thus, the refined site occupation factors are expected to be biased by the varying Nb content. The refinements indicate a preferential occupation of the Cr atoms on the $6h$ and the Al atoms on the $2a$ site along the entire homogeneity range of the C14 phase. This is also valid for samples quenched at 1450°C.

Since all C14 Laves phases investigated in this work so far exhibited a site occupation reversal, C14 $Nb(Al_{1-x}Cr_x)_2$ is the first example without such a reversal. Thus, it is of interest if the calculations are able to predict the correct behavior. The site occupation factors have been computed using FPLO and VASP. The results are plotted together with the experimental data in figure **7.6**.

There is a big difference between the results of the two types of calculations. The FPLO data show no site occupation reversal with a preferential occupation of the Cr atoms on the $6h$ site and are thus in agreement with the experimental results. Although, there are strong deviations for the $2a$ site occupation at high Cr concentrations. The VASP results however, show a completely different picture with a site occupation reversal at $x = 0.5$ and preferential occupation of the minority component on the $2a$ site. This discrepancy is very unusual since for

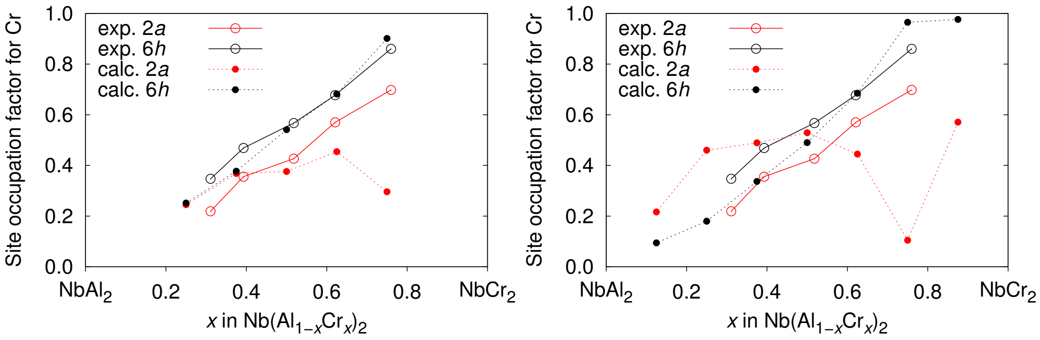

Figure 7.6: Site occupation factors for Cr in C14 Nb(Al$_{1-x}$Cr$_x$)$_2$ calculated with FPLO (left) and VASP (right).

all other calculations in this work no such fundamental difference between the two methods was observed. A reason for the wrong VASP results might again be the disregardance of magnetism, although the FPLO calculations were carried out nonmagnetic as well. Chromium is an antiferromagnet in its elemental form. C15 NbCr$_2$ was however reported to be more stable as a paramagnet as compared to an antiferromagnet [159] and no data on the magnetic properties of the ternary C14 phase Nb(Al$_{1-x}$Cr$_x$)$_2$ are available. To clarify this, the VASP calculations have been repeated with an initial magnetic moments on the Cr atoms in a ferromagnetic ordering. However, all calculations converged into a pure paramagnetic state. The resulting site occupation factors are equal to those obtained from the nonmagnetic calculations. Thus, in the case of C14 Nb(Al$_{1-x}$Cr$_x$)$_2$ the VASP calculations fail to yield results in agreement with the experimental data. Furthermore, the VASP results are completely different from the FPLO results.

7.4 Preferential site occupation – influence of the A atom

The site occupation behavior of many C14 Laves phases $A(B'_xB''_{1-x})_2$ in different systems is reported in the literature and has been discussed in this work. Quantum mechanical calculations combined with a statistical mechanics approach were used to compute the site occupation of some of the reported phases and the results have been compared with experimental findings. The computed results are generally in good agreement with the experiment. However, the fundamental reasons for the preferential occupation of a given atomic species on a specific crystallographic site is still unclear. One attempted explanation are nearest neighbor or pair interactions between B' and B'' atoms. The assumption is, that either like contacts B'-B' and B''-B'' or mixed contacts B'-B'' are energetically favored. And since the atomic environment around a $2a$ site differs from that around a $6h$ site, a species B' will prefer one of those sites over the other resulting in a preferential site occupation. The A atoms which ideally only and exclusively occupy the $4f$ sites of the crystal structure seem to be irrelevant in this approach. In order to investigate the influence of the A atoms and if B' and B'' pair interactions are the determining factor for preferential site occupation and site occupation reversal, the site occupation factors for nine different C14 Laves phases were computed. These are:

$$\begin{array}{lll} \mathrm{Zr(Cr_{1-x}Co_x)_2} & \mathrm{Zr(Al_{1-x}Cr_x)_2} & \mathrm{Zr(Al_{1-x}Co_x)_2} \\ \mathrm{Nb(Cr_{1-x}Co_x)_2} & \mathrm{Nb(Al_{1-x}Cr_x)_2} & \mathrm{Nb(Al_{1-x}Co_x)_2} \\ \mathrm{Ta(Cr_{1-x}Co_x)_2} & \mathrm{Ta(Al_{1-x}Cr_x)_2} & \mathrm{Ta(Al_{1-x}Co_x)_2} \end{array}$$

The results of these calculations are compiled in figure **7.7**. Each column of this 3x3 matrix contains the same B' and B'' atoms with different A atoms, while the lines contain the same A atom with varying B' and B'' atoms. Based on the site occupation behavior of these nine compounds it is possible to draw conclusion regarding the influence of the A atoms and the importance of the B'–B'' atom interactions on a very basic level.

The shape of the $6h$ curve can be described as approximately linear for all systems. Thus, the site occupation behavior and the presence of a site occupation reversal is mainly determined by the shape of the $2a$ curves. At least one site occupation reversal is observed for all systems. The first column of figure **7.7** contains Zr, Nb and Ta as A and Cr and Co as B' and B'' atoms. The shape of the curves is very similar to each other for all three systems. The different A atoms merely cause a shift of the two curves $2a$ and $6h$ toward or away from each other. This is especially clear for Nb and Ta as A atoms. For Ta the shift toward each other causes another crossing point of the $2a$ and $6h$ curves. A similar situation is observed in the second and the third column with Al and Cr, and Al and Co as B atoms, respectively. The $2a$ and $6h$ curves have the same shape and are shifted toward or away from each other. From the latter examples one could estimate that in general the B' and B'' atoms determine the shape of the $2a$ and $6h$ curves while the A atoms cause a small shift of those curves. However, Zr is an exception in all three columns. The obtained curve shapes for Zr differ from those with Nb or Ta. The reason for this strong influence of Zr are not known. It is therefore evident, that both A and B atoms have an effect on the site occupation behavior and it is not possible to make unambiguous statements regarding their particular influence.

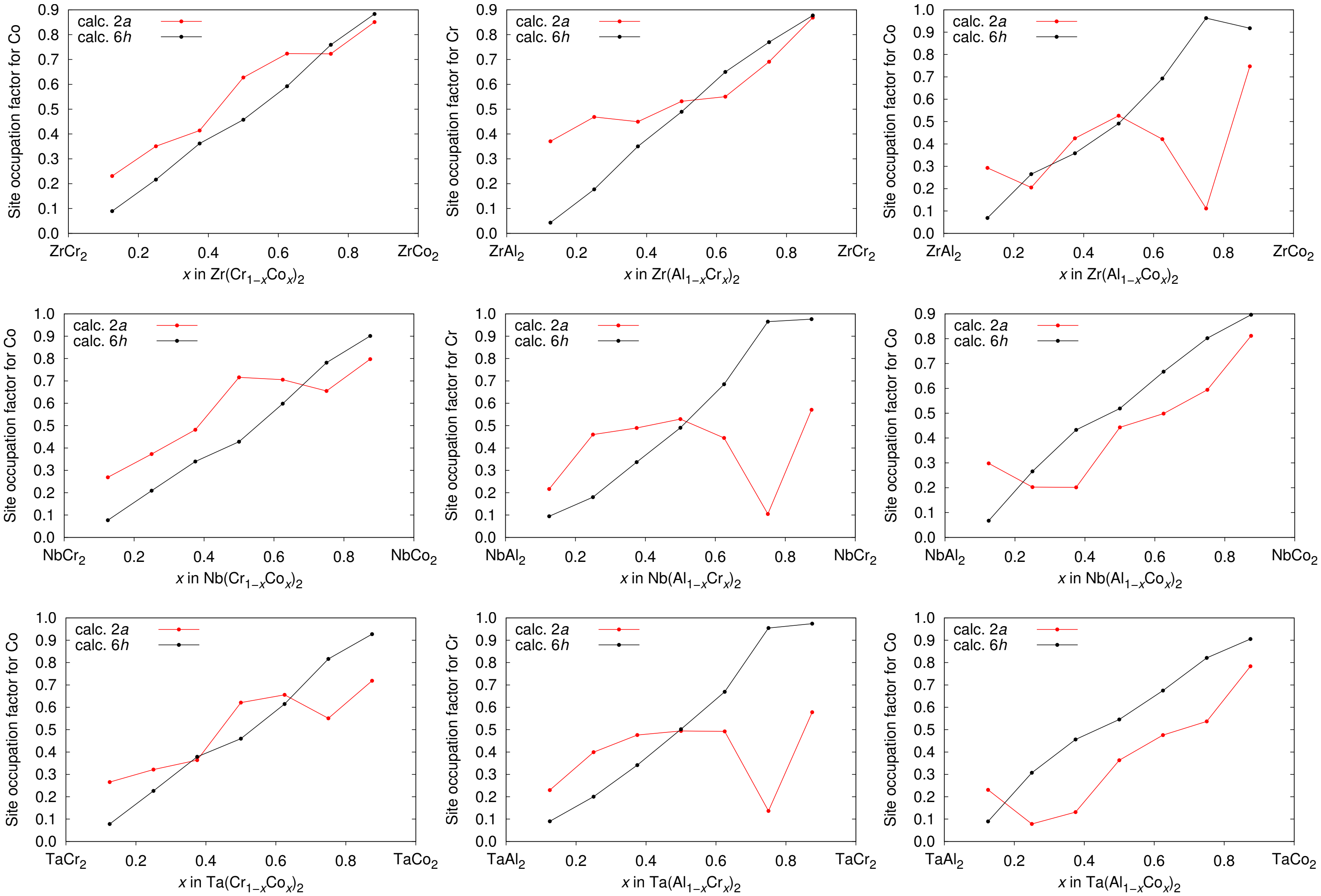

Figure 7.7: Calculated site occupation factors for nine different C14 Laves phases (Zr,Nb,Ta)((Cr,Al)$_{1-x}$(Co,Cr)$_x$)$_2$.

8 Summary

The aim of this study was to investigate and understand the phenomenon of substitutional disorder in binary and ternary Laves phases. This includes the experimental investigation and the theoretical modeling of firstly, the composition dependent stability of the various polytypes of Laves phases, their homogeneity ranges and lattice geometries and secondly, the actual distribution of the alloying elements in the crystal structure of the investigated compounds. To achieve this, theoretical and experimental methods were applied and the results of both were compared with each other. An important objective was to check the applicability of various approximations which allow to predict the phase stability and the distribution of atoms with the help of quantum mechanical calculations. Although, calculations based on specific approximations cannot replace experiments regarding reliability and precision, they might help to reduce the number of required samples and they are a way for the understanding of the chemical and physical behavior. The results obtained from the calculations in the form of composition dependent enthalpies of formation can be interpreted as stability criteria of the Laves phase polytypes. They can further be used as input data for CALPHAD, and thus drastically reduce the experimental effort.

The ternary systems Co–Cr–Nb and Fe–Ta–V with the two quasi binary sections $\mathrm{Nb(Cr_{1-x}Co_x)_2}$ and $\mathrm{Ta(V_{1-x}Fe_x)_2}$ were chosen as examples to carry out the investigations. A large number of alloys with compositions of $0 \leq x \leq 1$ were synthesized in both systems and the obtained specimens were investigated using XRPD, SEM, EDXS, WDXS, DTA, single crystal structure analysis, metallographic examinations and magnetization measurements. In addition to this, quantum mechanical calculations were performed and the results of both experiments and calculations were compared with each other.

Another major focus of this study was to examine the substitution type in form of the site occupation factors in ternary C14 Laves phases. They were investigated theoretically and experimentally in $\mathrm{Nb(Cr_{1-x}Co_x)_2}$ and $\mathrm{Ta(V_{1-x}Fe_x)_2}$. Further theoretical work was done on several other C14 Laves phases based on experimental results found in the literature. The unusual composition dependent behavior of the c/a ratio of the lattice parameters in hexagonal C14 Laves phases was also discussed.

In the Co–Cr–Nb system the experimental results were obtained first. The subsequent calculations were supposed to show whether they are able to reproduce the experimental results correctly. For $\mathrm{Nb(Cr_{1-x}Co_x)_2}$, the experimental and theoretical results consistently prove the stability of the two binary phases $\mathrm{NbCr_2}$ and $\mathrm{NbCo_2}$ in the cubic C15 structure type with only narrow homogeneity ranges. For compositions in the range of $0.127(3) \leq x \leq 0.937(3)$ a new true ternary Laves phase with the hexagonal C14 structure type is forming with a large homogeneity range. The calculations yielded a homogeneity range slightly shifted to higher Co concentrations with values of $0.14 \leq x \lesssim 0.96$. Narrow C14/C15 two-phase regions separate the C14 from the C15 phases in agreement with the calculations. The mean atomic volume, the lattice parameters and also the unusual S-shape of the c/a ratio within the stability range of the C14 structure type are qualitatively reproduced by the calculations. The range of values and especially the minimum of the c/a ratio at approximately 80% Co ($x = 0.8$) is well captured. The site occupation factors of Cr and Co on the two crystallographic sites $2a$ and $6h$ were obtained from single crystal structure analysis of samples with the hexagonal C14 structure type. They show the phenomenon of preferential site occupation with a site occupation reversal, where the minority component is preferentially occupying the $2a$ site. The calculated site occupation factors confirm the experimentally observed behavior and the existence and the type of site occupation reversal. Depending on the type of calculation, the point of site occupation reversal is shifted by $x = 0.08 - 0.14$ to higher Co concentrations.

The Fe–Ta–V system represents a more complicated system due to the magnetic properties of $\mathrm{TaFe_2}$ and $\mathrm{Ta(V_{1-x}Fe_x)_2}$ at low V concentrations. The magnetic properties of these compounds are not yet fully understood and they represent a special challenge for the calculations. In addition, no literature data is available on the ternary phase diagram and no ternary phases are reported. Thus, in order to obtain predictions concerning the stable polytypes and their homogeneity ranges the calculations in the Fe–Ta–V system were performed before the experiments. They were first carried out non-magnetic, spin polarization was subsequently introduced in the calculations with the simplified assumption of ferromagnetism. The calculated results were then checked by experimental work. In the case of $Ta(V_{1-x}Fe_x)_2$, the calculations also predict preferential site occupation with a site occupation reversal. In this case, however, the minority component preferentially occupies the 6*h* site of the crystal structure. A similar behavior as for example in $Zr(V_{1-x}Co_x)_2$, but the opposite as observed for $Nb(Cr_{1-x}Co_x)_2$ where the minority component preferentially occupies the 2*a* site. Unfortunately, no experimental data for $Ta(V_{1-x}Fe_x)_2$ is available to confirm this behavior. The calculated stability ranges of the Laves phase polytypes are in qualitative agreement with the experimental results obtained at 1150 °C. $TaFe_2$ crystallizes in the hexagonal C14 structure type with a large solubility of up to 43 at.% ($x = 0.35$) for the ternary element V. TaV_2 crystallizes in the cubic C15 structure type with a smaller homogeneity range. It can dissolve up to 8 at.% ($x = 0.125$) Fe. In addition, a new true ternary Laves phase with the hexagonal C36 structure type and a small homogeneity range of approximately $0.29 \leq x \leq 0.32$ is observed experimentally. Experimental investigations of the C36 phase are challenged by its small homogeneity range, the strong overlap of Bragg peaks with those of neighboring phases in X-ray powder diffraction and the low phase contrast in light optical as well as scanning electron microscopy. The single phase fields along the quasi-binary section TaV_2 – $TaFe_2$ are separated by a larger and a smaller two-phase region between C15/C36 (11 at.% Fe) and C36/C14 (~2 at.% Fe), respectively. The calculations predict an additional phase transition C15→C14 for $Ta(V_{1-x}Fe_x)_2$ at very low Fe contents close to TaV_2 which is not observed experimentally. However, it is known that pseudopotential calculations tend to make wrong predictions in the case of V containing Laves phases. A theoretical investigation of the stability of C36 can not be provided by the calculations due to the narrow homogeneity range of the C36 phase and the small number of theoretical data points. Furthermore, the calculated energy differences for the C14 and the C36 phase in the compositional range around $x = 0.3125$ are too small to draw a clear conclusion regarding the stability of C14 and C36. The agreement of the lattice parameters is also not satisfactory. The mean atomic volume as well as the lattice parameters differ in the slope and the *c* lattice parameter shows significant deviations from the experiment close to $TaFe_2$. The curve shape of the calculated c/a ratio shows even the opposite behavior compared to the experimental results.

When the magnetic properties of Fe and $TaFe_2$ are taken into account in the calculations of $Ta(V_{1-x}Fe_x)_2$, the obtained results improve markedly. The agreement of the calculated and the experimental lattice parameters improves significantly, particularly near $TaFe_2$. The shape of the c/a ratio curve which is wrong in the non-magnetic calculations, now properly shows the experimentally observed behavior. The agreement of the C14 and C15 homogeneity ranges is improved with respect to the experimental results, while the general stability of the polytypes does not change.

The small energy differences in the calculations between the three Laves phase polytypes pose a basic problem for this type of calculations. On the one hand, they are the reason for the experimentally observed strong temperature and composition dependence of the Laves phase polytypes and the fact that two or even all three polytypes are observed in many system. The calculations on the other hand need to be very precise and the obtained stability ranges are based on only small energy differences.

The investigations have shown that with reasonable computational effort, the stability ranges of the different Laves phase polytypes along quasi-binary sections can be predicted with acceptable accuracy. A similarly good agreement between calculated and experimental results was also evident for the lattice parameters and the site occupation factors. Alloys showing magnetic spin polarization presented a special computational challenge. The presence of magnetism can increase the computational effort considerably. Nevertheless, good results were also achieved with a strongly simplified model of the magnetic interactions in case of $Ta(V_{1-x}Fe_x)_2$. In summary it can be said, that the methods developed in this work help to minimize and to automatize the nonetheless significant effort of this type of calculations.

The properties and thus the applicability of metallic materials are linked inextricably to the crystallographic structure and the distribution of the alloying atoms in these structures. With the help of the methods examined in this work it is possible to identify potential new materials without the otherwise considerable experimental effort and to obtain information about the expected composition dependent structure types. Based on these predictions, is it now possible to plan and conduct the necessary experiments in Laves phase containing systems much more effectively. With the prospect of a continued strong increase in computing power, these calculations can easily be automated and even complex system with increasing supercells can be studied in the near future. In addition, this type of calculations is not limited to the relatively simple structures of Laves phases, but can be easily applied to other more complex structures.

A Appendix

A.1 vasp calculations

The following table lists all programs that were written and used during the preparation of this work, together with a brief description of there usage. The file extensions `*.sh` and `*.py` denote `bash` and `python` scripts, respectively. All scripts are run from a linux terminal.

The script `super.py` creates all possible atomic configurations in a given cell for a given composition. For each configuration a `*.xyz` file is created. An example of such a file is shown here[1]:

```
  9.760000000  0.000000000  0.000000000
 -2.440000000  4.226203970  0.000000000
  0.000000000  0.000000000  7.966000000
24 atoms from super16.py: 03 V Atoms
  0.000000000     0.000000000     0.000000000 23  1 V1
  0.000000000     0.000000000    -0.500000000 23  2 V2
  0.083333350     0.333333300     0.250000000 23  3 V3
  0.333333350    -0.166666700     0.250000000 26  4 Fe4
  0.083333350    -0.166666700     0.250000000 26  5 Fe5
  0.416666650    -0.333333300    -0.250000000 26  6 Fe6
  0.166666650     0.166666700    -0.250000000 26  7 Fe7
  0.416666650     0.166666700    -0.250000000 26  8 Fe8
 -0.500000000     0.000000000     0.000000000 26  9 Fe9
 -0.500000000     0.000000000    -0.500000000 26 10 Fe10
 -0.416666650     0.333333300     0.250000000 26 11 Fe11
 -0.166666650    -0.166666700     0.250000000 26 12 Fe12
 -0.416666650    -0.166666700     0.250000000 26 13 Fe13
 -0.083333350    -0.333333300    -0.250000000 26 14 Fe14
 -0.333333350     0.166666700    -0.250000000 26 15 Fe15
```

---

[1] The first column of this listing are line numbers which are not contained in the actual file!

```
20    -0.083333350     0.166666700    -0.250000000 26 16 Fe16
21     0.166666650    -0.333333300    -0.437500000 73 17 Ta1
22     0.333333350     0.333333300     0.062500000 73 18 Ta2
23     0.333333350     0.333333300     0.437500000 73 19 Ta3
24     0.166666650    -0.333333300    -0.062500000 73 20 Ta4
25    -0.333333350    -0.333333300    -0.437500000 73 21 Ta5
26    -0.166666650     0.333333300     0.062500000 73 22 Ta6
27    -0.166666650     0.333333300     0.437500000 73 23 Ta7
28    -0.333333350    -0.333333300    -0.062500000 73 24 Ta8
```

The first three lines contain the three lattice vectors defining the unit cell of the system. The fourth line is an arbitrary comment to identify the calculation. Each of the following lines (5-24) contains the definition for one atom in the unit cell. The three fractional atomic coordinates are followed by the atomic number, another consecutive number and the label of the atom.

To set up the VASP calculations for the above configuration a minimum of four files have to be created, namely `POSCAR`, `POTCAR`, `KPOINTS` and `INCAR`. The `POSCAR` files is created using the `xyz2pos`[2] utility. The file format is similar to that of the `*.xyz` file, its format is explained in the VASP manual [160]. The `POTCAR` file contains the pseudopotentials for each element in the compound. It is created by copying the appropriate `POTCAR` files of each element from the VASP potentials folder in the right order into one single `POTCAR` file. The `KPOINTS` and `INCAR` files for the three consecutive VASP runs are created on-the-fly by the bash script `jobscript.sh` which is shown here[3]:

```
#!/bin/sh
cat > KPOINTS <<!
Automatic mesh
0
Gamma
4 8 4
0. 0. 0.
!

cat >> INCAR <<!
 ISTART = 0
```

---

[2] `xyzi` is a combination of `awk` and `csh` code written by Marek Mihalkovic

[3] The first column of this listing are line numbers which are not contained in the actual file!

```
12    PREC = medium    #precision
13    NELM = 40    #maximum number of self-consistency loops
14    EDIFF = 1E-04    #break condition for the self-consistency loop
15    ALGO = VeryFast    #electronic minimization algorithm
16    LREAL = A
17    NSW = 25    #number of ionic steps
18    ISIF = 3    #relax everything
19    IBRION = 1    #quasi-newton algorithm for relaxing ions
20    ISMEAR = 1
21    ISYM = 0    #switch off symmetry
22    LWAVE = F
23    LCHARG = F
24   !
25
26   nohup mpirun -genv I_MPI_PIN off -np 1 vasp > output
27
28   vrename 1
29
30   nohup mpirun -genv I_MPI_PIN off -np 1 vasp > output
31
32   vrename 2
33
34   cat > INCAR <<!
35    ISTART = 0
36    PREC = medium
37    EDIFF = 1E-05
38    ALGO = VeryFast
39    LREAL = A
40    NSW = 1
41    ISIF = 2
42    IBRION = -1
43    ISMEAR = -5
44    ISYM = 0
45    LWAVE = F
46    LCHARG = F
47   !
48
49   nohup mpirun -genv I_MPI_PIN off -np 1 vasp > output
50
51   vrename 3
```

The first line identifies this file to be a bash script, a so-called *shebang*. Lines

2-8 create the `KPOINTS` file, with the kpoints 4 8 4 along the a, b and c lattice direction. Line 10-24 generate the `INCAR` file for the first two relaxation runs. For more information on the `INCAR` file consult the VASP manual [160]. The first run is started in line 26, its output is redirected to a file called `output`. After its successful termination `vrename 1` (line 28) renames the input and output files of the first run by appending the ending ".1" and copies the relaxed structure (`CONTCAR` file) into a `POSCAR` file as input structure for the second run. The next run is started and its output is renamed in lines 30 and 32. For the third and last run a new `INCAR` file is written (lines 34-47). This is a static run to obtain the total energy with higher accuracy (EDIFF), without relaxation of the lattice parameters (ISIF) and the ions (IBRION).

The `jobscript.sh` for the magnetic calculations is essentially the same with additional commands to define the magnetic properties on lines 22-25 and 48-52. `ISPIN`=2 tells VASP to perform a spin polarized calculation. The magnetic moments of the ions according to their order in the `POSCAR` file are given with the `MAGMOM` tag, 14 Fe atoms with an initial magnetic moment of $2\,\mu_B$ and 10 nonmagnetic Ta and V atoms in the present case. `LORBIT`=11 defines how and which output files are created, `VOSKOWN`=1 specifies the interpolation formula for the correlation part of the exchange and correlation functional.

```
 1   #!/bin/sh
 2   cat > KPOINTS <<!
 3   Automatic mesh
 4   0
 5   Gamma
 6   4 8 4
 7   0. 0. 0.
 8   !
 9
10   cat >> INCAR <<!
11    ISTART = 0
12    PREC = medium
13    NELM = 40
14    EDIFF = 1E-04
15    ALGO = VeryFast
16    LREAL = A
17    NSW = 25
18    ISIF = 3
```

```
 IBRION = 1
 ISMEAR = 1
 ISYM = 0
 ISPIN = 2    # 1: non spin polarized 2: spin polarized calculations
 MAGMOM = 14*2 10*0    # initial magnetic moment of the ions
 LORBIT = 11    # DOSCAR and lm decomposed PROCAR file
 VOSKOWN = 1    # Vosko, Wilk and Nusair interpolation
 LWAVE = F
 LCHARG = F
!

nohup mpirun -genv I_MPI_PIN off -np 1 vasp > output

vrename 1

nohup mpirun -genv I_MPI_PIN off -np 1 vasp > output

vrename 2

cat > INCAR <<!
 ISTART = 0
 PREC = medium
 EDIFF = 1E-05
 ALGO = VeryFast
 LREAL = A
 NSW = 1
 ISIF = 2
 IBRION = -1
 ISMEAR = -5
 ISYM = 0
 ISPIN = 2
 MAGMOM = 14*2 10*0
 LORBIT = 11
 VOSKOWN = 1
 LWAVE = F
 LCHARG = F
!

nohup mpirun -genv I_MPI_PIN off -np 1 vasp > output

vrename 3
```

Table 1.1: Computer programs written during the preparation of this work.

Script name	description
`abc.sh`	prints configuration and refined lattice parameters
`cpjobscript.py`	copy a modified `jobscript` to all configurations in a folder
`dir_test.sh`	test a directory for aborted, problematic or unusual calculations
`script_dir_test.py`	as above for all compositions
`eps2jpg`	creates high quality *.jpg files from *.eps files
`fake_pbs.py`	starts calculations, can be run as cronjob
`fout.sh`	prints total energy for FPLO calculations
`calc_times.py`	prints the time required for a single calculations
`get_calc_times.py`	as above for all compositions
`get_energy_values.sh`	prints the final total energy values
`get_mag_mom.py`	prints the calculated magnetic moments
`irre.sh`	prints the number of irreducible k-points
`modify_POSCAR.sh`	change the lattice parameters of all configurations in a folder
`occu16.py`	calculates the thermal averages of site occupation factors and lattice parameters for the 2 x 1 x 1 supercells and writes the configuration, total energy, lattice parameters and multiplicity to `datafile.txt`
`script_occu16.sh`	as above for all compositions
`occu8.py`	as `occy16.py` for unit cells
`script_occu8.sh`	as above for all compositions
`renew_vasp_calc.sh`	rebuild a single aborted calculation
`set_dirs.py`	runs after `super` scripts to setup directory structure and create VASP input files for all compositions
`set_single_dir.py`	as above for a single configuration
`sof_from_datafiles.py`	print the calculated site occupation factors for all compositions from `datafile.txt`
`super16_NbCrCo.py`	create unique configurations for a 2 x 1 x 1 supercell of C14 $\mathrm{Nb(Cr_{1-x}Co_x)_2}$
`super16_TaVFe.py`	as above for $\mathrm{Ta(V_{1-x}Fe_x)_2}$
`super8_C14.py`	create unique configurations for a C14 unit cell, elements are given as arguments* (see help for usage)
`C15_super.py`	create unique configurations for a C15 unit cell, elements are given as arguments* (see help for usage)
`super_C36.py`	create unique configurations for a C36 unit cell, elements are given as arguments* (see help for usage)
`tangent.py`	

* default is Nb, Cr and Co

A.2 Co–Cr–Nb system

Table 1.2: Crystallographic data and details on data collection and refinement of C14 $Nb(Cr_{1-x}Co_x)_2$ at nominal $x = 0.33$, 0.50, 0.67 and 0.80. From doctoral thesis of D. GRÜNER [52] and reference [137].

Crystallographic data				
Refined composition	$Nb(Cr_{0.69}Co_{0.31(2)})_2$ (21(2) at.% Co)	$Nb(Cr_{0.52}Co_{0.48(2)})_2$ (32(2) at.% Co)	$Nb(Cr_{0.34}Co_{0.67(3)})_2$ (44(2) at.% Co)	$Nb(Cr_{0.22}Co_{0.78(2)})_2$ (52(1) at.% Co)
Z	4			
Formula weight / g·mol^{-1}	201.19	203.56	206.31	207.66
$F(000)$	363.4	367.52	371.96	374.6
Crystal system	hexagonal			
Space group	$P6_3/mmc$			
a^* / pm	488.67(8)	486.90(6)	484.86(5)	483.19(2)
c^* / pm	801.3(2)	795.53(9)	788.69(7)	784.79(2)
Volume* / nm^3	0.16570(5)	0.16332(3)	0.16057(3)	0.15868(1)
Density / g·cm^{-3}	8.065	8.279	8.527	8.693
Crystal size / μm^3	25 × 40 × 40	15 × 20× 45	15 × 50 × 70	20 × 20 × 20
Data collection				
Diffractometer	Rigaku AFC7, Mercury CCD	Rigaku R-Axis Rapid, Imaging Plate		Rigaku R-Axis Spider, Imaging Plate Rotating anode
Radiation, wavelength	MoKα, $\lambda = 71.073$ pm			AgKα, $\lambda = 56.088$ pm
Monochromator	Graphite			Osmic X-ray optics
Temperature / K	293(2)			
Scan	ϕ, ω	ω	ω	ω
Bragg angle range 2θ	9.64–62.46°	9.66–69.81°	9.90–69.66°	7.67–115.96°
Index ranges	$-7 \leq h \leq 5$, $-6 \leq k \leq 6$, $-11 \leq l \leq 11$	$-7 \leq h \leq 7$, $-7 \leq k \leq 7$, $-11 \leq l \leq 12$	$-7 \leq h \leq 7$, $-7 \leq k \leq 7$, $-11 \leq l \leq 10$	$-14 \leq h \leq 8$, $-12 \leq k \leq 13$, $-23 \leq l \leq 21$
Absorption correction	multi-scan			
μ / mm^{-1}	21.18	22.69	24.39	32.84
$T_{min.}/T_{max.}$	0.622	0.609	0.549	0.604
Measured reflections	1190	2270	2475	7178
Unique reflections	120	163	152	912
R_{int}	0.024	0.052	0.041	0.033
Obs. reflections, $I > 2\sigma(I)$	116	157	151	725
Structure refinement				
Method	full-matrix least-squares on F^2			
No. of parameters	13	13	13	13
$R(F)$ / $R(F^2)$ ($I > 2\sigma(I)$)	0.023 / 0.044	0.032 / 0.059	0.025 / 0.055	0.035 / 0.055
$R(F)$ / $R(F^2)$ (all data)	0.026 / 0.046	0.035 / 0.060	0.025 / 0.055	0.044 / 0.057
Goodness-of-fit on F^2	1.274	1.496	1.563	1.504
Extinction coefficient x	0.012(2)	0.015(3)	0.015(3)	0.033(3)
$\Delta\rho_{min/max}$ / 10^{-6} e·pm^{-3}	−0.85 / 1.22	−0.95 / 0.98	−1.04 / 0.92	−3.74 / 3.72

* from calibrated powder data

Table 1.3: Atomic parameters and equivalent displacement parameters (in pm^2) for C14 $Nb(Cr_{1-x}Co_x)_2$ at nominal $x = 0.33$, 0.50, 0.67 and 0.80. From doctoral thesis of D. Grüner [52] and reference [137].

C14 $Nb(Cr_{1-x}Co_x)_2$, $x = 0.33$

Atom	Site	x	y	z	U_{eq}	Occ.
$M1$	$6h$	0.1703(2)	$2x$	1/4	69(4)	0.72(4) Cr + 0.28 Co
Nb1	$4f$	1/3	2/3	0.56252(9)	76(3)	1
$M2$	$2a$	0	0	0	69(5)	0.60(4) Cr + 0.40 Co

C14 $Nb(Cr_{1-x}Co_x)_2$, $x = 0.50$

Atom	Site	x	y	z	U_{eq}	Occ.
$M1$	$6h$	0.1708(2)	$2x$	1/4	60(3)	0.53(4) Cr + 0.47 Co
Nb1	$4f$	1/3	2/3	0.5634(1)	65(3)	1
$M2$	$2a$	0	0	0	66(6)	0.48(7) Cr + 0.52 Co

C14 $Nb(Cr_{1-x}Co_x)_2$, $x = 0.67$

Atom	Site	x	y	z	U_{eq}	Occ.
$M1$	$6h$	0.1703(2)	$2x$	1/4	55(3)	0.31(4) Cr + 0.69 Co
Nb1	$4f$	1/3	2/3	0.5639(1)	66(3)	1
$M2$	$2a$	0	0	0	60(5)	0.41(6) Cr + 0.59 Co

C14 $Nb(Cr_{1-x}Co_x)_2$, $x = 0.80$

Atom	Site	x	y	z	U_{eq}	Occ.
$M1$	$6h$	0.16956(3)	$2x$	1/4	57.7(4)	0.20(1) Cr + 0.80 Co
Nb1	$4f$	1/3	2/3	0.56412(3)	68.9(4)	1
$M2$	$2a$	0	0	0	61.1(7)	0.29(2) Cr + 0.71 Co

The data in table **1.6** and **1.8** are fitted with Redlich-Kister polynomials of 4^{th} order. The corresponding coeffients of these polynomials are given in table **1.7** and **1.10**, respectively.

The function of the common tangent on the Gibbs energy curves for C14 and C15 $Nb(Cr_{1-x}Co_x)_2$ in figure **5.7** on page 105 is given by:

$$G(x) = -321.3178 \cdot x - 25.8298 \tag{A.1}$$

Table 1.4: Anisotropic displacement parameters (in pm^2) for C14 $Nb(Cr_{1-x}Co_x)_2$ at nominal $x = 0.33$, 0.50, 0.67 and 0.80. From doctoral thesis of D. Grüner [52] and reference [137].

C14 $Nb(Cr_{1-x}Co_x)_2$, $x = 0.33$

Atom	U_{11}	U_{22}	U_{33}	U_{23}	U_{13}	U_{12}
$M1$	71(5)	68(6)	67(5)	0	0	$U_{22}/2$
Nb1	77(4)	U_{11}	73(4)	0	0	$U_{22}/2$
$M2$	66(7)	U_{11}	74(9)	0	0	$U_{22}/2$

C14 $Nb(Cr_{1-x}Co_x)_2$, $x = 0.50$

Atom	U_{11}	U_{22}	U_{33}	U_{23}	U_{13}	U_{12}
$M1$	68(4)	58(5)	51(5)	0	0	$U_{22}/2$
Nb1	68(3)	U_{11}	59(4)	0	0	$U_{22}/2$
$M2$	78(6)	U_{11}	42(9)	0	0	$U_{22}/2$

C14 $Nb(Cr_{1-x}Co_x)_2$, $x = 0.67$

Atom	U_{11}	U_{22}	U_{33}	U_{23}	U_{13}	U_{12}
$M1$	61(4)	45(5)	54(5)	0	0	$U_{22}/2$
Nb1	71(3)	U_{11}	56(4)	0	0	$U_{22}/2$
$M2$	71(6)	U_{11}	39(9)	0	0	$U_{22}/2$

C14 $Nb(Cr_{1-x}Co_x)_2$, $x = 0.80$

Atom	U_{11}	U_{22}	U_{33}	U_{23}	U_{13}	U_{12}
$M1$	57.2(6)	40.6(7)	69.7(8)	0	0	$U_{22}/2$
Nb1	68.0(5)	U_{11}	70.9(6)	0	0	$U_{22}/2$
$M2$	66.6(9)	U_{11}	50(1)	0	0	$U_{22}/2$

Table 1.5: Interatomic distances ($d < 320\,\text{pm}$) in pm for C14 Nb($Cr_{1-x}Co_x$)$_2$ at nominal $x = 0.33$, 0.50, 0.67 and 0.80. From doctoral thesis of D. Grüner [52] and reference [137].

			$x = 0.33$	$x = 0.50$	$x = 0.67$	$x = 0.80$
Nb1 –	3	$M1$	285.93(9)	284.56(9)	282.92(9)	282.06(2)
	6	$M1$	286.84(5)	285.14(5)	283.40(5)	282.23(1)
	3	$M2$	286.55(5)	285.60(5)	284.44(3)	283.47(1)
	1	Nb1	300.4(2)	296.8(2)	293.5(2)	291.75(4)
	3	Nb1	299.39(7)	298.68(6)	297.55(6)	296.57(2)
$M1$ –	2	$M1$	239.1(2)	237.5(2)	237.1(2)	237.40(5)
	2	$M1$	249.6(2)	249.4(2)	247.8(2)	245.79(5)
	2	$M2$	246.76(7)	245.54(7)	243.60(6)	242.12(2)
	2	Nb1	285.93(9)	284.56(9)	282.92(9)	282.06(2)
	4	Nb1	286.84(5)	285.14(5)	283.40(5)	282.23(1)
$M2$ –	6	$M1$	246.76(7)	245.54(7)	243.60(6)	242.14(2)
	6	Nb1	286.55(5)	285.60(4)	284.44(3)	283.47(1)

Table 1.6: Total energy values for the stable configurations of C14 and C15 Nb($Cr_{1-x}Co_x$)$_2$ calculated with VASP with medium precision. This data is plotted in figure **5.6** on page 104.

Composition x	Total energy [eV/atom]		Formula
	C14	C15	
0.0000	-9.6670	-9.6826	$NbCr_2$
0.0625	-9.5931	-9.5947	$Nb_8Cr_{15}Co_1$
0.1250	-9.5056	-9.4979	$Nb_8Cr_{14}Co_2$
0.1875	-9.4153	-9.4043	$Nb_8Cr_{13}Co_3$
0.2500	-9.3295	-9.3100	$Nb_8Cr_{12}Co_4$
0.3125	-9.2379	-9.2182	$Nb_8Cr_{11}Co_5$
0.3750	-9.1516	-9.1278	$Nb_8Cr_{10}Co_6$
0.4375	-9.0602	-9.0365	$Nb_8Cr_9Co_7$
0.5000	-8.9704	-8.9491	$Nb_8Cr_8Co_8$
0.5625	-8.8719	-8.8577	$Nb_8Cr_7Co_9$
0.6250	-8.7754	-8.7684	$Nb_8Cr_6Co_{10}$
0.6875	-8.6832	-8.6718	$Nb_8Cr_5Co_{11}$
0.7500	-8.5939	-8.5731	$Nb_8Cr_4Co_{12}$
0.8125	-8.4896	-8.4727	$Nb_8Cr_3Co_{13}$
0.8750	-8.3867	-8.3730	$Nb_8Cr_2Co_{14}$
0.9375	-8.2769	-8.2709	$Nb_8Cr_1Co_{15}$
1.0000	-8.1683	-8.1699	$NbCo_2$

Table 1.7: Coefficients of the Redlich-Kister polynomials fitted to the total energy values for the stable configurations of C14 and C15 Nb($Cr_{1-x}Co_x$)$_2$. These polynomials are plotted in figure **5.6** on page 104.

Coefficient	C14	C15
${}^0A$	-0.1975 ± 0.0071	-0.0908 ± 0.0023
${}^1A$	-0.0544 ± 0.0232	-0.1598 ± 0.0077
${}^2A$	-0.0628 ± 0.0746	0.0529 ± 0.0246
${}^3A$	0.0457 ± 0.0597	0.204 ± 0.0197
${}^4A$	-0.0874 ± 0.1276	-0.0851 ± 0.0421
RMS of residuals	0.0033	0.0011
Reduced χ^2	1.0859e-05	1.1833e-06

Table 1.8: Gibbs energy values for the stable configurations of C14 and C15 Nb($Cr_{1-x}Co_x$)$_2$ calculated with the help of equation 4.7 from the total energy values in table **1.6** at 1100 °C. This data is plotted in figure **5.7** on page 105.

Composition x	Gibbs energy [meV/atom]		Formula
	C14	C15	
0.0000	-7.232	-22.806	$NbCr_2$
0.0625	-45.019	-46.600	$Nb_8Cr_{15}Co_1$
0.1250	-65.509	-57.829	$Nb_8Cr_{14}Co_2$
0.1875	-81.787	-70.886	$Nb_8Cr_{13}Co_3$
0.2500	-101.579	-82.130	$Nb_8Cr_{12}Co_4$
0.3125	-114.687	-95.020	$Nb_8Cr_{11}Co_5$
0.3750	-132.493	-108.693	$Nb_8Cr_{10}Co_6$
0.4375	-144.411	-120.722	$Nb_8Cr_9Co_7$
0.5000	-157.334	-136.059	$Nb_8Cr_8Co_8$
0.5625	-160.920	-146.702	$Nb_8Cr_7Co_9$
0.6250	-165.940	-158.900	$Nb_8Cr_6Co_{10}$
0.6875	-174.561	-163.193	$Nb_8Cr_5Co_{11}$
0.7500	-185.380	-164.594	$Nb_8Cr_4Co_{12}$
0.8125	-180.330	-163.464	$Nb_8Cr_3Co_{13}$
0.8750	-175.620	-161.917	$Nb_8Cr_2Co_{14}$
0.9375	-162.595	-156.605	$Nb_8Cr_1Co_{15}$
1.0000	-147.224	-148.864	$NbCo_2$

Table 1.9: Experimental and calculated site occupation factors for Co at the $2a$ and $6h$ sites in C14 $\mathrm{Nb(Cr_{1-x}Co_x)_2}$. This data is plotted in figures **5.11**, **5.12** and **5.13** on pages 114 ff.

x	Co at $2a$	Co at $6h$
Experimental (fig. **5.11**)		
0.31	0.40	0.28
0.48	0.52	0.47
0.66	0.59	0.69
0.7725	0.698	0.797
FPLO fixed lattice parameters (fig. **5.12** (a))		
0.250	0.353	0.216
0.375	0.429	0.357
0.500	0.613	0.462
0.625	0.618	0.627
0.750	0.590	0.803
FPLO variable lattice parameters (fig. **5.12** (b))		
0.250	0.417	0.194
0.375	0.499	0.334
0.500	0.677	0.441
0.625	0.663	0.612
0.750	0.586	0.805

x	Co at $2a$	Co at $6h$
VASP unit cell (fig. **5.13** (a))		
0.125	0.274	0.075
0.250	0.369	0.211
0.375	0.483	0.339
0.500	0.713	0.429
0.625	0.709	0.597
0.750	0.656	0.782
0.875	0.807	0.898
VASP 2 x 1 x 1 supercell (fig. **5.13** (b))		
0.0000	0.000	0.000
0.0625	0.167	0.028
0.1250	0.308	0.064
0.1875	0.396	0.118
0.2500	0.449	0.184
0.3750	0.558	0.314
0.4375	0.610	0.380
0.5000	0.671	0.443
0.5625	0.711	0.513
0.6250	0.713	0.596
0.6875	0.660	0.697
0.7500	0.641	0.786
0.8125	0.670	0.860
0.8750	0.750	0.917
0.9375	0.871	0.960
1.0000	1.000	1.000

Table 1.10: Coefficients of the Redlich-Kister polynomials fitted to the Gibbs energy values for the stable configurations of C14 and C15 Nb($Cr_{1-x}Co_x$)$_2$. These polynomials are plotted in figure **5.7** on page 105.

Coefficient	C14	C15
^{0}A	-307.228 ± 7.767	-200.531 ± 2.692
^{1}A	-54.4362 ± 25.37	-159.791 ± 8.792
^{2}A	-83.6298 ± 81.59	32.0388 ± 28.27
^{3}A	45.7259 ± 65.33	204.044 ± 22.64
^{4}A	-137.13 ± 139.7	-134.691 ± 48.4
RMS of residuals	3.6065	1.2498
Reduced χ^2	13.0065	1.5619

Table 1.11: Labeling of the samples in this work and the corresponding sample names in the lab book and source data.

Sample	Name	Composition x	Sample	Name	Composition x
1	AK0217 [1]	0	13	DG0232[1]	0.50
2	AK026	0.02	14	AK002	0.57
3	AK027	0.03	15	AK013	0.60
4	AK028	0.05	16	DG0280[1]	0.67
5	AK029	0.08	17	AK034	0.75
6	AK016	0.10	18	AK020	0.80
7	AK055	0.15	19	AK058	0.90
8	AK017	0.20	20	DG0281[1]	0.92
9	AK035	0.25	21	AK021	0.94
10	DG0279[1]	0.33	22	AK033	0.98
11	AK018	0.40	23	DG0276[1]	1.00
12	AK001	0.42			

[1] samples from Daniel Grüner [52]

A.2.1 Supplementary metallographic images

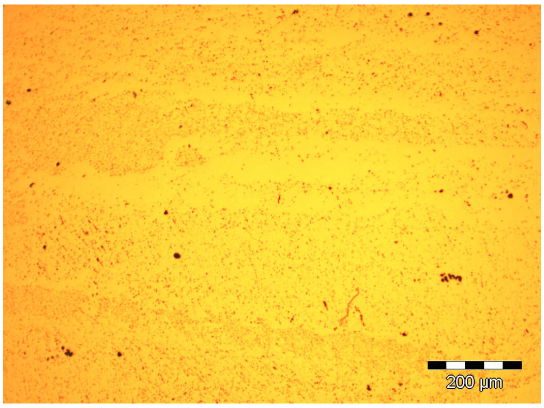

(1) No. 1 (brightfield)

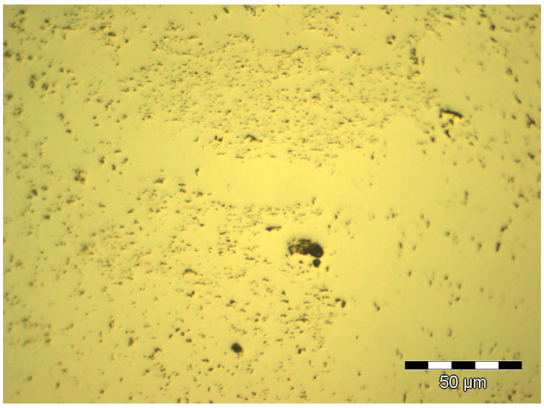

(2) No. 1 (polarized light)

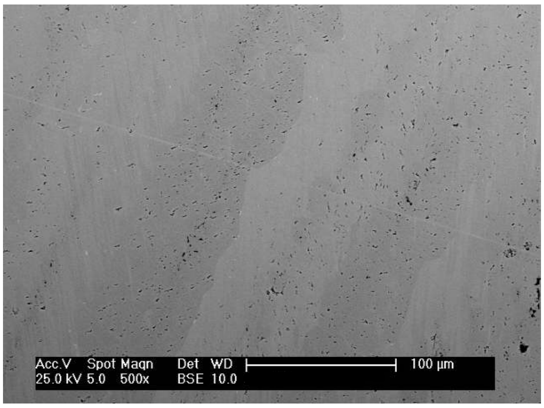

(3) No. 1 (SEM, BSE)

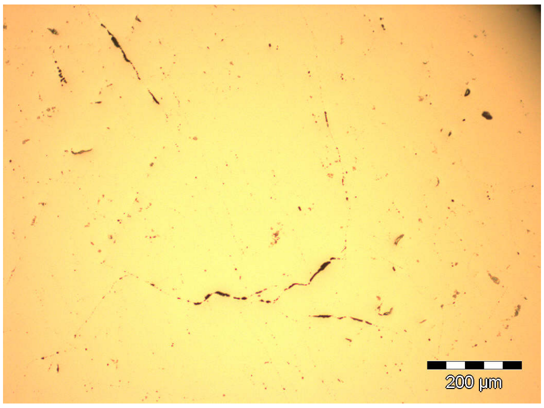

(4) No. 2 (brightfield)

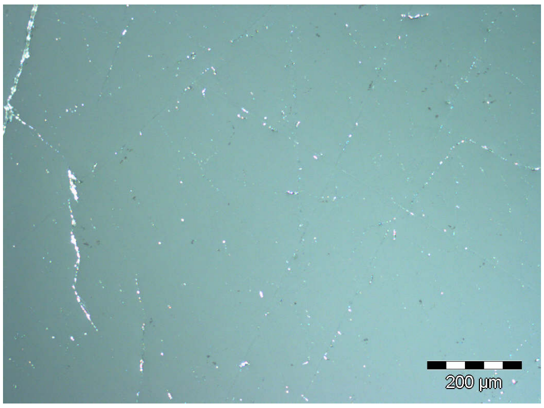

(5) No. 2 (polarized light)

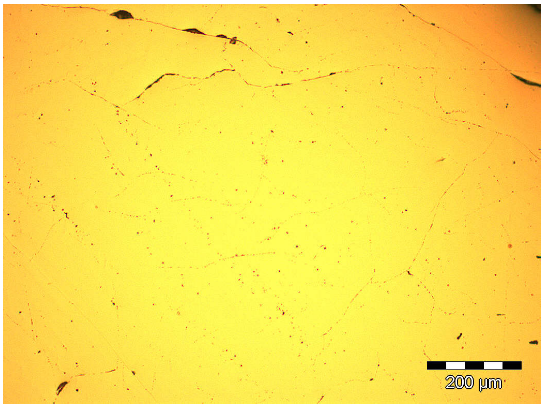

(6) No. 5 (brightfield)

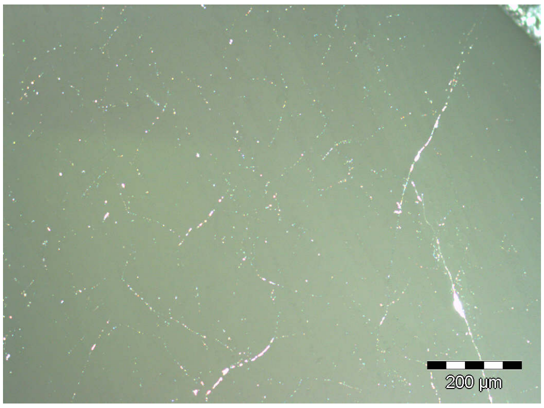

(7) No. 5 (polarized light)

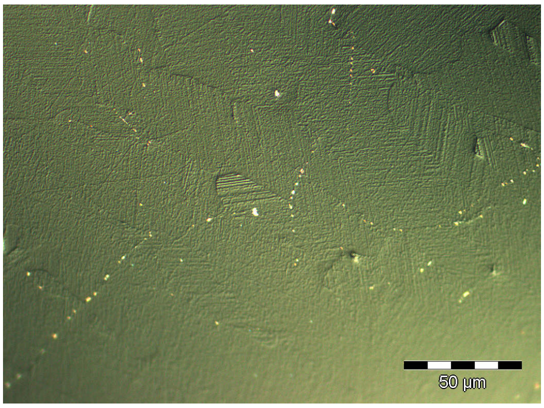

(8) No. 5, etched (DIC)

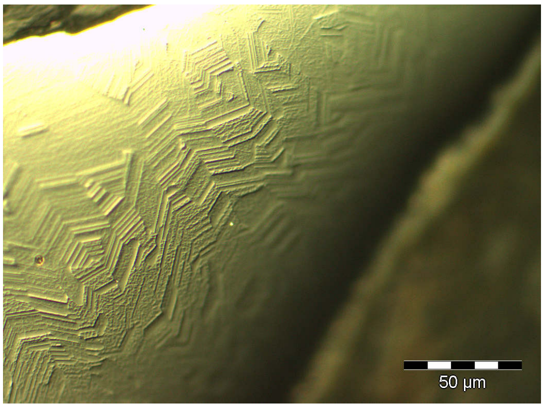

(9) No. 5, etched (DIC)

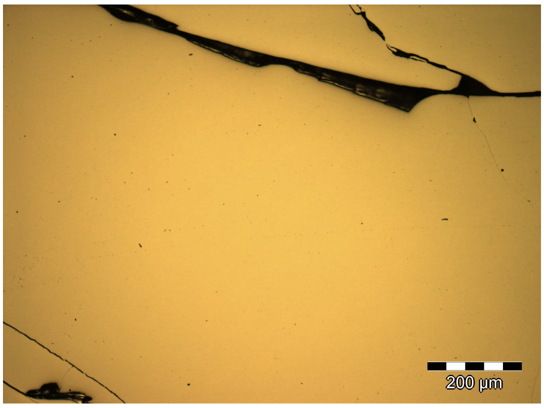

(10) No. 6 (brightfield)

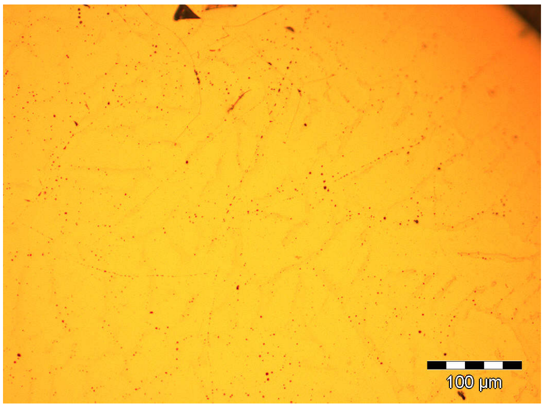

(11) No. 6, etched (brightfield)

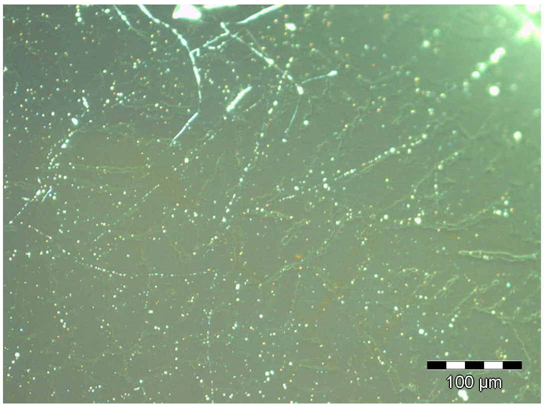

(12) No. 6, etched (polarized light)

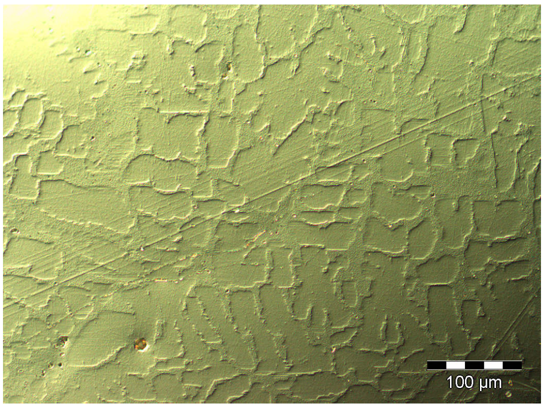

(13) No. 6, etched (DIC)

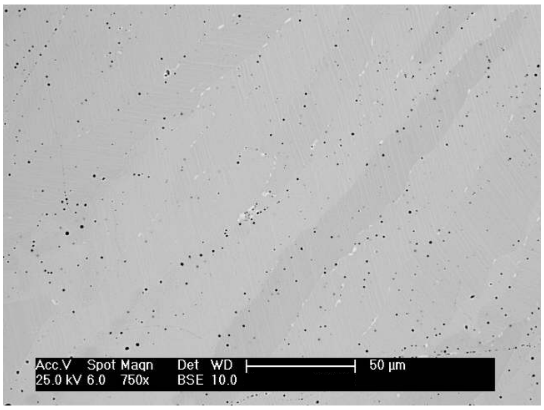

(14) No. 6 (SEM, BSE)

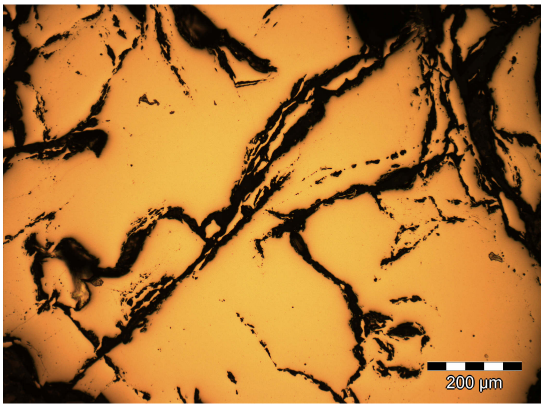

(15) No. 7 (brightfield)

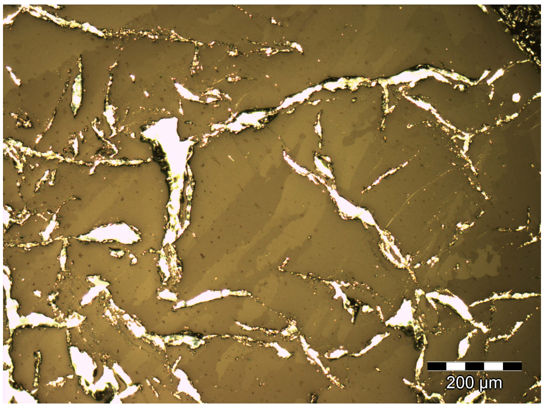

(16) No. 7 (polarized light)

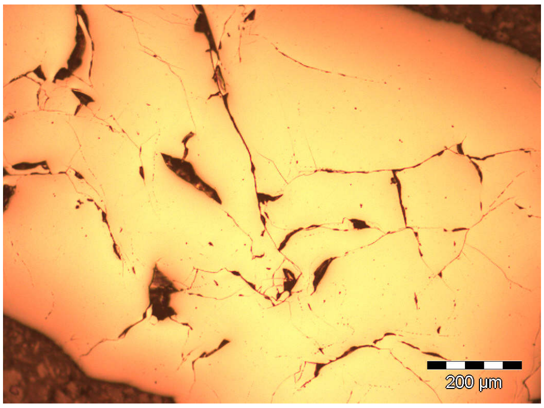

(17) No. 9 (brightfield)

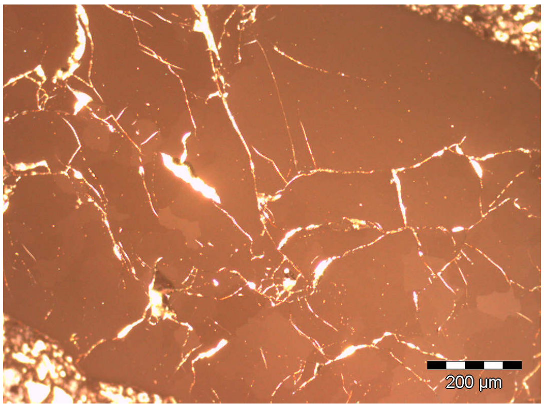

(18) No. 9 (polarized light)

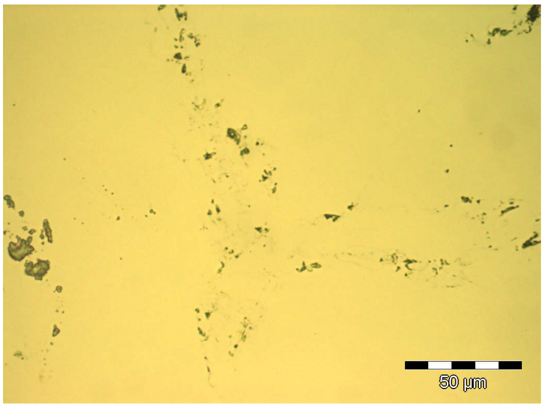

(19) No. 10 (brightfield)

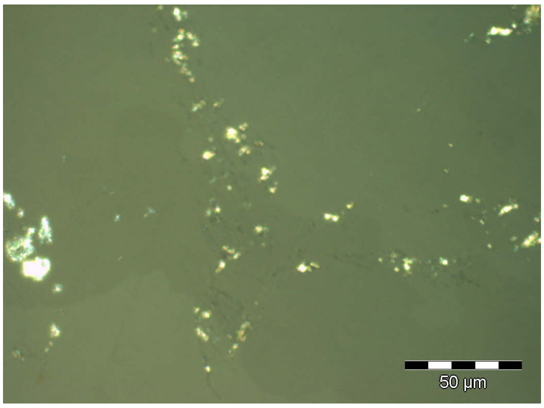

(20) No. 10 (polarized light)

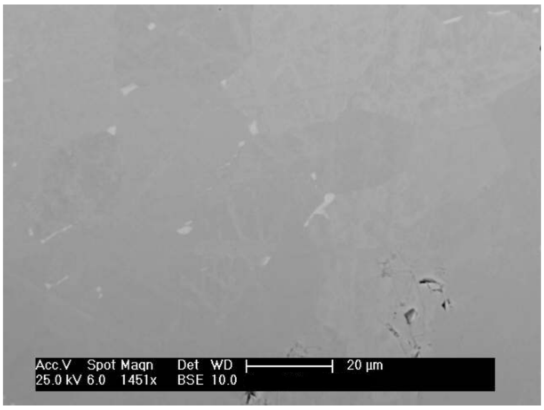

(21) No. 10 (SEM, BSE)

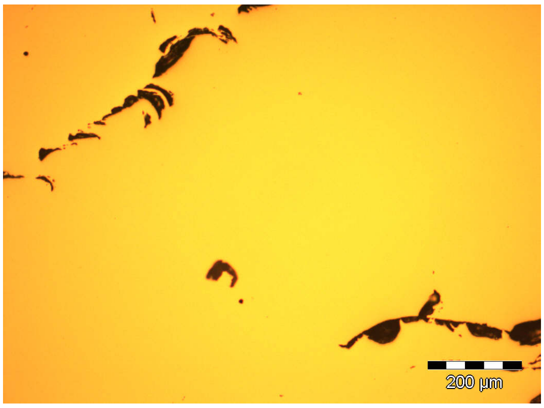

(22) No. 13 (brightfield)

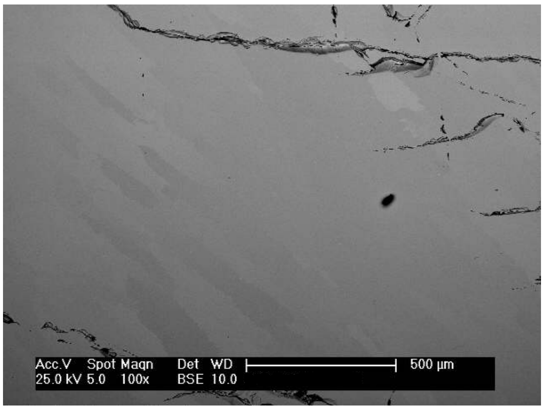

(23) No. 13 (SEM, BSE)

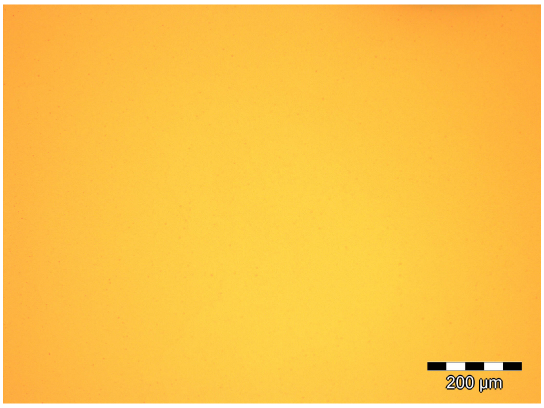

(24) No. 15 (brightfield)

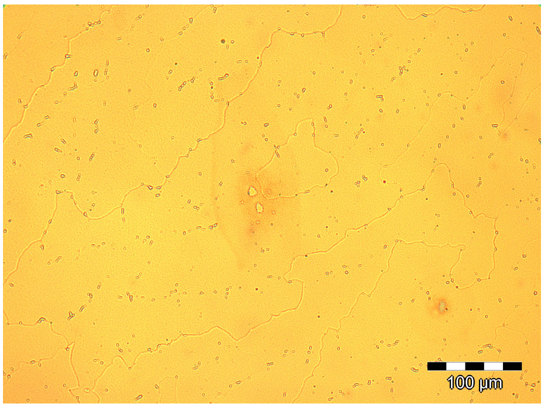

(25) No. 15, etched (brightfield)

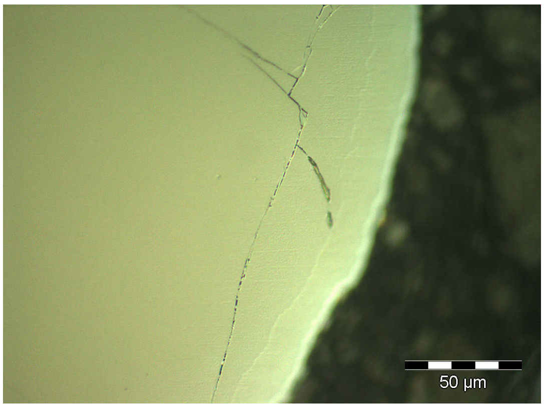

(26) No. 16 (brightfield)

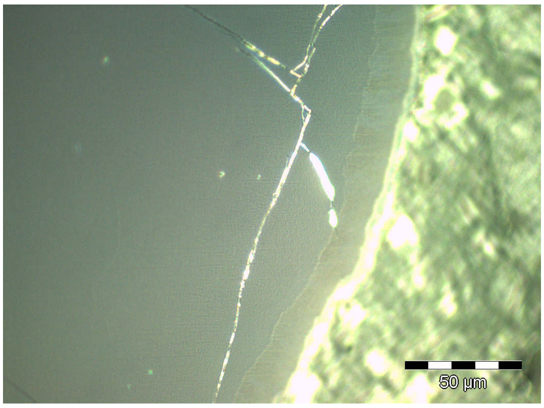

(27) No. 16 (polarized light)

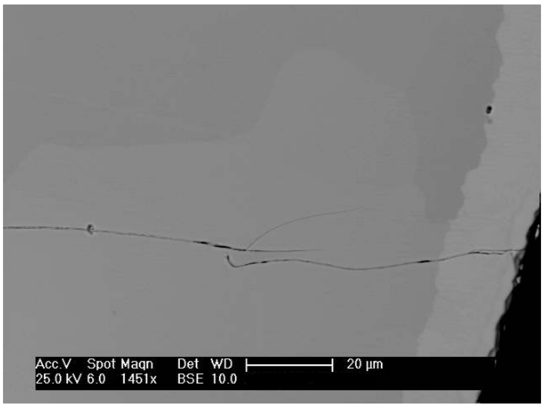

(28) No. 16 (SEM, BSE)

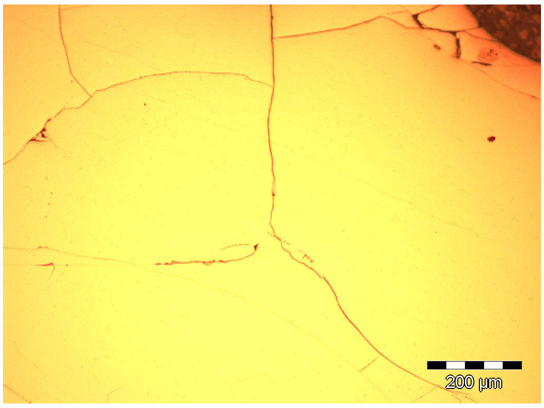

(29) No. 18 (brightfield)

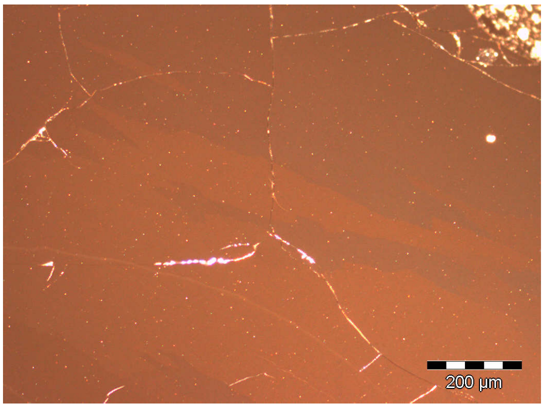

(30) No. 18 (polarized light)

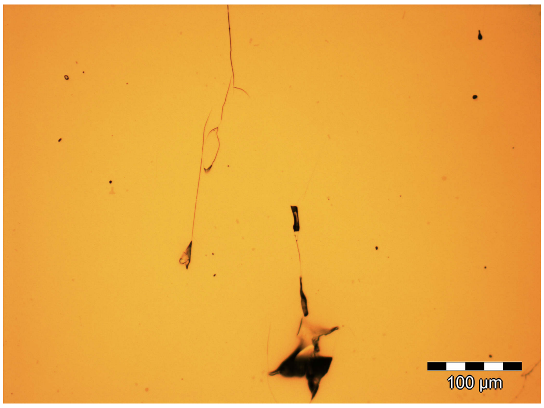

(31) No. 19 (brightfield)

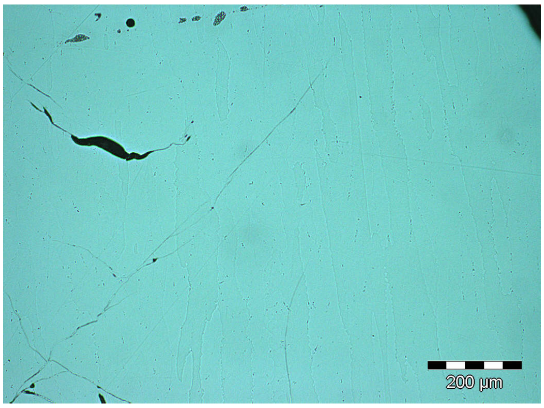

(32) No. 20 (brightfield)

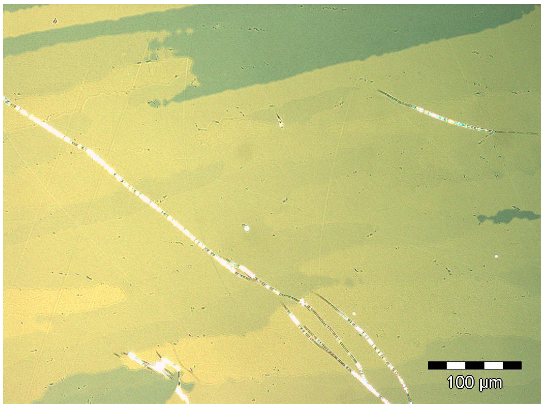

(33) No. 20 (polarized light)

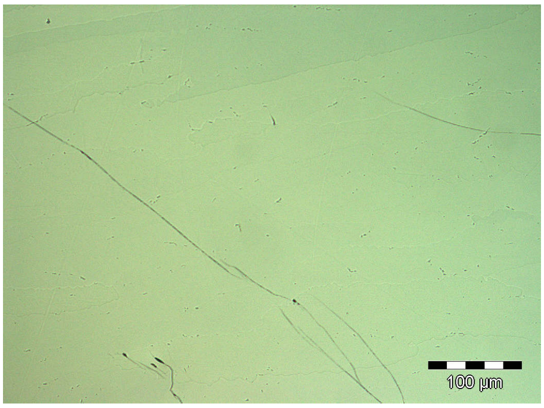

(34) No. 20 (DIC)

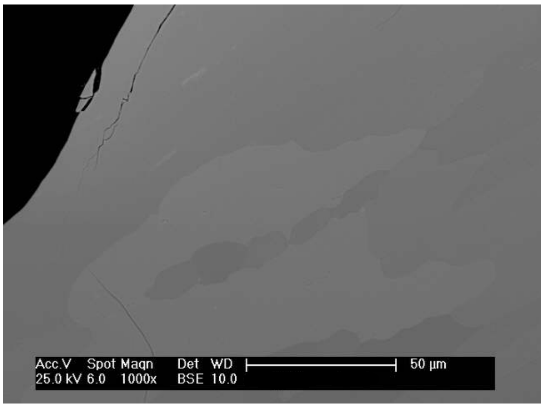

(35) No. 20 (SEM, BSE)

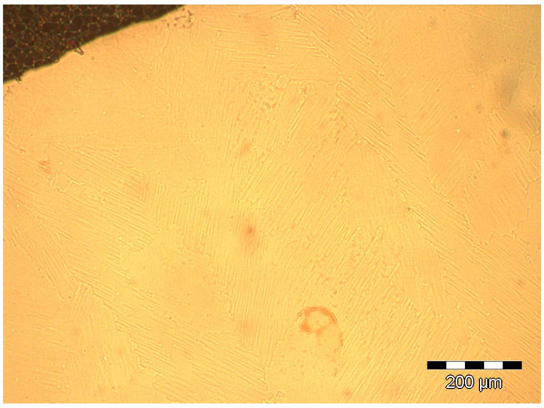

(36) No. 21 (brightfield)

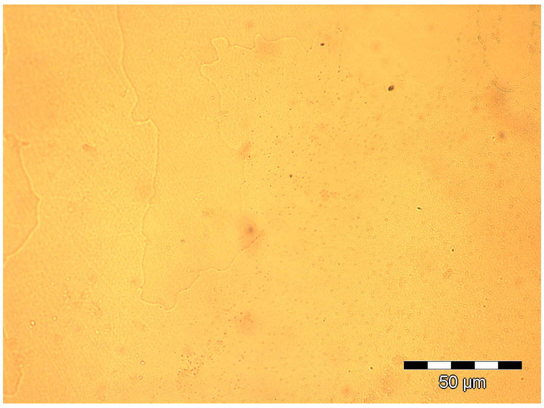

(37) No. 22 (brightfield)

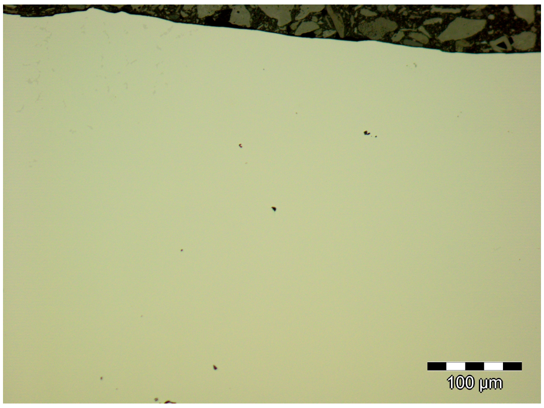

(38) No. 23 (brightfield)

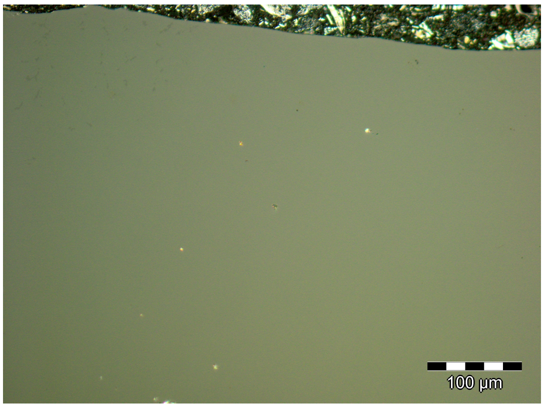

(39) No. 23 (polarized light)

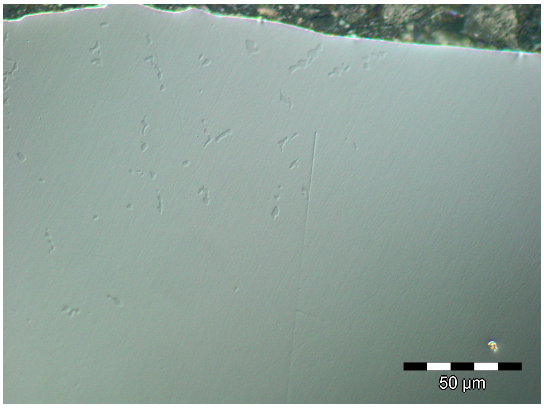

(40) No. 23 (DIC)

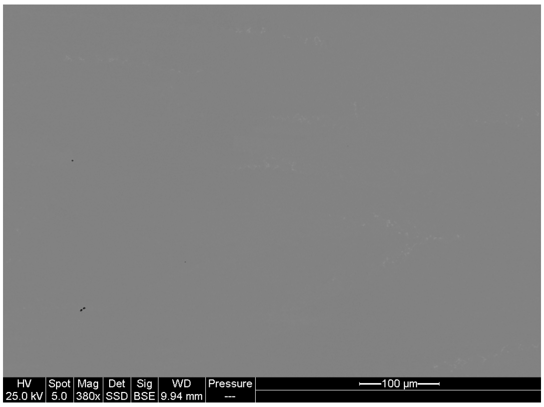

(41) No. 23 (SEM, BSE)

A.3 Fe–Ta–V system

Table 1.12: Total energy values for the stable configurations of C14 and C15 $Ta(V_{1-x}Fe_x)_2$ calculated with VASP with medium precision. This data is plotted in figure **6.2** on page 124.

Composition x	Total energy [eV/atom]		Formula
	C14	C15	
0.0000	-9.9574	-9.9431	TaV_2
0.0625	-9.9637	-9.9771	$Ta_8V_{15}Fe_1$
0.1250	-9.9623	-9.9880	$Ta_8V_{14}Fe_2$
0.1875	-9.9496	-9.9735	$Ta_8V_{13}Fe_3$
0.2500	-9.9330	-9.9509	$Ta_8V_{12}Fe_4$
0.3125	-9.9130	-9.9195	$Ta_8V_{11}Fe_5$
0.3750	-9.8947	-9.8888	$Ta_8V_{10}Fe_6$
0.4375	-9.8696	-9.8596	$Ta_8V_9Fe_7$
0.5000	-9.8442	-9.8364	$Ta_8V_8Fe_8$
0.5625	-9.8133	-9.8027	$Ta_8V_7Fe_9$
0.6250	-9.7882	-9.7757	$Ta_8V_6Fe_{10}$
0.6875	-9.7578	-9.7501	$Ta_8V_5Fe_{11}$
0.7500	-9.7383	-9.7287	$Ta_8V_4Fe_{12}$
0.8125	-9.6966	-9.6783	$Ta_8V_3Fe_{13}$
0.8750	-9.6591	-9.6304	$Ta_8V_2Fe_{14}$
0.9375	-9.6189	-9.5872	$Ta_8V_1Fe_{15}$
1.0000	-9.5818	-9.5490	$TaFe_2$

The data in table **1.12** and **1.14** are fitted with Redlich-Kister polynomials of 4^{th} order. The corresponding coeffients of these polynomials are given in table **1.13** and **1.15**. The function of the common tangent on the Gibbs energy curves for C14 and C15 $Ta(V_{1-x}Fe_x)_2$ in figure **6.3** on page 125 is given by:

$$G(x) = -35.8245 \cdot x - 247.1713$$

Table 1.13: Coefficients of the Redlich-Kister polynomials fitted to the total energy values for the stable configurations of C14 and C15 Ta($V_{1-x}Fe_x$)$_2$. These polynomials are plotted in figure **6.2** on page 124.

Coefficient	C14	C15
^0A	-0.2908 ± 0.0066	-0.3396 ± 0.0081
^1A	0.0610 ± 0.0217	0.0516 ± 0.0265
^2A	-0.2266 ± 0.0697	-0.6436 ± 0.0852
^3A	0.0991 ± 0.0558	0.5249 ± 0.0682
^4A	0.1453 ± 0.1194	0.3770 ± 0.1458
RMS of residuals	0.0031	0.0038
Reduced χ^2	9.5026e-06	1.4185e-05

Table 1.14: Gibbs energy values for the stable configurations of C14 and C15 Ta($V_{1-x}Fe_x$)$_2$ calculated calculated with the help of equation 4.7 from the total energy values in table **1.12** at 1100 °C. This data is plotted in figure **6.3** on page 125.

Composition x	Gibbs energy [meV/atom]		Formula
	C14	C15	
0.0000	-127.787	-113.513	TaV_2
0.0625	-171.626	-184.899	$Ta_8V_{15}Fe_1$
0.1250	-203.778	-229.494	$Ta_8V_{14}Fe_2$
0.1875	-223.415	-247.258	$Ta_8V_{13}Fe_3$
0.2500	-238.080	-255.920	$Ta_8V_{12}Fe_4$
0.3125	-248.427	-254.997	$Ta_8V_{11}Fe_5$
0.3750	-259.832	-253.945	$Ta_8V_{10}Fe_6$
0.4375	-263.786	-253.808	$Ta_8V_9Fe_7$
0.5000	-266.851	-259.069	$Ta_8V_8Fe_8$
0.5625	-263.728	-253.098	$Ta_8V_7Fe_9$
0.6250	-265.807	-253.257	$Ta_8V_6Fe_{10}$
0.6875	-261.944	-254.235	$Ta_8V_5Fe_{11}$
0.7500	-268.244	-258.569	$Ta_8V_4Fe_{12}$
0.8125	-251.516	-233.211	$Ta_8V_3Fe_{13}$
0.8750	-237.882	-209.181	$Ta_8V_2Fe_{14}$
0.9375	-220.201	-188.517	$Ta_8V_1Fe_{15}$
1.0000	-201.947	-169.148	$TaFe_2$

Table 1.15: Coefficients of the Redlich-Kister polynomials fitted to the Gibbs energy values for the stable configurations of C14 and C15 $Ta(V_{1-x}Fe_x)_2$. These polynomials are plotted in figure **6.3** on page 125.

Coefficient	C14	C15
^0A	-400.453 ± 7.25	-449.24 ± 8.89
^1A	61.0227 ± 23.68	51.6055 ± 29.04
^2A	-247.431 ± 76.16	-664.448 ± 93.38
^3A	99.0545 ± 60.98	524.799 ± 74.77
^4A	95.7557 ± 130.4	327.511 ± 159.8
RMS of residuals	3.3665	4.1276
Reduced χ^2	11.3331	17.037

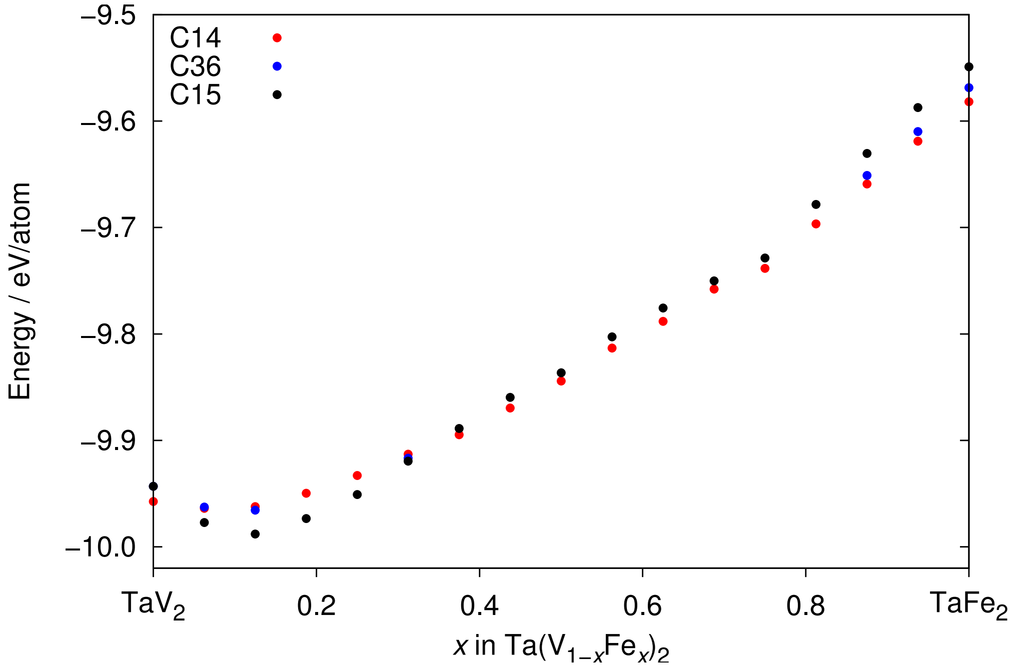

Figure 1.1: Total energy values of the stable configurations of C15, C14 and additionally selected compositions of C36 $Ta(V_{1-x}Fe_x)_2$. The total energy of the C36 phase lies always in between the values for C14 and C15. This is especially important at the composition $x = 0.3125$ where C36 is the experimentally the stable polytype. The numerical data for this plot is given in tables **1.12** and **1.16**.

Table 1.16: Total energy values for the stable configurations of C36 Ta($V_{1-x}Fe_x$)$_2$ calculated with VASP with medium precision. This data is plotted in figure **1.1**.

Composition x	Total energy [eV/atom]	Formula
	C36	
0.0000	-9.9431	TaV_2
0.0625	-9.9626	$Ta_8V_{15}Fe_1$
0.1250	-9.9656	$Ta_8V_{14}Fe_2$
0.3125	-9.9166	$Ta_8V_{11}Fe_5$
0.8750	-9.6510	$Ta_8V_2Fe_{14}$
0.9375	-9.6099	$Ta_8V_1Fe_{15}$
1.0000	-9.5686	$TaFe_2$

Table 1.17: Calculated site occupation factors for Fe at the $2a$ and $6h$ sites in C14 Ta($V_{1-x}Fe_x$)$_2$. This data is plotted in figure **6.14** on page 140.

x	Fe at $2a$	Fe at $6h$
VASP unit cell		
0.125	0.123	0.126
0.250	0.151	0.283
0.375	0.190	0.437
0.500	0.461	0.513
0.625	0.653	0.616
0.750	0.909	0.697
0.875	0.981	0.840

x	Fe at $2a$	Fe at $6h$
VASP 2 x 1 x 1 supercell		
0.0000	0.000	0.000
0.0625	0.050	0.067
0.1250	0.099	0.134
0.1875	0.148	0.201
0.2500	0.238	0.254
0.3125	0.318	0.311
0.3750	0.388	0.371
0.4375	0.482	0.423
0.5000	0.561	0.480
0.5625	0.647	0.534
0.6250	0.744	0.585
0.6875	0.808	0.647
0.7500	0.886	0.705
0.8125	0.924	0.775
0.8750	0.963	0.846
0.9375	0.982	0.923
1.0000	1.000	1.000

Table 1.18: Total energy values for the stable configurations of C14 and C15 $Ta(V_{1-x}Fe_x)_2$ with ferromagnetic ordering. This data is plotted in figure **6.19** on page 145.

Composition x	Total energy [eV/atom]		Formula
	C14	C15	
0.6875	-9.7601	-9.7563	$Ta_8V_5Fe_{11}$
0.7500	-9.7405	-9.7352	$Ta_8V_4Fe_{12}$
0.8125	-9.6997	-9.6901	$Ta_8V_3Fe_{13}$
0.8750	-9.6639	-9.6526	$Ta_8V_2Fe_{14}$
0.9375	-9.6264	-9.6184	$Ta_8V_1Fe_{15}$
1.0000	-9.5932	-9.5878	$TaFe_2$

Table 1.19: Gibbs energy values for the stable configurations of C14 and C15 $Ta(V_{1-x}Fe_x)_2$ with ferromagnetic ordering. This data is plotted in figure **6.20** on page 146.

Composition x	Gibbs energy [meV/atom]		Formula
	C14	C15	
0.6875	-264.166	-260.382	$Ta_8V_5Fe_{11}$
0.7500	-270.410	-265.060	$Ta_8V_4Fe_{12}$
0.8125	-254.573	-244.976	$Ta_8V_3Fe_{13}$
0.8750	-242.659	-231.386	$Ta_8V_2Fe_{14}$
0.9375	-227.713	-219.717	$Ta_8V_1Fe_{15}$
1.0000	-213.381	-207.925	$TaFe_2$

Table 1.20: Labeling of the samples in this work and the corresponding sample names in the lab book and source data.

Sample	Name	Composition x	Sample	Name	Composition x
1	AK122	0.00	21	AK151	0.65
2	AK120_2	0.00	22	AK-DA_4[1]	0.70
3	AK141_2	0.00	23	AK160	0.70
4	AK152	0.03	24	AK161	0.75
5	AK134	0.1	25	AK-DA_5[1]	0.80
6	AK145	0.125	26	AK126	0.80
7	AK146	0.25	27	AK154	0.85
8	AK156	0.29	28	AK174	0.85
9	AK132	0.3	29	AK125	0.90
10	AK-DA3_2[1]	0.3	30	AK173	0.90
11	AK157	0.31	31	AK168_YD[2]	0.91
12	AK176_2	0.31	32	AK172	0.95
13	AK153	0.325	33	AK167_YC[2]	0.95
14	AK177_2	0.33	34	AK171	0.98
15	AK149	0.35	35	AK170	1.00
16	AK131	0.40	36	AK124	1.00
17	AK158	0.45	37	AK135	1.00
18	AK130	0.50	38	AK136	1.00
19	AK159	0.50	39	AK137	1.00
20	AK138	0.60	40	AK139	1.00

[1] samples prepared by students during a practical training

[2] samples from Yoshihiro Yamada, Division of Electronic Materials and Devices University of Hyogo, Shosha, Himeji, Japan

A.3.1 Supplementary metallographic images

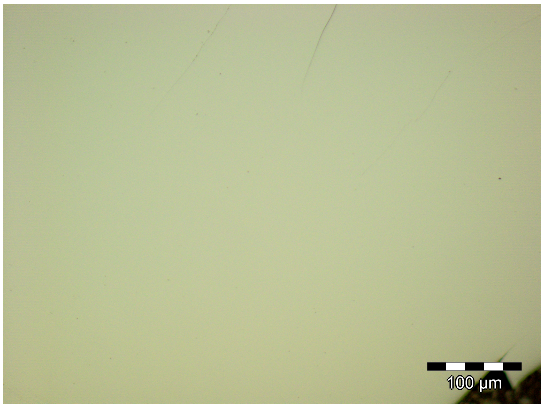

(1) No. 1 (brightfield)

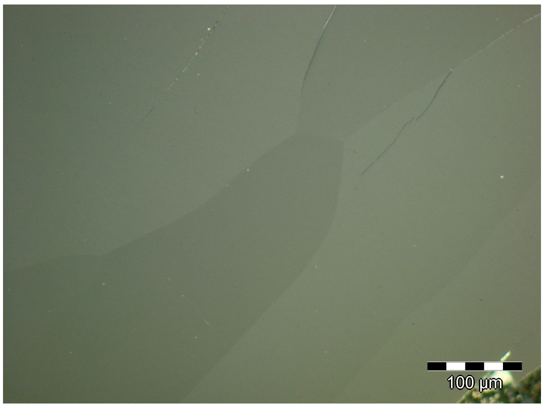

(2) No. 1 (polarized light)

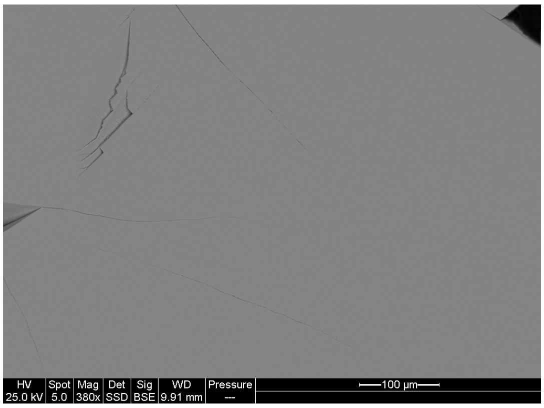

(3) No. 1 (SEM, BSE)

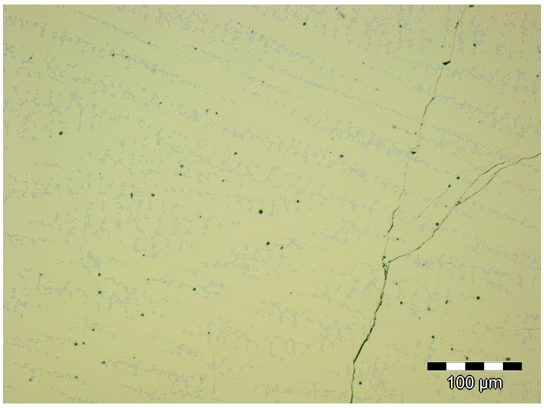

(4) No. 3 (brightfield)

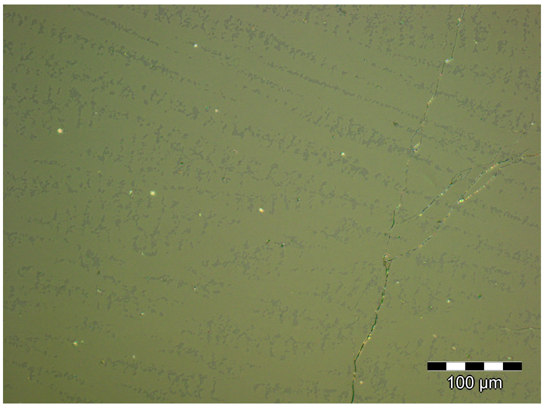

(5) No. 3 (polarized light)

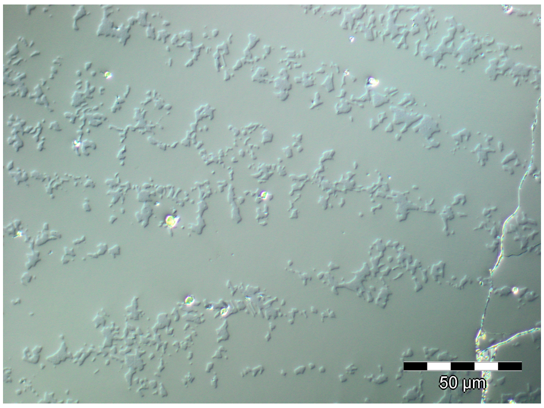

(6) No. 3 (DIC)

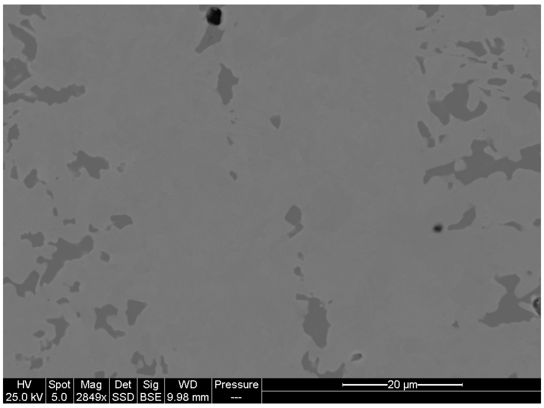

(7) No. 3 (SEM, BSE)

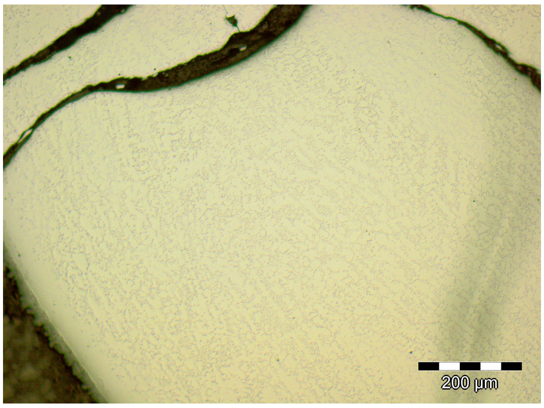

(8) No. 4 (brightfield)

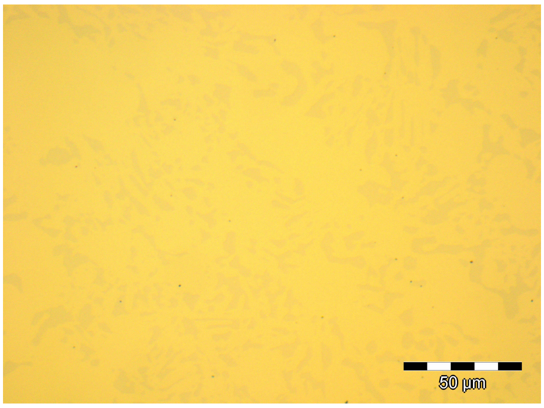

(9) No. 4 (brightfield)

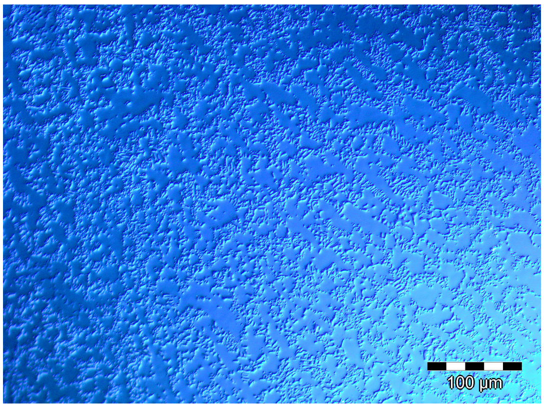

(10) No. 4 (DIC)

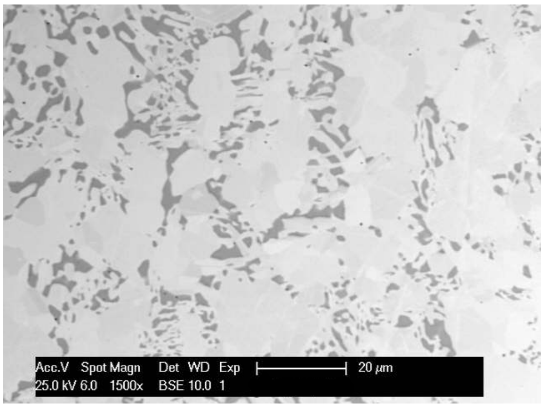

(11) No. 4 (SEM, BSE)

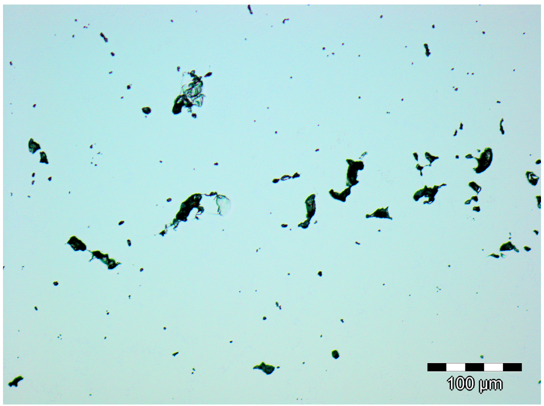

(12) No. 6 (brightfield)

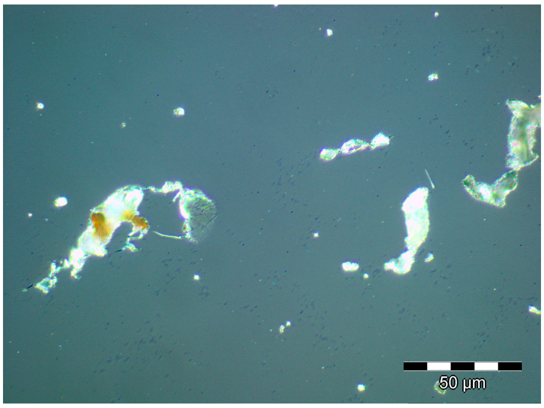

(13) No. 6 (polarized light)

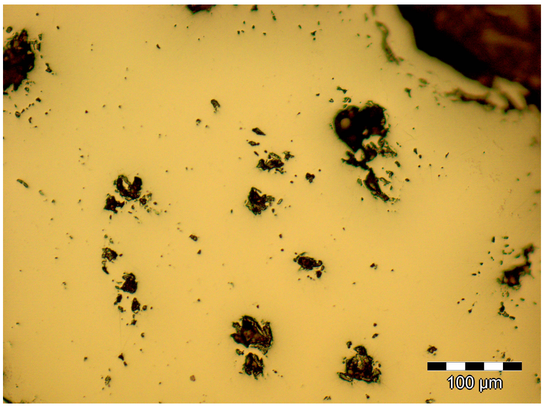

(14) No. 7 (brightfield)

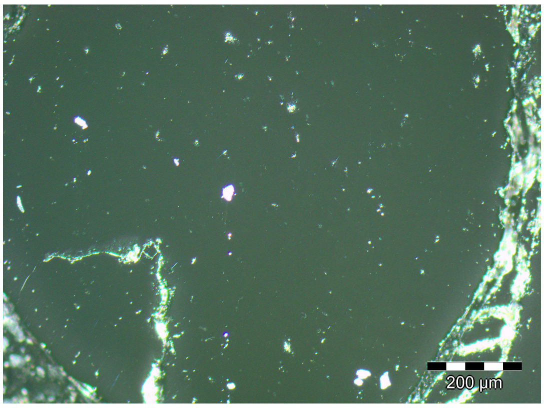

(15) No. 7 (polarized light)

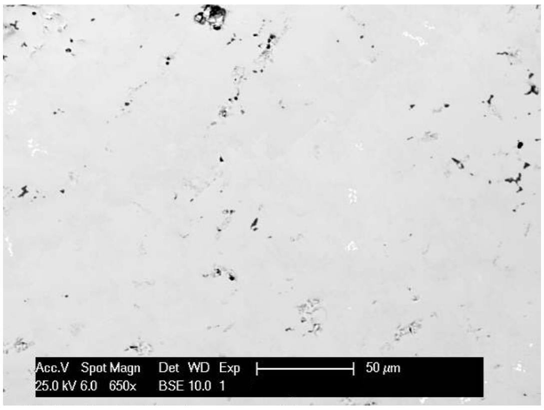

(16) No. 7 (SEM, BSE)

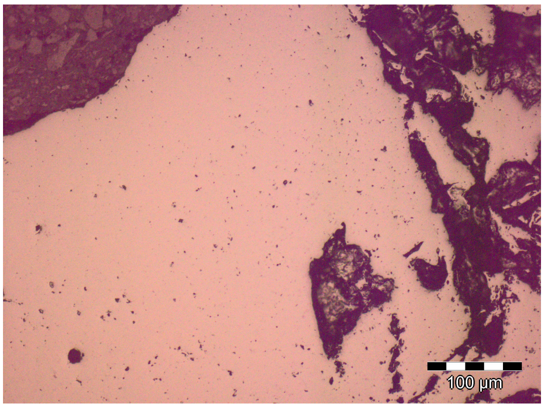

(17) No. 10 (brightfield)

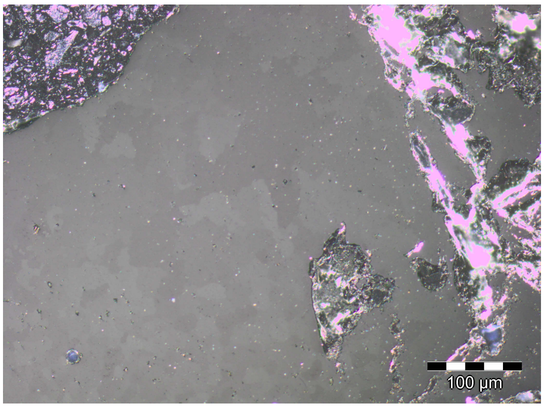

(18) No. 10 (polarized light)

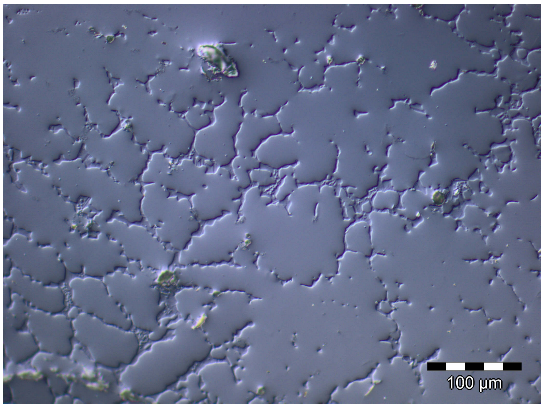

(19) No. 10 (DIC)

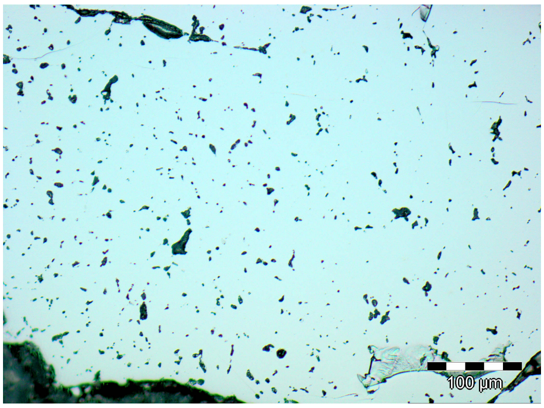

(20) No. 11 (brightfield)

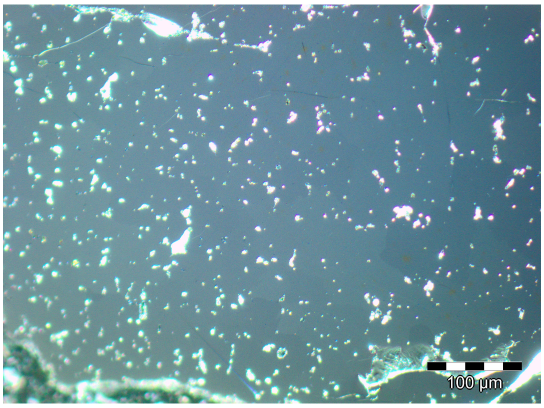

(21) No. 11 (polarized light)

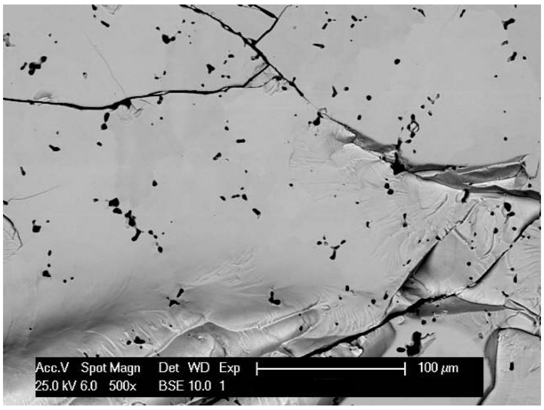

(22) No. 11 (SEM, BSE)

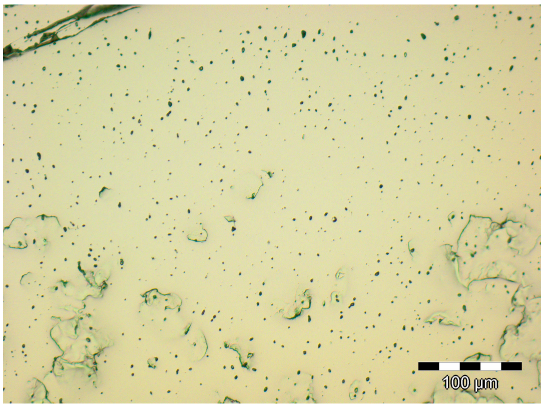

(23) No. 13 (brightfield)

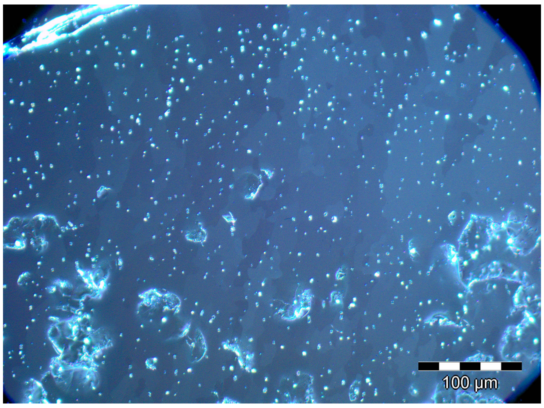

(24) No. 13 (polarized light)

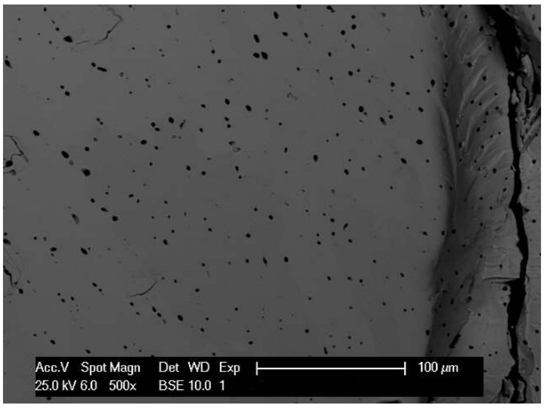

(25) No. 13 (SEM, BSE)

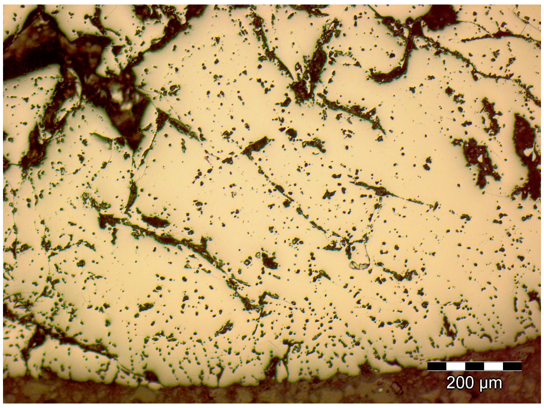

(26) No. 15 (brightfield)

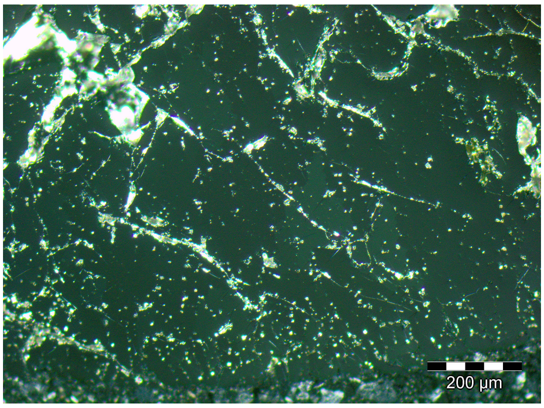

(27) No. 15 (polarized light)

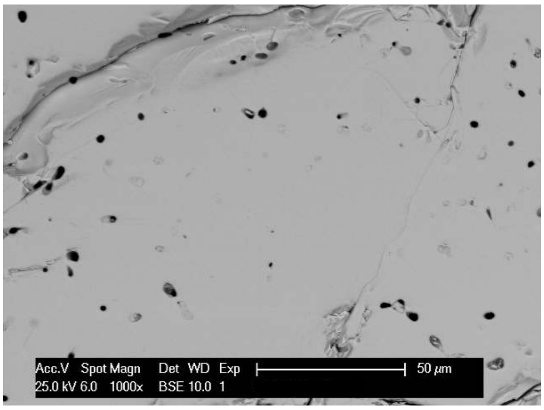

(28) No. 15 (SEM, BSE)

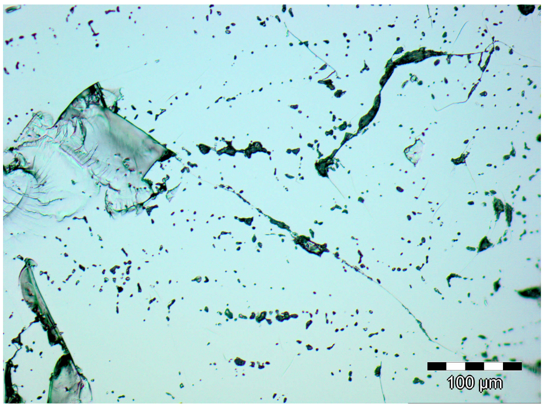

(29) No. 16 (brightfield)

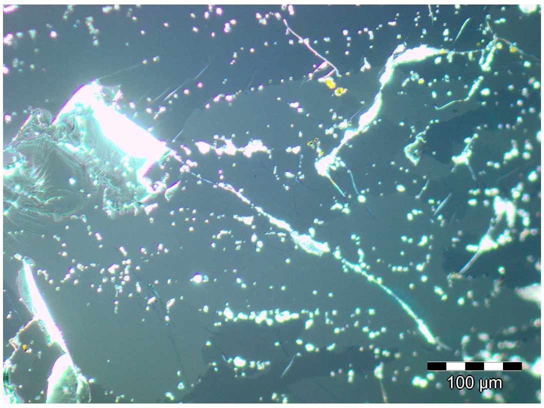

(30) No. 16 (polarized light)

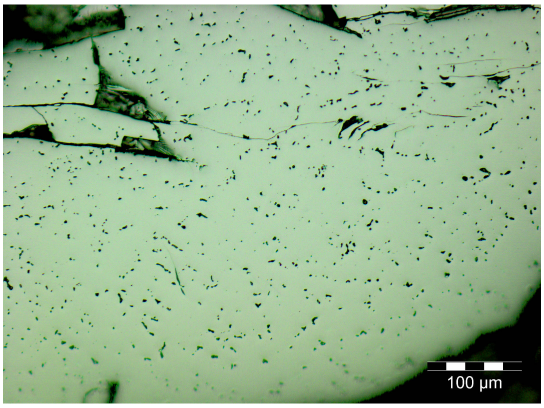

(31) No. 17 (brightfield)

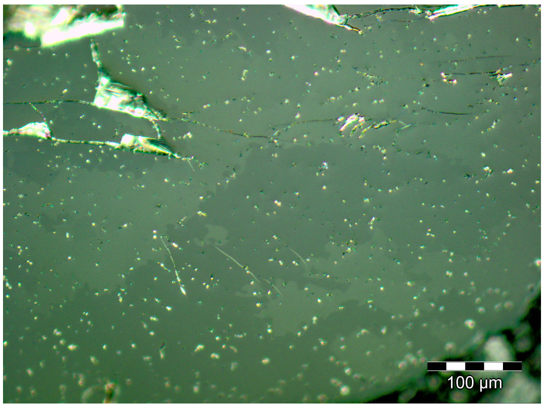

(32) No. 17 (polarized light)

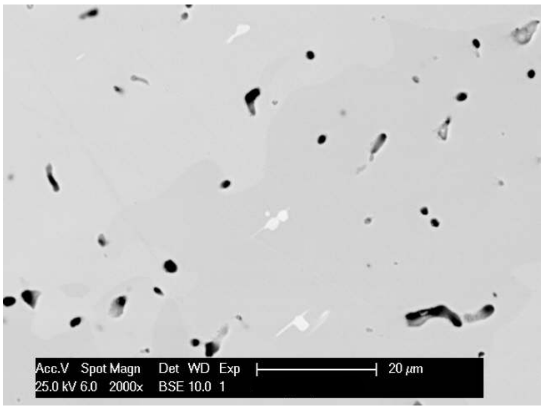

(33) No. 17 (SEM, BSE)

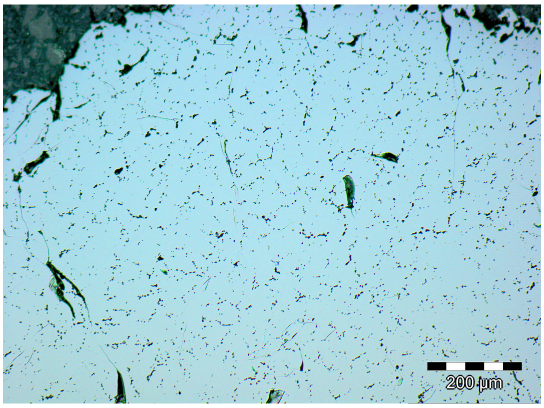

(34) No. 19 (brightfield)

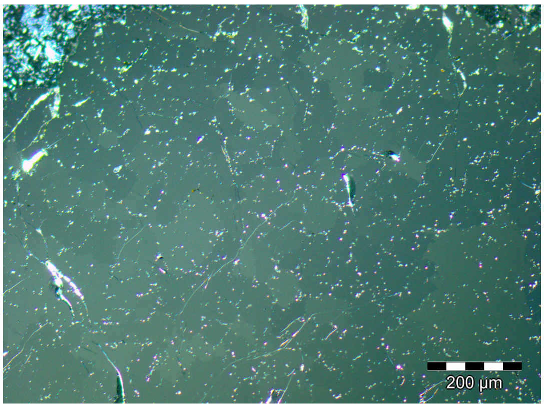

(35) No. 19 (polarized light)

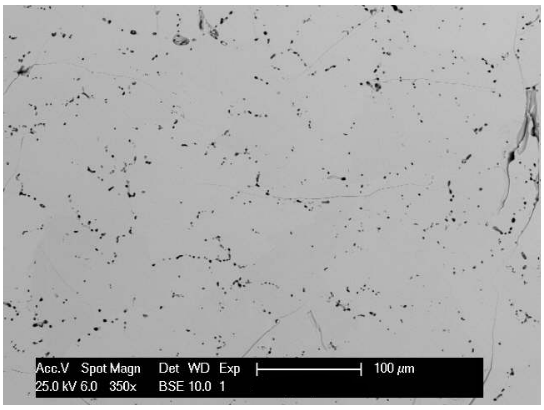

(36) No. 19 (SEM, BSE)

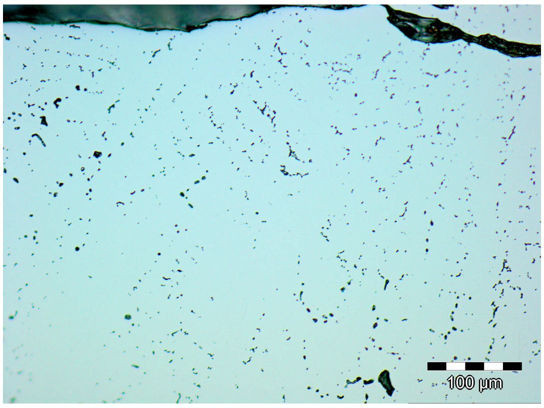

(37) No. 20 (brightfield)

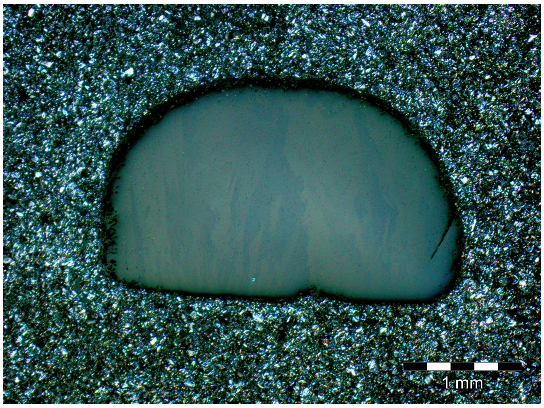

(38) No. 21 (polarized light)

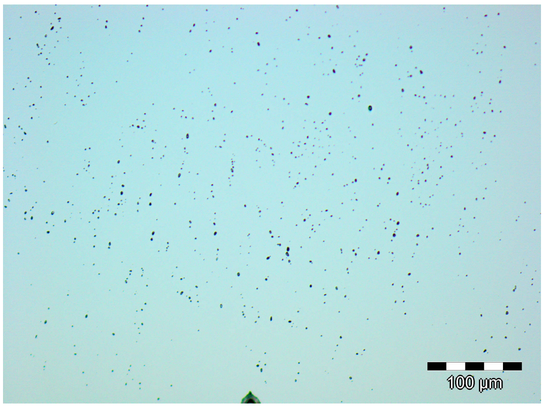

(39) No. 21 (brightfield)

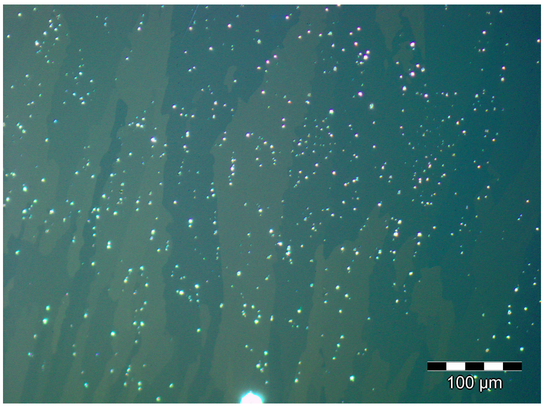

(40) No. 21 (polarized light)

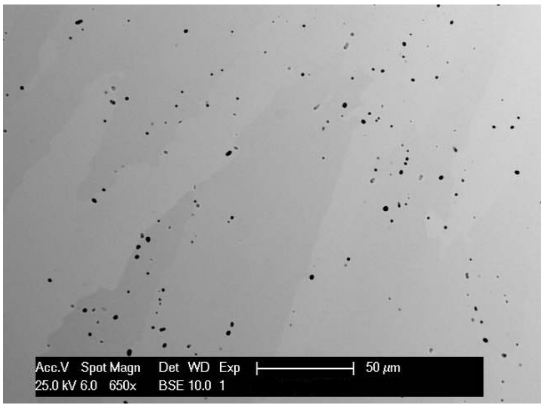

(41) No. 21 (SEM, BSE)

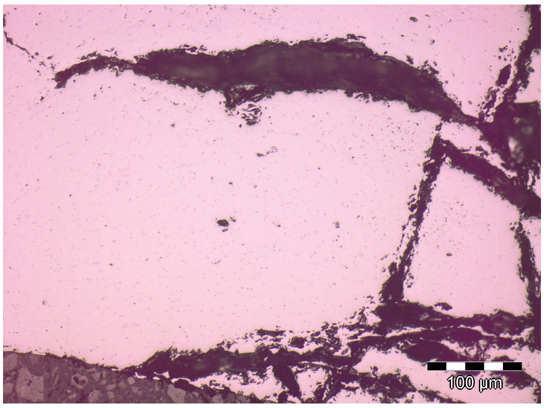

(42) No. 22 (brightfield)

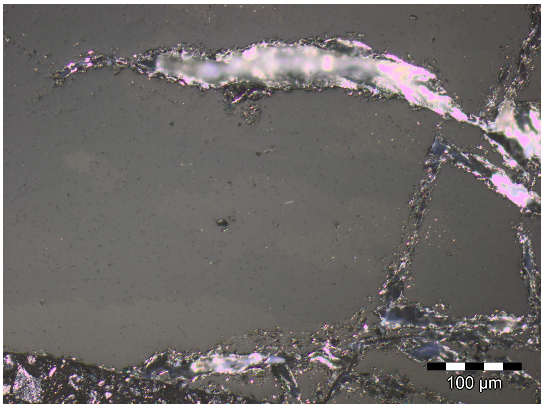

(43) No. 22 (polarized light)

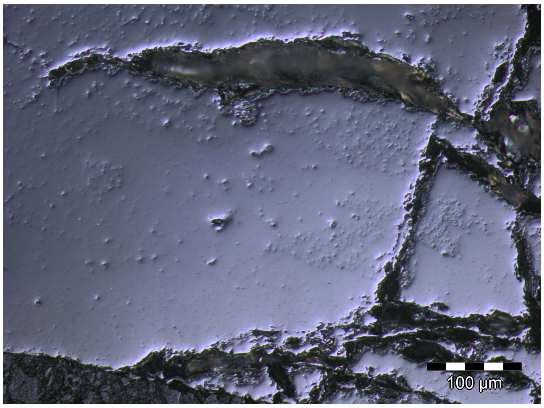

(44) No. 22 (DIC)

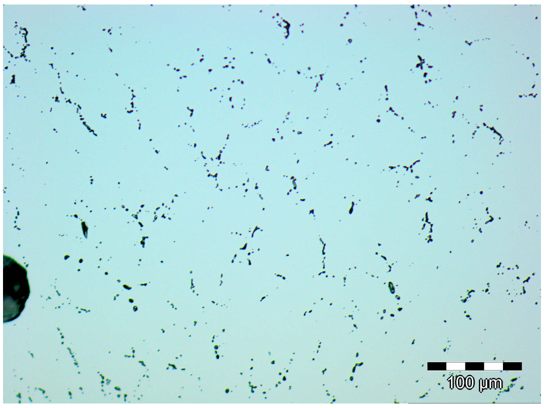

(45) No. 23 (brightfield)

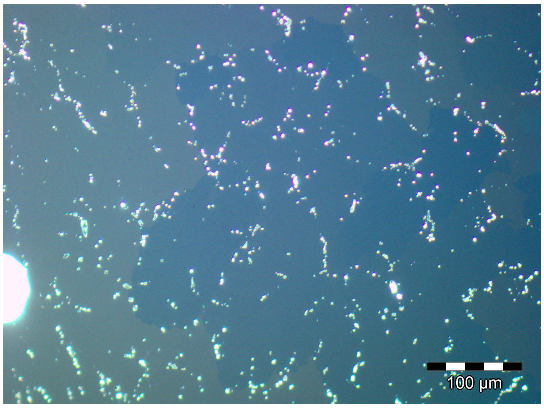

(46) No. 23 (polarized light)

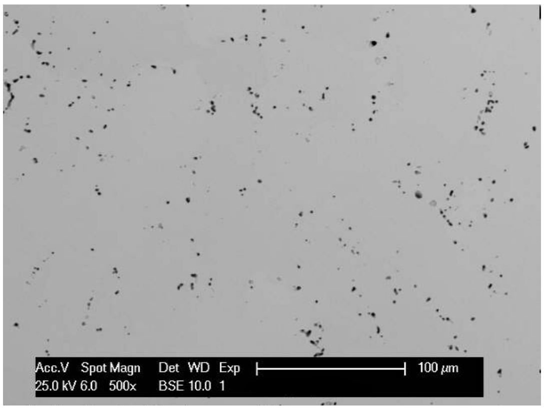

(47) No. 23 (SEM, BSE)

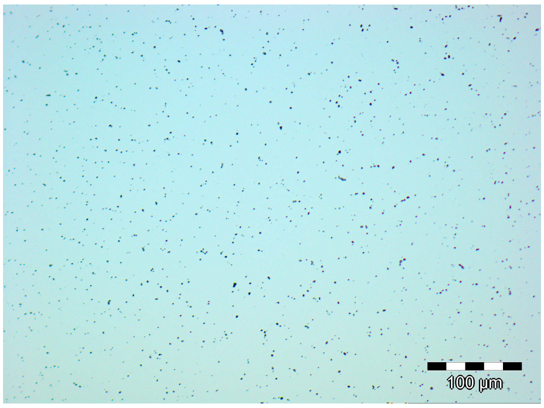

(48) No. 24 (brightfield)

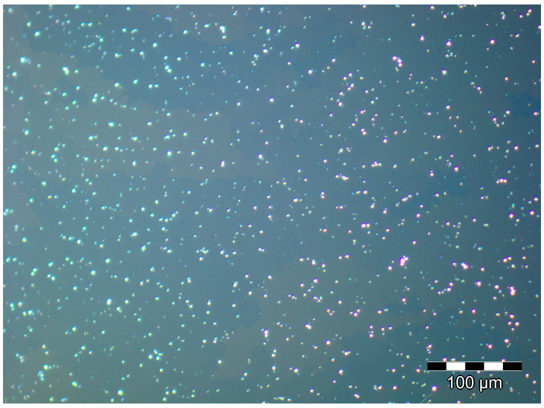

(49) No. 24 (polarized light)

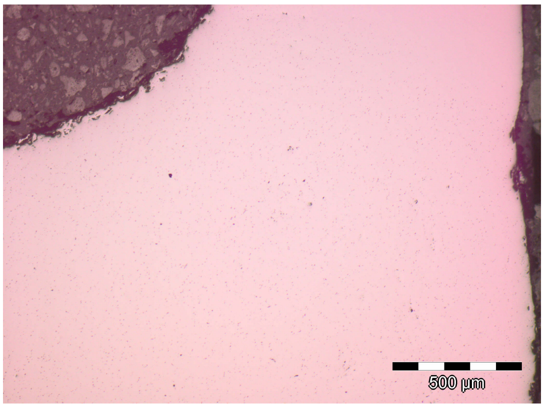

(50) No. 25 (brightfield)

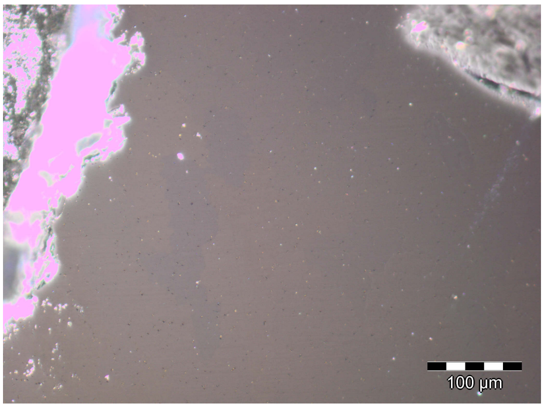

(51) No. 25 (polarized light)

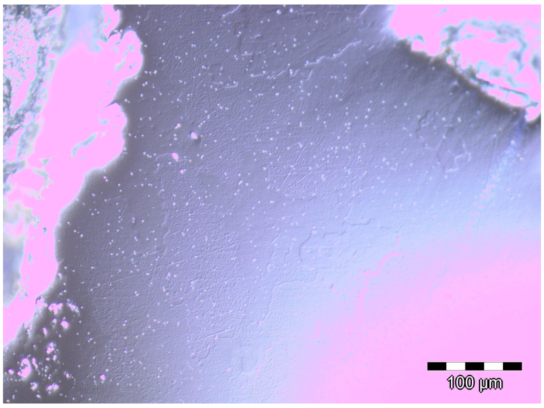

(52) No. 25 (DIC)

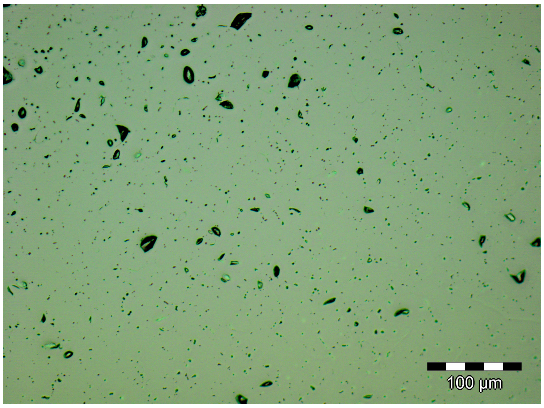

(53) No. 28 (brightfield)

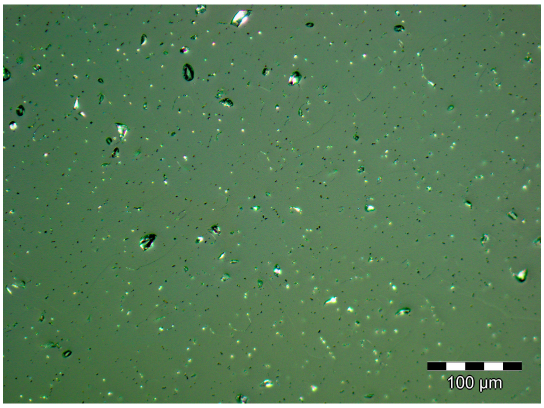

(54) No. 28 (polarized light)

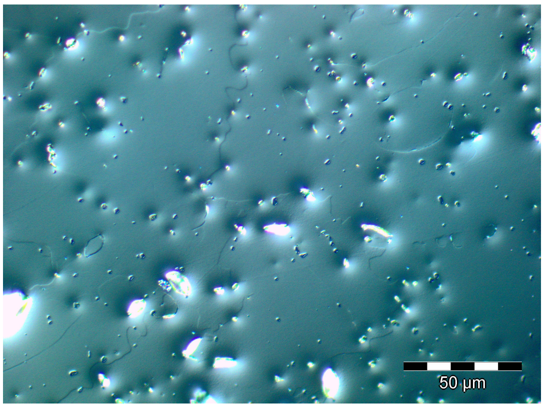

(55) No. 28 (DIC)

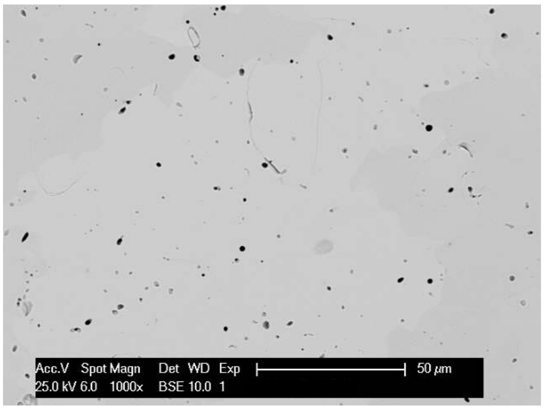

(56) No. 28 (SEM, BSE)

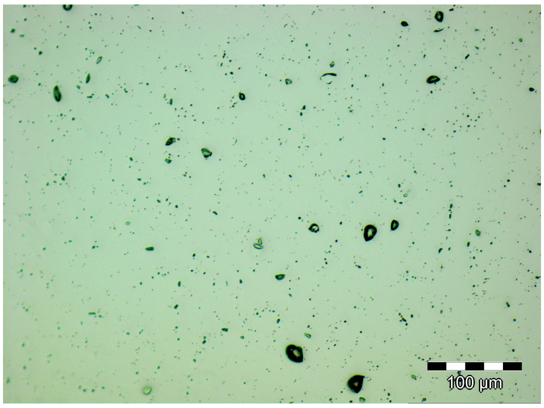

(57) No. 30 (brightfield)

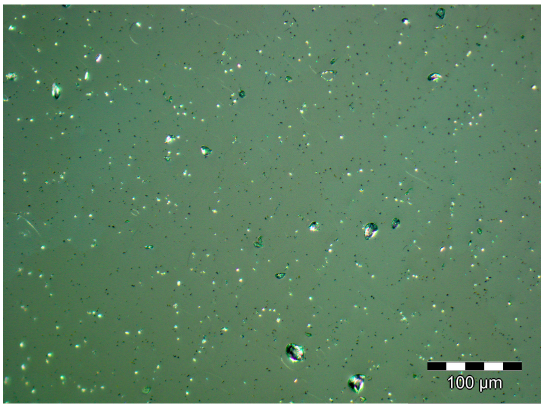

(58) No. 30 (polarized light)

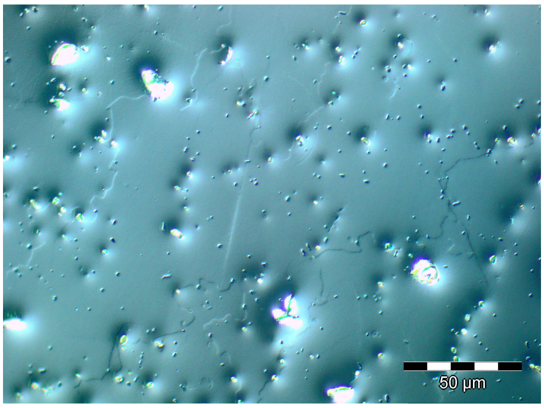

(59) No. 30 (DIC)

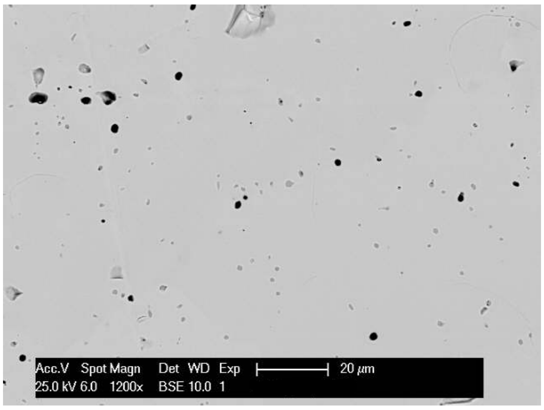

(60) No. 30 (SEM, BSE)

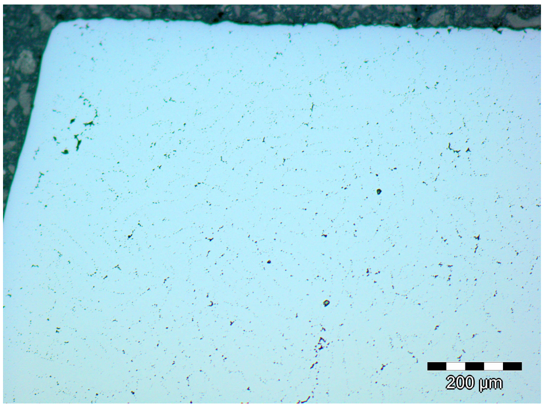

(61) No. 31 (brightfield)

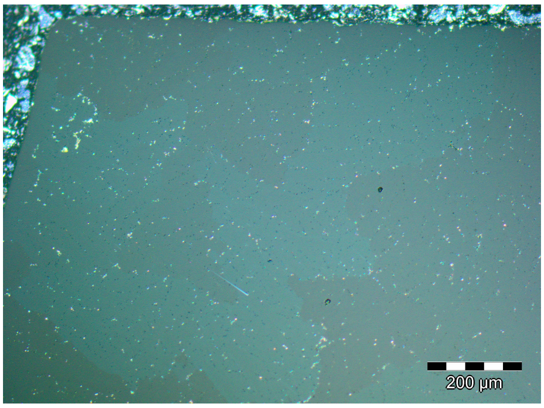

(62) No. 31 (polarized light)

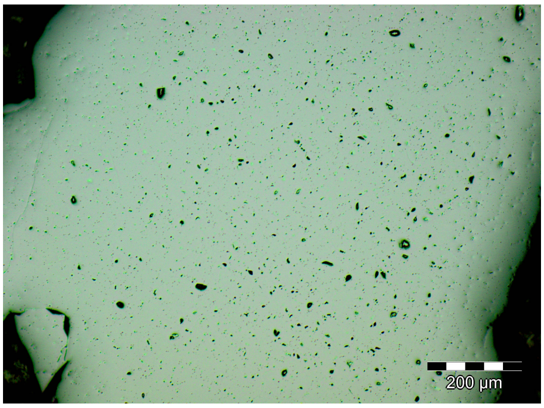

(63) No. 32 (brightfield)

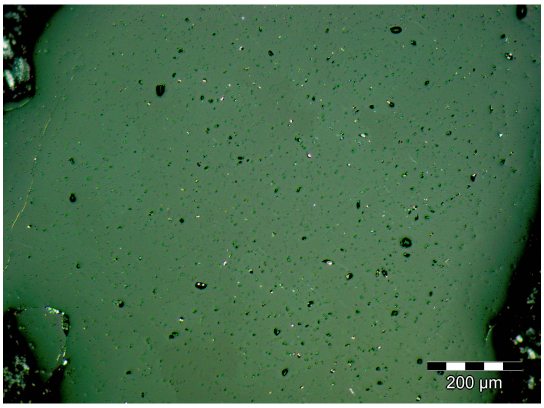

(64) No. 32 (polarized light)

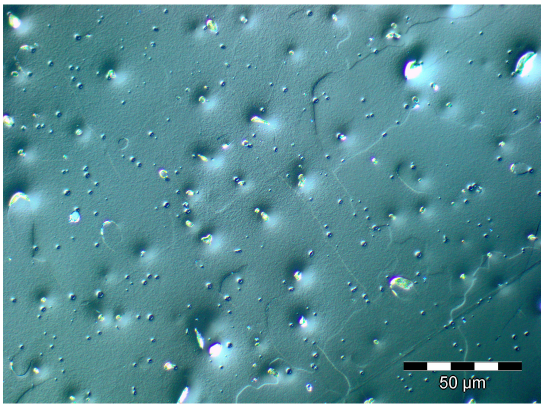

(65) No. 32 (DIC)

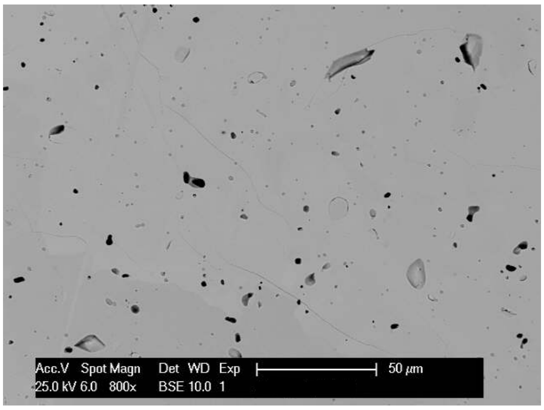

(66) No. 32 (SEM, BSE)

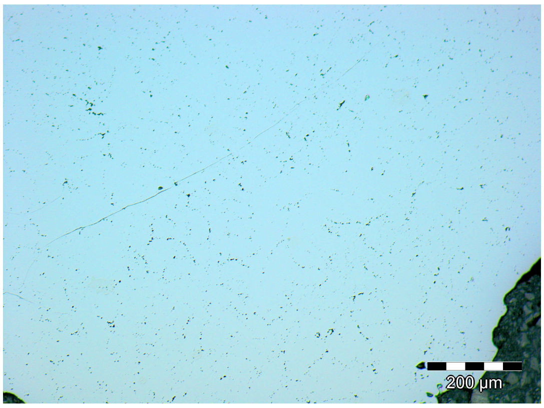

(67) No. 33 (brightfield)

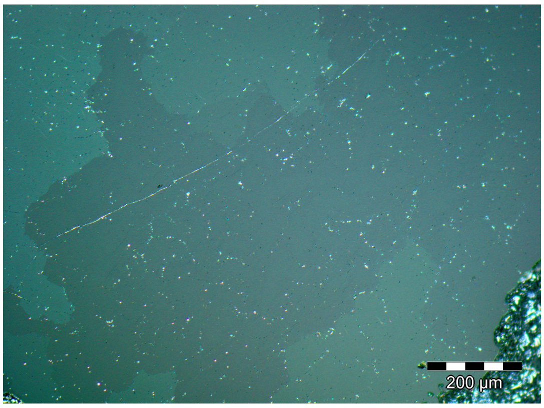

(68) No. 33 (polarized light)

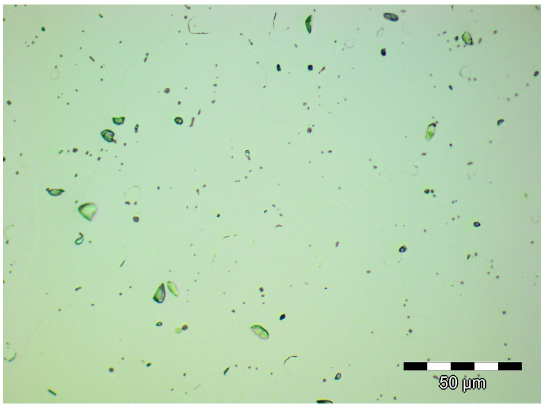

(69) No. 34 (brightfield)

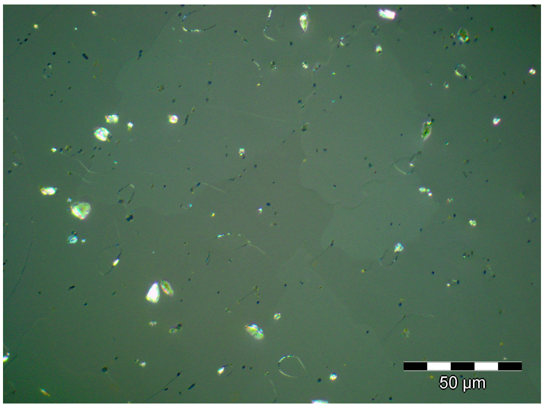

(70) No. 34 (polarized light)

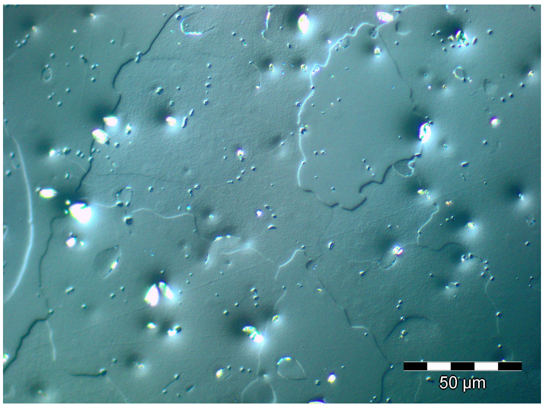

(71) No. 34 (DIC)

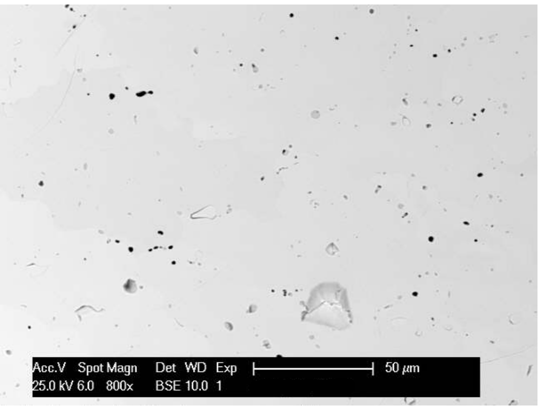

(72) No. 34 (SEM, BSE)

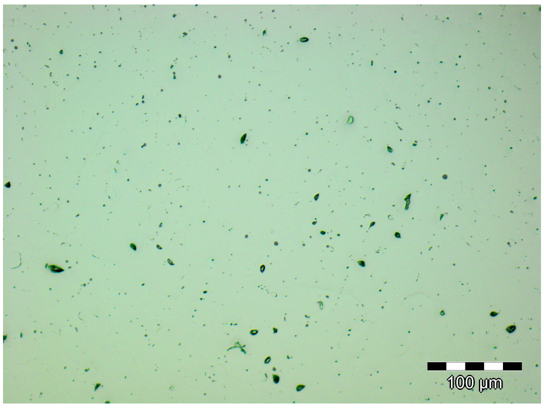

(73) No. 35 (brightfield)

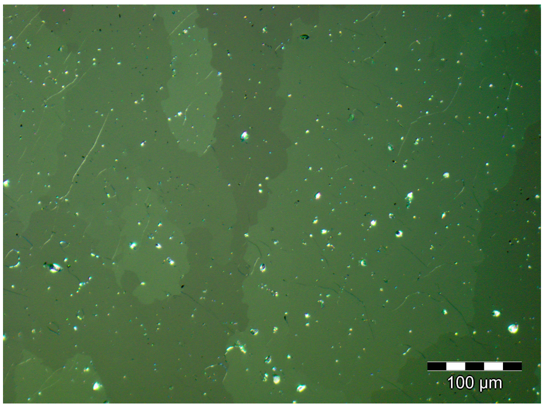

(74) No. 35 (polarized light)

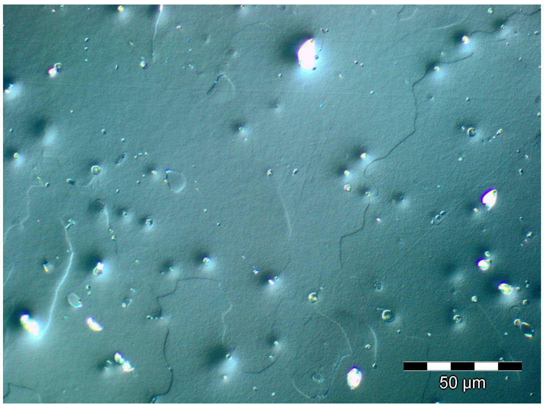

(75) No. 35 (DIC)

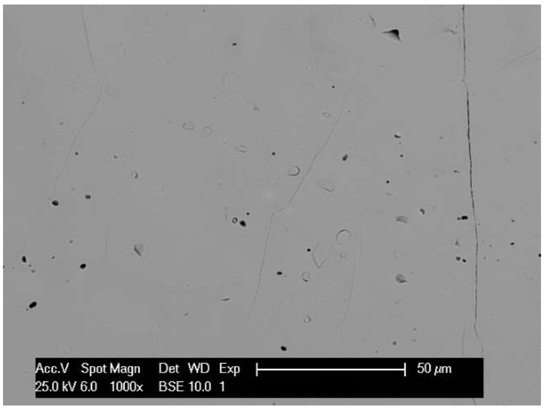

(76) No. 35 (SEM, BSE)

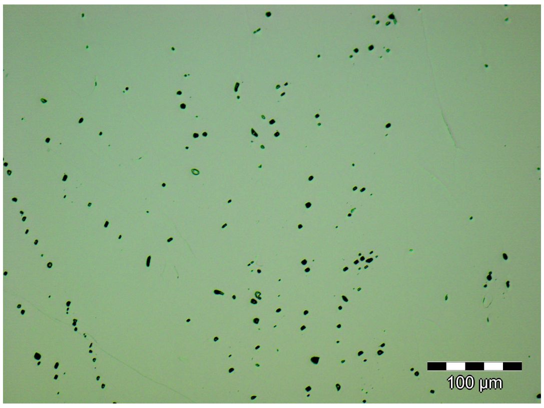

(77) No. 36 (brightfield)

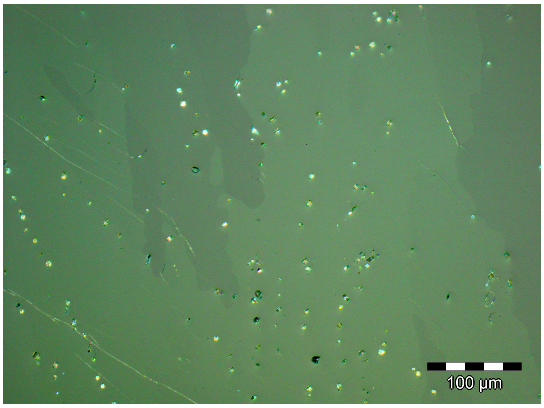

(78) No. 36 (polarized light)

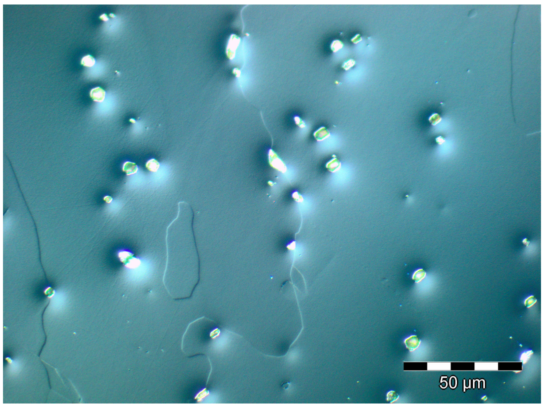

(79) No. 36 (DIC)

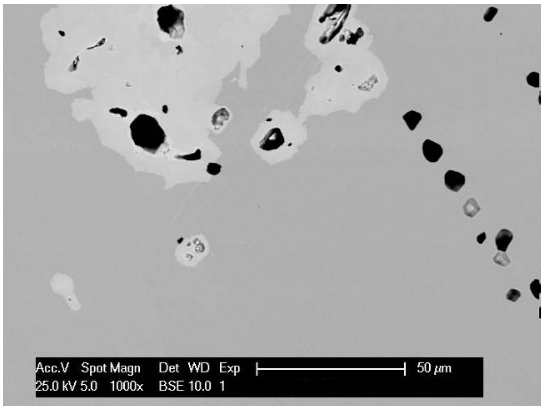

(80) No. 36 (SEM, BSE)

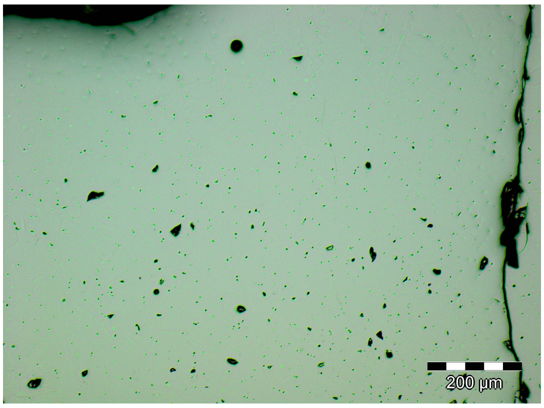

(81) No. 38 (brightfield)

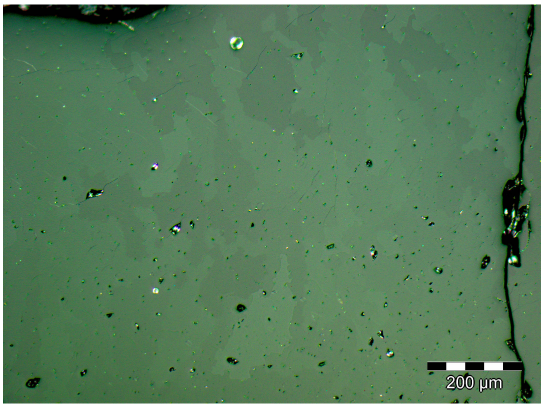

(82) No. 38 (polarized light)

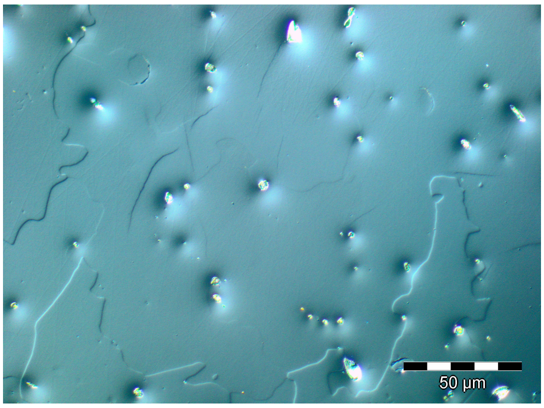

(83) No. 38 (DIC)

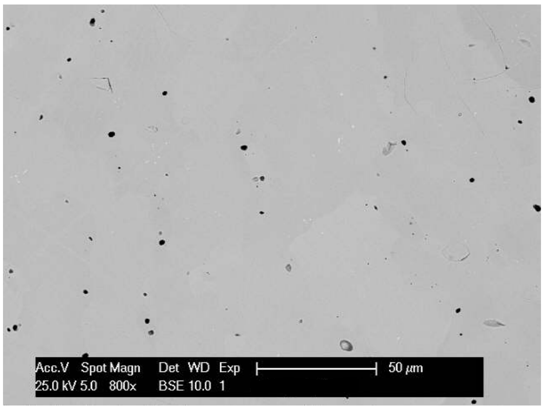

(84) No. 38 (SEM, BSE)

Bibliography

[1] G. E. R. Schulze, *Metallphysik*, Akademie-Verlag **1967**.

[2] M. Brando, W. J. Duncan, D. Moroni-Klementowicz, C. Albrecht, D. Grüner, R. Ballou, F. M. Grosche, Logarithmic Fermi-Liquid Breakdown in $NbFe_2$, *Physical Review Letters* **2008**, *101*(2), 026401.

[3] Y. Horie, S.-i. Kawashima, Y. Yamada, G. Obara, T. Nakamura, Magnetic properties of $Ta(Fe_{1-x}T_x)_2$ with T=V, Cr, Mn, Co and Ni, *Journal of Physics: Conference Series* **2010**, *200*(3), 032078.

[4] J. Zhu, *Metallurgical Factors Controlling the Phase Stability and Mechanical Behavior of Transition-Metal Laves Alloy Systems*, Dissertation, University of Tennesse, Knoxville, USA **1998**.

[5] W. Y. Kim, I. D. Yeo, M. S. Kim, T. Takasugi, Phase relation and room temperature mechanical property of Cr_2Zr based laves phase, Kang, S. G. and Kobayashi, T. (Editor), *Designing, Processing and Properties of Advanced Engineering Materials, PTS 1 and 2*, volume 449–4 of *Materials Science Forum* **2004** pages 805–808.

[6] Materials Genome – Accelerating materials discovery through advanced scientific computing and innovative design tools, `http://www.materialsgenome.org`, last accessed 07/18/2011.

[7] T. Kalil, C. Wadia, Materials Genome Initiative: A Renaissance of American Manufacturing, `http://www.whitehouse.gov/blog/2011/06/24/materials-genome-initiative-renaissance-american-manufacturing`, last accessed 07/18/2011.

[8] J. P. Holdre, Materials Genome Initiative for Global Competitiveness, *Executive Office of the President of the Unites States, National Science and Technology Council* **2011**.

[9] J. B. Friauf, The crystal structures of two intermetallic compounds, *Journal of the American Chemical Society* **1927**, *49*(Part 2), 3107–3114.

[10] J. B. Friauf, The crystal structure of magnesium di-zincide, *Physical Review* **1927**, *29*(1), 0034–0040.

[11] F. Laves, H. Witte, Die Kristallstruktur des $MgNi_2$ und seine Beziehung zu den Typen des $MgCu_2$ und $MgZn_2$, *Metallwirtschaft* **1935**, *14*, 645–649.

[12] G. E. R. Schulze, Zur Kristallchemie der intermetallischen AB_2-Verbindungen (Laves-Phasen), *Zeitschrift für Elektrochemie und angewandte physikalische Chemie* **1939**, *45*(12), 849–865.

[13] S. Samson, *Developments in the Structural Chemistry of Alloy Phases*, pages 65–106, Plenum Press **1969**.

[14] W. Borchardt-Ott, *Kristallographie. Eine Einführung für Naturwissenschaftler*, Springer **1997**.

[15] F. Stein, M. Palm, G. Sauthoff, Structure and stability of Laves phases. Part I. Critical assessment of factors controlling Laves phase stability, *Intermetallics* **2004**, *12*(7–9), 713–720.

[16] F. C. Frank, J. S. Kasper, Complex alloy structures regarded as sphere packing 1. Definitions and basic principles, *Acta Crystallographica* **1958**, *11*(3), 184–190.

[17] F. C. Frank, J. S. Kasper, Complex alloy structures regarded as sphere packing 2. Analysis and classification of representative structures, *Acta Crystallographica* **1959**, *12*(7), 483–499.

[18] P. Paufler, Early work on Laves phases in East Germany, *Intermetallics* **2011**, *19*(4), 599–612.

[19] Y. Komura, Stacking Faults and Two New Modifications of the Laves Phase in Mg–Cu–Al System, *Acta Crystallographica* **1962**, *15*, 770–778.

[20] Y. Komura, M. Mitarai, I. Nakatani, H. Iba, T. Shimuzu, Structural Changes in the Alloy Systems of Mg–Zn–Cu and Mg–Zn–Ag Related to the Friauf-Laves Phases, *Acta Crystallogr. B* **1970**, *26*, 666–668.

[21] Y. Komura, A. Nakaue, M. Mitarai, Crystal Structure of an New Stacking Variant of a Friauf-Laves Phase in the System Mg–Cu–Ni, *Acta Crystallogr. B* **1972**, *28*, 727–732.

[22] Y. Komura, M. Mitarai, A. Nakaue, S. Tsujimoto, The Relation between Electron Concentration and Stacking Variants in the Alloy Systems Mg–Cu–Ni, Mg–Cu–Zn and Mg–Ni–Zn, *Acta Crystallogr. B* **1972**, *28*, 976–978.

[23] Y. Komura, Y. Kitano, Long-Period Stacking Variants and their Electron-Concentration Dependence in the Mg-Base Friauf Laves Phases, *Acta Crystallogr. B* **1977**, *33*, 2496–2501.

[24] Y. Komura, K. Tokunaga, Structural Studies of Stacking Variants in Mg-base Friauf-Laves Phases, *Acta Crystallogr. B* **1980**, *36*, 1548–1554.

[25] Y. Komura, E. Kishida, M. Inoue, The Crystal Structure of the Laves Phase in the Mg–Zn–Ag-System. I, *J. Phys. Soc. Jpn* **1967**, *23*, 398–404.

[26] S. Amerioun, S. I. Simak, U. Häussermann, Laves-Phase Structural Changes in the System $CaAl_{2-x}Mg_x$, *Inorganic Chemistry* **2003**, *42*(5), 1467–1474.

[27] F. Stein, A. Palm, G. Sauthoff, Structure and stability of Laves phases part II - structure type variations in binary and ternary systems, *Intermetallics* **2005**, *13*(10), 1056–1074.

[28] J. G. C. Neto, S. G. Fries, H. L. Lukas, S. Gama, G. Effenberg, Thermodynamic Optimisation of the Nb–Cr System, *Calphad – Computer Coupling of Phases Diagrams and Thermochemistry* **1993**, *17*(3), 219–228.

[29] J. M. Aufrecht, *Phase Transformations in the $NbCr_2$ and $HfCr_2$ Laves Phases*, Dissertation, Universität Stuttgart **2010**.

[30] J. Aufrecht, A. Leineweber, A. Senyshyn, E. J. Mittemeijer, The absence of a stable hexagonal Laves phase modification ($NbCr_2$) in the Nb–Cr system, *Scripta Materialia* **2010**, *62*(5), 227–230.

[31] X.-w. Nie, Comments on The absence of a stable hexagonal Laves phase modification ($NbCr_2$) in the Nb–Cr system, *Scripta Materialia* **2011**, *64*(10), 990–993.

[32] A. Leineweber, J. Aufrecht, A. Senyshyn, E. J. Mittemeijer, Reply to comments on the absence of a stable hexagonal Laves phase modification ($NbCr_2$) in the Nb–Cr system, *Scripta Materialia* **2011**, *64*(10), 994–997.

[33] F. Stein, D. Jiang, M. Palm, G. Sauthoff, D. Grüner, G. Kreiner, Experimental reinvestigation of the Co–Nb phase diagram, *Intermetallics* **2008**, *16*(6), 785–792.

[34] J. Gschneidner, A. Karl, V. K. Pecharsky, Binary rare earth Laves phases - an overview, *Zeitschrift für Kristallographie* **2006**, *221*(5–7), 375–381.

[35] M. Palm, G. Inden, N. Thomas, The Fe–Al–Ti system, *Journal of Phases Equlibria* **1995**, *16*(3), 209–222.

[36] F. Chu, D. J. Thoma, P. G. Kotula, S. Gerstl, T. E. Mitchell, I. M. Anderson, J. Bentley, Phase stability and defect structure of the C15 Laves phase $Nb(Cr,V)_2$, *Acta Materialia* **1998**, *46*(5), 1759–1769.

[37] Q. Yao, H. Xing, S. Liu, J. Sun, Theoretical prediction of ternary site occupancies in $ZrCr_2$ and $NbCr_2$ Laves phases, *2006 BIMW: 2006 Beijing International Materials Week, Pts 1-4 - Magnesium - Aluminium Materials - Aerospace Materials - Superconducting and Functional Materials*, volume 546–549 of *Materials Science Forum* **2007** pages 1451–1454.

[38] Q. Yao, J. Sun, D. Lin, S. Liu, B. Jiang, First-principles studies of defects, mechanical properties and electronic structure of Cr-based Laves phases, *Intermetallics* **2007**, *15*(5-6), 694–699.

[39] Q. Yao, J. Sun, Y. Zhang, B. Jiang, First-principles studies of ternary site occupancy in the C15 $NbCr_2$ Laves phase, *Acta Materialia* **2006**, *54*(13), 3585–3591.

[40] M. Palm, W. Sanders, G. Sauthoff, Phase equilibria in the Ni–Al–Ta system, *Zeitschrift für Metalkunde* **1996**, *87*(5), 390–398.

[41] X. Yan, X. Q. Chen, A. Grytsiv, P. Rogl, R. Podloucky, V. Pomjakushin, H. Schmidt, G. Giester, Crystal structure, phase stability and elastic properties of the Laves phase $ZrTiCu_2$, *Intermetallics* **2008**, *16*(5), 651–657.

[42] A. Grytsiv, X.-Q. Chen, V. T. Witusiewicz, P. Rogl, R. Podloucky, V. Pomjakushin, D. Maccio, A. Saccone, G. Giester, F. Sommer, Atom order and thermodynamic properties of the ternary Laves phase $Ti(Ti_yNi_xAl_{1-x-y})_2$, *Zeitschrift für Kristallographie* **2006**, *221*(5–7), 334–348.

[43] M. Bououdina, B. Lambert-Andron, B. Ouladdiaf, S. Pairis, D. Fruchart, Structural investigations by neutron diffraction of equi-atomic Zr–Ti(V)–Ni(Co) compounds and their related hydrides, *Journal of Alloys and Compounds* **2003**, *356*, 54–58.

[44] D. Akhtar, R. Gopalan, T. P. Rajasekharan, On a New Metastable Phase in the Al–Mg System, *Zeitschrift für Metallkunde* **1987**, *78*, 201–203.

[45] F. Chu, D. P. Pope, The Laves Phase Field in the Hf–V–Nb System, *Scripta Metallurgica et Materialia* **1992**, *26*(3), 399–404.

[46] X. G. Yang, Y. Q. Lei, W. K. Zhang, G. M. Zhu, Q. D. Wang, Effect of alloying with Ti, V, Mn on the electrochemical properties of Zr–Cr–Ni based Laves phase metal hydride electrodes, *Journal of Alloys and Compounds* **1996**, *243*(1–2), 151–155.

[47] A. M. Gabay, V. S. Gaviko, Ferromagnetic $Zr_{1-x}Mn_xCo_2$ laves phase compounds, *Journal of Magnetism and Magnetic Materials* **2003**, *260*(3), 425–430.

[48] J. G. Faller, L. P. Skolnick, Atomic Arrangements in the C14 laves phase $Zr(VCo)_2$, *Transactions of the Metallurgical Society of Aime* **1963**, *227*(3), 687–695.

[49] A. E. Dwight, C. W. Kimball, R. S. Preston, S. P. Taneja, L. Weber, Crystallographic and Mössbauer Study of (Sc, Y, Ln) (Fe, Al)$_2$ Intermetallic Compounds, *Journal of Less-Common Metals* **1975**, *40*(3), 285–291.

[50] K. H. Lieser, H. Witte, Untersuchungen in den ternären Systemen Magnesium-Kupfer-Zink, Magnesium-Nickel-Zink und Magnesium-Kupfer-Nickel, *Zeitschrift für Metallkunde* **1952**, *43*(11), 396–401.

[51] E. Stein, G. Sauthoff, M. Palm, Phases and phase equilibria in the Fe–Al–Zr system, *Zeitschrift für Metallkunde* **2004**, *95*(6), 469–485.

[52] D. Grüner, *Untersuchungen zur Natur der Laves-Phasen in Systemen der Übergangsmetalle*, Dissertation, Technische Universität Dresden **2007**.

[53] J. H. Zhu, C. T. Liu, L. M. Pike, P. K. Liaw, Enthalpies of formation of binary Laves phases, *Intermetallics* **2002**, *10*(6), 579–595.

[54] A. Ormeci, A. Simon, Y. Grin, Topologie der Kristallstruktur und chemische Bindung in Laves-Phasen, *Angewandte Chemie* **2010**, *122*(47), 9182–9186.

[55] H. Erschbaumer, R. Podloucky, P. Rogl, G. Temnitschka, R. Wagner, Atomic modelling of Nb, V, Cr, and Mn substitutions in γ-TiAl. 1: c/a-ratio and site preference, *Intermetallics* **1993**, *1*(2), 99–106.

[56] M. H. F. Sluiter, K. Esfarjani, Y. Kawazoe, Site occupation reversal in the Fe-Cr σ-phase, *Physical Review Letters* **1995**, *75*(17), 3142–3145.

[57] Y. L. Hao, R. Yang, Y. Y. Cui, D. Li, The effect of Ti/Al ratio on the site occupancies of alloying elements in γ-TiAl, *Intermetallics* **2000**, *8*(5–6), 633–636.

[58] C. Jiang, D. J. Sordelet, B. Gleeson, Site preference of ternary alloying elements in Ni_3Al: A first-principles study, *Acta Materialia* **2006**, *54*(4), 1147–1154.

[59] C. Jiang, B. Gleeson, Site preference of transition metal elements in Ni_3Al, *Scripta Materialia* **2006**, *55*(5), 433–436.

[60] S. B. Legoas, S. Frota-Pessôa, Site preference energies for 3d impurities in $ZrFe_2$, *Physical Review B* **2000**, *61*(19), 12566–12569.

[61] P. G. Kotula, C. B. Carter, K. C. Chen, D. J. Thoma, F. Chu, T. E. Mitchell, Defects and site occupancies in Nb–Cr–Ti C15 laves phase alloys, *Scripta Materialia* **1998**, *39*(4–5), 619–623.

[62] H. Okaniwa, D. Shindo, M. Yoshida, T. Takasugi, Determination of site occupancy of additives X (X=V, Mo, W and Ti) in the Nb–Cr–X Laves phase by ALCHEMI, *Acta Materialia* **1999**, *47*(6), 1987–1992.

[63] C. Jiang, Site preference of early transition metal elements in C15 $NbCr_2$, *Acta Materialia* **2007**, *55*(5), 1599–1605.

[64] D. Grüner, F. Stein, M. Palm, J. Konrad, A. Ormeci, W. Schnelle, Y. Grin, G. Kreiner, Preparation, phase stability and structure of the C36 Laves phase $Nb_{1-x}Co_{2+x}$, *Zeitschrift für Kristallographie* **2006**, *221*(5–7), 319–333.

[65] G. Kreiner, D. Grüner, Y. Grin, F. Stein, M. Palm, A. Ormeci, Structure and Disorder of the Laves Phases in the Co–Nb System, Palm, M. and Bewlay, B. P. and He, Y. H. and Takeyama, M. and Wiezorek, J. M. K. (Editor), *Advanced Intermetallic-Based Alloys for Extreme Environment and Energy Applications*, volume 1128 of *Materials Research Society Symposium Proceedings* **2009** pages 487–492.

[66] M. Bououdina, J. Soubeyroux, D. Fruchart, P. de Rango, Structural studies of Laves phases $Zr(Cr_{1-x}Ni_x)_2$ with 0<=x<=0.4 and their hydrides, *Journal of Alloys and Compounds* **1997**, *257*(1–2), 82–90.

[67] O. Prymak, F. Stein, A. Kerkau, A. Ormeci, G. Kreiner, G. Frommeyer, D. Raabe, Phase equilibria in the ternary Nb-Cr-Al system and site occupation in the hexagonal C14 Laves phase $Nb(Al_xCr_{1-x})_2$, Palm, M. and Bewlay, B. P. and He, Y. H. and Takeyama, M. and Wiezorek, J. M. K. (Editor), *Advanced Intermetallic-Based Alloys for Extreme Environment and Energy Applications*, volume 1128 of *Materials Research Society Symposium Proceedings* **2009** pages 499–504.

[68] O. Dovbenko, F. Stein, M. Palm, O. Prymak, Experimental determination of the ternary Co–Al–Nb phase diagram, *Intermetallics* **2010**, *18*(11), 2191–2207.

[69] X.-L. Yan, X.-Q. Chen, A. Grytsiv, P. Rogl, R. Podloucky, H. Schmidt, G. Giester, X.-Y. Ding, On the ternary Laves phases $Ti(Mn_{1-x}Al_x)_2$ with $MgZn_2$-type, *Intermetallics* **2008**, *16*(1), 16–26.

[70] X. L. Yan, X. Q. Chen, A. Grytsiva, V. T. Witusiewicz, P. Rogl, R. Podloucky, V. Pomjakushin, G. Giester, Site preference, thermodynamic, and magnetic properties of the ternary Laves phase $Ti(Fe_{1-x}Al_x)_2$ with the crystal structure of the $MgZn_2$-type, *International Journal of Materials Research* **2006**, *97*(4), 450–460.

[71] X. Yan, A. Grytsiv, P. Rogl, H. Schmidt, G. Giester, The ternary Laves phase Nb($Ni_{1-x}Al_x$)$_2$ with $MgZn_2$-type, *Calphad-Computer Coupling of Phase Diagrams and Thermochemistry* **2009**, *33*(1), 11–16.

[72] M. Conrad, C. Pohling, H. Webert, B. Harbrecht, Atomic ordering in the Laves phases L1 V($Co_{1-x}Si_x$)$_2$ (x = 0.43 and 0.56), *Zeitschrift für Kristallographie* **2006**, *221*(5–7), 349–356.

[73] X. Yan, A. Grytsiv, P. Rogl, H. Schmidt, G. Giester, A. Saccone, X.-Q. Chen, Laves phases in the ternary systems Ti–{Pd, Pt}–Al, *Intermetallics* **2009**, *17*(5), 336–342.

[74] D. Mazzone, P. Manfrinetti, M. L. Fornasini, Phases in the Al–Yb–Zn system between 25 and 50 at.% ytterbium, *Journal of Solid State Chemistry* **2009**, *182*(9), 2344–2349.

[75] X. L. Yan, X.-Q. Chen, A. Grytsiv, V. T. Witusiewicz, P. Rogl, R. Podloucky, G. Giester, On the ternary Laves phases {Sc,Ti}$_2$M$_3$Si (M = Cr, Mn, Fe, Co, Ni) with $MgZn_2$-type, *Journal of Alloys and Compounds* **2007**, *429*(1–2), 10–18.

[76] S. Ishikawa, T. Matsuo, N. Takata, M. Takeyama, Site Occupation and Defect Structure of Fe_2Nb Laves Phase in Fe–Nb–M Ternary Systems at Elevated Temperatures, Palm, M and Bewlay, BP and He, YH and Takeyama, M and Wiezorek, JMK (Editor), *Advanced Iintermetallic-Based Alloys for Extreme Environment and Energy Applications*, volume 1128 of *Materials Research Society Symposium Proceedings*, Mat Res Soc **2009** pages 463–468, Symposium on Advanced Intermetallic-Based Alloys for Extreme Environment and Energy Applications held at the 2008 MRS Fall Meeting, Boston, MA, DEC 01-04, 2008.

[77] E. J. Gabe, Y. Le Page, J.-P. Charland, F. L. Lee, P. S. White, *NRCVAX* – an interactive program system for structure analysis, *Journal of Applied Crystallography* **1989**, *22*(4), 384–387.

[78] F. Laves, *Theory of Alloy Phases*, American Society of Metals **1955**.

[79] J. D. Sofo, J. P. Abriata, Ab initio calculation of the c/a ratio of hexagonal Cu–Zn alloys, Hernandez, S. and Clark, J. W. (Editor), *Condensed Matter Theories, Vol 16*, volume 16 of *Condensed Matter Theories* **2001** pages 101–108.

[80] K. Young, T. Ouchi, M. A. Fetcenko, Pressure-composition-temperature hysteresis in C14 Laves phase alloys: Part 1. Simple ternary alloys, *Journal of Alloys and Compounds* **2009**, *480*(2), 428–433.

[81] M. Venkatraman, J. Neumann, The Cr–Nb (Chromium-Niobium) system, *Journal of Phase Equilibria* **1986**, *7*, 462–466.

[82] J. Aufrecht, A. Leineweber, E. J. Mittemeijer, Metastable Hexagonal Modifications of the $NbCr_2$ Laves Phase as Function of Cooling Rate., *Materials Research Society Symposium Proceedings*, volume 1128 **2009** pages 481–486.

[83] H. Okamoto, Cr–Nb (Chromium-Niobium), *Journal of Phase Equilibria* **1993**, *14*, 534–535.

[84] D. J. Thoma, J. H. Perepezko, An experimental evaluation of the phase relationships and solubilities in the Nb–Cr system., *Materials Science and Engineering A* **1992**, *156*, 97–108.

[85] C. He, F. Stein, M. Palm, D. Raabe, Thermodynamic Re-assessment of the Co–Nb system, *Materials Research Society Symposium Proceedings*, volume 1128 **2009** pages 239–244.

[86] H. Okamoto, Co–Nb (Cobalt-Niobium), *Journal of Phase Equilibria and Diffusion* **2010**, *31*(1), 94–95.

[87] A. Leineweber, M. Leoni, Simulation of layer-faulting in Nb_2Co_7 intermetallic compound using DIFFaX, *Zeitschrift für Kristallographie* **2009**, *30*(Part 2 Suppl. 30), 423–428.

[88] L. Siggelkow, U. Burkhardt, G. Kreiner, M. Palm, F. Stein, Unusual mechanical behaviour of the intermetallic phase Nb_2Co_7, *Materials Science and Engineering A-Structural Materials Properties Microstructure and Processing* **2008**, *497*(1–2), 174–180.

[89] F. Stein, M. Palm, G. Frommeyer, P. Jain, S. Kumar, L. Siggelkow, D. Grüner, G. Kreiner, A. Leineweber, Microstructural Investigations of the Unusual Deformation Behavior of Nb_2Co_7, *Materials Research Society Symposium Proceedings*, volume 1128 **2009** pages 457–462.

[90] K. Gupta, The Co–Cr–Nb (Cobalt-Chromium-Niobium) system, *Journal of Phase Equilibria and Diffusion* **2006**, *27*, 173–177.

[91] J. M. Drapier, J. L. Brouver, D. Coutsouradis, Refractory metals und intermetallic precipitates in cobalt-chromium alloys, *Cobalt* **1965**, *27*, 59–72.

[92] E. Ganglberger, H. Nowotny, F. Benesovsky, Ternäre Phasen mit $MgZn_2$-Typ, *Monatshefte für Chemie / Chemical Monthly* **1965**, *96*, 1658–1659.

[93] N. I. Kaloev, E. M. Sokolvskaya, A. K. Abramyan, R. V. Kalagova, Isothermal section of the cobalt-chromium-niobium system at 1273 K, *Soviet Non-ferrous Metals Research* **1986**, *6*, 89–91.

[94] J. Smith, O. Carlson, The Ta–V (Tantalum-Vanadium) system, *Journal of Phase Equilibria* **1983**, *4*, 284–289.

[95] W. Rostoker, A. Yamamoto, A Survey of Vanadium Binary System, *Transactions of the American Society of Metals* **1954**, *146*, 1136–1167.

[96] J. F. Smith, C. O. N., *Binary Alloy Phase Diagrams, Second Edition*, pages 3434–3438, ASM International, Materials Park, Ohio **1990**.

[97] E. M. Savicky, J. V. Efimov, Supraleitende metallische Verbindungen und ihre Legierungen, *Monatshefte für Chemie / Chemical Monthly* **1972**, *103*, 270–287.

[98] A. P. Nefedov, E. M. Sokolovskaya, A. T. Grigor'ev, V. I. Chechernikov, I. Sokolova, L. S. Guzei, Phase transformations in the solid state in alloys of vanadium with tantalum, *Vestnik Moskovskogo Universiteta, Seriya 2: Khimiya* **1965**, *21*(5), 42–47.

[99] C. A. Danon, C. Servant, A thermodynamic evaluation of the Ta–V system, *Journal of Alloys and Compounds* **2004**, *366*(1–2), 191–200.

[100] J. Pavlů, J. Vřešťál, X.-Q. Chen, P. Rogl, Thermodynamic modeling of Laves phases in the Ta–V system: Reassessment using first-principles results, *Calphad – Computer Coupling of Phases Diagrams and Thermochemistry* **2011**, *35*(1), 103–108.

[101] H. Okamoto, Ta–V (Tantalum-Vanadium), *Journal of Phase Equilibria and Diffusion* **2005**, *26*, 298–299.

[102] P. Villars, Pauling File - Inorganic Materials Database and Design System, Computer program **2002**, version 1.0, Release 2002/1.

[103] L. Swartzendruber, E. Paul, The Fe–Ta (Iron-Tantalum) system, *Journal of Phase Equilibria* **1986**, *7*, 254–259.

[104] G. Coelho, J. Neto, S. Gama, C. Ribeiro, Experimental study of the iron-tantalum equilibrium diagram, *Journal of Phase Equilibria* **1995**, *16*, 121–128.

[105] A. M. Bardos, D. I. Bardos, P. A. Beck, The Effective Atomic Radius of Silicon in Ternary Laves Phase Alloys, *Transactions of the Metallurgical Society of AIME* **1963**, *227*, 991–993.

[106] Z. Blazina, S. Pavkovic, On Friauf-Laves Phases in the $Ta_{1-x}Al_xT_2$ and $Ta_{1-x}Si_xT_2$ (T = Cr, Mn, Fe, Co, Ni) Systems, *Journal of the Less Common Metals* **1989**, *155*(2), 247–253.

[107] K. Kuo, Ternary Laves and Sigma-Phases of Transition Metals, *Acta Metallurgica* **1953**, *1*(6), 720–724.

[108] R. H. Jones, V. F. Zackay, E. R. Parker, Laves Phase Precipitation in Fa–Ta alloys, *Metallurgical Transactions* **1972**, *7*, 2835–2842.

[109] A. Raman, On the Tantalum-Iron system, *Transactions of the Indian Institute of Metals* **1966**, *19*, 202–205.

[110] L. Swartzendruber, E. Paul, *Binary Alloy Phase Diagrams, Second Edition*, pages 1776–1778, ASM International, Materials Park, Ohio **1990**.

[111] *STOE Win XPOW, Version 1.2 Stoe & Cie. GmbH, Darmstadt 2001.*

[112] H. M. Rietveld, Line profiles of neutron powder-diffraction peaks for structure refinement, *Acta Crystallographica* **1967**, *22(1)*, 151.

[113] H. M. Rietveld, Profile refinement method for nuclear und magnetic structures, *Acta Crystallographica* **1980**, *A36*, 610–614.

[114] V. Petricek, M. Dusek, L. Palatinus, Jana2006. The crystallographic computing system **2006**.

[115] *CrystalClear: An Integrated Program for the Collection and Processing of Area Detector Data, Rigaku Corporation, ©1997-2002.*

[116] M. Born, R. Oppenheimer, Zur Quantentheorie der Molekeln, *Annalen der Physik* **1927**, *389*(20), 457–484.

[117] P. Hohenberg, W. Kohn, Inhomogeneous Electron Gas, *Physical Review* **1964**, *136*(3B), B864–B871.

[118] W. Kohn, L. J. Sham, Self-Consistent Equations Including Exchange and Correlation Effects, *Phys. Rev.* **1965**, *140*(4A), A1133–A1138.

[119] G. Kresse, J. Hafner, Ab initio molecular dynamics for liquid metals, *Physical Review B* **1993**, *47*(1), 558–561.

[120] G. Kresse, J. Hafner, Ab initio molecular-dynamics simulation of the liquid-metal–amorphous-semiconductor transition in germanium, *Physical Review B* **1994**, *49*(20), 14251–14269.

[121] G. Kresse, J. Furthmüller, Efficiency of ab-initio total energy calculations for metals and semiconductors using a plane-wave basis set, *Computational Materials Science* **1996**, *6*(1), 15–50.

[122] G. Kresse, J. Furthmüller, Efficient iterative schemes for ab initio total-energy calculations using a plane-wave basis set, *Physical Review B* **1996**, *54*(16), 11169–11186.

[123] G. Kresse, J. Hafner, Norm-conserving and ultrasoft pseudopotentials for first-row and transition elements, *Journal of Physics: Condensed Matter* **1994**, *6*(10), 8245–8257.

[124] G. Kresse, D. Joubert, From ultrasoft pseudopotentials to the projector augmented-wave method, *Physical Review B* **1999**, *59*(3), 1758–1775.

[125] H. J. Monkhorst, J. D. Pack, Special points for Brillouin-zone integrations, *Physical Review B* **1976**, *13*(12), 5188–5192.

[126] K. Koepernik, H. Eschrig, Full-potential nonorthogonal local-orbital minimum-basis band-structure scheme, *Physical Review B* **1999**, *59*(3), 1743–1757.

[127] I. Opahle, K. Koepernik, H. Eschrig, Full-potential band-structure calculation of iron pyrite, *Physical Review B* **1999**, *60*(20), 14035–14041.

[128] A. Prince, *Alloy Phase Equlibria*, Elsevier Publishimg Company **1966**.

[129] S. Stølen, T. Grande, *Chemical Thermodynamics of Materials — Macroscopic and Microscopic Aspects*, Wiley & Sons, Ltd. **2004**.

[130] O. Redlich, A. T. Kister, Algebraic Representation of Thermodynamic Properties and the Classification of Solutions, *Industrial and Engineering Chemistry* **1948**, *40*(2), 345–348.

[131] M. Hillert, Partial Gibbs energies from Redlich-Kister polynomials, *Thermochimica Acta* **1988**, *129*(1), 71–75.

[132] P. K. Janert, *Gnuplot in Action*, Manning, Greenwich **2010**.

[133] *http://www.scipy.org/Cookbook/Finding_Convex_Hull*.

[134] J. P. Perdew, K. Burke, M. Ernzerhof, Generalized Gradient Approximation Made Simple, *Physical Review Letters* **1996**, *77*(18), 3865–3868.

[135] P. E. Blöchl, Projector augmented-wave method, *Physical Review B* **1994**, *50*(24), 17953–17979.

[136] A. Kerkau, *Untersuchungen zum Stabilitätsbereich und zur Fehlordnung der ternären Laves-Phase Nb(*$Cr_{1-x}Co_x$*)*$_2$, Diplomarbeit, Technische Universität Dresden **2007**.

[137] A. Kerkau, D. Grüner, A. Ormeci, Y. Prots, H. Borrmann, W. Schnelle, E. Bischoff, Y. Grin, G. Kreiner, Site Occupation Reversal in the C14 Laves Phase Nb($Cr_{1-x}Co_x$)$_2$, *Zeitschrift für Anorganische und Allgemeine Chemie* **2009**, *635*(4-5), 637–648.

[138] D. Lide (Editor), *CRC Handbook of chemistry and physics*, CRC Press, 87 edition **2006**.

[139] M. G. Louise, E. Parthé, STRUCTURE TIDY - a computer program to standardize crystal structure data, *Journal of Applied Crystallography* **1987**, *20*, 139–143.

[140] H. Wada, M. Hada, M. Shiga, Y. Nakamura, Low Temperature Specific Heat of Laves Phase AFe_2 Compounds (A = Nb, Ta and Ti), *Journal of the Physical Society of Japan* **1990**, *59*, 701–705.

[141] H. Wada, M. Shiga, Y. Nakamura, Weak Ferromagnetism of $Ta_{1-x}Ti_xFe_2$, *Journal de Physique* **1988**, *49*, 267–268.

[142] A. M. Van Der Kraan, K. H. J. Buschow, The Fe-57 Isomer Shift in Intermetallic Compounds of Iron, *Physica B & C* **1986**, *4138*, 55–62.

[143] Y. Muraoka, M. Shiga, Y. Nakamura, Magnetic Properties and Thermal Expansion of ($Zr_{1-x}Ta_x$)Fe_2, *Physica Status Solidi A - Applied Research* **1983**, *78*, 717–722.

[144] B. S. Bokshtein, N. P. D'Yakonova, G. S. Nikol'skii, Y. D. Yagodkin, The Correlation between the Isomeric Shift for the Iron-57 Nuclei and Interaction Parameters of Components in Transition Metal Laves Phases of RFe_2-Type (R = Transition Metal), *Russian Journal of Physical Chemistry* **1977**, *51*, 1273–1276.

[145] R. P. Elliott, W. Rostoker, On the Occurrence of Laves Type Phases Among Transition Elements, *Transactions of the American Society of Metals* **1958**, *50*, 617–633.

[146] H. J. Wallbaum, Ergebnisse der röntgenographischen Strukturuntersuchung von Legierungen der Zusammensetzung AB_2 der Eisenmetalle mit Titan, Zirkon, Niob und Tantal, *Zeitschrift für Kristallographie* **1941**, *103*, 391–402.

[147] L. S. Guzei, E. M. Sokolovskaya, I. G. Sokolova, G. V. Vysotskaya, G. N. Ronami, S. M. Kuznetsova, Phase Equlibria in the system Vanadium–Tantalum-Hafnium, *Vestnik Moskovskogo Universiteta Seriya 2 Khimiya* **1970**, *11*(6), 696–699.

[148] H. Lueken, *Magnetochemie: Eine Einführung in Theorie und Anwendung*, Teubner **1999**.

[149] A. Ormeci, F. Chu, J. M. Wills, T. E. Mitchell, R. C. Albers, D. J. Thoma, S. P. Chen, Total-energy study of electronic structure and mechanical behavior of C15 Laves phase compounds: $NbCr_2$ and HfV_2, *Physical Review B* **1996**, *54*(18), 12753–12762.

[150] D. Moroni-Klementowicz, M. Brando, C. Albrecht, W. J. Duncan, F. M. Grosche, D. Grüner, G. Kreiner, Magnetism in $Nb_{1-y}Fe_{2+y}$: Composition and magnetic field dependence, *Physical Review B* **2009**, *79*(22), 224410.

[151] W. J. Duncan, O. P. Welzel, D. Moroni-Klementowicz, C. Albrecht, P. G. Niklowitz, D. Grüner, M. Brando, A. Neubauer, C. Pfleiderer, N. Kikugawa, A. P. Mackenzie, F. M. Grosche, Quantum phase transitions in $NbFe_2$ and $Ca_3Ru_2O_7$, *Physica Status Solidi B* **2010**, *247*(3), 544–548.

[152] U. Müller, *Inorganic Structural Chemistry*, Wiley **2007**.

[153] V. V. Petkov, V. N. Svechnikov, On the Character of Laves Phases Interaction in the Systems $Zr(Fe,Co,Ni)_2$–ZrV_2, *Dopovidi Akademii Nauk Ukrains'koi RSR, Seriya A: Fiziko-Tekhnichni ta Matematichni Nauki* **1972**, *32*, 664–667.

[154] P. Villars, A. Prince, H. Okamoto, *Handbook of Ternary Alloy Phase Diagrams: Co–Fe–Ni — Cu–Mg–Sb*, Handbook of Ternary Alloy Phase Diagrams, ASM International **1997**.

[155] D. Shaltiel, I. Jacob, D. Davidov, Hydrogen absorption and desorption properties of AB_2 laves-phase pseudobinary compounds, *Journal of the Less Common Metals* **1977**, *53*(1), 117–131.

[156] O. Prymak, F. Stein, The ternary CrâĂŞAlâĂŞNb phase diagram: Experimental investigations of isothermal sections at 1150, 1300 and 1450°C, *Journal of Alloys and Compounds* **2012**, *513*, 378 – 386.

[157] C. He, F. Stein, Thermodynamic Assessment of the Cr–Al–Nb System, *International Journal of Materials Research* **210**, *11*, 1369–1375.

[158] V. Raghavan, Al–Cr–Nb (Aluminum-Chromium-Niobium), *Journal of Phase Equilibria and Diffusion* **2011**, *online first*, 1–2.

[159] S. Asano, S. Ishida, Magnetism and Crystal-Structure of Laves Phase-Compounds, *Journal of Physics F-Metal Physics* **1988**, *18*(3), 501–515.

[160] *VASP the GUIDE*, Computational Physics, Faculty of Physics, Universität Wien, Sensengasse 8, A-1130 Wien, Austria **2009**.

List of publications and conference contributions

Publications

1. D. Grüner, E. Bischoff, A. Kerkau, A. Ormeci, Y. Prots, H. Borrmann and G. Kreiner, Site occupation reversal in the C14 Laves phase $Nb(Cr_{1-x}Co_x)_2$, *Zeitschrift für Anorganische und Allgemeine Chemie* **2008**, 634(11), 2040.

2. O. Prymak, F. Stein, A. Kerkau, A. Ormeci, G. Kreiner, G. Frommeyer and D. Raabe, Phase equilibria in the ternary Nb-Cr-Al system and site occupation in the hexagonal C14 Laves phase $Nb(Al_xCr_{1-x})_2$, *Materials Research Society Symposium Proceedings* **2009**, 1128, 499–504.

3. A. Kerkau, D. Grüner, A. Ormeci, Y. Prots, H. Borrmann, W. Schnelle, E. Bischoff, Y. Grin and G. Kreiner, Site Occupation Reversal in the C14 Laves Phase $Nb(Cr_{1-x}Co_x)_2$, *Zeitschrift für Anorganische und Allgemeine Chemie* **2009**, 635(4-5), 637–648.

Publications that were not covered in this thesis

1. B. Davaasuren, E. Dashjav, A. Kerkau, G. Kreiner, W. Schnelle, F. R. Wagner and R. Kniep, Synthesis, Crystal and Electronic Structure of a Samarium Carbochromate(III), $Sm_2[Cr_2C_3]$, *Zeitschrift für Anorganische und Allgemeine Chemie* **2009**, 635(12), 1741–1745.

2. K. Meier, C. Koz, A. Kerkau and U. Schwarz, Crystal structure of samarium pentagermanide, $SmGe_5$, *Zeitschrift für Kristallographie – New Crystal Structures* **2009**, 224(3), 349–350.

3. K. Meier, A. Kerkau and U. Schwarz, Crystal structures of gadolinium pentagermanide, $GdGe_5$ and neodymium pentagermanide, $NdGe_5$, *Zeitschrift für Kristallographie – New Crystal Structures* **2009**, 224(3), 373–374.

4. A. Kerkau and G. Kreiner, Crystal structure of niobium aluminium cobalt, $Nb(Al_{0.62}Co_{0.38})_2$, *Zeitschrift für Kristallographie – New Crystal Structures* **2010**, 225(4), 621–622.

5. A. Kerkau, L. Wu, K. S. Park, Y. Prots, M. Brando, M. C. Meigan, C. Aronson and G. Kreiner, Crystal structure of Yttrium Diiron Decaaluminide, YFe_2Al_{10}, *Zeitschrift für Kristallographie – New Crystal Structures* **2012**, accepted.

Oral presentations

1. A. Kerkau, D. Grüner, A. Ormeci, A. Leineweber and G. Kreiner, Site occupancy reversal in the C14 Laves phase $Nb(Cr_{1-x}Co_x)_2$, *The Nature of Laves Phases IX*, Stuttgart, Germany **2007**.
2. A. Kerkau, Local structure of the Laves phase C15-$NbCo_2$ – First results, *The Nature of Laves Phases X*, Dresden, Germany **2008**.
3. A. Kerkau, Preferential site occupation in C14 Laves phases $A(B'_{1-x}B''_x)_2$ with A=Hf, Nb, Zr and B=Al, Cr, Co, *The Nature of Laves Phases XI*, Düsseldorf, Germany **2008**.
4. A. Kerkau, Site occupation reversal in ternary C14 Laves phases $A(B'_{1-x}B''_x)_2$, *6. Mitteldeutsches Anorganiker Nachwuchssymposium (MANS)*, Freiberg, Germany **2008**.
5. A. Kerkau, A. Ormeci, D. Grüner, E. Bischoff, H. Borrmann, Y. Grin and G. Kreiner, Homogeneity range and substitutional disorder in the ternary C14 Laves phase $Nb(Cr_{1-x}Co_x)_2$, *Fall Meeting of the Materials Research Society*, Boston, USA **2008**.
6. A. Kerkau, The local structure of Laves phases, *The Nature of Laves Phases XII*, Dresden, Germany **2009**.
7. A. Kerkau, c/a-ratio in hexagonal Laves phases and in the ternary Fe–Ta–V system, *The Nature of Laves Phases XIII*, Düsseldorf, Germany **2009**.
8. A. Kerkau, Yu. Grin and G. Kreiner, Cell Geometry, Short Range Order and Phase Stability of Ternary Laves Phases $A(B'_{1-x}B''_x)_2$ by First-Principles Calculations, *CMAC Days*, Liverpool, England **2011**.

Poster presentations

1. A. Kerkau, G. Kreiner and A. Ormeci, Theoretical Study of Site Preference in Ternary C14 Laves Phases $A(B'_{1-x}B''_x)_2$, *16. International Conference on Solid Compounds of Transition Elements (SCTE)*, Dresden, Germany **2008**.
2. A. Kerkau, E. Bischoff, A. Ormeci, Y. Prots, H. Borrmann, D. Grüner and G. Kreiner, Site Occupation Reversal in the C14 Laves Phase $\mathrm{Nb(Cr_{1-x}Co_x)_2}$, *13. Vortragstagung der GDCh-Fachgruppe Festkörperchemie und Materialforschung*, Bayreuth, Germany **2008**.
3. L. Siggelkow, A. Kerkau, U. Burkhardt, G. Kreiner, M. Palm, F. Stein and W. Carillo-Cabrera, Unusual Mechanical Behavior of the Intermetallic Phase $\mathrm{Nb_2Co_7}$, *4. CMA European School in Material Science*, Ljubljana, Slovenia **2009**.
4. A. Kerkau and G. Kreiner, Stability Range and Preferential Site Occupation of the Laves Phases $\mathrm{Ta(V_{1-x}Fe_x)_2}$, *17. International Conference on Solid Compounds of Transition Elements (SCTE)*, Annecy, France **2010**.
5. A. Kerkau and G. Kreiner, Stability Range and Preferential Site Occupation of the Laves Phases $\mathrm{Ta(V_{1-x}Fe_x)_2}$, *CMAC Days*, Dresden, Germany **2010**.
6. P. Khuntia, M. Baenitz, M. Brando, A. Kerkau, G. Kreiner and F. Steglich, Quantum Criticality in $\mathrm{Ta(Fe_{1-x}V_x)_2}$ Probed by ^{51}V NMR and Magnetization, *DPG Frühjahrstagung*, Berlin, Germany **2012**.

Curriculum vitae

Personal Data

Name: Alexander Kerkau

Date of birth: June 9th, 1980

Place of birth: Dresden, Germany

Education

12/2007 – present	Max Planck Institute for Chemical Physics of Solids (MPI CPFS), Dresden; candidate for Dr. rer. nat.
10/2000 – 11/2007	Technical University Dresden (TUD), study course: Werkstoffwissenschaft; Diplom-Ingenieur
08/1997 – 07/1999	Gymnasium Kreuzschule, Dresden; advanced courses: mathematics, physics; Abitur

Work experience

08/2006 – 12/2006	Queen's University, Department of Physics, Engineering Physics & Astronomy, Kingston, Ontario, Kanada; student research assistant
09/2004 – 02/2005	Hilti Corporation, Schaan, Principality of Liechtenstein; student research assistant

Attended workshops and lectures

1. 2. CMA European School in Material Science – Properties and Application of Complex Metallic Alloys, Ljubljana, Slovenia, May 21 – 26, **2007**.
2. Workshop – The Nature of Laves Phases IX, Stuttgart, Germany, September 20 – 21, **2007**.

3. PDF Powder Diffraction Workshop – Total Scattering Pair Distribution Function analysis using X-rays and neutrons: powder diffraction and complementary techniques, Grenoble, France, October 22 – 23, **2007**.
4. Lecture: Chemie der Nebengruppenelemente, Prof. Gloe, TU-Dresden, **2008**.
5. Lecture: Festkörperchemie 2, Prof. Kieback / Prof. Grin, TU-Dresden, **2008**.
6. Workshop – The Nature of Laves Phases X, Dresden, Germany, January 10, **2008**.
7. Workshop – The Nature of Laves Phases XI, Düsseldorf, Germany, June 16 –17, **2008**.
8. 6. Kieler Workshop – Fehler, Fallen und Probleme in der Einkristallstrukturanalyse, July 20 – 24, **2008**.
9. Lecture: Anorganische Festkörperchemie, Prof. Ruck, TU-Dresden, **2008/2009**.
10. Lecture: Ungewöhnliche Metalle, Prof. Ruck, TU-Dresden, **2009**.
11. Workshop – The Nature of Laves Phases XII, Dresden, Germany, January 30, **2009**.
12. 4. CMA European School in Material Science – Mechanical Properties of Complex Metallic Alloys, Ljubljana, Slovenia, May 25 – 30, **2009**.
13. Max Planck PhDnet Soft Skill Seminar: Scientific Posters, Dresden, Germany June 26, **2009**.
14. Workshop on Preparation, Thermodynamics, Phase Equilibria, Solidification and Structures of Alloys and Intermetallic Compounds, Ulaanbaatar, Mongolia, September 1 – 11, **2009**.
15. DFT meets Solid State Chemistry & 8th Tutorial Hands-on-FPLO, Dresden, Germany, October 25 – 29, **2009**.
16. Workshop – The Nature of Laves Phases XIII, Düsseldorf, Germany, November 10, **2009**.
17. Lecture: Chemische Bindung, Prof. Seifert, TU-Dresden, **2009/2010**.

18. Lecture: Fachinformatik in der Werkstoffwissenschaft, Prof. Bauch, TU-Dresden, **2009/2010**.
19. 5. CMA European School in Material Science – Properties of Complex Metallic Alloys: Modeling, Simulation and Experiment, Ljubljana, Slovenia, May 24 – 29, **2010**.
20. Jana2006 – A Crystallographic Computing System, Dresden, Germany, September 22 – 24, **2010**.

Versicherung

Hiermit versichere ich, dass ich die vorliegende Arbeit ohne unzulässige Hilfe Dritter und ohne Benutzung anderer als der angegebenen Hilfsmittel angefertigt habe; die aus fremden Quellen direkt oder indirekt übernommenen Gedanken sind als solche kenntlich gemacht. Die Arbeit wurde bisher weder im Inland noch im Ausland in gleicher oder ähnlicher Form einer anderen Prüfungsbehörde vorgelegt.

Die vorliegende Dissertation wurde unter Betreuung von Herrn Prof. Juri Grin und Herrn Priv.-Doz. Dr. Guido Kreiner in der Zeit von Dezember 2007 bis August 2012 am Max-Planck-Institut für Chemische Physik fester Stoffe in Dresden angefertigt.

Es haben keine früheren erfolglosen Promotionsverfahren stattgefunden.

Ich erkenne die Promotionsordung der Fakultät Mathematik und Naturwissenschaften der Technischen Universität Dresden vom 23.02.2011 in vollem Umfang an.

Dresden, den

(Alexander Kerkau)